COMSAT
Technical Review

Volume 17 Number 2, Fall 1987

COMSAT TECHNICAL REVIEW is published twice a year by Communications Satellite Corporation (COMSAT). Subscriptions, which include the two issues published within a calendar year, are: one year, $15 U.S.; two years, $25; three years, $35; single copies, $10; article reprints, $2.50. Overseas air mail delivery is available at an additional cost of $18 per year. Make checks payable to COMSAT and address to Records Department, Communications Satellite Corporation, 22300 Comsat Drive, Clarksburg, MD 20871-9475, U.S.A.

ISSN 0095-9669

COMSAT TECHNICAL REVIEW

Volume 17 Number 2, Fall 1987

Index: digital transmission, error control, small terminals, coding, modulation, demodulation, modems

Differentially coherent FEC block coding

S. A. RHODES

(Manuscript received October 24, 1986)

Abstract

Principles of differentially coherent communications on a symbol-by-symbol basis are extended to code blocks. The relative phasings of code patterns within each block and the relative carrier phases of successive blocks are used to produce binary phase-shift keying (BPSK) combined with block coding for forward error correction (FEC) coding. Differentially coherent block coding (DCBC) can yield significant coding gain relative to the performance of uncoded BPSK with differentially coherent detection (DC-BPSK).

DCBC is of particular importance for low-speed digital communications where the channel dynamics of oscillator phase noise and Doppler rate may not allow reliable coherent detection. For the case of a static channel corrupted by additive Gaussian noise, DCBC is shown to yield better performance than coded DC-BPSK with other FEC codings of similar complexity. A code block of length $N = 16$ BPSK symbols for DCBC enables a coding gain of 3.9 dB to be achieved relative to uncoded DC-BPSK performance at a bit error probability of 10^{-6}.

Introduction

Although binary phase-shift keying (BPSK) is not very efficient in terms of bandwidth utilization, it is efficient on a power basis when used in conjunction with coding for forward error correction (FEC) coding. Also, binary modulation is the least sensitive to performance degradation caused by channel imperfections. Therefore, BPSK is usually employed for low-speed communications for which bandwidth efficiency is not critical.

Optimum BPSK performance requires the use of coherent detection. For maximum power efficiency, the BPSK carrier is fully modulated, which results in a suppressed-carrier transmission. In order to obtain the carrier reference required for coherent demodulation of BPSK, the modulation must be removed and the carrier phase averaged over some number of symbol intervals to increase the signal-to-noise power ratio (S/N) of the reference. In the case of low energy-per-bit to noise-power-density ratio (E_b/N_o) operation achieved by using powerful FEC coding, sufficient S/N of the reference for coherent detection can only be obtained by averaging carrier phase over many received BPSK symbols.

At information rates below 1,000 bit/s, the channel may not remain static over the averaging interval necessary to obtain the coherent reference. At such low speed, the dynamics of oscillator phase noise and Doppler rate can result in significant changes in the carrier phase over the averaging interval, making coherent detection impractical over some communications channels.

A typical solution to the problem of dynamic phase at low speed involves the use of differentially coherent (DC) detection. For DC-PSK, the preceding symbol serves as a noisy coherent reference for detection of the present symbol. Because the message is conveyed by relative rather than absolute phase, coherence is required only over two symbol intervals for DC-PSK.

Uncoded DC-BPSK performance is only slightly inferior to uncoded coherent BPSK for communications over a static channel at low bit error probabilities. Consequently, DC-BPSK is a good choice for low-speed communications that have adequate E_b/N_o to provide a low bit error probability, such as $P_b = 10^{-6}$, without FEC coding. FEC coding is employed to enable low P_b to be achieved at low E_b/N_o. Unfortunately, coded DC-BPSK performs quite poorly at a low P_b compared to coded coherent BPSK, with E_b/N_o requirements increased by 2 dB or more when $P_b = 10^{-6}$. Hence, coded DC-BPSK may not be an appropriate solution for low-speed communications over a channel that supports only a low E_b/N_o.

For low-speed applications, it is desirable to achieve coded communications that are fairly insensitive to channel dynamics but do not suffer the performance reduction of coded DC-BPSK. Although the phase coherence of the received transmission may not be maintained over a sufficient number of BPSK symbols for reliable coherent detection to be feasible at low E_b/N_o, quasi-coherence may be manifested over an interval as large as an FEC code block of moderate length. A combined modulation/coding scheme of differentially coherent block coding (DCBC) is described that makes use of both the coherence over a short code block and the relative carrier phases of the present and preceding blocks. By using quasi-coherence over two code blocks, DCBC can provide coding performance for low-speed communications over a dynamic channel which is almost as good as the performance of coded BPSK with coherent detection over a static channel.

Reuse of the energy in the previous symbol allows DC-BPSK to have a 3-dB performance superiority over orthogonal binary frequency-shift keying (BFSK). The same principle of energy reuse is extended to blocks in DCBC by using the carrier phase of the previous code block as a phase reference for the present code block. Although the modulation within each block is BPSK, there are four possible phase angles for the carrier. The use of quaternary differential phase encoding of the carrier for successive code blocks provides two additional information bits per block.

Detection of quaternary phase-shift keying (QPSK) is usually performed separately for the binary components of the quaternary modulation. Although these components are orthogonal for coherent detection, the noisy reference for DC-QPSK detection results in cross-coupling interference between the binary components. In order for DC-QPSK not to degrade overall DCBC decoding performance, a special encoding of two chips per BPSK symbol has been incorporated that cancels the cross-coupling interference.

In this paper, DCBC is described in terms of signal generation and demodulation/decoding of this new form of coded modulation. Theoretical performance evaluations are also presented. It is shown that DCBC performance is superior to that of coded DC-BPSK with FEC coding of comparable complexity. Therefore, DCBC is a suitable signaling method for low-speed applications in which oscillator phase noise and/or Doppler rate do not allow reliable coherent detection.

Quantitative evaluations for DCBC were made only for the static channel, and further work will be necessary in order to assess the additional degradation caused by phase dynamics as a function of such factors as modulation rate and phase noise density. At present, it can only be stated qualitatively that some suitable combinations of modulation rate and phase dynamics for DCBC exist for which quasi-coherence is maintained over more than the two symbol intervals required for DC-BPSK detection, but less than the number of symbol intervals necessary to extract a reliable carrier reference for coherent detection.

Description of DCBC

DCBC exploits two properties of DC-BPSK. First, DC-BPSK can be considered as a degenerate set of two orthogonal codewords of length $N = 1$ each. This interpretation is based on obtaining two orthogonal envelopes from the sums and differences of the present and preceding PSK symbols. DCBC extends the block length to $N = 2^n$. Second, DCBC extends the differentially coherent concept of DC-BPSK to DC detection between two code blocks. The code

block for DCBC consists of an orthogonal code set of N words of length N each. Also, each code block of N symbols has four possible carrier phases relative to the carrier phase for the previous code block.

For orthogonal codes [1],[2], the $N = 2^n$ codewords are obtained from a basis set of n codewords plus the codeword of all zeros. As an example, Table 1 presents the extended basis set of $n + 1$ words for an orthogonal code of length $N = 8$. The total orthogonal set consists of all the linear combinations of words from the orthogonal basis set, as given in Table 2.

TABLE 1. EXTENDED BASIS SET FOR GENERATING AN ORTHOGONAL CODE OF LENGTH $N = 8$

BASIS NUMBER	CODE WORD							
0	0	0	0	0	0	0	0	0
$2^0 = 1$	0	1	0	1	0	1	0	1
$2^1 = 2$	0	0	1	1	0	0	1	1
$2^2 = 4$	0	0	0	0	1	1	1	1

TABLE 2. DERIVATION OF AN ORTHOGONAL CODE FROM ITS BASIS SET

ORTHOGONAL WORD NUMBER	TERMS OF BASIS SET	CODE WORD							
0	0	0	0	0	0	0	0	0	0
1	1	0	1	0	1	0	1	0	1
2	2	0	0	1	1	0	0	1	1
3	1 + 2	0	1	1	0	0	1	1	0
4	4	0	0	0	0	1	1	1	1
5	1 + 4	0	1	0	1	1	0	1	0
6	2 + 4	0	0	1	1	1	1	0	0
7	1 + 2 + 4	0	1	1	0	1	0	0	1

By itself, each orthogonal word of length $N = 2^n$ BPSK modulation symbols represents n information bits. With the two additional information bits sent by quaternary differential coding of the carrier phases of successive code blocks, a total of $b = n + 2$ information bits are conveyed by each block. The n information bits with values of 0 and 1 are represented for the mth code block by d_{mj}, where j takes on values from 0 to $n - 1$. In general, the word number for the mth code block is related to the bit values, d_{mj}, as follows:

$$w_m = \sum_{j=0}^{n-1} d_{mj} 2^j \quad . \tag{1}$$

In the transmission of a code block by BPSK, binary 0 and 1 values for the N code symbols of each word are mapped into modulation coefficients of $+1$ and -1, respectively. Let D_{mi} denote the modulation coefficient for the ith BPSK symbol of the mth code block. Then the BPSK transmission is defined during this modulation symbol by

$$s_{mi}(t) = \sqrt{2C}\, D_{mi} \cos(2\pi f_c t - \theta_m) \tag{2}$$

where C = carrier power
$f_c = \omega_c/2\pi$ = carrier frequency
θ_m = carrier phase for the mth code block.

There are four possible values of θ_m which are related to the carrier phase θ_{m-1} for the previous block by quaternary differential encoding. Let λ_m denote the phase change for the mth code block. Then,

$$\theta_m = \theta_{m-1} + \lambda_m \tag{3}$$

where the change λ_m in carrier phase can take on values of 0, 0.5π, π, and 1.5π radians.

It is convenient for the carrier to be generated as the sum of two quadrature components with individual "modulation" coefficients, A_m and B_m. With θ_m constrained to values of -0.75π, -0.25π, $+0.25\pi$, and $+0.75\pi$ radians, these coefficients have ± 1 values in accordance with

$$A_m = \sqrt{2}\cos\theta_m$$
$$B_m = \sqrt{2}\sin\theta_m \quad . \tag{4}$$

Hence the QPSK carrier for the mth block may be obtained from the sum of two BPSK signals that have carriers which are in phase quadrature, as

$$\sqrt{2}\cos(\omega_c t - \theta_m) = A_m \cos\omega_c t + B_m \sin\omega_c t \quad . \tag{5}$$

Then, the transmission during the ith symbol of the mth block can be expressed in the following form, which is very useful for signal generation:

$$S_{mi}(t) = \sqrt{C}\, D_{mi}[A_m \cos(\omega_c t) + B_m \sin(\omega_c t)] \quad . \tag{6}$$

For coherent demodulation of QPSK into two binary components, the signal constellation lies along a set of orthogonal axes that is offset by 0.25π radians relative to the coherent phase reference at 0° along the x axis. Similarly, the carrier phase reference, Λ_m, for DC-QPSK is the carrier phase of the previous code block shifted by 0.25π rad, as

$$\Lambda_m = \theta_{m-1} - 0.25\pi \quad . \tag{7}$$

Then the phase shift ζ for DC-QPSK is defined as the difference between θ_m and the reference phase, as

$$\zeta_m = \theta_m - \Lambda_m = \lambda_m + 0.25\pi \quad . \tag{8}$$

It follows that the carrier phase for the mth code block is

$$\theta_m = \Lambda_m + \zeta_m = (\theta_{m-1} - 0.25\pi) + \zeta_m \quad . \tag{9}$$

The change, λ_m, in carrier phase is determined from the binary logic values of two information bits, α_m and β_m. These bits can take on values of 0 and 1 to yield

$$\lambda_m = 0.5\pi(\alpha_m - \beta_m) + \pi\alpha_m\beta_m \quad . \tag{10}$$

Corresponding to each pair of information bits, α_m and β_m, is a pair of binary differential modulation coefficients a_m and b_m. Each of these coefficients takes on ± 1 values, as given by

$$\begin{aligned} a_m &= \sqrt{2}\cos\zeta_m = 1 - 2\alpha_m \\ b_m &= \sqrt{2}\sin\zeta_m = 1 - 2\beta_m \end{aligned} \quad . \tag{11}$$

It is therefore possible to express the carrier for the mth code block by

$$\begin{aligned} \sqrt{2}\cos(\omega_c t - \theta_m) &= \sqrt{2}\cos(\omega_c t - \Lambda_m - \zeta_m) \\ &= a_m\cos(\omega_c t - \Lambda_m) + b_m\sin(\omega_c t - \Lambda_m) \end{aligned} \quad . \tag{12}$$

Thus, an alternative expression for the transmitted signal is

$$S_{mi}(t) = \sqrt{C}\,D_{mi}[a_m\cos(\omega_c t - \Lambda_m) + b_m\sin(\omega_c t - \Lambda_m)] \quad . \tag{13}$$

Vector notation is useful in defining the relationships of the absolute modulation coefficients, A_m and B_m, to the differential coefficients, a_m and b_m. Let the carrier vectors for the $(m-1)$th and mth code blocks be defined as

$$\begin{aligned} C_{m-1} &= \sqrt{2}e^{j\theta_{m-1}} = A_{m-1} + jB_{m-1} \\ C_m &= \sqrt{2}e^{j\theta_m} = A_m + jB_m \end{aligned} \quad . \tag{14}$$

Similarly, the differential carrier phase vector may be defined by

$$c_m = \sqrt{2}e^{j\zeta_m} = a_m + jb_m \quad . \tag{15}$$

The reference vector for differential QPSK has unity magnitude and a phase angle of Λ_m, as

$$R_m = e^{j\Lambda_m} = e^{j(\theta_{m-1} - 0.25\pi)} = \frac{A_{m-1} + B_{m-1}}{2} - j\frac{A_{m-1} - B_{m-1}}{2} \quad . \tag{16}$$

With these definitions, the QPSK vector for the carrier of the mth block is given by the product of R_m and c_m, as

$$C_m = A_m + jB_m = c_m R_m \quad .$$

Hence, the binary components of the QPSK carrier vector for the mth code block are obtained as follows, as

$$\begin{aligned} A_m &= a_m\frac{A_{m-1} + B_{m-1}}{2} + b_m\frac{A_{m-1} - B_{m-1}}{2} \\ B_m &= b_m\frac{A_{m-1} + B_{m-1}}{2} - a_m\frac{A_{m-1} - B_{m-1}}{2} \end{aligned} \quad . \tag{17}$$

Coherent detection of DCBC transmissions can be performed if the modulation symbol rate is sufficiently high so that phase coherence is maintained over several code blocks. In such a case, the transmission would be as just described. However, the major interest in terms of DCBC communications is in channels that are not quasi-static over a sufficient number of modulation symbols for a reliable coherent reference to be obtained. In DC-QPSK detection of the differential carrier phase for successive code blocks, there is cross-coupling interference between the two binary components, a_m and b_m, of the

differential carrier vector. As explained later, this cross-coupling would cause performance deterioration for DCBC without some compensation to nullify the interference. A novel method of precoding of the symbol waveforms has been formulated that allows cancellation of the cross-coupling interference so that orthogonality is achieved in the DC-QPSK detection of a_m and b_m.

In the precoding for cross-coupling cancellation, each BPSK symbol of duration T_s is divided into two modulation chips of duration 0.5 T_s each. With two chips per BSPK modulation symbol, the signal bandwidth is doubled. The application of DCBC would be for signals with low symbol rates, R_s, and corresponding narrow bandwidth. In such cases, the long-term frequency uncertainty of the transmission may dominate actual signal bandwidth in determining the required frequency allocation. Therefore, spectral spreading by a factor of 2 as a result of the precoding may not significantly affect bandwidth efficiency.

Carrier phase for the mth code block has a value of θ_m, which is equal to the reference phase Λ_m plus the differential phase ζ_m. The transmission is modified in the precoding so that the direction of rotation for the differential phase is reversed on the second chip of each symbol interval. Thus, the carrier phases, θ_m and θ'_m, for the first and second chips of each symbol of the mth code block are given by

$$\begin{aligned} &\text{First chip:} && \theta_m = \Lambda_m + \zeta_m \\ &\text{Second chip:} && \theta'_m = \Lambda_m - \zeta_m \quad . \end{aligned} \tag{18}$$

Reversal of the rotation of ζ_m is equivalent to using the complex conjugate of the differential QPSK vector. Hence, the differential carrier vectors for the two chips of each BPSK symbol are

$$\begin{aligned} &\text{First chip:} && c_m = a_m + jb_m = \sqrt{2}e^{+j\zeta_m} \\ &\text{Second chip:} && c'_m = a_m - jb_m = \sqrt{2}e^{-j\zeta_m} \quad . \end{aligned} \tag{19}$$

Generation of DCBC transmission

Figure 1 illustrates the encoding and modulation required to generate the DCBC transmission. During each code block of $N = 2^n$ BPSK modulation symbols, $b = n + 2$ information bits are used to determine the total encoding for the transmission. Two of these bits, α_m and β_m, define the carrier phase angle for the mth code block, and the other n bits select the orthogonal word that determines the BPSK modulation for the N symbols of the mth code block.

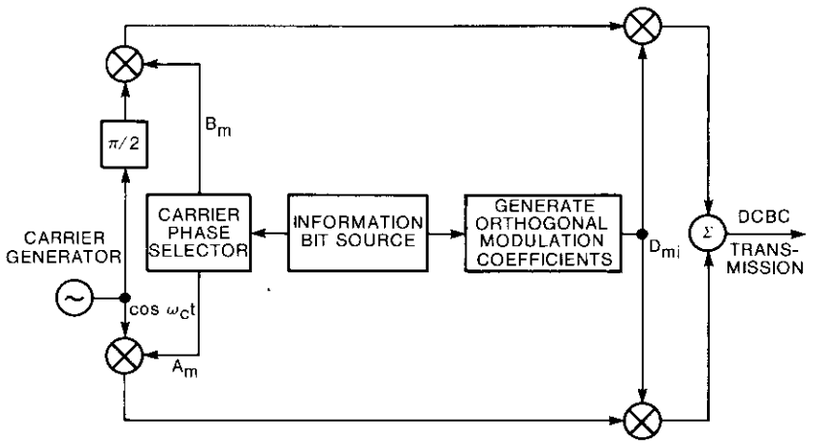

Figure 1. *Block Diagram for Generation of DCBC Transmission*

Coefficients A_m and B_m determine the carrier phase angle for the first chip of each BPSK symbol of the mth code block. The second chip of each symbol has a carrier phase θ'_m based on coefficients A'_m and B'_m, where

$$\begin{aligned} A'_m &= +a_m \frac{A_{m-1} + B_{m-1}}{2} - b_m \frac{A_{m-1} - B_{m-1}}{2} \\ B'_m &= -b_m \frac{A_{m-1} + B_{m-1}}{2} - a_m \frac{A_{m-1} - B_{m-1}}{2} \quad . \end{aligned} \tag{20}$$

Note that the coefficients for the carrier phase vector are related to their values in the previous block and to the differential coefficients, a_m and b_m. Table 3 presents this relationship.

TABLE 3. MAPPING FOR DC-QPSK CARRIERS

INFORMATION BIT VALUES		DIFFERENTIAL COEFFICIENTS		CARRIER PHASE CHANGE, λ_m	DIFFERENTIAL PHASE*	COEFFICIENTS FOR CARRIER VECTOR			
						1st CHIPS		2nd CHIPS	
β_m	α_m	b_m	a_m	(rad)	(rad)	B_m	A_m	B'_m	A'_m
0	0	+1	+1	0	$+0.25\pi$	$+B_{m-1}$	$+A_{m-1}$	$-A_{m-1}$	$+B_{m-1}$
0	1	+1	−1	$+0.5\pi$	$+0.75\pi$	$+A_{m-1}$	$-B_{m-1}$	$-B_{m-1}$	$-A_{m-1}$
1	1	−1	−1	π	-0.75π	$-B_{m-1}$	$-A_{m-1}$	$+A_{m-1}$	$-B_{m-1}$
1	0	−1	+1	-0.5π	-0.25π	$-A_{m-1}$	$+B_{m-1}$	$+B_{m-1}$	$+A_{m-1}$

* $\zeta_m = \lambda_m + \pi/4$.

The sequence of BPSK modulation coefficients for the orthogonal code as a function of the n information bit values may be generated by many techniques, including a lookup table. As an example, the coefficients are listed in Table 4 for the orthogonal word set of $N = 8$ codewords based on $n = 3$ information bits. The m subscript for the block number is omitted in this table; consequently, the modulation coefficients are listed as D_i rather than D_{mi}.

TABLE 4. MODULATION COEFFICIENTS FOR AN ORTHOGONAL CODE OF LENGTH $N = 8$

WORD NUMBER,	INFORMATION BIT VALUES			BPSK MODULATION COEFFICIENTS							
W	d_2	d_1	d_0	D_0	D_1	D_2	D_3	D_4	D_5	D_6	D_7
0	0	0	0	+1	+1	+1	+1	+1	+1	+1	+1
1	0	0	1	+1	−1	+1	−1	+1	−1	+1	−1
2	0	1	0	+1	+1	−1	−1	+1	+1	−1	−1
3	0	1	1	+1	−1	−1	+1	+1	−1	−1	+1
4	1	0	0	+1	+1	+1	+1	−1	−1	−1	−1
5	1	0	1	+1	−1	+1	−1	−1	+1	−1	+1
6	1	1	0	+1	+1	−1	−1	−1	−1	+1	+1
7	1	1	1	+1	−1	−1	+1	−1	+1	+1	−1

Although the n information bits may be mapped into modulation coefficients simply by a lookup table, there is a mathematical relationship between the two representations. Figure 2 illustrates an analytical approach in which the words of an orthogonal FEC code of length $N = 8$ are generated by a convolutional technique that uses $n = 3$ shift registers in parallel. Simpler encodings can be employed, but the convolutional technique gives a clear indication of the structure of the orthogonal words. Note that the use of n input information bits can yield $N = 2^n$ different words, where N is also the word length. Orthogonal codes and their generation are described in References 1 and 2.

Processing of the received DCBC transmission

A demodulator/decoder (Figure 3) is required for the reception of DCBC. The code block is decoded by digital processing of the baseband outputs, X and Y, for the detected BPSK chips. The demodulation uses quadrature carrier references with the correct frequency, but an arbitrary phase, to obtain the two baseband components. Low-pass filterings of X and Y are matched to the spectrum of the transmitted chip waveforms in order to maximize S/N

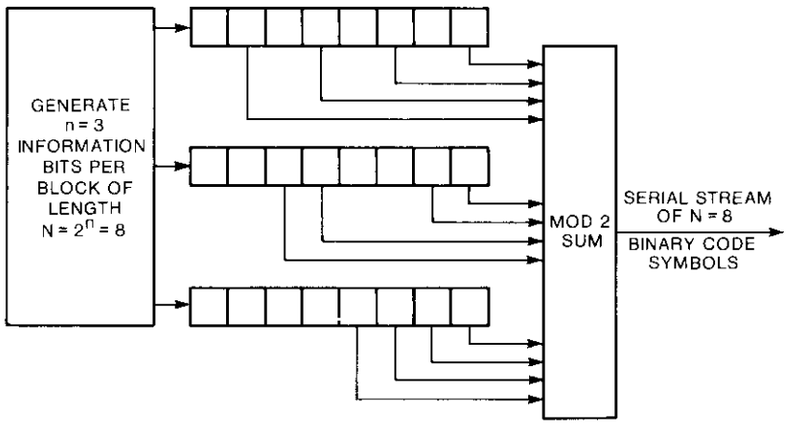

Figure 2. *Convolutional Method of Generating Block Code of Length* $N = 2^n$

prior to detection sampling once per chip, or twice per BPSK symbol interval. When overall Nyquist [3] filtering is used to zero the intersymbol interference (ISI) at the detection sampling instants, the matched filter has the square-root of the total Nyquist response.

A carrier synchronizer is required in the DCBC demodulator to provide the frequency reference for the quadrature demodulation. Also, a chip or symbol synchronizer provides the clock timing to control the detection sampling instants. Additionally, a block synchronizer is necessary in order to obtain time alignment with the beginning of each code block. These synchronizers must derive their references from the fully modulated, suppressed-carrier BPSK transmission. Methods of synchronization and synchronizer performance are not addressed in this paper. Refer to References 4, 5, and 6 for synchronization background. Perfect synchronizations are assumed later in the performance evaluation of DCBC communications over a static channel that is impaired only by additive white Gaussian noise (AWGN).

The received transmission is corrupted by additive noise from the channel and delayed by the propagation time that introduces a fixed phase delay, θ_s. Neglecting the noise terms, the following equations yield the signal expressions for the two chips of the ith BPSK symbol interval of the mth code block:

$$r_{mi} = \sqrt{2C}\, D_{mi} \cos(\omega_c t - \theta_s - \theta_m)$$
$$r'_{mi} = \sqrt{2C}\, D_{mi} \cos(\omega_c t - \theta_s - \theta'_m) \qquad (21)$$

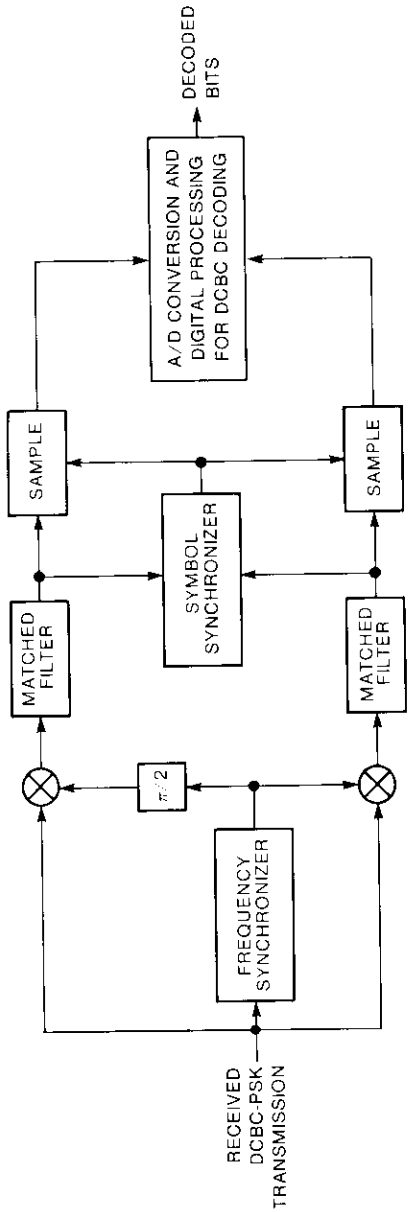

Figure 3. *Block Diagram for Signal Detection and Decoding of DCBC Transmissions*

where θ_m is the carrier phase for the mth block and θ'_m is the modified carrier phase for the second chip of each BPSK symbol interval. These angles are related to the reference angle (Λ_m) for DC-QPSK and to the differential carrier phase (ζ_m) by

$$\begin{aligned} \theta_m &= \Lambda_m + \zeta_m \\ \theta'_m &= \Lambda_m - \zeta_m \quad . \end{aligned} \tag{22}$$

For quadrature demodulation, the frequency reference has the same frequency, $f_c = \omega_c/2\pi$, as the carrier of the received transmission. However, the phase angle (θ_R) of the reference is some constant that is in error by an unknown value (Δ) with respect to the phase $\Lambda_m + \theta_s$ of an ideal coherent reference. Thus, the quadrature references for demodulation are

$$\begin{aligned} p(t) &= \sqrt{2}\cos(\omega_c t - \theta_R) \\ q(t) &= \sqrt{2}\sin(\omega_c t - \theta_R) \end{aligned} \tag{23}$$

where $\theta_R = \Lambda_m + \theta_s - \Delta$.

After quadrature demodulation and matched filtering of the quadrature components, detection produces the following two pairs of samples for the two chips of the ith BPSK symbol of the mth code block:

$$\text{First chip:} \begin{cases} X_{mi} = \sqrt{C}\, D_{mi}\cos(\Delta + \zeta_m) \\ Y_{mi} = \sqrt{C}\, D_{mi}\sin(\Delta + \zeta_m) \end{cases}$$

$$\text{Second chip:} \begin{cases} X'_{mi} = \sqrt{C}\, D_{mi}\cos(\Delta - \zeta_m) \\ Y'_{mi} = \sqrt{C}\, D_{mi}\sin(\Delta - \zeta_m) \end{cases} \quad . \tag{24}$$

These demodulation pairs can also be represented as complex samples:

$$\begin{aligned} Z_{mi} &= X_{mi} + jY_{mi} = \sqrt{C}\, D_{mi}\exp[j(\Delta + \zeta_m)] \\ Z'_{mi} &= X_{mi} - jY_{mi} = \sqrt{C}\, D_{mi}\exp[j(\Delta - \zeta_m)] \quad . \end{aligned} \tag{25}$$

Each code block is decoded sequentially in two steps. First, decisions are made on the n information bits of the mth orthogonal code block by determining which of the N orthogonal binary words corresponds best with

the $2N$ complex chip samples for the N BPSK symbols. A second processing is then employed to determine the two bits that are conveyed by the differential phase ζ_m of the carrier of the mth code block relative to the reference phase derived from the carrier of the $(m - 1)$th block.

Let U_{mk} and V_{mk} describe the two quadrature correlations for the modulation coefficients, D_{ki}, of the kth codeword, with the corresponding quadrature detection components, X_{mi} and Y_{mi}, for the first halves of the N symbols of the mth block. Similarly, use U'_{mk} and V'_{mk} to define the quadrature correlation components of the modulation coefficients of the kth of N codewords, with the corresponding quadrature detection components for the second half of the N symbols of the mth block. The resulting equations are

$$U_{mk} = \sum_{i=0}^{N-1} D_{ki} X_{mi}$$

$$V_{mk} = \sum_{i=0}^{N-1} D_{ki} Y_{mi}$$

$$U'_{mk} = \sum_{i=0}^{N-1} D_{ki} X'_{mi}$$

$$V'_{mk} = \sum_{i=0}^{N-1} D_{ki} Y'_{mi} \quad . \tag{26}$$

Note that coherent addition was employed to obtain the quadrature components over each half of the N symbol intervals. There is a $\pm\pi/2$-rad ambiguity as to the phasing of the second chip of each symbol relative to the phase of the first chip. Hence, block decoding based on coherent addition over both halves of the symbol would require that word correlations for both relative phasings be included, which would double the number of correlations. It is simpler to form separate metrics for each half and then add them, which is a form of noncoherent combining. Metrics based on envelopes are obtained from the correlations as follows:

$$\gamma_{mk} = [(U_{mk})^2 + (V_{mk})^2]^{0.5}$$

$$\gamma'_{mk} = [(U'_{mk})^2 + (V'_{mk})^2]^{0.5} \quad . \tag{27}$$

The noncoherent combining of these two metrics then yields an overall metric for the kth codeword, as

$$\Gamma_{mk} = \gamma_{mk} + \gamma'_{mk} \quad . \tag{28}$$

Overall metrics for all N orthogonal words are compared, and decoding selects the word with the greatest metric. The k subscript for the winning word will be dropped so that this decoded word for the mth block, and its corresponding correlations and metrics, will have only the m subscript. Also, the FEC decoder outputs the n bits associated with the winning word. This winning word has correlation coefficient pairs U_m, V_m, and U'_m, V'_m. Also, the metrics for each half of this word are termed γ_m and γ'_m, and its overall metric is Γ_m. A small performance loss is associated with the noncoherent combining necessary to obtain the overall metrics, as shown later in an evaluation of decoding error probability.

Multiplication of the detection voltages by the corresponding modulation coefficients of the corrected codeword is essentially a process of modulation removal. If additive noise does not result in decoding error, then U_m and V_m are the quadrature components of the carrier for the mth block. Thus, a signal vector $W_m = U_m + jV_m$ may be defined for the carrier of the mth code block. A reference vector, R_m, for differential QPSK detection of the carrier phase of the mth block will have already been obtained from the vector W_{m-1} for the previous or $(m - 1)$th block. The reference R_{m+1} for differential QPSK detection of the carrier phase of the $(m + 1)$th block can now be obtained from W_m, as

$$R_{m-1} = e^{j\hat{\Lambda}_{m+1}} = e^{j(\hat{\theta}_m - 0.25\pi)} \tag{29}$$

where, except for phase error from noise,

$$\hat{\theta}_m = \theta_m + \theta_s - \theta_R = \zeta_m + \Delta \quad . \tag{30}$$

Until differential QPSK detection is performed, there is a $\pm 90°$ ambiguity as to the phase angle of the second chip of each symbol relative to the first chip. It is important to determine the phase reference for the next block independently of the preceding reference, R_m. Otherwise, an error in obtaining one reference will propagate into errors for succeeding reference vectors. This independence is obtained by sacrificing only half of the energy in the block—that obtained from the first chips of the N symbols. In differential QPSK detection, the chips for the first and second halves are combined in order to separate the binary components of the differential vector. Hence, the reference is actually used for binary (rather than quaternary) detection of the two orthogonal components, a_m and b_m, of the quaternary differential phase. Thus, the phase reference for differential BPSK detection has the same energy as the binary component that is being detected, which is the normal situation for differentially coherent detection.

Because of additive noise, there will be some phase error, ϕ, in the reference used for differential detection of the carrier phase, ζ_m, of the mth code block. Therefore, this reference vector is represented as

$$R_m = e^{j\hat{\Lambda}_m} = e^{j(\hat{\theta}_m + 0.25\pi)} \tag{31}$$

where $\hat{\Lambda}_m = \Lambda_m + \theta_s - \theta_R - \phi = \Delta - \phi$.

The two sets of quadrature correlations for the winning orthogonal word are used for differential detection, using the reference R_m. Assuming that the word is correct, the BPSK modulation is removed in the correlations so that the two words formed by the first and second chips of the N symbols are

$$W_m = U_m + jV_m = \sqrt{C}\exp[j(\Delta + \zeta_m)]$$

and

$$W'_m = U'_m + jV'_m = \sqrt{C}\exp[j(\Delta - \zeta_m)] \quad . \tag{32}$$

Multiplication of each vector by the complex conjugate of the estimated reference vector yields

$$w_m = u_m + jv_m = W_m R_m^* = \sqrt{C}\, e^{+j(\phi + \zeta_m)}$$

and

$$w'_m = u'_m + jv'_m = W'_m R_m^* = \sqrt{C}\, e^{+j(\phi - \zeta_m)} \quad . \tag{33}$$

Identification of the quadrature components of the differential vectors gives insight into how the cross-coupling interference of the binary coefficients a_m and b_m of the differential QPSK carrier phase may be cancelled. Note that

$$\begin{aligned}
u_m &= +\sqrt{C}\cos(\phi + \zeta_m) = +\sqrt{C/2}\,[a_m\cos\phi - b_m\sin\phi] + \alpha \\
v_m &= +\sqrt{C}\sin(\phi + \zeta_m) = +\sqrt{C/2}\,[b_m\cos\phi + a_m\sin\phi] + \beta \\
u'_m &= +\sqrt{C}\cos(\phi - \zeta_m) = +\sqrt{C/2}\,[a_m\cos\phi + b_m\sin\phi] + \alpha' \\
v'_m &= +\sqrt{C}\sin(\phi - \zeta_m) = -\sqrt{C/2}\,[b_m\cos\phi - a_m\sin\phi] + \beta'.
\end{aligned} \tag{34}$$

In these expressions, additive noise is shown with components α_m, β_m, α'_m, and β'_m. Variables x_m and y_m can now be formed from linear combinations of the previous components so that cross-coupling is eliminated, as

$$\begin{aligned}
x_m &= \frac{+u_m + u'_m}{2} = \sqrt{C/2}\, a_m\cos\phi + \frac{+\alpha + \alpha'}{2} \\
y_m &= \frac{+v_m - v'_m}{2} = \sqrt{C/2}\, b_m\cos\phi + \frac{+\beta - \beta'}{2} \quad .
\end{aligned} \tag{35}$$

Note the orthogonality of the binary coefficients a_m and b_m in the preceding equations. Thus, it is readily evident that differential QPSK detection of the carrier phase has been reduced to two binary differential BPSK detections. Decisions on a_m and b_m are made from the polarities of x_m and y_m, respectively, as

$$\begin{aligned}
\hat{a}_m &= \mathrm{Sgn}(x_m) \\
\hat{b}_m &= \mathrm{Sgn}(y_m) \quad .
\end{aligned} \tag{36}$$

Decoding performance

DCBC performance over a static AWGN channel will now be determined. Performance is expressed as the bit error probability, P_b, *vs* E_b/N_o, where N_o is the noise power density and E_b is the received signal energy per information bit. DCBC performance will be given for both the coherent and noncoherent cases of detection, where the latter is of primary interest. Coding gain is also calculated relative to uncoded BPSK performance.

In the coherent case, there is orthogonality in detecting the binary differential components, a_m and b_m, without any chip precoding. Therefore, N binary symbols would be detected rather than $2N$ chips. For coherent detection, the probability of error [7] in selecting between the correct codeword and another orthogonal word is given for an AWGN channel by

$$P_1 = \Phi[(E_w/N_o)^{0.5}] \tag{37}$$

where Φ is the normalized complementary Gaussian distribution function defined by

$$\Phi(\mu) = \frac{1}{\sqrt{2\pi}}\int_{\mu}^{\infty} e^{-0.5v^2}\, dv \quad . \tag{38}$$

Also, the word energy for DCBC with $b = n + 2$ bits per block is

$$E_w = bE_b = (n + 2)\, E_b \quad . \tag{39}$$

It is equally likely that any of the wrong $N - 1$ orthogonal words will be decoded when there is a decoding error. Hence, the word error probability is approximated by the union bound of the sum of $N - 1$ error probabilities, as

$$P_w \sim (N - 1)\, P_1 = (N - 1)\, \Phi[(bE_b/N_o)^{0.5}] \quad . \tag{40}$$

Out of the n bits conveyed by the orthogonal word of length $N = 2^n$, the average number of bit errors per incorrect word is

$$\bar{e}_b = \frac{n}{2} \frac{N}{N - 1} \quad . \tag{41}$$

Because there are a total of $b = n + 2$ information bits, the orthogonal word detection on n bits results in a bit error probability contribution given by

$$P_{b1} = P_w(\bar{e}_b/b) = \frac{nN}{2(n + 2)} \Phi[(bE_b/N_o)^{0.5}] \quad . \tag{42}$$

An error in decoding the orthogonal word of either the present (mth) block or the preceding block will result in an error in the differential detection of carrier phase. The probability of occurrence is $2P_w$, and an average of one bit decision will be in error, a_n or b_n. Even if both orthogonal words are decoded correctly, there is still some chance (although unlikely) of an error in detection of the differential carrier phase, ζ_m.

In obtaining an upper bound on error probability, a pessimistic assumption will be made by calculating the probability of differential error independent of the fact that both carrier sections resulted in correct orthogonal word detections. The unconditional probability of error with coherent detection of each carrier vector is based on one of the two vector decisions having an error of $\pm\pi/2$ radians, which has a probability of approximately $4P_1$. Again, only one bit decision (on a_n or b_n) will be in error. As before, errors of π radians are not considered because their probabilities are much less than those for $\pm\pi/2$ errors in detection. Also, the very low probability that decision errors are made on both vectors is ignored. Therefore, the total contribution to bit error probability from the differential QPSK decoding when coherent detection is employed is approximated by

$$P_{b2} = (2P_w + 4P_1)\left(\frac{1}{b}\right) = \frac{2N + 2}{n + 2} \Phi[(bE_b/N_o)^{0.5}] \quad . \tag{43}$$

Both contributions to bit error probability are summed to approximate the total P_b for DCBC decoding performance with coherent detection, as

$$P_b = P_{b1} + P_{b2} = \frac{(n + 4)N + 4}{2(n + 2)} \Phi[(bE_b/N_o)^{0.5}] \quad . \tag{44}$$

With respect to the determination of coding gain, the performance reference is that of uncoded BPSK with coherent detection, for which

$$p_b = \Phi[(2E_b/N_o)^{0.5}] \quad . \tag{45}$$

Asymptotic coding gain is the gain at very high E_b/N_o and correspondingly low P_b. This gain is given by the ratio of multiplication factors for E_b/N_o in the error probability expressions. In dB, the asymptotic gain is

$$G_a = 10 \log g_a = 10 \log (b/2) \quad . \tag{46}$$

Decoding performance as P_b *vs* E_b/N_o is presented in Figure 4 for DCBC with coherent detection. The performance of uncoded coherent BPSK is shown as a reference. DCBC performance is plotted parametrically in block length $N = 2^n$, for $N = 4$, 8, 16, and 32. The actual duration of the block is equal to the number $b = n + 2$ of information bits times the inverse of the bit rate, R_b. Thus, $N = 32$ corresponds to only $n + 2 = 7$ bit intervals. Note how the coding gains approach their asymptotic values at low P_b. For example, $G_a = 4.8$ dB for $N = 16$ and $b = 6$. The coding gain is seen to be about 3.2 dB at $P_b = 10^{-3}$ and increases to 4.0 dB at $P_b = 10^{-6}$.

The performance of DCBC transmitted over an AWGN channel can now be determined for the case of noncoherent detection. In this case, the probability of error for two orthogonal words would be a function P_1 if the symbols were not divided into two chips with different phasings. The function P_1 is the usual binary error probability for orthogonal coding of

$$P_1 = 0.5 \exp(-0.5\, E_w/N_o) \tag{47}$$

where $E_w/N_o = bE_b/N_o = (n + 2)\, E_b/N_o$.

With the first and second halves of each BPSK symbol divided into two modulation chips, coherent addition had to be performed separately over the two halves of the word. Noncoherent combining was then used to obtain the word metric. Marcum [8] has derived the general expression for the bit error probability P_j with noncoherent addition of some number j of terms. For

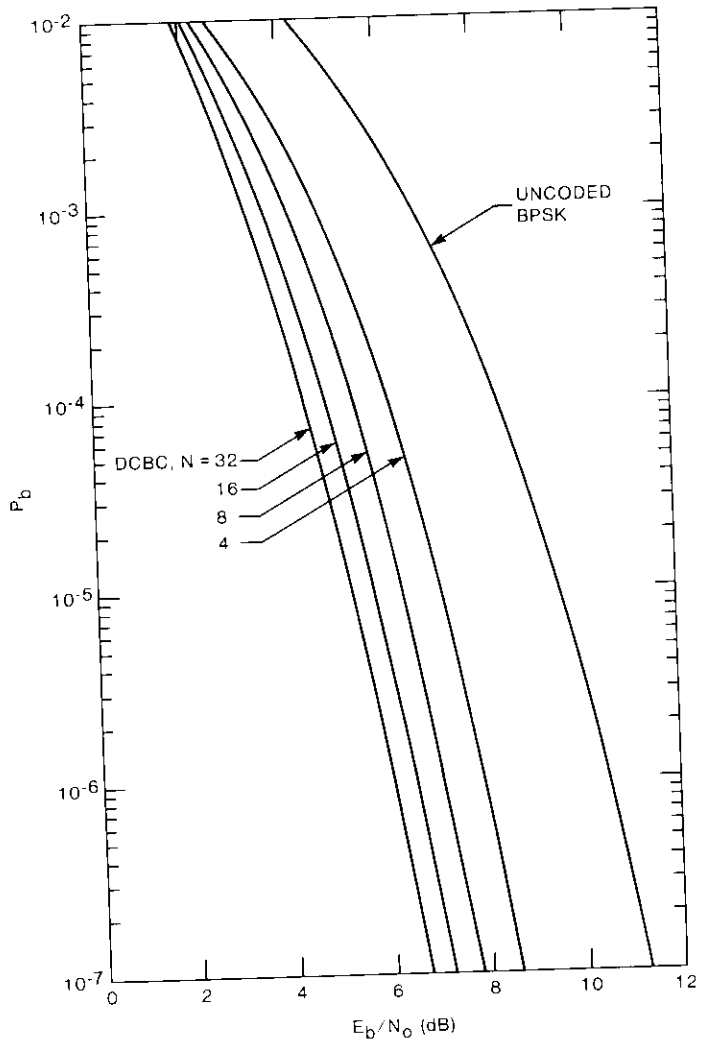

Figure 4. *DCBC Performance With Coherent Detection*

$j = 2$ terms, this expression reduces to some $P_2 = KP_1$, where the multiplier is given for the case of interest by

$$K = 1 + \frac{E_w/N_o}{8} = 1 + \frac{n+2}{8} E_b/N_o \quad . \tag{48}$$

Since there are actually $N = 2^n$ orthogonal words, the word error probability is approximated by its union bound of

$$P_w \simeq (N-1)\,P_2 = (N-1)KP_1 \quad . \tag{49}$$

Out of the $b = n + 2$ total bits conveyed per code block, the average number of bit errors associated with a decision on the n bits of the orthogonal word is

$$\bar{e}_b = \frac{n}{2}\,\frac{N}{N-1} \quad . \tag{50}$$

It follows that the contribution of bit errors for the orthogonal word to overall bit error probability is approximated by

$$P_{b1} = P_w(\bar{e}_b/b) = \frac{nN}{2(n+2)} KP_1 = \frac{nN}{4(n+2)} K \exp(-0.5\, bE_b/N_o) \quad . \tag{51}$$

Next, the probability of decision errors on the two differential coefficients, a_m and b_m, will be evaluated. It is assumed that incorrect decoding of the orthogonal word for either the present (mth) or the previous block will result in conditional error probabilities of 0.5 for both a_m and b_m. Thus, one bit (a_m or b_m) will be in error, on the average, with an event error probability of $2P_w$. Also, even when the two orthogonal words are correctly decoded, there is a small probability that the phase errors in the carrier vectors will result in decision errors for a_m or b_m. Using a pessimistic assumption that correct word decoding has no influence on the phase error distributions for the carrier vectors, each of the two bit decisions will correspond to conventional differentially coherent BPSK detection. However, only half of the word energy is used for the two terms in each decision, so the probability of decision error for each bit is

$$P_1 = 0.5 \exp(-0.5\, E_w/N_o) = 0.5 \exp(-0.5\, bE_b/N_o) \quad . \tag{52}$$

Therefore, the contribution of decision errors on a_m and b_m to bit error probability is

$$P_{b2} = (2P_w + 2P_1)(1/b) = \frac{(2N - 2)K + 2}{n + 2} P_1 \quad . \tag{53}$$

Both contributions to bit error probability are summed to approximate DCBC decoding performance when noncoherent detection is employed, as

$$P_b = P_{b1} + P_{b2} = \frac{N(n + 4)K - (4K - 4)}{2(n + 2)} P_1 \quad . \tag{54}$$

Coding gain for DCBC in the noncoherent case is relative to the performance of uncoded BPSK with differentially coherent detection. For transmission over an AWGN channel, this reference performance of DC-BPSK is

$$p_b = 0.5 \exp(-E_b/N_o) \quad . \tag{55}$$

Therefore, the asymptotic coding gain is the same as for the coherent case, 10 log $(b/2)$.

Decoding performance for DCBC transmitted over an AWGN channel is presented in Figure 5 for the case of noncoherent detection. The DCBC performance of P_b *vs* E_b/N_o is plotted for block lengths of $N = 4$, 8, 16, and 32. Also, the performance of DC-BPSK is included as a reference for calculating coding gain. As for the coherent case, the coding gain for DCBC with noncoherent detection approaches its asymptotic value as P_b is decreased by increasing E_b/N_o. For example, $G_a = 4.8$ dB when the block length is $N = 16$. As seen from Figure 5, the coding gain is 3.1 dB at $P_b = 10^{-3}$ and increases to 3.9 dB at $P_b = 10^{-6}$.

Performance discussion

Performance results for DCBC communications over an AWGN channel were determined for both coherent detection and noncoherent detection, as plotted in Figures 4 and 5, respectively. Table 5 summarizes the results for the coherent case in terms of the E_b/N_o required in order to achieve bit error probabilities from $P_b = 10^{-2}$ to 10^{-7}. A similar summary for the noncoherent case is given in Table 6.

For the coherent case, coding gain for DCBC is defined relative to the performance of uncoded BPSK. As seen from Table 5, the coding gains for all four code lengths are close to their asymptotic values when $P_b < 10^{-5}$. One outstanding feature of DCBC communications is that significant coding gain is provided at fairly high P_b, such as $P_b = 10^{-2}$. Many types of FEC

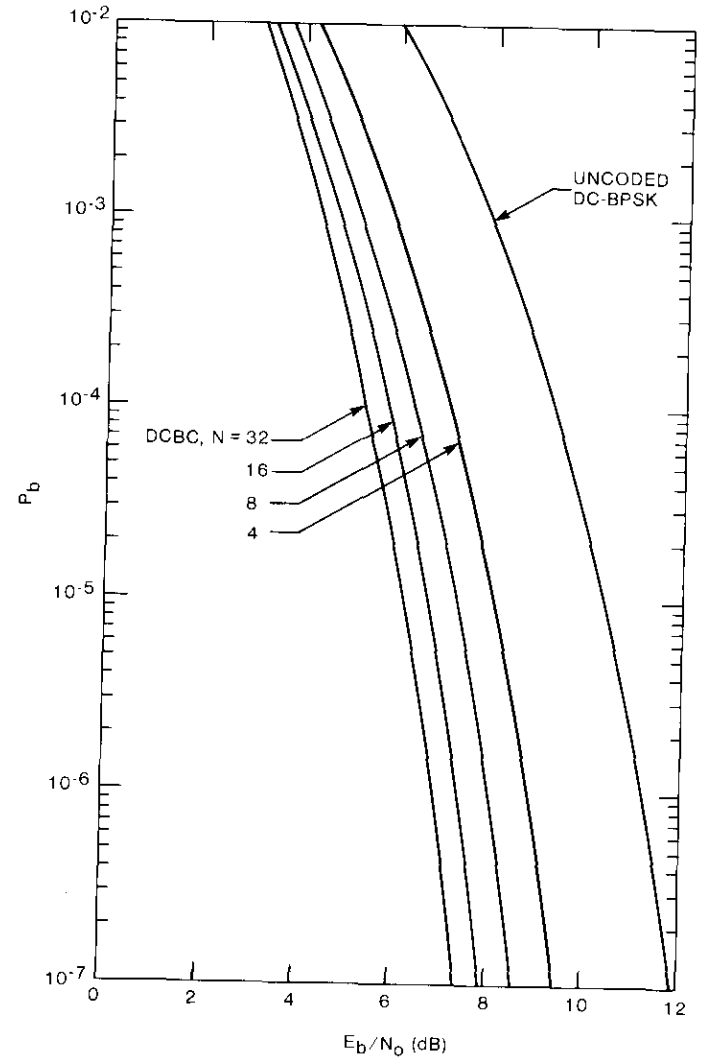

Figure 5. *DCBC Performance With Noncoherent Detection*

TABLE 5. PERFORMANCE FOR DCBC SIGNALING OVER AN AWGN CHANNEL WITH COHERENT DETECTION

BIT ERROR PROBABILITY, P_b	UNCODED E_b/N_o REQUIREMENTS (dB)		REQUIRED E_b/N_o FOR DCBC OF DIFFERENT BLOCK LENGTHS N (dB)				CODING GAINS RELATIVE TO UNCODED BPSK (dB)			
	COHERENT BPSK	DC-BPSK	$N = 4$	$N = 8$	$N = 16$	$N = 32$	$N = 4$	$N = 8$	$N = 16$	$N = 32$
10^{-2}	4.3	5.9	2.5	2.2	2.0	1.8	1.8	2.1	2.3	2.5
10^{-3}	6.8	7.9	4.8	4.1	3.6	3.3	2.0	2.7	3.2	3.5
10^{-4}	8.4	9.3	6.1	5.4	4.8	4.4	2.3	3.0	3.6	4.0
10^{-5}	9.6	10.3	7.1	6.3	5.7	5.3	2.5	3.3	3.9	4.3
10^{-6}	10.5	11.2	7.9	7.1	6.5	6.0	2.6	3.4	4.0	4.5
10^{-7}	11.3	11.9	8.6	7.8	7.2	6.7	2.7	3.5	4.1	4.6
Asymptotic Coding Gain (dB)			3.0	4.0	4.8	5.4	3.0	4.0	4.8	5.4

TABLE 6. PERFORMANCE FOR DCBC SIGNALING OVER AN AWGN CHANNEL WITH NONCOHERENT DETECTION

BIT ERROR PROBABILITY, P_b	UNCODED E_b/N_o REQUIREMENTS (dB)		REQUIRED E_b/N_o FOR DCBC OF DIFFERENT BLOCK LENGTHS N (dB)				CODING GAINS RELATIVE TO UNCODED DC-BPSK (dB)			
	COHERENT BPSK	DC-BPSK	$N = 4$	$N = 8$	$N = 16$	$N = 32$	$N = 4$	$N = 8$	$N = 16$	$N = 32$
10^{-2}	4.3	5.9	4.2	3.7	3.3	3.1	1.7	2.2	2.6	2.8
10^{-3}	6.8	7.9	5.8	5.2	4.8	4.4	2.1	2.7	3.1	3.5
10^{-4}	8.4	9.3	7.1	6.4	5.8	5.4	2.2	2.9	3.5	3.9
10^{-5}	9.6	10.3	8.1	7.3	6.6	6.1	2.2	3.0	3.7	4.2
10^{-6}	10.5	11.2	8.8	8.0	7.3	6.8	2.4	3.2	3.9	4.4
10^{-7}	11.3	11.9	9.4	8.6	7.9	7.3	2.5	3.3	4.0	4.6
Asymptotic Coding Gain (dB)			3.0	4.0	4.8	5.4	3.0	4.0	4.8	5.4

coding exhibit coding loss (negative coding gain) for $P_b > 10^{-3}$ and significant coding gain only when $P_b < 10^{-4}$.

DCBC is primarily intended as a coding solution for dynamic channels where coherent detection may not be reliable. Reliable coherent demodulation requires an S/N of greater than 10 dB for carrier synchronization. This S/N must be achieved after squaring or some other nonlinear technique is employed for modulation removal. Squaring results in an S/N loss of at least 6 dB, so that at low E_b/N_o an averaging interval of 16 or more information bits is required. DCBC with noncoherent detection still utilizes quasi-coherence over an interval of two code blocks. Thus, the DCBC word length N should be restricted to values for which the number of information bits in two blocks is less than 16. Note that $b = n + 2 = 7$ bits per DCBC block are conveyed when $N = 32$, which is the largest DCBC block under consideration.

When coherent detection is feasible, BPSK modulation with convolutional FEC coding, soft quantization, and Viterbi decoding [9],[10] may currently be the most powerful form of practical communications at low E_b/N_o. The Viterbi algorithm implements maximum-likelihood path decoding that can readily accommodate the improved performance afforded by soft-quantized symbol detection. A 16-state convolutional FEC code of rate 0.5 can provide a Hamming distance of $k = 7$. With this code, coded BPSK has an asymptotic coding gain of 10 log (7/2), or 5.4 dB, relative to ideal coherent detection of BPSK transmitted over an AWGN channel. At $P_b = 10^{-6}$, the required E_b/N_o is approximately 5.7 dB, compared to 10.5 dB for uncoded BPSK. Thus the coding gain is 4.8 dB. However, at $P_b = 10^{-3}$, the E_b/N_o requirement is 3.3 dB for a coding gain of 3.5 dB, relative to BPSK. Paths at greater than the minimum distance begin to affect the Viterbi performance at higher P_b, so that the coding gain drops below 2 dB at $P_b = 10^{-2}$.

DCBC with length $N = 16$ is roughly comparable in complexity to 16-state Viterbi decoding. As seen from Table 5, DCBC with coherent detection provides a coding gain of 4 dB at $P_b = 10^{-6}$, which is 0.8 dB inferior to 16-state Viterbi performance. However, at $P_b = 10^{-3}$, DCBC with $N = 16$ achieves a coding gain of 3.2 dB, which is only 0.3 dB inferior to the Viterbi performance. Furthermore, DCBC with $N = 16$ obtains a coding gain of 2.3 dB at $P_b = 10^{-2}$, which is slightly better than for coded BPSK with 16 code states and Viterbi decoding. Thus, DCBC is a viable alternative to coded BPSK with Viterbi decoding in applications such as voice communications at low E_b/N_o, where a P_b range of 10^{-3} to 10^{-2} may be acceptable.

Table 6 summarizes DCBC performance over an AWGN channel with noncoherent detection. Uncoded DC-BPSK is used as a reference for coding gain. The use of noncoherent detection for robustness of performance under conditions of dynamic carrier phase results in an increase in the E_b/N_o

requirement for the static AWGN channel. However, DCBC performance is degraded less by noncoherent performance than are other methods of FEC coding. In fact, the coding gain for DCBC in the noncoherent case is virtually the same as for the coherent case. This means that noncoherent detection causes almost the same performance loss for DCBC as it does for uncoded BPSK.

At present, coded DC-BPSK is a popular solution for low E_b/N_o operation of digital communications at information rates that are so low that the channel dynamics make coherent detection unreliable. With coded DC-BPSK, the detection output results in noncoherent branch metrics. The noncoherent addition of branch metrics to obtain path metrics results in a severe performance penalty for Viterbi decoding of DC-BPSK. For the case of coded BPSK with coding of rate 0.5 and 16 code states, the performance at $P_b = 10^{-6}$ is degraded by more than 2 dB. Even relative to uncoded DC-BPSK, the coding gain is significantly decreased. At $P_b = 10^{-6}$, the E_b/N_o requirement is 7.9 dB, for only a 3.3-dB coding gain.

DCBC performance with noncoherent detection yields a 3.9-dB coding gain at $P_b = 10^{-6}$ for a code with $N = 16$ orthogonal words. At $P_b = 10^{-3}$, the performance differences are greater. For example, DCBC with $N = 16$ provides a coding gain of 3.1 dB at $P_b = 10^{-3}$, while the Viterbi decoding of coded DC-BPSK provides a gain of only 1.9 dB. Hence, DCBC with noncoherent detection appears to be an attractive approach for low-speed BPSK communications at low E_b/N_o when coherent detection is not feasible.

Summary

DCBC is a new method of combined modulation/coding that uses relative phases of BPSK symbols over short orthogonal code blocks. Each block of length $N = 2^n$ conveys n information bits as an orthogonal code, while QPSK differential coding of the carrier phases for successive code blocks provides an additional 2 bits. Methods of signal generation and reception have been described for DCBC. Also, the performance of DCBC over an AWGN channel was determined for different block lengths.

DCBC is primarily intended for use in low-speed coded BPSK communications to provide good performance over a dynamic channel in which oscillator phase noise and Doppler rate would cause coherent detection to be of questionable reliability. When coherent detection is feasible, DCBC performance is better than for the noncoherent case. However, at low bit error probabilities such as $P_b = 10^{-6}$, DCBC with coherent detection does not perform as well as coded BPSK with Viterbi decoding of similar complexity. There is a slight performance advantage with DCBC at $P_b = 10^{-2}$. Thus, DCBC with coherent detection may be a viable alternative to coherent coded BPSK with Viterbi decoding for applications in which low E_b/N_o is required and P_b values in the range of 10^{-3} to 10^{-2} are acceptable. Voice communications for low-cost terminals is one potential application.

In the case of noncoherent detection, Viterbi decoding of coded DC-BPSK experiences severe performance degradation from the noncoherent addition of branch metrics to obtain path metrics. By utilizing quasi-coherence over two block lengths, DCBC performance is not degraded significantly by noncoherent detection. Therefore, DCBC with noncoherent detection can provide large coding gain for a static AWGN channel and still exhibit robust performance with respect to a dynamic channel.

DCBC performance with noncoherent detection is superior to coded DC-BPSK with Viterbi decoding of the same complexity. For a block of length $N = 16$, the required E_b/N_o for DCBC communications to achieve $P_b = 10^{-6}$ over an AWGN channel is 7.3 dB. Thus, the coding gain is 3.9 dB relative to the 11.2-dB required E_b/N_o for uncoded DC-BPSK at $P_b = 10^{-6}$. Viterbi decoding of coded DC-BPSK with coding of rate 0.5 and 16 code states achieves a coding gain of 3.3 dB, which is 0.6 dB inferior to DCBC. Because it can maintain significant coding gain at high P_b values, DCBC has an even greater performance advantage of 1.4 dB at $P_b = 10^{-3}$.

References

[1] S. W. Golomb *et al.*, *Digital Communications With Space Applications*, Englewood Cliffs, New Jersey: Prentice-Hall, 1964, pp. 106–134.

[2] W. C. Lindsey and M. K. Simon, *Telecommunications Systems Engineering*, Englewood Cliffs, New Jersey: Prentice-Hall, 1973, pp. 185–226.

[3] R. W. Lucky, J. Salz, and E. J. Weldon, *Principles of Data Communication*, New York: McGraw-Hill, 1968, pp. 45–54.

[4] J. J. Stiffler, *Theory of Synchronous Communications*, Englewood Cliffs, New Jersey: Prentice-Hall, 1971, pp. 153–261.

[5] F. M. Gardner, *Phaselock Techniques*, 2nd ed., New York: John Wiley and Sons, 1979.

[6] J. J. Spilker, Jr., *Digital Communications by Satellite*, Englewood Cliffs, New Jersey: Prentice-Hall, 1977.

[7] J. M. Wozencraft and I. M. Jacobs, *Principles of Communication Engineering*, New York: John Wiley and Sons, 1979.

[8] J. I. Marcum, "Statistical Theory of Target Detection by Pulsed Radar," *IEEE Transactions on Information Theory*, Vol. IT-6, No. 2, April 1960, pp. 59–267.

[9] A. J. Viterbi, "Error Bounds for Convolutional Codes and an Asymptotically Optimum Decoding Algorithm," *IEEE Transactions on Information Theory*, Vol. IT-13, No. 2, April 1967, pp. 260–269.

[10] J. A. Heller and I. M. Jacobs, "Viterbi Decoding for Satellite and Space Communications," *IEEE Transactions on Communications*, Vol. COM-14, No. 5, Part 2, October 1971, pp. 835–848.

[11] G. C. Clark, Jr., and J. B. Cain, *Error-Correction Coding for Digital Communications*, New York: Plenum Press, 1981, pp. 34–35, 250–252.

Smith A. Rhodes received a B.S.E.E. from Virginia Polytechnic Institute in 1959 and an M.S.E.E. from North Carolina State University in 1962. From 1959 to 1965 he was a Member of the Technical Staff at Bell Laboratories, where he was engaged in various communications system studies. From 1965 to 1968 he was involved in digital communications studies for the R&D directorate of Page Communications. At Computer Services Corporation, he participated in digital satellite communications studies for military applications from 1968 to 1974. Since joining COMSAT in 1974 Mr. Rhodes has been engaged in system studies for satellite communications. He is currently a Senior Scientist in the Communications Research Department of the Communications Techniques Division at COMSAT Laboratories. His primary interests are in the digital communications area of modulation, synchronization, and error control. Mr. Rhodes is a member of the IEEE groups on Communications and Information Theory.

Index: coding, communication satellites, digital transmission, error control

Decoding the eight-state partial unit-memory code

F. HEMMATI

(Manuscript received July 13, 1987)

Abstract

Efficient methods are presented for full-serial and full-parallel implementation of a decoder for the eight-state partial unit memory code of rate 4/8. The proposed high-speed, maximum-likelihood decoder employs a fast Hadamard transform architecture for computing branch metrics, and the concept of coset codes is used to minimize the complexity of hardware implementation. The high decoding speed is achievable because four information bits are produced at each decoding step, compared to only one information bit for codes of rate 1/2.

Introduction

Unit memory codes of rate $R = k/n$, gcd* $(k, n) \neq 1$ were defined and constructed by Lee [1]. Subsequently, Lauer [2] showed that partial unit memory (PUM) codes are optimal because they exhibit maximum Hamming free distance, d_f, for given values of R, k, and μ (number of encoder states). Among the several classes of optimum PUM codes generated by Lauer, the eight-state code of rate 4/8, with $d_f = 8$, is the most attractive. This code is equivalent to the 16-state unit memory code of rate 4/8, its d_f equals the free distance for the optimum 32-state convolutional code of rate 1/2, and it can be efficiently decoded (soft-decision, maximum-likelihood) by using Hadamard transform techniques and the Viterbi algorithm.

* gcd: greatest common denominator.

A major factor in the hardware implementation complexity of a maximum-likelihood, high-speed decoder for the class of unit memory or PUM codes is the excessive number of operations required for computing branch metrics. However, the special properties and structure of these codes can be employed to compute the set of branch metrics synergistically rather than individually, resulting in a significant reduction in the complexity of the computations.

The structure of the PUM code of rate 4/8 is principally based on the Reed-Muller code of length 8. For any m and r, $0 \leq r \leq m$, there is a binary rth-order Reed-Muller code, $R(r, m)$, with the following properties:

Length: $n_0 = 2^m$

Dimension: $k_0 = 1 + \binom{m}{1} + \binom{m}{2} + \cdots + \binom{m}{r}$

Minimum Distance: $d = 2^{m-r}$.

The set of output blocks associated with transitions terminating on each state in the trellis diagram for the eight-state PUM code of rate 4/8 can be regarded as a coset of $R(1, 3)$. Hence, well-known and efficient techniques for soft-decision decoding of $R(1, 3)$ [3], [4] can be used to compute the branch metrics. This property, as well as other unique properties of this code, may be employed to implement a low-complexity, high-speed decoder for the code of interest. High-speed decoding is achievable because four information bits are produced at each decoding step, compared to only one information bit for codes of rate 1/2.

A block diagram of the encoder is presented, followed by an investigation of the properties of the generated code. Efficient methods are then discussed for finding the inner product (correlation) of a received block with codewords of the first-order Reed-Muller codes, and efficient approaches are presented for full-serial and full-parallel hardware implementation of the decoder. These decoders can operate at very high speed with minimal hardware complexity.

Encoding

Figure 1 is a block diagram of the encoder for the PUM code of rate 4/8. Let $I_t = (i_{1t}, i_{2t}, i_{3t}, i_{4t})$ be the binary 4-tuple input block at time t. The binary 8-tuple output block $Y_t = (y_{1t}, y_{2t}, \ldots, y_{8t})$ is generated by

$$Y_t = I_t G_0 + I_{t-1} G_1 \qquad (1)$$

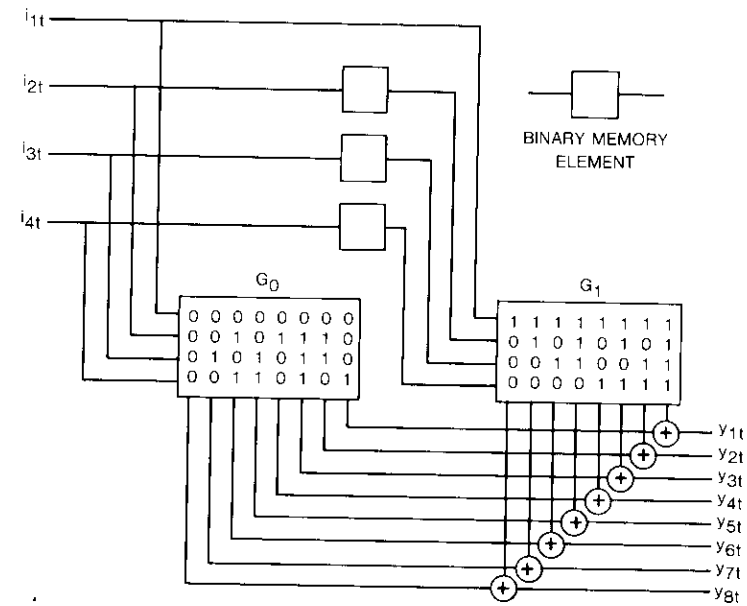

Figure 1. *Encoder for Partial Unit-Memory Code of Rate 1/2*

where

$$G_0 = \begin{bmatrix} 0 & 0 & 0 & 0 & 0 & 0 & 0 & 0 \\ 0 & 0 & 1 & 0 & 1 & 1 & 1 & 0 \\ 0 & 1 & 0 & 1 & 0 & 1 & 1 & 0 \\ 0 & 0 & 1 & 1 & 0 & 1 & 0 & 1 \end{bmatrix}$$

$$G_1 = \begin{bmatrix} 1 & 1 & 1 & 1 & 1 & 1 & 1 & 1 \\ 0 & 1 & 0 & 1 & 0 & 1 & 0 & 1 \\ 0 & 0 & 1 & 1 & 0 & 0 & 1 & 1 \\ 0 & 0 & 0 & 0 & 1 & 1 & 1 & 1 \end{bmatrix} .$$

The matrices G_0 and G_1 are obtained by performing elementary row and column operations on the subgenerator matrices for this code (given in Reference 2) so that G_1 can be identified as the generator matrix for the first-order Reed-Muller code of length 8, $R(1, 3)$. The advantages of the selected basis for G_0 and G_1 will be discussed below.

The set of all possible input 4-tuples generates 16 transitions between the eight encoder states. Hence, each trellis state can be connected to its eight subsequent states by double branches (Figure 2). The output blocks associated

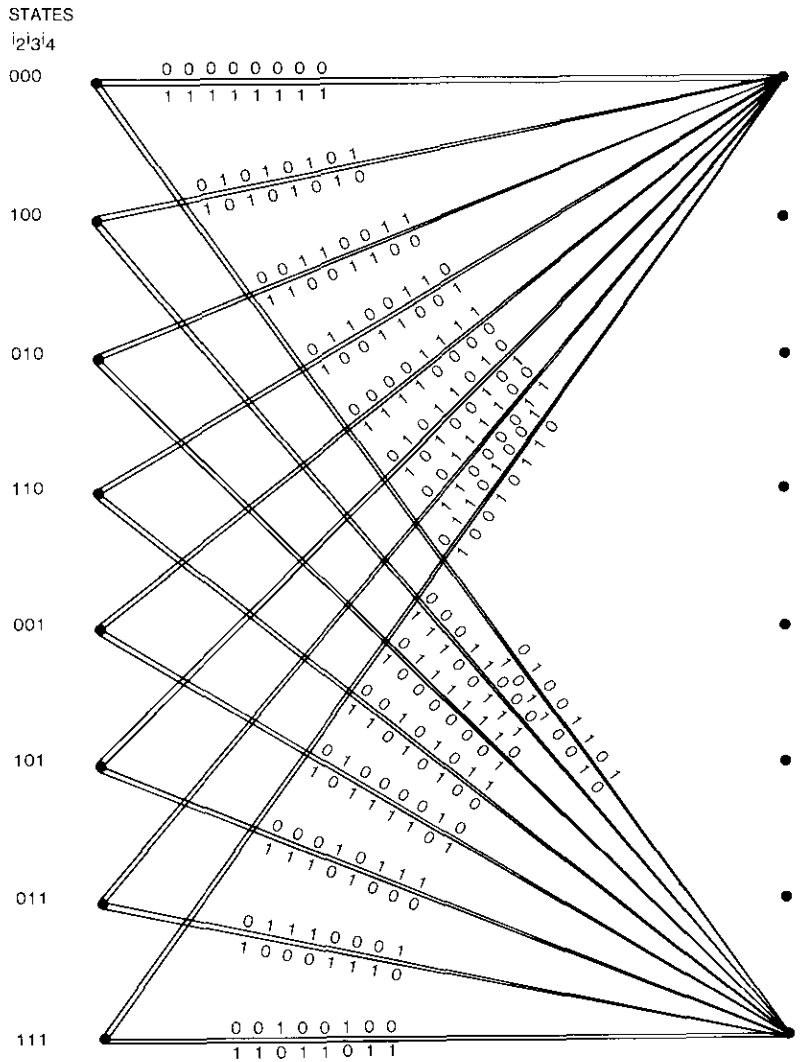

Figure 2. *Trellis Diagram for Eight-State Partial Unit-Memory Code of Rate 1/2*

with double-branch transitions are equivalent to a (8, 1, 8) repetition code, where (n_0, k_0, d) denotes a block code of length n_0, dimension k_0, and minimum Hamming distance d. Moreover, the set of sixteen 8-tuples, W_0, associated with eight double branches terminating in the all-zero state constitutes the first-order Reed-Muller code of length 8 with a minimum Hamming distance of 4. This occurs because G_1 is a generator matrix for $R(1, 3)$, and the 16 codewords in W_0 are generated by input blocks

$$I_t = (i_{1t}, 0, 0, 0)$$

$$i_{1t} = 0 \text{ or } 1$$

$$I_{t-1} = (i_{1,t-1}, i_{2,t-1}, i_{3,t-1}, i_{4,t-1}) \quad .$$

The set of codewords in W_0 consists of the union of V_0 and its binary complement, $\overline{V}_0$ (Figure 3). V_0 and $\overline{V}_0$ correspond to the input blocks $I_t = (0, 0, 0, 0)$ and $I_t = (1, 0, 0, 0)$, respectively. Decomposition of W_0 into V_0 and $\overline{V}_0$ reduces the complexity of computations for a soft-decision decoder by a factor of 2. Let $x_j = \underline{R} \cdot \underline{v}_j$ be the correlation (inner product) of a block of received channel symbols, $\underline{R}$, with a codeword $v_j \in V_0$, $j = 1, \ldots, 8$. Then $y_j = \underline{R} \cdot \bar{v}_j = -x_j$, where $\bar{v}_j \in \overline{V}$ is the binary complement of v_j. Hence, it is sufficient to compute either x_j or y_j.

V_0	$\overline{V}_0$
0 0 0 0 0 0 0 0	1 1 1 1 1 1 1 1
0 1 0 1 0 1 0 1	1 0 1 0 1 0 1 0
0 0 1 1 0 0 1 1	1 1 0 0 1 1 0 0
0 1 1 0 0 1 1 0	1 0 0 1 1 0 0 1
0 0 0 0 1 1 1 1	1 1 1 1 0 0 0 0
0 1 0 1 1 0 1 0	1 0 1 0 0 1 0 1
0 0 1 1 1 1 0 0	1 1 0 0 0 0 1 1
0 1 1 0 1 0 0 1	1 0 0 1 0 1 1 0

Figure 3. *Set of Codewords in* W_0

The last property of this code is based on the theory of coset codes. Let W_i be the set of sixteen 8-tuples associated with eight double branches terminating in the ith trellis state, $0 \leq i \leq 7$. Then, W_i can be written as

$$W_i = C_i + W_0 \quad , \qquad 0 \leq i \leq 7 \quad .$$

In terms of the theory of coset codes, W_i is a coset of W_0. The set of coset representatives

$$C = \begin{bmatrix} C_7 \\ C_6 \\ C_5 \\ C_4 \\ C_3 \\ C_2 \\ C_1 \\ C_0 \end{bmatrix} = \begin{bmatrix} 0 & 1 & 0 & 0 & 1 & 1 & 0 & 1 \\ 0 & 1 & 1 & 1 & 1 & 0 & 0 & 0 \\ 0 & 0 & 0 & 1 & 1 & 0 & 1 & 1 \\ 0 & 0 & 1 & 0 & 1 & 1 & 1 & 0 \\ 0 & 1 & 1 & 0 & 0 & 0 & 1 & 1 \\ 0 & 1 & 0 & 1 & 0 & 1 & 1 & 0 \\ 0 & 0 & 1 & 1 & 0 & 1 & 0 & 1 \\ 0 & 0 & 0 & 0 & 0 & 0 & 0 & 0 \end{bmatrix}$$

constitutes an (8, 3, 4) block code, with a generator matrix of

$$\begin{bmatrix} 0 & 0 & 1 & 0 & 1 & 1 & 1 & 0 \\ 0 & 1 & 0 & 1 & 0 & 1 & 1 & 0 \\ 0 & 0 & 1 & 1 & 0 & 1 & 0 & 1 \end{bmatrix}$$

which comprises the last three rows of G_0. The following example clarifies this point. Theoretical and formal definitions of coset codes are presented in the Appendix.

Example. W_7 (the set of 16 codewords corresponding to eight double branches terminating on the "all-one" state) is generated by modulo-2 vector addition, bit by bit, of $C_7 = (0\ 1\ 0\ 0\ 1\ 1\ 0\ 1)$ to W_0. As shown in Figure 4, W_7 is equivalent to $R(1, 3)$; that is, its distance distribution is equivalent to that for $R(1, 3)$.

A major factor in the complexity of the hardware implementation of a maximum-likelihood, high-speed decoder for this code is the excessive number of operations required in order to compute the branch metrics. This shortcoming can be alleviated by using the concept of coset codes and employing an efficient method for computing the inner product of a received block of eight symbols with 16 codewords in $R(1, 3)$.

V_7	$\bar{V}_7$
0 1 0 0 1 1 0 1	1 0 1 1 0 0 1 0
0 0 0 1 1 0 0 0	1 1 1 0 0 1 1 1
0 1 1 1 1 1 1 0	1 0 0 0 0 0 0 1
0 0 1 0 1 0 1 1	1 1 0 1 0 1 0 0
0 1 0 0 0 0 1 0	1 0 1 1 1 1 0 1
0 0 0 1 0 1 1 1	1 1 1 0 1 0 0 0
0 1 1 1 0 0 0 1	1 0 0 0 1 1 1 0
0 0 1 0 0 1 0 0	1 1 0 1 1 0 1 1

Figure 4. *Set of Codewords in* W_7 *(the union of* V_7 *and* $\bar{V}_7$*)*

Branch metric computation

This section examines the computational complexity of several techniques used to find the inner product of a received block with the 16 codewords in $R(1, 3)$. Here, it is more convenient to denote codewords by vectors of $+1$ and -1, rather than 0's and 1's. The transformation

$$a_i = (-1)^{b_i} \tag{2}$$

replaces $b_i = 0$ with $a_i = 1$, and replaces $b_i = 1$ with $a_i = -1$. Note that modulo-2 addition of two elements, $b_i + b_j$, in 0, 1 notation is equivalent to $a_i \cdot a_j$ in $+1$, -1 notation. Also, this transformation [equation (2)] replaces Hamming distance calculation with inner product computation. Thus, finding a codeword (in 0, 1 notation) which is closest, in the sense of Hamming distance, to a block of received binary symbols is equivalent to finding a codeword which has the largest inner product with the block of soft-detected received symbols.

The following is a rough estimate of the complexity of computations required for two techniques used to find the inner product of a received block with codewords in $R(1, 3)$. A computation is defined as a binary operation, such as addition or comparison. Multiplication by $+1$ or -1 is also considered a binary operation; however, taking the absolute value of a real number is a trivial operation which is not considered a binary operation in this analysis.

Exhaustive computation

The inner product of two vectors can be computed directly. Assuming the set of 16 codewords is available in a lookup table, the computation of inner products takes $8 \times 16 + 7 \times 16 = 240$ steps. However, since the codewords in $\bar{V}_0$ are binary complements of codewords in V_0, the 16 inner

products appear in pairs with opposite signs. Hence, the number of computations can be reduced to $8 \times 8 + 7 \times 8 = 120$ by computing eight inner products of the received block with codewords in V_0 and selecting the inner product with the largest absolute value.

Fast Hadamard transform

The fast Hadamard transform computes the 16 inner products synergistically, rather than individually, as in the exhaustive-computation method. The Hadamard matrix of order 8 can be obtained by permuting rows of V_0. Thus, as shown in Figure 5, the fast Hadamard transform can be used to efficiently compute the 16 inner products in 24 steps.

This method, also known as the Green machine [3], is used for efficient decoding of Reed-Muller codes of the first order [3],[4]. It can also be used to decode multidimensional coded modulation schemes in which the block code associated with the parallel branches between encoder states constitutes a first-order Reed-Muller code.

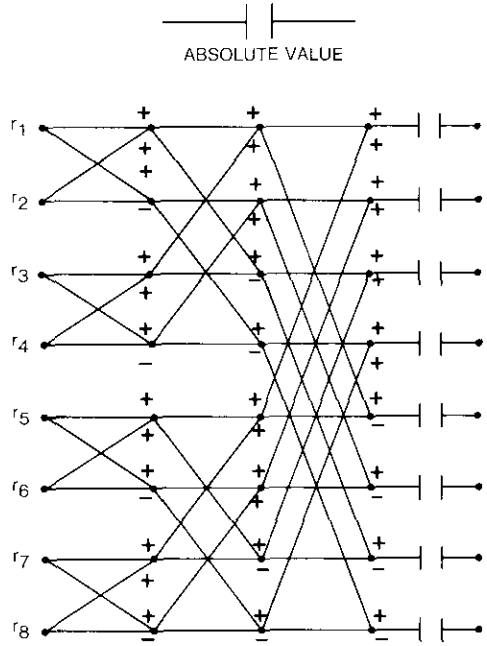

Figure 5. *Decoding the (8, 4, 4) Code by Using Fast Hadamard Transform*

Decoding

This section presents efficient methods for full-serial and full-parallel implementation of the decoder.

Full-serial implementation

Figure 6 is a block diagram of a Viterbi algorithm decoder which serially processes the eight states of the trellis diagram. The decoder consists of four main parts:

- A *correlator* for computation of cosets W_i, $0 \leq i \leq 7$. The set of coset representatives, C, is stored in a cyclic table.
- *Fast Hadamard transform hardware* for computation of branch metrics.
- A *Viterbi decoder* consisting of an eight-way add-compare-select (ACS) unit and state metric tables.
- A *traceback circuit* consisting of three trellis steps for the path memory.

The traceback unit, synchronization, control, and clocking are not shown in the figure.

For a received block of eight channel symbols, $\underline{r}$, the decoder finds the path with the largest metric value terminating on each trellis state. This simple serial implementation achieves a high decoding speed for the code under consideration because each decoding step yields four information bits, rather than only one information bit as in convolutional codes of rate 1/2.

Full-parallel implementation

A full-parallel processor for decoding the PUM code of rate 4/8 consists of eight ACS units processing the eight encoder states simultaneously. Computation of the absolute value of $8 \times 8 = 64$ branch metrics by eight separate fast Hadamard transform circuits involves $8 \times 24 = 192$ binary additions. The following method combines the function of the eight Hadamard transforms and computes the absolute value of the 64 branch metrics by performing 88 binary additions [4].

For a given block of eight soft-detected channel symbols, $\underline{r} = (r_1, r_2, r_3, r_4, r_5, r_6, r_7, r_8)$, perform the following:

a. Compute $r_1 \pm r_2, r_3 \pm r_4, r_5 \pm r_6, r_7 \pm r_8$. (8 binary operations)

b. Compute $[(r_1 \pm r_2) \pm (r_3 \pm r_4)]$ and $[(r_5 \pm r_6) \pm (r_7 \pm r_8)]$ by combining the results of step (a). (16 binary operations)

c. Finally, compute $[(r_1 \pm r_2) \pm (r_3 \pm r_4)] \pm [(r_5 \pm r_6) \pm (r_7 \pm r_8)]$ for all possible combinations in which the number of minus signs is

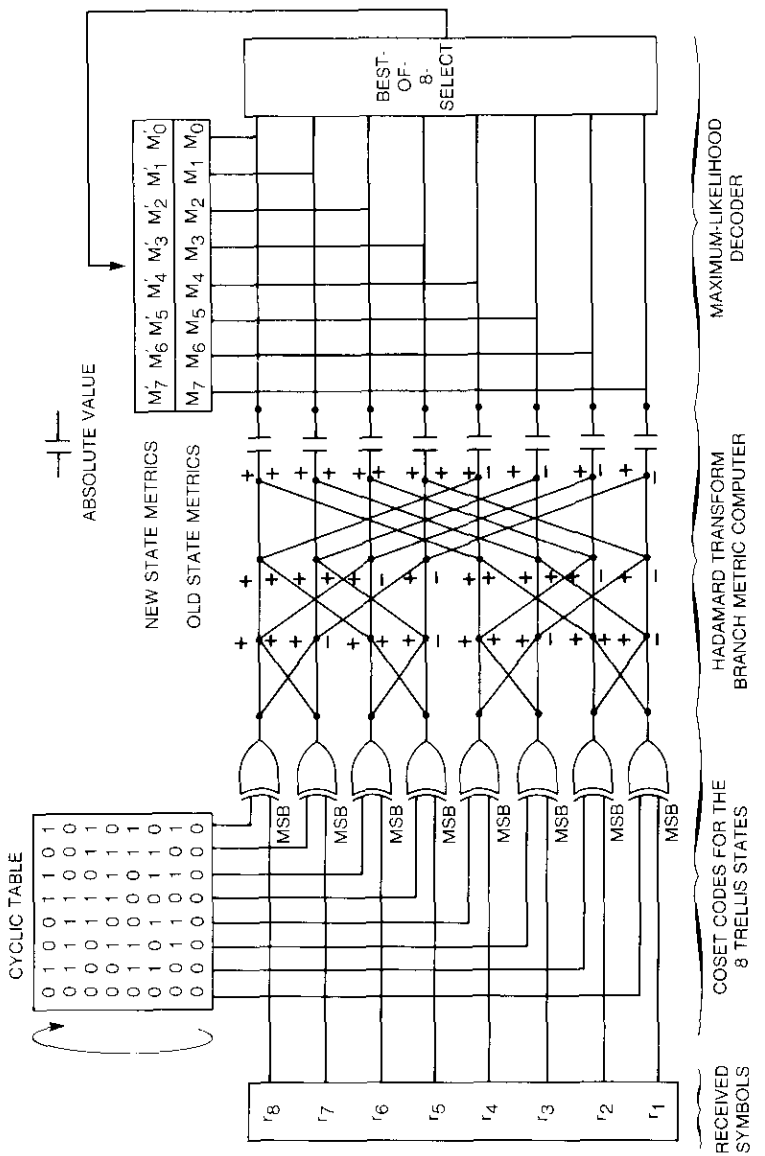

Figure 6. *Implementation for Serial Processing of Eight Trellis States*

even,* and then take the absolute value of each sum. ($8 \times 8 = 64$ binary operations)

The maximum-likelihood decoder can also be implemented by using two or four ACS units. The complexity of branch metric computers, in terms of the number of required binary adders, is summarized in Table 1 for decoders with one, two, four, or eight ACS units. Compared to the full-serial implementation, the hybrid implementation with two ACS units increases the decoding speed by a factor of 2, while the increment in the number of adders for the branch metric computations is negligible.

TABLE 1. COMPLEXITY OF BRANCH METRIC COMPUTERS FOR SEVERAL DECODER ARCHITECTURES

NUMBER OF 8-WAY ACS UNITS	NUMBER OF BINARY ADDERS	RELATIVE SPEED
1 (full-serial)	24	1
2	32	2
4	48	4
8 (full-parallel)	88	8

Conclusions

The structural properties of the PUM code of rate 4/8 have been exploited to design a high-speed, low-complexity decoder. In particular, the fast Hadamard transform technique significantly reduces the hardware implementation complexity of the branch metric computer.

References

[1] L-N. Lee, "Short, Unit-Memory, Byte-Oriented, Binary Convolutional Codes Having Maximal Free Distance," *IEEE Transactions on Information Theory*, Vol. IT-22, No. 3, May 1976, pp. 349–352.

[2] G. S. Lauer, "Some Optimal Partial-Unit Memory Codes," *IEEE Transactions on Information Theory*, Vol. IT-25, No. 2, March 1979, pp. 240–243.

[3] F. J. MacWilliams and N. J. Sloane, *The Theory of Error Correcting Codes*, New York: North Holland, 1977.

[4] G. D. Forney, Jr., "Coset Codes I: Binary Codes and Lattices," IEEE Communications Theory Workshop, Palm Springs, California, April 1986.

* There are $\binom{7}{0} + \binom{7}{2} + \binom{7}{4} + \binom{7}{6} = 64$ such instances.

Appendix. Coset codes

This appendix presents theoretical and formal definitions of the coset codes.

Let S be an Abelian group with elements s. Elements s are n-dimensional binary vectors if S is a binary linear block code of length n. An m-way partition of S is a division of the elements of S into m subsets, T_i, $1 \leq i \leq m$. In terms of group theory, one subset (T) is a subgroup of S of order m, and the quotient group S/T has m elements. These elements are T and $m - 1$ cosets of T. (Recall that "zero" is an element of the subgroup T.) Let $c \in S$, but $c \notin T$, then the coset of T containing c is $T + c = \{t + c: t \in T\}$. The element c is called a coset representative. The set of coset representatives (including "zero") constitutes the quotient group S/T.

Example 1. Let $S = \{000, 001, 010, 011, 100, 101, 110, 111\}$ be the (3, 3, 1) "universe code" containing all the possible binary 3-tuples with a minimum Hamming distance of 1. A two-way partition of S yields the subgroup $T_0 = \{000, 011, 101, 110\}$ and its coset $T_1 = \{111, 100, 010, 001\}$. We can always write $T_0 = 000 + T_0$ and $T_1 = 111 + T_0$. The subgroup T_0 is the (3, 2, 2) single-parity check code, and the set of coset representatives $S/T = \{000, 111\}$ is the (3, 1, 3) repetition code.

Example 2. Let $S = (3, 3, 1)$, as defined in example 1. A four-way partition of S yields the subgroup $T_0 = \{000, 111\}$ and its cosets $T_1 = 011 + T_0$; $T_2 = 110 + T_0$; and $T_3 = 101 + T_0$. In this case, $T_0 = (3, 1, 3)$ and $S/T = (3, 2, 2)$.

Farhad Hemmati received an M.S.E.E. and Ph.D. from Illinois Institute of Technology in 1973 and 1977, respectively. Since joining COMSAT Laboratories in 1982 he has worked on coding techniques and various signal processing methods for satellite channels. He is currently a Staff Scientist in the Communications Research Department, where his primary research interests are coding, spread spectrum, and multiple access.

Index: distortion, modulation, demodulation, modems, speech processing, telephone transmission

Evaluation of ADPCM coders for digital circuit multiplication equipment

S. DIMOLITSAS, F. L. CORCORAN, M. ONUFRY, AND H. G. SUYDERHOUD

(Manuscript received May 21, 1987)

Abstract

This paper describes test results for a set of experimental procedures designed to objectively measure the performance of four adaptive differential pulse-code modulation (ADPCM) algorithms that use signals other than voice. These algorithms have been under consideration by the International Telegraph and Telephone Consultative Committee (CCITT) as possible low-bit-rate coders for incorporation in digital circuit multiplication equipment. The results presented pertain to voiceband data modems operating at 9,600 bit/s or higher, and include analog performance measurements for each of the algorithms considered.

Introduction

In 1984, a 32-kbit/s adaptive differential pulse-code modulation (ADPCM) algorithm, Recommendation G.721, [1] was adopted by the International Telegraph and Telephone Consultative Committee (CCITT). This recommendation was subsequently modified and is presently awaiting standardization [2] following the discovery of certain instabilities and problems relating to the Bell 202 series [3] and the CCITT V.23 series of modems [4]. Studies preceding the adoption of Recommendation G.721 showed that the algorithm also performed well with signals other than voice (such as voiceband data) at rates not exceeding 4,800 bit/s [5]. However, the same studies revealed that

higher voiceband data rates could not readily be supported, particularly data transmitted at 9,600 bit/s and conforming to Recommendations V.29 [6] and V.32 [7]. Because it is desirable, from an international traffic viewpoint, to provide a transparent environment for voiceband data for bit rates that include 9.6 kbit/s in digital circuit multiplication equipment (DCME) [8], an Ad Hoc Group was established within CCITT Study Group XVIII, under Questions 25 and 31, to select an algorithm for this purpose.

This paper describes the results of a set of objective measurements for four algorithms, at data rates of 9,600 bit/s or higher. The tested algorithms include one developed by Alcatel, representing the French Administration [Centre National d'Etudes des Telecommunications (CNET)]; one developed by ECI Telecom, Ltd., representing the Israeli Administration; and two developed by OKI Electric Industry Co., Ltd., and Kokusai Denshin Denwa Co., Ltd. (KDD), representing the Japanese Administration. These tests were conducted between October 1986 and May 1987 at COMSAT Laboratories in Clarksburg, Maryland, which was the host test laboratory for the CCITT Ad Hoc Group.

While the results presented here strongly influenced the selection of a specific approach as a CCITT Recommendation, these objective measurements were not the sole factor used in assessing the suitability of any particular algorithm for deployment in digital circuit multiplication systems. In particular, DCME integration aspects (such as bearer channel frame structure), subjective performance with speech, data detection or data rate discrimination capability (as needed), network aspects (such as synchronous coding capability), and maintenance aspects, as well as overall complexity issues, played a significant role in the algorithm selection process.

Algorithm description

This section briefly describes the key features of the algorithms under consideration.

The CNET algorithm

The CNET algorithm is an extension of the present CCITT Recommendation G.721 [1], which specifies a 32-kbit/s ADPCM algorithm employing an adaptive pole/zero predictor and an adaptive quantizer. The predictor consists of two-pole sign stochastic gradient and six-zero sign stochastic gradient adaptive filters. The quantizer can adaptively track the input signal statistics by recursive adaptation of its step size. Furthermore, the quantizer operates in two modes: locked and unlocked. In the locked mode the quantizer adapts slowly, while in the unlocked mode it adapts more rapidly to the encoded signal statistics. The locked mode of operation is typical during voiceband data transmission, while the unlocked mode is typical during speech coding. Finally, a synchronous tandeming algorithm is employed at the decoder to ensure that quantization noise is noncumulative during multiple digital ADPCM coder interconnections.

The principal differences between the 32-kbit/s G.721 [1] and the G.721 extension tested lie in the adoption of a 5-bit quantizer resulting in a 40-kbit/s data stream [9], and the use of a data detector [10] and data rate discriminator [11] to ensure that all data above 4,800 bit/s are encoded by the 40-kbit/s algorithm. It should be noted that all data at rates equal to or less than 4,800 kbit/s, as well as speech, continue to be encoded by the 32-kbit/s G.721 in this approach.

The ECI algorithm

This approach uses a data-optimized algorithm for the encoding of all data traffic. The structure of this approach differs from both G.721 and the CNET algorithm [9] in that the ADPCM encoder input is first band-limited to 3.2 kHz and then down-sampled at 6.4 kHz. This is accomplished by means of a 100-tap symmetric finite impulse response interpolating filter operating at a 32-kHz sampling rate. In this way, 5-bits-per-sample quantization can be employed on the 6.4-kHz samples, while the bearer channel bit rate remains equal to 32 kbit/s [12]. Because of the symmetric nature of this interpolating filter (which is necessary in order to avoid the introduction of group delay distortion into the data transmission), a flat delay equal to 6 ms is introduced. This delay is equally distributed between encoder and decoder; however, because of the narrower band of the interpolated signal, higher prediction gains are achievable. This approach employs G.721 as the speech coding algorithm and uses a data detection algorithm to ensure routing of nonspeech traffic through this data-optimized algorithm. Unlike the other approaches, however, the synchronous operation of two or more coders in tandem [13] is no longer possible due to the band-limiting filters used in the encoder and decoder.

The OKI/KDD algorithms

In contrast to both previously described coders, the OKI/KDD algorithms employ a different predictive structure than the G.721-based predictor [1]. This adaptive structure is composed of a 10th-order adaptive zero predictor, a 4th-order adaptive-pole predictor, and a 16th-order fixed-pole predictor [14]. The relative contributions from each of these filters are controlled by a set of adaptive gain coefficients, while stability of the higher order pole filter can be monitored by means of the Hurwitz-based cascaded structure [15].

These algorithms differ in another substantial way from the other approaches. The first algorithm employs a 4-bit quantization mode of operation (32 kbit/s), and data are treated the same as speech. Thus, no speech or data detection mechanism is necessary. Furthermore, transparency of 9.6-kbit/s data is possible. When variable bit rate encoding is used (i.e., 24 kbit/s to create overload channels), all algorithms require the use of speech/data discrimination to avoid encoding data at 24 kbit/s.

An additional mode of operation employing a 5-bit (40-kbit/s) quantizer is also possible. This gives rise to a second algorithm which, due to its higher bit rate, enables further improvement in performance with 9.6-kbit/s data and allows DCME transparency for higher speed data.

The data modem/voice codec test facility

The data modem/voice codec test (DMVCT) facility is a computer-controlled measurement system consisting of several measuring, calibrating, and active units linked in a chain (Figure 1). This configuration enables the independent level adjustment of modulated voiceband data at several points along the chain, appropriate filtering, passage through any ADPCM or PCM codecs, and the introduction of channel bit errors or degradation of the data signal by injection of noise or other channel impairments (as described in CCITT Report R-28 [16]). Finally, it is possible to collect and analyze the returned (or receive) signal and all other system parameters so that important signal statistics such as bit error ratios, channel signal-to-noise ratios (*S*/*N*s), link bit errors, and the type and level of impairments can be obtained in a detailed tabular format.

The entire test chain is centered around the bit error rate test system (BERTS), Data Sentry 10. The Data Sentry provides the source data for the transmit half of the modem, to which the BERTS is connected by means of the bi-directional RS232C interface. In addition, the Data Sentry analyzes the received modem data and measures single errors, blocks, block length, block errors, seconds of test, and error-free seconds, all of which are parameters that can be used to interpret the quality of the received data.

The Data Sentry is connected to a Wavetek 6000 computer by means of an IEEE-488 bus. The other devices on this bus are an HP5150A printer, which provides a detailed tabulation of the source data; an HP8903A audio analyzer for on-line measurement of signal, noise, and distortion levels; and a Wavetek 6000 switching system for analog path control. The Wavetek 6000, which acts as the DMVCT system controller, collects and analyzes the various data. A specially formatted graphics output of the error burst length distribution can be obtained on the Wavetek 6010 graphics printer.

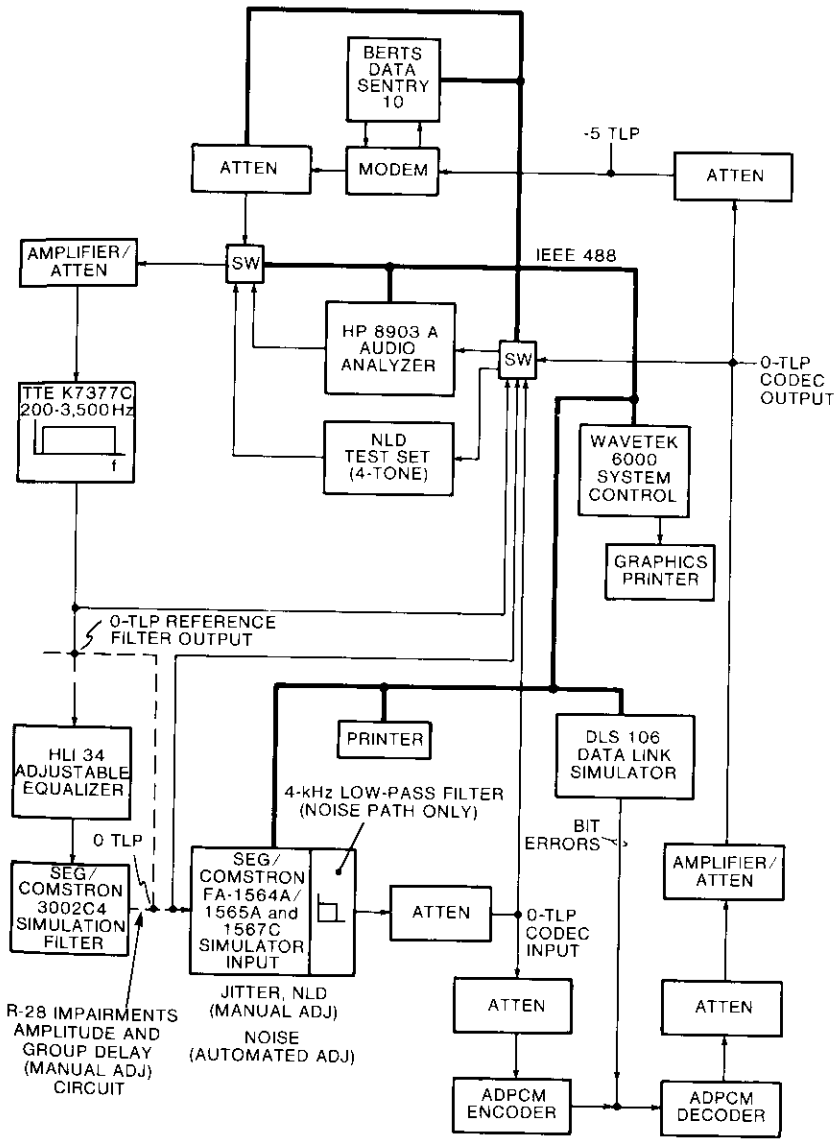

Figure 1. *Data Modem Voice Codec Test Facility Block Diagram*

The audio analyzer is connected to various nodes in the test setup signal path by means of the analog switching system. The analyzer acts both as a source and as a measurement device for automatic calibration measurements made prior to every bit-error measurement run. A number of attenuators and amplifier/attenuators along the signal path ensure that a proper signal level is maintained throughout the entire network and that calibration can be easily and accurately performed at the input and output of each active component, both before and after an experiment is conducted.

R-28 impairments [16] can be included by introducing the optional line simulator, consisting of an HLI34 adjustable equalizer in series with a SEG/Comstron 3002-C4 simulation filter. An additional impairment unit consisting of the three SEG/Comstron FA1564A/FA1565A/FA1567C modules enables the introduction of jitter and nonlinear amplitude distortion by means of a computer-controlled switching system. Furthermore, the FA1565A noise module enables the *S/N* to be automatically adjusted under computer control. A 4-kHz low-pass filter has also been provided in the noise path to ensure maximum undistorted noise output.

Finally, the General Data Products DLS106 data link simulator allows the injection of bit errors into the ADPCM encoder/decoder link. This simulator has been modified for an IEEE-488 bus interface, so that error rates between 10^{-9} to 10^{-3} bit/s can be automatically introduced under full computer control.

DMVCT facility calibration

All of the test points monitored by the DMVCT system are defined as zero transmission level points (TLPs). The levels are adjusted, a PCM codec is inserted at the codec test location, and reference measurements are made for the modems that will be used in the algorithm performance testing. The analog impairments (R-28) specified in Reference 16 are introduced, and the reference measurements are repeated.

The program-controlled noise level adjustment range is -27 to -51 dBm0p, and the system noise level at the codec input is -82 dBm0p. The line error rate adjustment range is 1×10^{-3} to 1×10^{-9}. Additional calibration details are given in the Appendix.

Results

A number of modems were employed to test ADPCM performance with voiceband data. In the figures presented here, these modems are designated as follows:

Curve	*Modem*
A	Codex 2640 (V.29)
B	OKI JVLSI (V.29)
C	Codex LSI 96 (V.29)
D	Racal Milgo Omni Mode (V.29)
E	Codex 2260 (V.32)
F	Codex 2366 (V.33)

Modems A through E operated at 9,600 bit/s, while modem F operated at 14,400 bit/s.

The objective analog measurements are shown in Figures 2, 3, and 4. Specifically, Figure 2 shows the variation of signal-to-quantization distortion ratio (*S/Q*) for a 1-kHz C-notched measurement in decibels, as a function of input signal level in dBm0 for a single encoding and for two and three

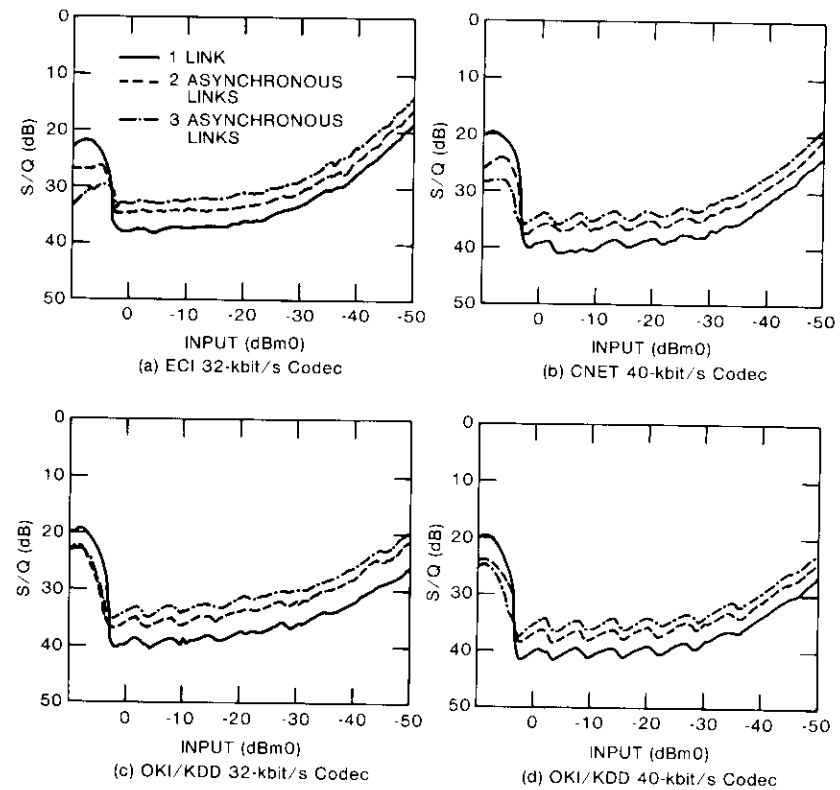

Figure 2. *Variation of Signal-to-Distortion Ratio With Input Signal Level*

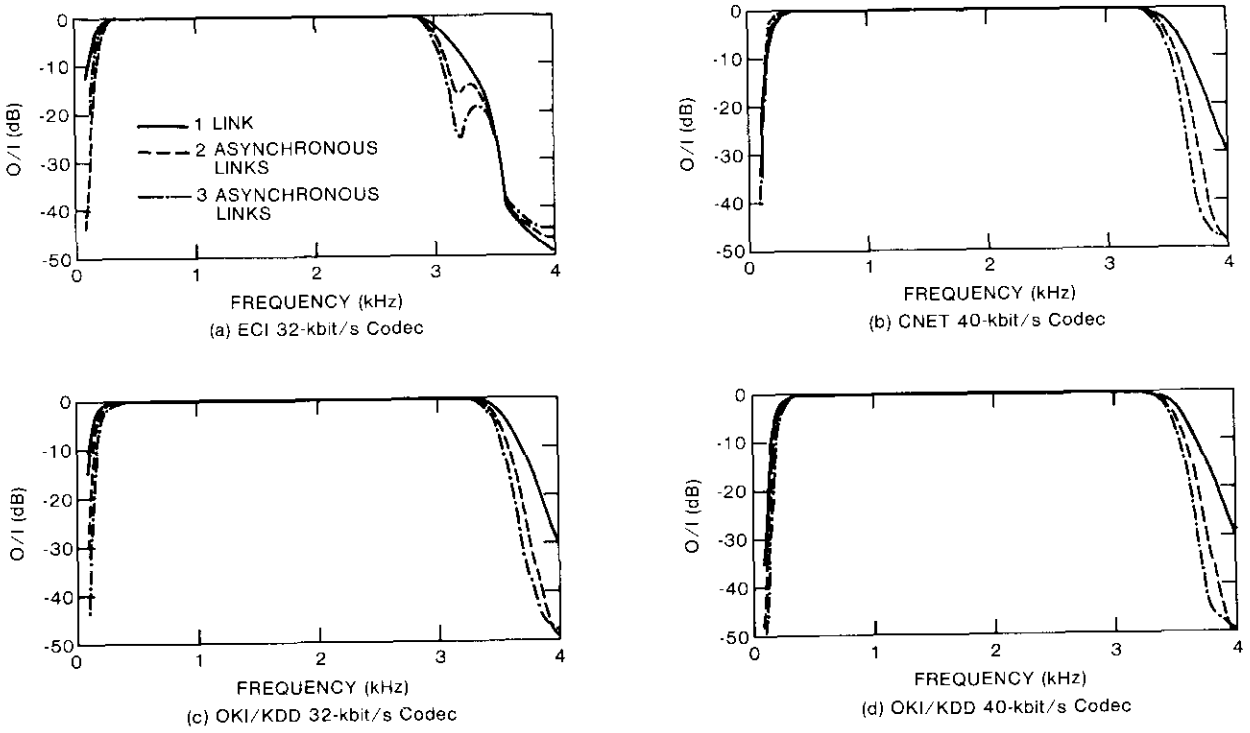

Figure 3. *Frequency Distortion at −15 dBm0 Input Data Level*

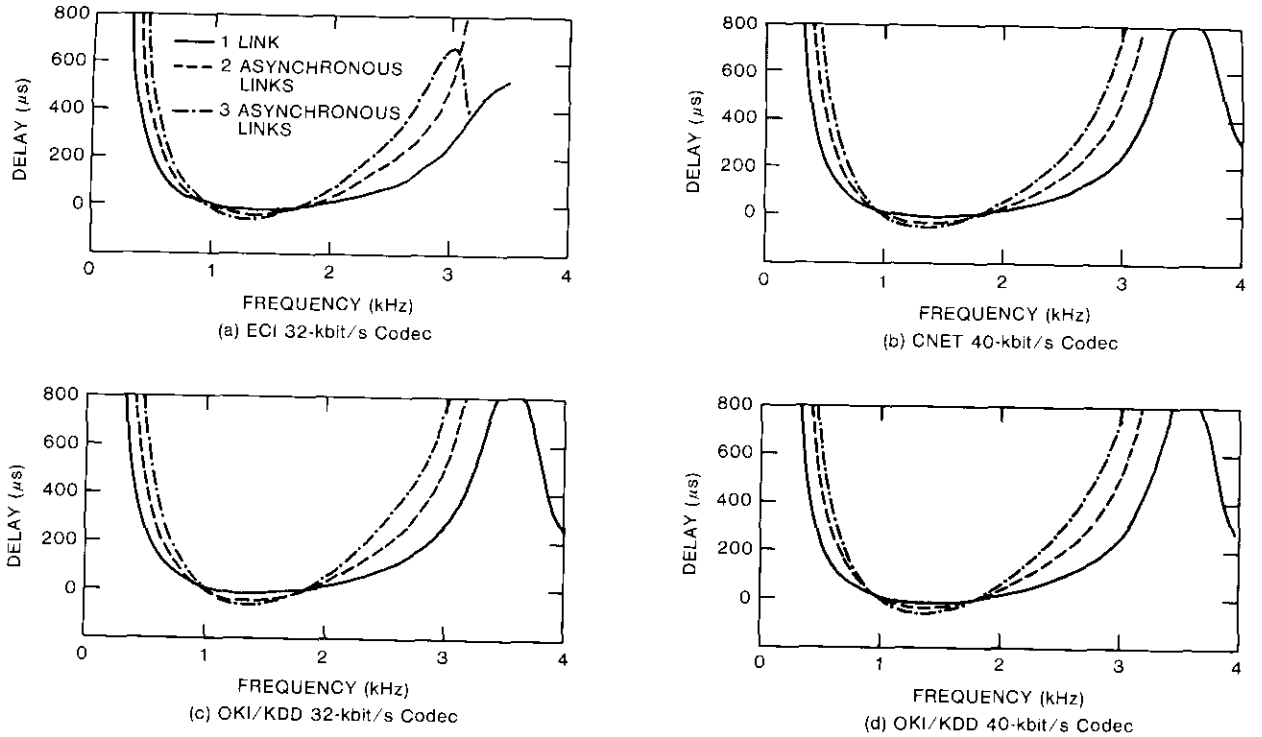

Figure 4. *Group Delay Distortion at −15 dBm0 Input Data Level*

asynchronous tandem encodings. Figure 3 depicts the variation of output-over-input amplitude distortion (O/I) in decibels, with input frequency in kilohertz at an input signal level of -15 dBm0, for one encoding and for two and three asynchronous encodings. The variation of group delay in microseconds as a function of input frequency in kilohertz at an input signal level of -15 dBm0 for one encoding and for two and three asynchronous encodings is shown in Figure 4.

The results of measurements with voiceband data modems are given in Figures 5 through 10. In all tests, the same analog (R-28) impairments used in G.721 testing were employed. Figure 5 shows the variation of modem block error ratio (MBLER) (511 bits/block) as a function of S/N in dBp at a -15 dBm0 input signal level. Characteristics are depicted for four V.29 modems produced by different manufacturers and operating at 9,600 bit/s. Modem signal power is measured as the rms value of the data signal at the codec input. Flat noise was injected prior to the first codec link and was subsequently psophometrically weighted in computing the S/N. Figures 6 and 7 show the performance obtained for two and three asynchronous encodings under the same conditions.

It should be noted that during the initial phase of these tests a 32-level quantizer version of the CNET algorithm was provided. Following deliberations by the Ad Hoc Group, it was decided that an odd-level (31-level) quantizer version would be preferable because, among other considerations, experimental performance with voiceband data could be improved, the zeros-density problem on the T-carrier system would be alleviated (by elimination of the 00000 output code), and idle channel stability would be enhanced. For these reasons, both a 32-level and subsequently a 31-level quantizer version of the CNET algorithm were provided and tested over the course of these experiments. Because of the consistently superior performance of the 31-level version, all results are shown for the odd-level quantizer, with the exception of Figures 6b and 7b (modems B and D) where the 31-level version was not tested.

Figure 8 depicts the V.29 modem performance in the presence of digital link bit errors. The results obtained show the variation of MBLER with line error rate (LER) for a single encoding, for the best (modem A) and worst (modem D) V.29 modems tested. Figure 9 shows the variation of MBLER with S/N for three asynchronous encodings for a typical V.32 modem (modem E) operating at 9,600 bit/s. An additional impairment of a -12 dB echo return loss, together with some minor modifications of the test facility configuration, were used to simulate the two-wire network topology. Finally, Figure 10 illustrates the variation of MBLER with S/N for a typical V.33 modem (modem F) operating at 14.4-kbit/s voiceband data rate.

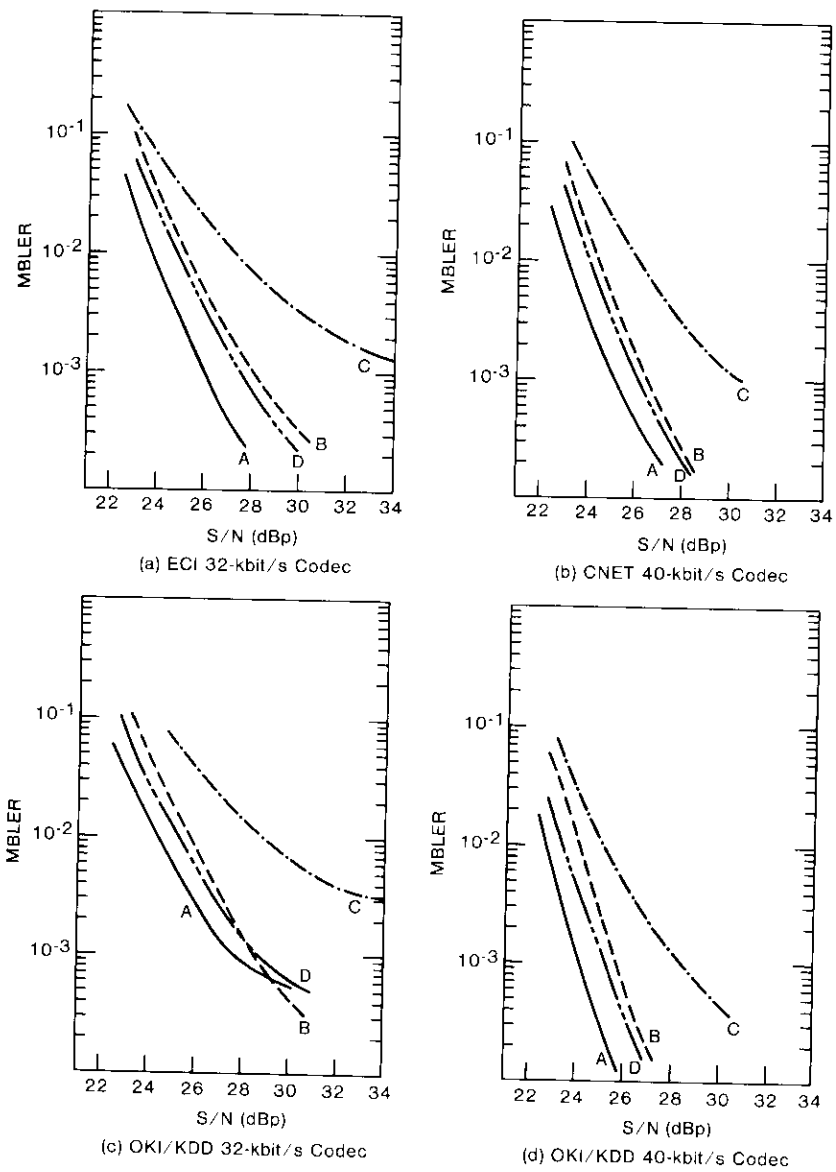

Figure 5. *V.29 Modem Performance With R-28 Analog Impairments (1 Link) for Four Modems Operating at 9,600 bit/s*

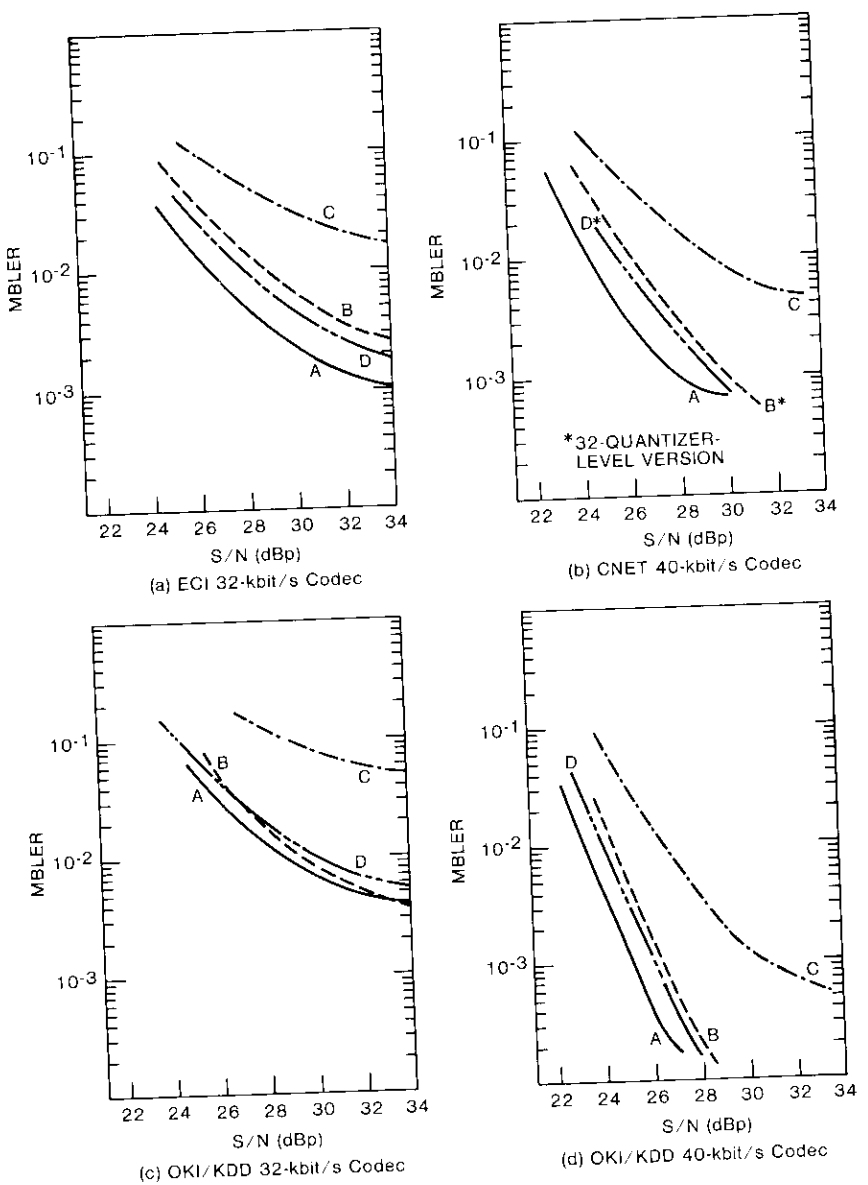

Figure 6. *V.29 Modem Performance With R-28 Analog Impairments (2 Asynchronous Links) for Four Modems Operating at 9,600 bit/s*

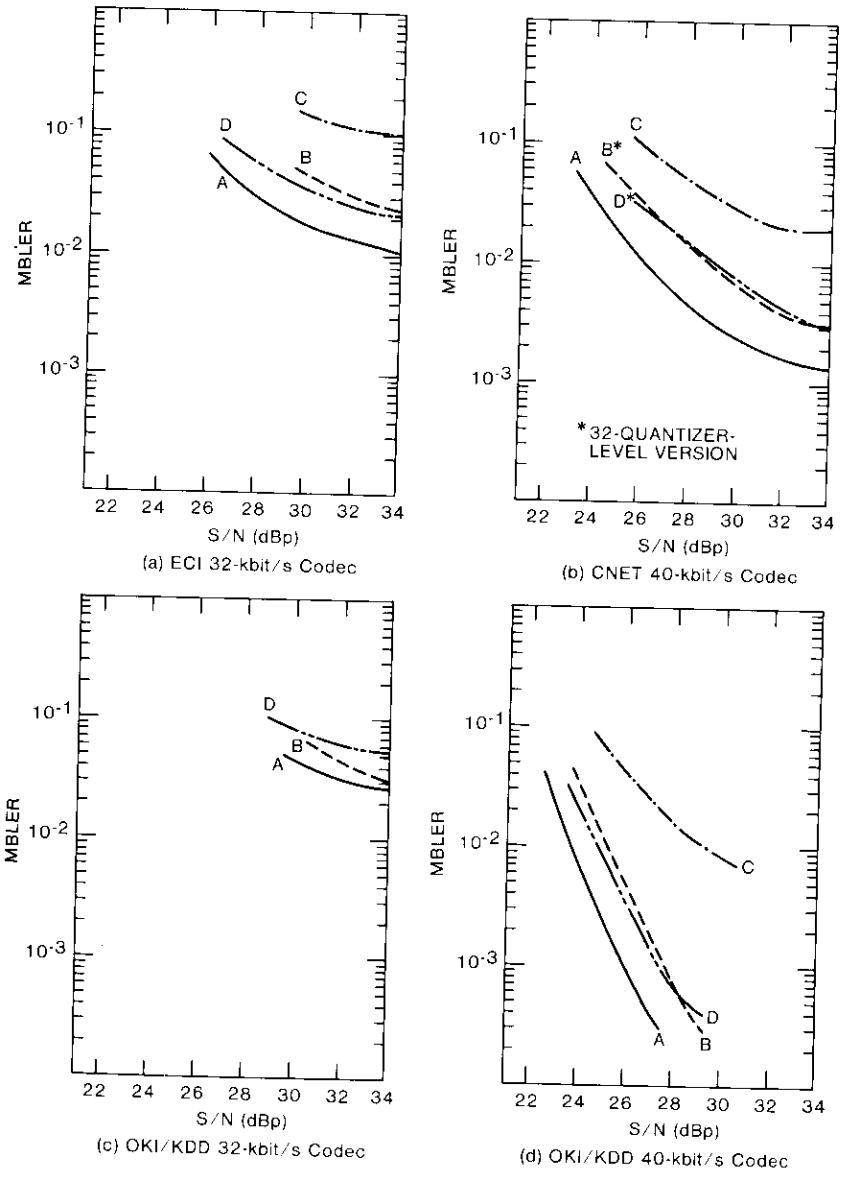

Figure 7. *V.29 Modem Performance With R-28 Analog Impairments (3 Asynchronous Links) for Four Modems Operating at 9,600 bit/s*

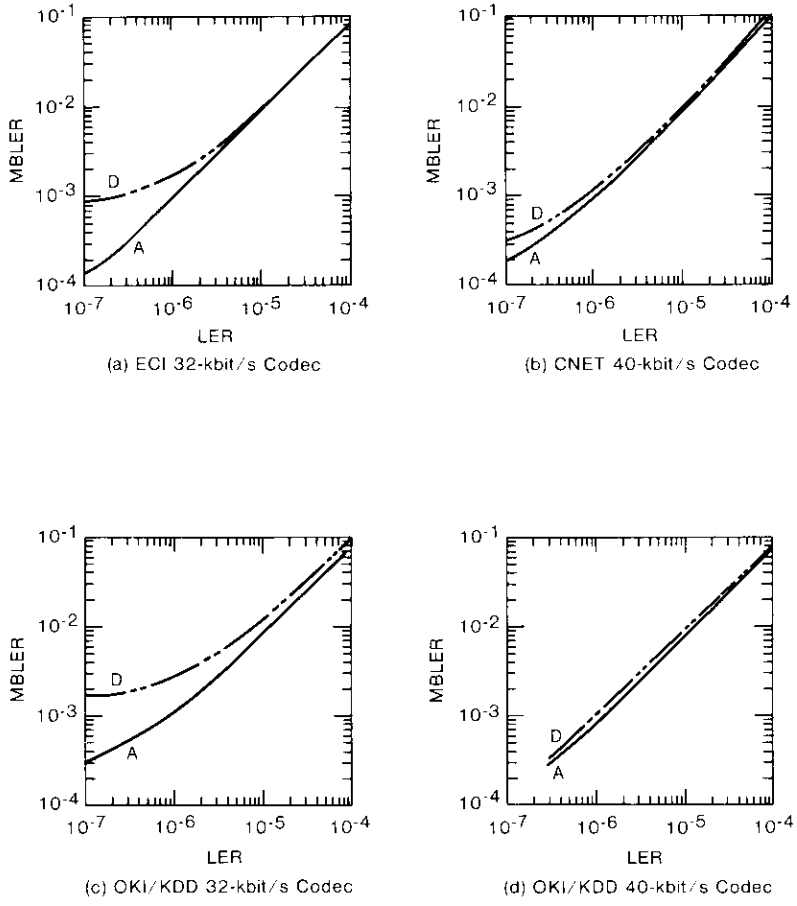

Figure 8. *V.29 Modem Performance With R-28 Analog Impairments (1 Link) for Two Modems Operating at 9,600 bit/s*

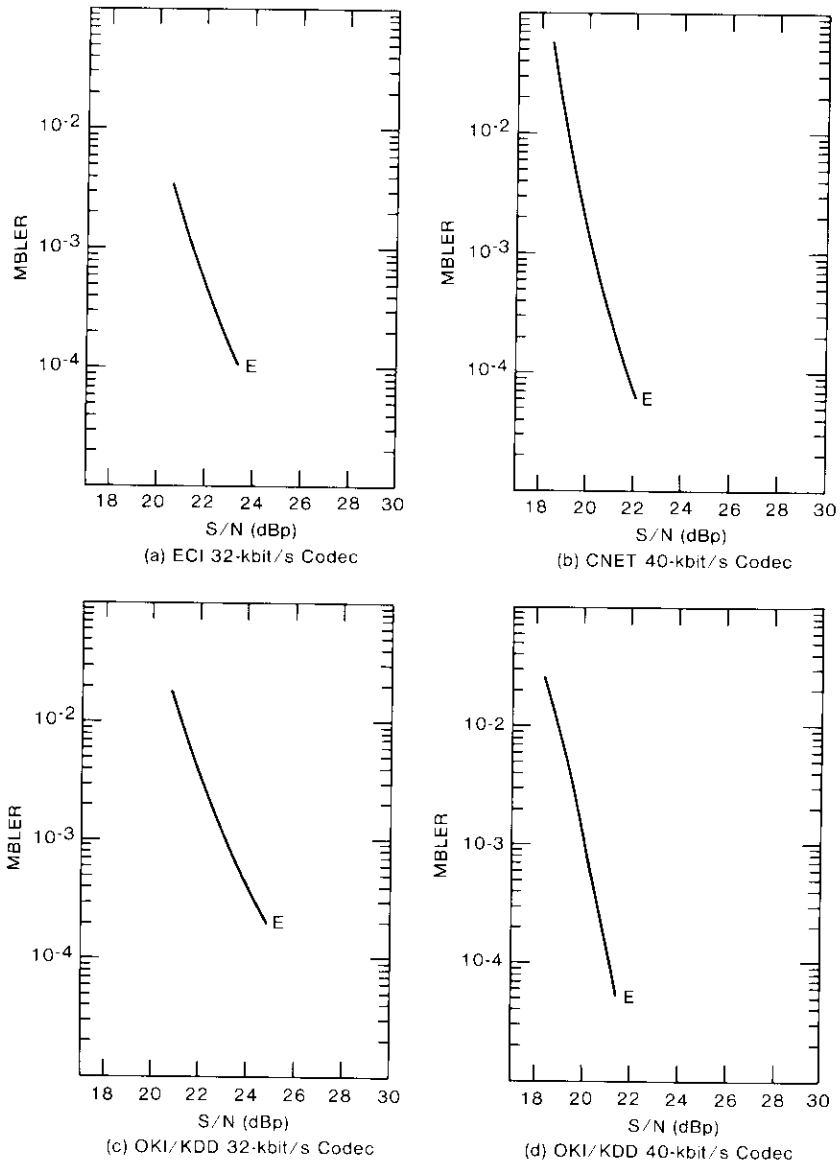

Figure 9. *V.32 Modem Performance With R-28 Analog Impairments (3 Asynchronous Links) for a Typical Modem Operating at 9,600 bit/s With −12 dB Echo Return Loss*

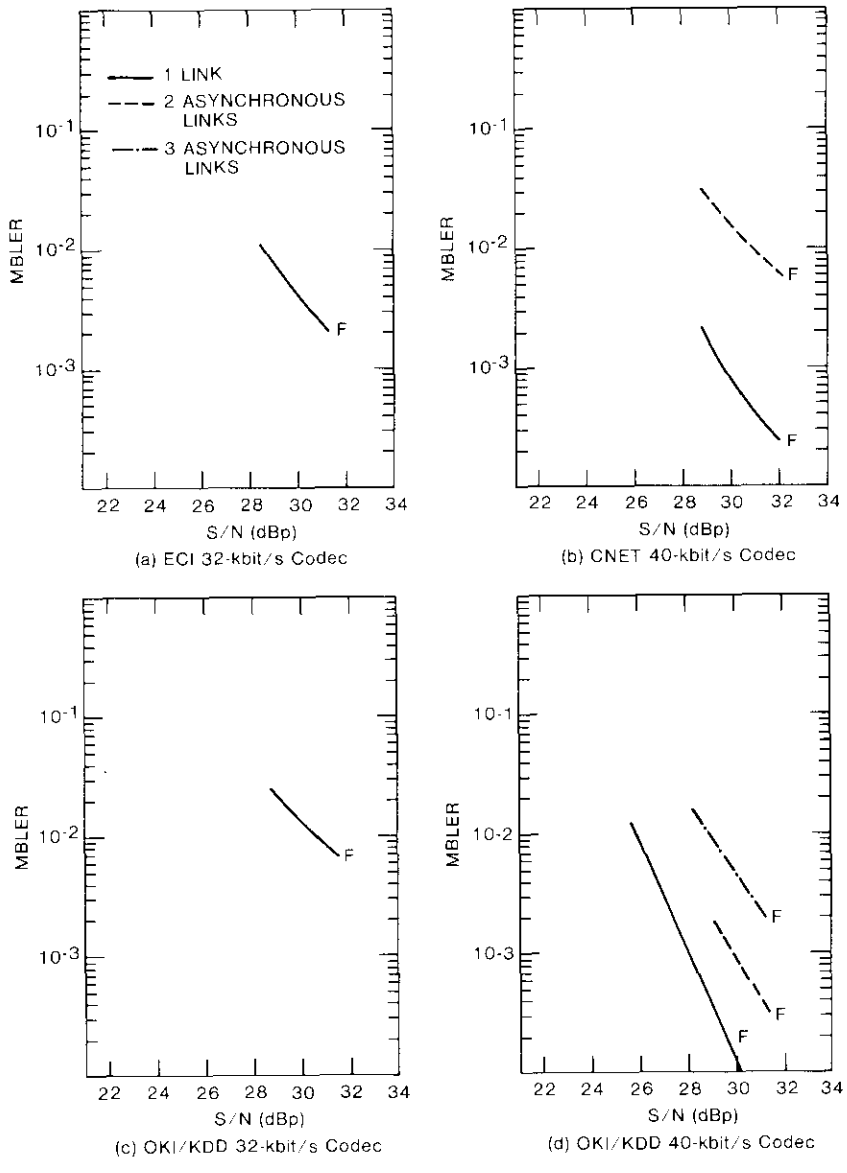

Figure 10. *V.33 Modem Performance With R-28 Analog Impairments for a Typical Modem Operating at 14,400 bit/s*

Figure 11 shows the baseline performance of each of the modems, tested with a μ-law PCM codec [17]–[19] in the link (with and without analog impairments). Table 1 summarizes some additional analog performance measurements for each of the ADPCM codecs.

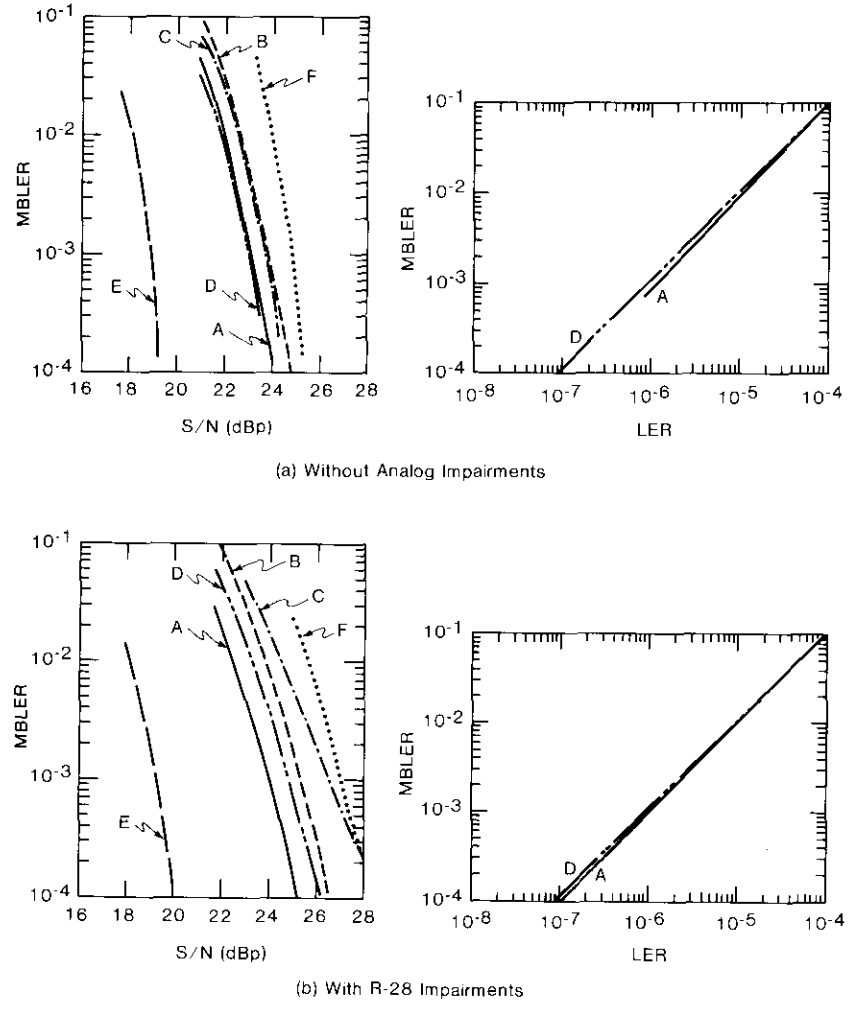

Figure 11. *Modem Baseline Measurements With a Typical μ-Law PCM Codec at 64-kbit/s*

TABLE 1. CODEC ANALOG PERFORMANCE MEASUREMENTS

CODEC	PHASE JITTER PEAK-TO-PEAK (deg)	AMPLITUDE JITTER PEAK (%)	NONLINEAR DISTORTION (dB)	
			2ND-ORDER	3RD-ORDER
ECI, 32 kbit/s				
1 Link	−1.1	−1.5	−54	−47
2 Asynchronous Links	−1.5	−2.4	−51	−45
3 Asynchronous Links	−1.9	−3.2	−48	−43
OKI, 32 kbit/s				
1 Link	−1.3	−1.4	−54	−48
2 Asynchronous Links	−1.7	−2.0	−46	−45
3 Asynchronous Links	−2.1	−2.6	−49	−42
OKI, 40 kbit/s				
1 Link	−0.8	−1.0	−59	−52
2 Asynchronous Links	−1.1	−1.5	−55	−49
3 Asynchronous Links	−1.3	−1.0	−54	−47
CNET, 40 kbit/s				
1 Link	−1.0	−1.0	−56	−52
2 Asynchronous Links	1.4	−1.5	−53	−49
3 Asynchronous Links	−1.7	−1.7	−49	−46

Based on these results, the following observations can be made. With regard to the analog measurements, no substantial difference exists between the various approaches, although for the ECI codec, which band-limits the input signal to 6.4 kHz, the corresponding amplitude and group delay distortion are clear.

In terms of V.29 modem performance, substantial variability in performance exists among the four different modems used. However, for a given modem, performance ranking of the different algorithms was possible in terms of decreasing MBLER with *S/N*. This ranking places the OKI/KDD 40-kbit/s algorithm first, with the CNET 40-kbit/s, ECI 32-kbit/s, and the OKI/KDD 32-kbit/s ADPCMs being second, third, and fourth, respectively. This ranking is only valid for asynchronous tandem connections. For synchronous tandem connections, the order of the last two ADPCM codecs is reversed, as the ECI 32-kbit/s algorithm does not provide for a synchronous coding adjustment [1].

With regard to the V.32 modems, the performance of all codecs was superior to that of the V.29 modems at three asynchronous tandem encodings. Finally, with the higher bit rate V.33 modem, the same performance ranking as with the V.29 modems is maintained for the different ADPCM algorithms. However, this modem cannot be readily supported by all codecs because adequate performance is not possible through any two asynchronous tandem encodings.

Conclusions

The results obtained in this study indicate that performance ranking of the different algorithms is possible in asynchronous and synchronous tandem configurations. Although this ranking is different in the two cases, it does indicate performance bounds that can be expected with each codec.

The CCITT Ad Hoc Group within Study Group XVIII, in considering these codecs as possible solutions to the DCME voiceband data transparency, established minimum performance criteria consisting essentially of voiceband data transparency of V.29 modems operating at 9,600 bits/s over two asynchronous encodings. Transparency was defined as a MBLER of 0.01 or less, achievable at a *S/N* of 30.5 dBp or less. In this respect, all of the codecs meet these requirements with all modems except modem D, which is an older V.29 design no longer manufactured.

These measurements were an essential factor in the CCITT's selection of the optimum codec algorithm for DCME. However, in making its final selection the CCITT also gave due consideration to factors outside of this performance framework, including DCME complexity and prior standards.

Acknowledgments

The authors would like to thank Alcatel, ECI Telecom, Inc., and OKI Electric Industry Co., Ltd., for providing their codecs, and the CCITT for consenting to use COMSAT Laboratories for these tests. In addition, the authors are grateful to Racal Milgo Corporation, Codex Corporation, Concord Data Corporation, and Kokusai Denshin Denwa Co., Ltd., whose kind technical assistance and generous loan of equipment made this study possible.

References

[1] CCITT, "32-kbit/s Adaptive Differential Pulse Code Modulation (ADPCM)," Recommendation G.721, *Red Book*, Fascicle III.3, 1984, pp. 125–160.

[2] CCITT, "Report of the Meeting of Working Party XVIII/8: Speech Processing," Study Group XVIII, Contribution COM 18, No. R-20, Geneva, July 1986.

[3] "Data Sets 202S and 202T Interface Specification," Bell System Technical Reference Publication 41212, July 1976.

[4] CCITT, "600/1200-Baud Modem Standardized for Use in the General Switched Telephone Network," Recommendation V.23, *Red Book*, Fascicle VIII.1, 1984, pp. 94–100.

[5] J. M. Raulin, W. R. Belfield, and T. Nishitani, "Objective Test Results for the 32-kb/s ADPCM Coder," IEEE Global Telecommunications Conference, Atlanta, Georgia, November 1984, *Conference Record*, pp. 786–790.

[6] CCITT, "9600 Bits per Second Modem Standardized for Use on Point-to-Point 4-Wire Leased Telephone-Type Circuits," Recommendation V.29, *Red Book*, Fascicle VIII.1, 1984, pp. 203–215.

[7] CCITT, "A Family of 2-Wire, Duplex Modems Operating at Data Signalling Rates of Up to 9600 bit/s for Use on the General Switched Telephone Network and on Leased Telephone-Type Circuits," Recommendation V.32, *Red Book*, Fascicle VIII.1, 1984, pp. 221–238.

[8] "DCME Standard" (Composite Draft), T1Y1.2/86-103, November 1986.

[9] CCITT, "Description of a 40-kbit/s ADPCM Algorithm for Use in DCME," Ad Hoc Group Q25/XVIII, Document 13, Annex 2, September 1986.

[10] CCITT, "Description of a Speech and Data Discriminator for Use in Digital Circuit Multiplication Equipment," Ad Hoc Group Q25/XVIII, Document 13, Annex 3, September 1986.

[11] CCITT, "Description of a Data Rate Analyzer for Use in Digital Circuit Multiplication Equipment," Ad Hoc Group Q25/XVIII, Document 13, Annex 4, September 1986.

[12] CCITT, "Voiceband Data Optimized Algorithm," Ad Hoc Group Q25/XVIII, Document 33, September 1986.

[13] M. Taka, R. Maruta, and A. LeGuyader, "Synchronous Tandem Algorithm for 32-kbit/s ADPCM," *IEEE Transactions on Communications*, Vol. COM-33, No. 12, December 1985, pp. 1309–1314.

[14] CCITT, "High-Level Description of Advanced 32-kbit/s ADPCM," Ad Hoc Group Q25/XVIII, Document 27, September 1986.

[15] S. Dimolitsas and U. Bhaskar, "Hurwitz Stability Analysis of an ADPCM System," *COMSAT Technical Review*, Vol. 17, No. 1, Spring 1987, pp. 105–125.

[16] CCITT, "Report of the Meeting of Working Party XVIII/2: Speech Processing," Study Group XVIII, Contribution COM 18, No. R-28, Geneva, December 1983.

[17] CCITT, "Pulse Code Modulation (PCM) of Voice Frequencies," Recommendation G.711, *Red Book*, Fascicle II.3, pp. 85–93.

[18] CCITT, "Testing/Phase I: Results of an Objective Performance Evaluation of ADPCM Coders for DCME Voiceband Data Transparency," Ad Hoc Group Q25/XVIII, Document 74, January 1987.

[19] COMSAT Laboratories, Private communication, August 1987.

Appendix. Test setup calibration

For four-wire modem testing, the input attenuator is adjusted under computer control so that the level of the data-modem signal at the output of the reference channel filter is equal to −15 dBm when measured rms/unweighted at 0 TLP. The parameters of the line-simulation filter combination are adjusted to provide 0-dB gain, and this filter is bypassed when conducting no-analog-impairment reference measurements. The line-impairment generator is adjusted for an input reference level of −15 dBm and an input-to-output gain of 15 dB. A 15-dB pad ensures that 0 TLP is maintained at the codec input, and appropriate attenuation is inserted for the proper codec input level. The periodic sequence of character signals (based on Table 6 of Recommendation G.711 [17]) is applied to the μ-law PCM decoder, which is then adjusted for a 0-dBm0 output. The codec input-to-output gain is adjusted so that it equals 0 dB. The decoded ADPCM signal is amplified in order to produce 0 TLP at the codec output, and then attenuated by 5 dB to provide a signal level of −20 dBm at the data modem input.

For two-wire modem testing, the data signal from the SLIC is also presented to the line simulator at a level of −15 dBm0, but is returned to the SLIC at a level appropriate for the two-wire modem. Since the SLIC is calibrated for a 0-TLP four-wire interface at both the send and receive ports, the data signal is returned to the SLIC at the same level as would be measured with these ports directly connected to each other. A single 32-kbit/s ADPCM codec was interfaced in the return path of the SLIC for this test.

For channel *S/N vs* modem BER tests, Gaussian noise from the noise module of the line simulator is added to the data signal at the output of the line-impairment generator. The noise level is set under computer control to a value between −27 and −51 dBm0p for nominal channel *S/N*s of 12 to 36 dB relative to the calibration tone. The signal level is measured rms/unweighted, and the noise level is measured rms/psophometric weighted, both at 0 TLP at the input of the μ-law PCM codec. Channel BER is set, as required, within the range 1×10^{-4} to 1×10^{-8}. The noise level produced by the test system prior to the codec is nominally −82 dBm0p.

Spiros Dimolitsas received a B.Sc. (with Honors) in physics and mathematics from Sussex University, Great Britain, in 1977; an M.Sc. and Dipl. Eng. Q.M.C. in nuclear reactor engineering from London University in 1979; and a D.Phil. in computer engineering and digital signal processing from Sussex University in 1982. From 1982 to 1983 he worked for High Energy and Nuclear Equipment S.A. in Geneva, Switzerland, and later for the Mayo Clinic and for MOSTEK Corporation, where he was involved in digital image processing (CT) and modem design (V.32), respectively. He joined COMSAT Laboratories in 1986 and has been involved in studies of linear and nonlinear voice processing systems, with special emphasis on adaptive IIR filters, coder stability, and noise cancellation techniques. He is presently a Member of the Technical Staff in the Communications Techniques Division. Recently, he has been COMSAT's representative to the CCITT experts' group on ADPCM voiceband data transparency for digital circuit multiplication equipment. Dr. Dimolitsas is a member of the IEEE Communications Society; the IEEE Acoustics, Speech, and Signal Processing Society; the European Association for Signal Processing (EURASIP); and the Technical Committee of the ASME Society on Active Noise Control.

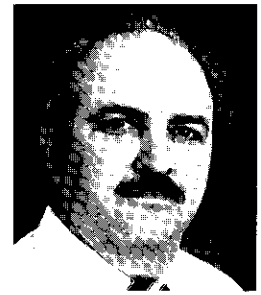

Franklin L. Corcoran is an Associate Staff Member in the Communications Techniques Division at COMSAT Laboratories. He is currently active in digital sound-program codec development, and has been a technical consultant to other divisions at COMSAT in the specification, design, and testing of speech and program codecs. He is a specialist in the objective and subjective testing of speech codecs and has developed a speech codec objective test system, an automated data modem/speech codec BER testing facility, and a computer-aided subjective evaluation facility which integrates speech sample presentation with the acquisition and analysis of test data. He was heavily involved in the CCITT Study Group XVIII Ad Hoc Group test program to select an ADPCM algorithm for use in digital circuit multiplication equipment, and was previously involved with CCITT as the COMSAT Technical Representative in the joint COMSAT/BNR/BellCore contribution to the subjective evaluation of the wideband teleconferencing codec described in CCITT Recommendation G.722. Before joining COMSAT in 1970, Mr. Corcoran was an Engineering Specialist at Night Vision Laboratories, Ft. Belvoir, Virginia, where he developed a subjective test capability for night observation devices. He received a basic engineering education at the Massachusetts Institute of Technology, followed by 4 years of electronics R&D in the U.S. Army Security Agency.

Michael Onufry received a B.S. degree from Pennsylvania State University in 1962, and performed graduate work at both Northeastern University and George Washington University. He is currently Manager of the Voice Band Processing Department in the Communications Techniques Division at COMSAT Laboratories. His experience includes echo canceller development, 64-kbit/s PCM and 32-kbit/s ADPCM, digital speech interpolation development, and encoding of speech. He has been active in planning and implementing international field trials in the INTELSAT network, and is responsible for subjectively assessing various speech processing devices. Since 1977 Mr. Onufry has been the COMSAT Representative to CCITT Study Group XV, where he has been a Special Rapporteur for questions concerning echo cancellers, syllabic companders, and digital circuit multiplication equipment. He is a member of IEEE, and Past President of the Maryland Chapter of the ASSP.

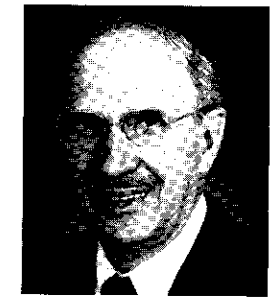

Henri G. Suyderhoud received the Ingenieur Degree in electrical engineering from Delft Technological University in the Netherlands in 1955, and the M.S. degree in applied mathematical statistics from Rutgers, New Brunswick, in 1966. After joining COMSAT Laboratories in 1968, he became involved in research on echo suppression and echo cancellation, and the development of subjective evaluation techniques. He became Section Head in 1969 and Department Manager in 1974. In 1981 he assumed the position of Senior Scientist and Assistant to the Executive Director of the Communications Techniques Division, where his responsibilities encompass various special projects including CCITT coordination, speech research, and R&D planning.

Prior to joining COMSAT Laboratories, Mr. Suyderhoud was employed for more than 11 years at Bell Laboratories, where he worked on exchange area and high-density broadband carrier transmission engineering, conducted the first laboratory experiments with echo cancellation, and helped develop standards for picture-phone transmission. He is a Senior Member of IEEE and a member of the American Statistical Association and the AAAS.

Index: communications satellites, redundancy, time division multiple access

Network control processor for a TDMA system

O. SURYADEVARA, T. J. DEBETTENCOURT, AND R. B. SHULMAN

(Manuscript received April 13, 1987)

Abstract

Two unique aspects of designing a network control processor (NCP) to monitor and control a demand-assigned, time-division multiple-access (TDMA) network are described. The first involves the implementation of redundancy by synchronizing the databases of two geographically remote NCPs. The two sets of databases are kept in synchronization by collecting data on both systems, transferring databases, sending incremental updates, and the parallel updating of databases. A periodic audit compares the checksums of the databases to ensure synchronization.

The second aspect involves the use of a tracking algorithm to dynamically reallocate TDMA frame space. This algorithm detects and tracks current and long-term load changes in the network. When some portions of the network are overloaded while others have excess capacity, the algorithm automatically calculates and implements a new burst time plan.

Introduction

The Deutsches Fernmelde Satellitensystem (DFS) was recently developed to provide efficient telecommunications capability for high-intensity traffic by using a multi-transponder satellite [1]. This system offers distributed voice, data, television, and heavy route trunking facilities, and uses demand-assigned, time-division multiple-access (TDMA) techniques to allocate satellite channels. TDMA techniques achieve maximum efficiency in the use of satellite transponders because several traffic terminals can use the transponder resources in a synchronized, sequential, time-shared fashion [2]–[7].

The TDMA system (Figure 1) consists of the following five major components:

a. *A geostationary satellite* that handles TDMA traffic.

b. *A reference terminal* (RT) which coordinates the timing of traffic terminal bursts into the TDMA frame. The RT also implements various commands, including real-time changes to the burst time plan (BTP).

c. *Traffic terminals* (TTs) to receive and transmit the customer's traffic. These terminals are real-time processors that track the TDMA frame and route customer traffic into the TDMA frame sub-bursts.

d. *A network control processor* (NCP), the main computer for monitoring and controlling the TDMA network. The NCP provides a variety of central processing unit-intensive functions, such as operator interface, network monitoring and control, billing report generation, and channel reservation.

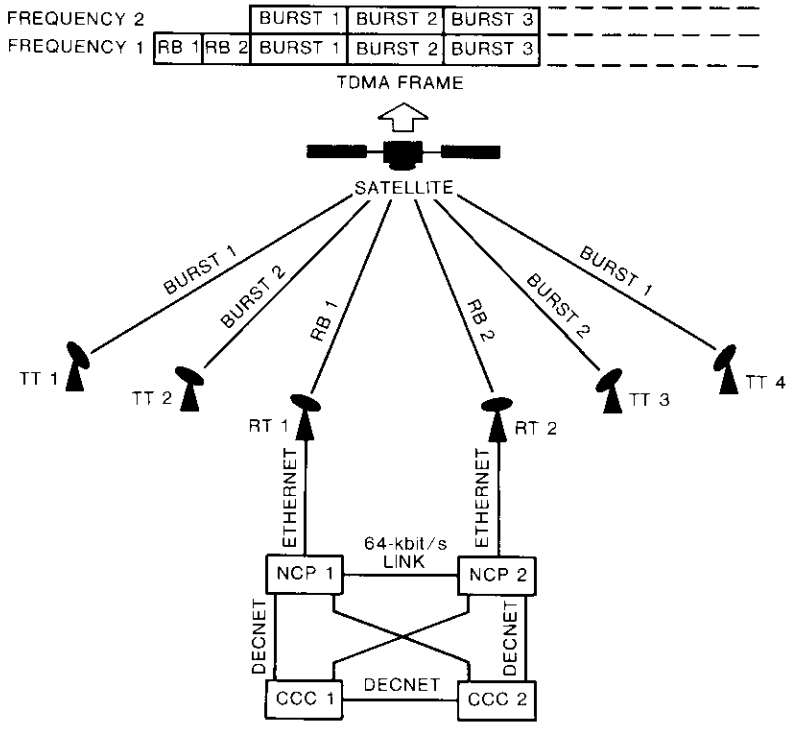

Figure 1. *TDMA System Block Diagram: Two-Transponder Configuration*

c. *A central control computer* (CCC) that interfaces with the central network operator and performs off-line duties such as receiving user requests to reserve satellite channels.

The RT, NCP, and CCC processors are duplicated for redundancy, as shown. Connections between a set of processors (e.g., RT 1, NCP 1, and CCC 1) are all local networks, mainly the Ethernet type. The CCC 1 and CCC 2 are colocated, but the NCP 1 and RT 1 are geographically remote from the NCP 2 and RT 2. Connections between corresponding processors (e.g., NCP 1 and NCP 2) are dedicated terrestrial 64-kbit/s links.

A highly responsive network control facility is needed to ensure proper functioning of the TDMA network [8],[9]. The NCP plays a crucial role in network monitoring and control. This paper presents a general description of the NCP, followed by a detailed discussion of two new design aspects: off-site redundancy, and dynamic load tracking and frame reconfiguration.

Functions of the network control processor

The NCP, a Micro-VAX II running the Micro-VMS operating system, provides the following functions and high-level interfaces necessary for network control:

a. *Operator Interface.* The NCP provides the primary operator interface for the TDMA system. Appropriate operator screens and menus are generated and transmitted to the video display unit. Operator inputs are received and transformed into messages for transmission to the rest of the system.

b. *Reservation Request Implementation.* The NCP creates BTPs to implement reservation requests from the CCC. These reservation BTPs are calculated and coordinated with the BTPs generated by the frame reconfiguration subsystem described below.

c. *Monitoring and Control.* The NCP allows the operator to monitor and control the TDMA network in real time.

d. *Error/Alarm Message Handling.* The NCP provides the operator with current equipment status and error/alarm messages regarding events in the TDMA system.

e. *Traffic Reports.* The NCP initiates traffic measurements as requested by the CCC, and creates traffic reports as needed. Traffic data such as transponder load, call type, and inbound/outbound traffic at the terminal are maintained separately for each traffic terminal.

f. *Billing (Call Data).* The NCP collects and formats billing information for customer equipment that is directly connected to the TDMA system. Reports are periodically sent to the CCC for customer billing.

g. *Route List and Numbering Plan.* The NCP maintains the traffic routing configuration for all traffic terminals in the system. It accepts, verifies, and implements CCC commands for establishing trunk groups, trunks, and routes. It also maintains the call signaling information (numbering plan) for calls in the network.

h. *Subscriber Lists.* The NCP maintains and updates information on all subscribers under the control of the CCC. It implements commands to create, delete, display, and change subscriber information.

i. *Internetwork Message Routing.* The NCP serves as a physical and logical connection between the traffic terminals, the reference terminals, and the CCC, allowing them to exchange monitoring and control information.

j. *Off-Site Redundancy and Switchover.* Two NCPs at different sites are always in a warm-standby redundancy configuration. The databases are constantly updated and kept redundant for a quick and smooth switchover in case of a failure in the primary NCP.

k. *Dynamic Load Tracking and Frame Reconfiguration.* The NCP dynamically tracks the load distribution in the TDMA network and calculates and implements a new BTP when needed.

The last two functions are the most significant and will be discussed in detail.

Off-site redundancy and switchover

To satisfy service availability requirements, two NCPs are located at different sites (one primary and the other secondary). Both NCPs are active at all times, and in the event of a failure in the primary, the secondary takes over. Due to the geographic separation between the two NCPs, problems of remote (off-site) redundancy are encountered. Traditional schemes for on-site redundancy depend on hardware or software solutions that exploit the close proximity of the processors [10]–[12]. The large databases in the NCP, combined with a relatively slow land link (64 kbit/s), make the problem of off-site redundancy especially difficult to solve. NCP redundancy also posed major problems because of the following:

- existing interdependent databases,
- existing nonredundant software,
- memory-based databases,

- time constraints for system delivery, and
- hardware constraints (only one Micro-VAX at each location, as shown in Figure 2).

In general, the redundancy scheme should provide for uninterrupted availability of the NCP in the event of any single failure. Switchovers between the primary and secondary sites must be quick and smooth. Once data are accepted at the NCP from the rest of the system, the NCP becomes solely responsible for these data.

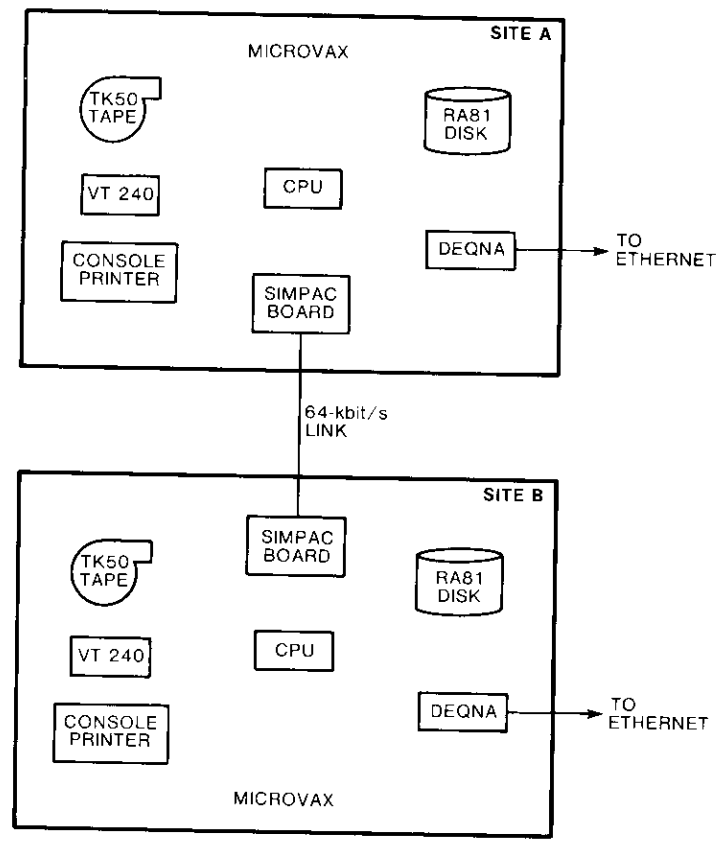

Figure 2. *Redundant NCP Hardware*

Database currency and consistency

One component of the overall database redundancy requires that the data on the disk be current at all times. The VAX virtual memory architecture brings pages of memory in from the disk as they are needed for modification. Since these pages are not written back to disk until the memory is needed by another task in the system, data in memory may be lost in the event of power failure. To prevent such losses, each application running in the NCP performs a forced update to disk and waits for the update to complete before proceeding. This was accomplished by inserting calls to the VMS system service routine, SYS$UPDSECW, at critical points in each application task. This ensures that the data on the disk stay current up to the last critical point. Updates are performed only at critical points in the task, since continuous updates to disk slow down the processor (due to the large amount of disk I/O).

Database updates on the secondary NCP

The redundancy scheme requires that the databases in the secondary NCP be kept up to date. Since these databases were not initially designed for redundancy, they tend to be large and not well structured. Thus, when a change occurs in a database, it is not possible to tell which part of the database changed without analyzing its complete structure. Considering the slow data rate (64 kbit/s) of the link between the primary and secondary, considerable time (approximately 20 minutes) would be required for a complete transfer of databases from one NCP to the other. This delay was unacceptable, as was the delay involved in capturing the database changes and relaying them to the secondary NCP. Hence, it became necessary for the two NCPs to operate and maintain databases independently of each other in some subsystems. The problems posed by the slow link between primary and secondary NCPs, as well as the nature of the existing nonredundant code and interdependent databases, made it necessary to incorporate different database update designs for each subsystem. These designs will now be examined in greater detail.

Individual tasks that change the databases know exactly what data are changing and where such changes occur. Therefore, it should be possible for each task to transmit these changes to the secondary NCP, where they would be incorporated to reflect the new state of the databases. This implies that the individual tasks which perform the updates should transmit the changes from the primary to the secondary NCP. These messages would contain the detailed information needed to properly update the database. However, major changes to the application code are required in order to capture the database changes, format them into messages, and send them to the secondary. New code is also necessary in the secondary to decode the messages and update

the database. Although this database update scheme was not acceptable for the existing application code, it was easily incorporated into the alarm control database (which was designed later). Figure 3 is a schematic dataflow diagram of this design.

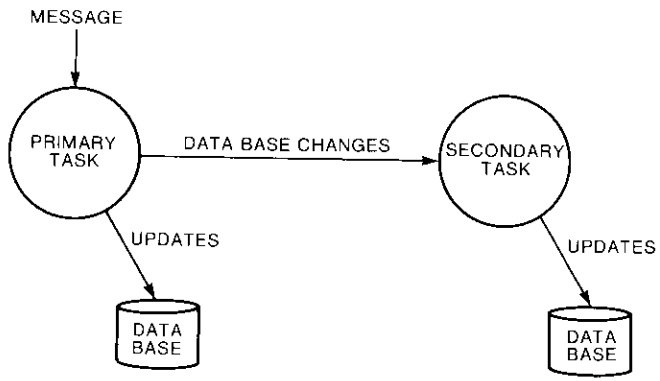

Figure 3. *Incremental Updates by Individual Tasks*

Another alternative is to transfer the entire database whenever there is a change, as shown in Figure 4. This approach is reasonable only for a very small database and when the changes are extensive. Also, in subsystems that generate new data inside the NCP, it is not desirable to generate parallel data in both NCPs due to possible inconsistencies. As transfer of the database is ideal for this situation, this approach was used for the operator interface and the frame reconfiguration. However, transfers of entire databases were held to a minimum and performed at times of low load.

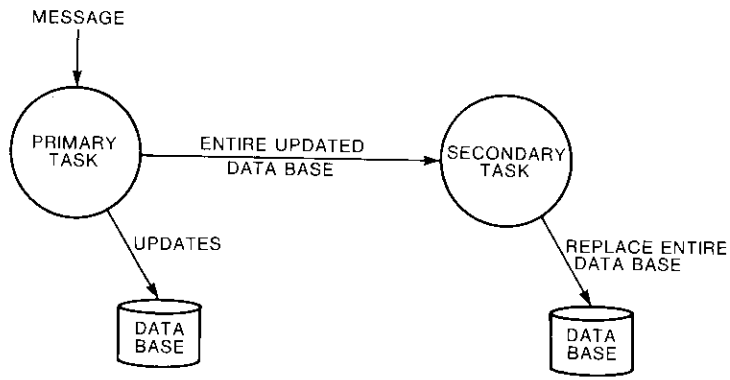

Figure 4. *Copy of Database for Small Databases*

A better way to update large databases is to duplicate the incoming message that causes the database changes and send the copy to the secondary, which then makes the required changes to the databases. This approach appears advantageous when the databases are large and the message containing the instructions is small. A secondary version of the application task would process the message and update the database as needed, resulting in a situation similar to parallel processing. However, unlike parallel processing, the secondary task only updates the database, but does not perform any other functions of the primary task. This scheme was implemented via the two interfaces between the NCPs and the rest of the TDMA system: the CCC router and the TDMA router.

The CCC router process in the NCP maintains the links between the CCC and the NCP. Only the CCC router in the primary NCP receives data from the CCC. Data redundancy is maintained by having the CCC router in the primary NCP relay all messages it receives to the CCC router in the secondary. This ensures that the two NCP applications receive the same stream of input data from the CCC. The primary application updates its database and sends a reply message to the CCC. Then the secondary application updates its database. If a network switchover should occur when a message is in transit, the CCC will fail to receive a reply to the message and will retransmit to the new primary NCP. Note that the CCC can send messages only as fast as the primary NCP can forward them to its secondary.

The TDMA router processes in the two NCPs communicate with each other to exchange messages. The primary TDMA router relays messages to the secondary TDMA router for processing by the secondary task. This is similar to the CCC router process described above.

Figure 5 is a dataflow diagram of the redundancy scheme. This simple scheme involves minimal code changes to create a secondary version of the task (whose only role will be updating the database), although it works only for subsystems which collect information. It was implemented for two subsystems: subscriber, and route list/numbering plan.

It is also possible for two tasks in the two machines to operate in parallel, independent of each other and maintaining their own databases. Through parallel updates (see Figure 6), the processes in both NCPs receive the same input and produce the same output, thus simultaneously updating the databases. Consequently, subsystems with large and rapidly changing databases (such as the call statistics subsystem) are run in parallel. If the task's code is complicated, as in the reservations subsystem, it is best not to change it to support redundancy. Therefore, reservation and call-data databases are updated in parallel.

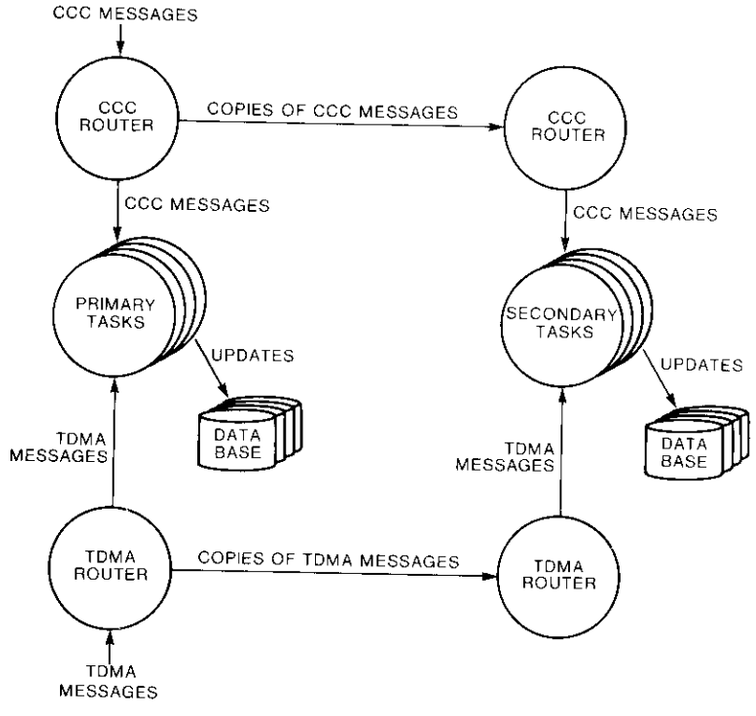

Figure 5. *Indirect Incremental Updates via Messages*

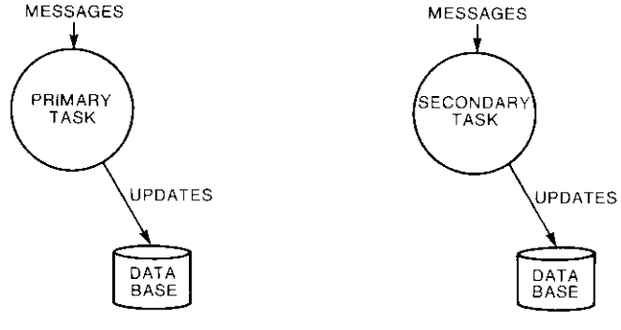

Figure 6. *Parallel Updates of Databases*

Startup and switchover scenarios

A periodic link test message between the NCP and its reference terminal indicates the reference terminal state (primary or secondary) to the NCP. When the NCP first comes up, it immediately goes into the state indicated by its reference terminal. If the reference terminal indicates a secondary state, the NCP initiates a database down-load procedure (described below) from the primary before becoming operational. Also, if an NCP is taken down for maintenance or goes down due to hardware faults, it initiates a database down-load when it again comes up. If all links between the NCPs fail, database changes cannot be sent to the secondary. Thus, when the links return to service, a complete database down-load is necessary. Whenever the primary cannot communicate with its secondary, the primary continues to operate normally, keeping all of its own databases up to date, but without the backup provided by the secondary. In this situation, failure of the primary NCP would be disastrous. To avoid this problem, periodic snapshots of the NCP databases are sent to a backup device (VAX 11/730) when necessary.

When the secondary NCP or the link between the primary and secondary returns to service, the NCP databases must be resynchronized. This is accomplished by having the secondary send checksums of its databases to the primary. These checksums are then compared with the checksums of the respective databases in the primary, and databases that have changed are copied by the secondary. During the copy process, tasks on the primary are disabled from making changes to the databases, and tasks on the secondary are stopped/suspended and restarted in order to begin referencing the newly copied data files. This procedure is called a database down-load. Whenever a primary is restoring a database in the secondary, all communications with the CCC and TDMA are suspended to prevent changes to the databases that are being copied. When the transfer is complete, the NCPs resume the CCC and TDMA communications.

The NCP must continue to function under the following two kinds of network switchovers:

a. Both NCPs are operating normally when the reference terminals switch over due to either rain fade or hardware fault.

b. A hardware/software failure occurs in the primary NCP and the reference terminals call for a switchover.

Under normal operation, all databases in the two NCPs are the same and switchover involves no data transfer. Thus, a switchover is almost instantaneous. When the secondary NCP learns of a switchover from its reference terminal, it sends a "takeover" message to the primary NCP. In the event that communications with the reference terminal are not functioning, this message alerts the primary NCP to a switchover in order to avoid creating a network with two primary NCPs.

Periodic checks on the health of the NCP will pinpoint problems with hardware or software. Since the two NCPs maintain two sets of data, the databases should be as similar as possible during normal operation. However, the databases may occasionally lose synchronization due to communications failures. To detect such failures, the secondary NCP periodically calculates the checksums of all its databases and sends these checksums to the primary NCP. The primary NCP then compares the checksums against its databases. If there is disagreement, the primary determines that a database down-load is needed and informs the secondary NCP. Both NCPs then execute the down-load procedure.

In addition, a health-check routine periodically checks whether all tasks are running on the NCP. If it notices that any task is not running, it sets the health of the NCP to *software fault*. This information is returned to the reference terminal in the link test. The reference terminal may then decide to switch over if it detects poor NCP health.

Dynamic load tracking and frame reconfiguration

All traffic in the TDMA frame is coordinated using the structure shown in Figure 7. Each reference terminal generates reference bursts (RBs) (one per transponder) for the TDMA frame. This is followed by various traffic bursts from the traffic terminals. The NCP configures this TDMA frame for use by the reference terminals and traffic terminals. The load distribution in this real-time network changes dynamically as new calls are originated and old calls are terminated.

To maintain optimal system operation, the NCP can continuously monitor the network load distribution and dynamically reallocate frame space to increase the efficiency of transponder utilization. Simulation studies [13] have led to the development of an empirical tracking algorithm, presented below.

As shown in Figure 7, the first two bursts are reference bursts (set up by the reference terminals) which provide a reference point to the traffic terminals. Database bursts are used for down-loading data to the traffic terminals; other bursts may be required for signaling and control. Next, a reservation burst carries reserved traffic bursts in frame space reserved by customers. This is followed by the main traffic burst (MTB), which carries the dynamic traffic between traffic terminals and is governed by a BTP.

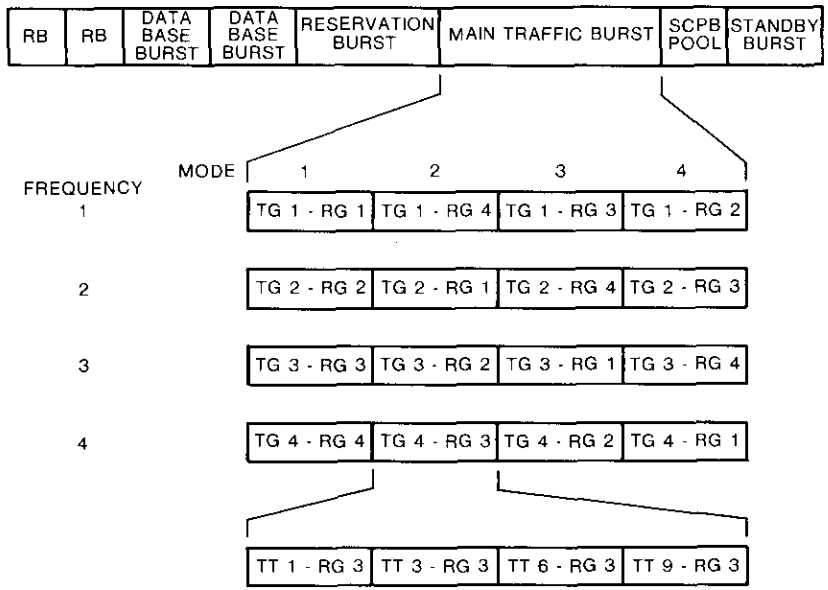

Figure 7. *TDMA Frame and Switching Modes: Four-Transponder Configuration*

Since there are multiple transponders, the traffic terminals are organized into transmit groups (TGs) and receive groups (RGs) [1]. All terminals in a transmit group share a common up-link frequency. Terminals can receive on all down-link frequencies, but will only use one down-link at any given time. All terminals listening on a common frequency belong to a receive group and must "hop" in unison to their next assigned down-link several times per frame. To allow for these receive frequency changes, the MTB field is divided into switching modes, with the traffic terminals listening on one frequency for the duration of a switching mode, and then hopping to the next frequency. As each transmit group talks to every receive group, traffic to or from any traffic terminal can occur.

The MTB is followed by the single-channel-per-burst (SCPB) pool, which is the overflow pool [14]. Calls that cannot fit into the MTB are put into the SCPB pool. Channel allocation in the SCPB pool is done dynamically by the reference terminal.

The BTP is the schedule which allocates the frame among transmitters and receivers via the MTB and the SCPB pool. Dynamic load tracking and frame reconfiguration involves the automatic collection of traffic statistics, deciding whether a new BTP is needed, and optionally calculating and implementing a new BTP. The NCP generates, stores, and distributes the BTP based on the traffic patterns in the network, as well as on other operator inputs. Wolfe [1] provides a detailed explanation of the special algorithms used to calculate the BTP, while Trusty, King, and Roach [15] give a general treatment of BTP calculation. Statistics collection, load calculation, and the tracking algorithm are described in the following subsections.

Statistics collection and evaluation

Each traffic terminal tracks various statistics related to its up-link and down-link traffic. Of particular interest are statistics regarding call attempts, call clears, and call holding times. Traffic terminals report their statistics to the NCP every 15 minutes. *Call attempts* are the number of incoming calls initiated during the sampling period (15 minutes), and *call clears* are the number of calls terminated during the sampling period. *Holding times* are the sum of the duration of the calls that cleared during the sampling period.

The traffic terminals send the collected statistics to the NCP via the reference terminal. If all traffic terminals were to send their traffic reports at the same time, the network would be flooded with these reports. Thus, the reporting time for the terminals is staggered over a 2-minute interval, with a 1-second delay between the start of any two traffic reports.

Raw statistics are collected at the NCP by a call statistics collection process. This process handles conversion from 68000 to VAX format, errors in transmission, and other errors, before entering the statistics into the database.

After the required statistics have been collected, they are evaluated by the dynamic tracker process in the NCP, which analyzes the statistics to detect changes in the network load distribution. The dynamic tracker examines call attempts, clears, and holding time statistics to determine an offered load measurement which is representative of the amount of load that was offered to the traffic terminal. The offered load from each terminal to each receive group is then summed into the group load matrix. In addition to group loads, other bounds are considered in the tracking algorithm, as described below.

Load and bound calculations

The offered load from any TTi to any other TTj is the product of net call attempt rate and average holding time (in sampling period units). This is the same as

$$\text{Load}\,(i,j) = \frac{\text{Number of call attempts} \times \text{Accumulated holding time}}{\text{Sampling period} \times \text{Number of call clears}} \qquad (1)$$

This equation, with call statistics for all active traffic terminals in the system, is the basis for an offered load matrix. If call attempts or clears for a sampling period are zero or out of range due to transmission problems, statistics from the previous sampling period are used to calculate current load. This ensures that the terminal will remain in the network with at least the load reported in the last interval.

Next, the offered load from every terminal to each receive group is calculated. Current receive group assignments are used in the following summing formula. The offered load from terminal i to receive group k is

$$\text{Current group load } (i,k) = \sum_j \text{Load } (i,j) \tag{2}$$

where j ranges from 1 to the maximum terminals in receive group k, but only uses the values of active terminals in group k. Similarly, the prior group load is calculated from the load matrix that was used to calculate the last implemented BTP.

A bound sets the limits by which the current group load may differ from the prior group load before it is counted as an overload or underload in the tracking algorithm. Calculation of the bound involves two intermediate calculations:

$$\text{Group attempts } (i,k) = \sum_j (\text{Attempts at terminal } i)_j \tag{3}$$

and

$$\text{Group clears } (i,k) = \sum_j (\text{Clears at terminal } i)_j \quad . \tag{4}$$

The bound fraction is a statistical measure of system requirements, depending on the amount of traffic flow and other operating conditions, and is determined by the operator's confidence level, as

$$\text{Bound fraction } (i,k) = \sqrt{\frac{C \cdot \text{Group attempts } (i,k) + \text{Group clears } (i,k) + 1}{\text{Group attempts } (i,k) \cdot \text{Group clears } (i,k)}} \tag{5}$$

where C is Gauss confidence level. The bound is the product of the load and the bound fraction.

The confidence level can be used to increase or decrease the bounds, making the dynamic tracking algorithm less sensitive or more sensitive to changes in network load distribution. This is achieved by considering only loads that differ from their previous values by an amount greater than the bound. When the network is being initially brought up, the operator sets the confidence level low (10 to 20 percent) to take into account all load variations. Once the network is operating close to its optimal level, the confidence level can be set high (80 to 90 percent) to prevent transient load changes from triggering a new BTP calculation.

Starting with an overload and underload counter set to zero, the current group load matrix is examined. Whenever the current load exceeds the previous load plus the bound, the excess is summed into an overload counter. Conversely, when the current load falls short of the previous load less the bound, the deficit is added to an underload counter. Overload and underload are calculated using the following inequalities:

If Current group load (i,k) > Prior group load (i,k) + [Prior group load (i,k) · Bound fraction (i,k)]

then Current overload = Old overload + Current group load (i,k) − Prior group load (i,k) − [Prior group load (i,k) · Bound fraction (i,k)]

otherwise,

If Current group load (i,k) < Prior group load (i,k) − [Prior group load (i,k) · Bound fraction (i,k)]

then Current underload = Old underload + Prior group load (i,k) − Current group load (i,k) − [Prior group load (i,k) · Bound fraction (i,k)]

where i spans the number of traffic terminals and k spans the number of reference terminals.

Tracking algorithm

If the current offered load to a receive group exceeds the prior load by the bound, the excess is tallied into an overload count. If it falls short of the prior load by the bound, the deficit is tallied into an underload count. If the overload and underload are both greater than an operator-defined threshold over the entire system, a new BTP is calculated and implemented.

Every time a new BTP is implemented, the accumulated database is cleared, the present load matrix is copied into the prior load matrix, and the present call statistics data block is copied directly into the accumulated database.

If the overload and underload tests fail, the dynamic tracker process updates the accumulated database to include the most recent statistics. The same tests are then repeated on load statistics accumulated since the last frame change. This ensures that long-term changes to the load distribution (which may escape short-term tests) are also detected.

An overload greater than zero implies a demand for greater frame space in some parts of the network, while an underload greater than zero implies an excess of frame space. Thus, if both the overload and underload are greater than zero, it should be possible to transfer excess frame space from one part of the network to another. When the dynamic tracker process determines that such a redistribution of frame space will optimize system performance, it calculates a new BTP. The dynamic tracker process omits the statistics evaluation for one period after the implementation of a new BTP (to avoid being triggered by transients from the implementation of the new BTP).

Although it is possible to reconfigure the network if the overload and underload are greater than zero, an operator input threshold must first be considered. Only if both the overload and underload exceed this threshold is a new BTP calculated. This allows the operator to fine-tune the tracking algorithm so that it does not calculate a new BTP at every iteration. A small threshold, close to the average daily load fluctuations, allows the tracking algorithm to closely track the network, while a large threshold essentially locks-in the current BTP. The operator can also make the tracking more or less sensitive to load changes by setting the confidence level. Both the confidence level and the threshold govern the tracking algorithm. The confidence level controls the overload and underload calculation, while the threshold controls the final decision on whether or not a new BTP is calculated.

Note that this algorithm works only within the current MTB size. When a traffic terminal finds its burst space fully occupied with existing calls, it begins using the SCPB buffer space [2]. The SCPB pool is essentially intended to absorb short-term overloads. Thus, in the case of a TDMA frame with a large SCPB, even a large overload will not result in reconfiguration if the underload is smaller than the threshold. Only when both the overload and underload exceed the threshold will a new BTP be calculated. Until then, the SCPB will be used to accommodate the overload.

Finally, the NCP allows the operator to turn off the tracking algorithm when desired. It also allows the operator to create test BTPs using various burst sizes, frame boundaries, and other parameters. Thus, the operator can calculate an appropriate BTP and implement it. The dynamic tracker process continues to update long-term loads for possible future use, even while the tracking algorithm is disabled.

Conclusions

The NCP performs several significant functions in a TDMA network, including off-site redundancy and dynamic frame reconfiguration. It also plays a crucial role in monitoring, controlling, and coordinating network operations. Remotely located NCPs posed some unique redundancy problems not encountered by redundancy designs where both NCPs are on site. These problems have been addressed using a variety of techniques, depending on subsystem requirements.

The NCP fine-tunes the network for maximum performance by periodically collecting statistics from the network and by using tracking algorithms to decide if a new BTP is needed. If a new BTP is necessary, it is automatically calculated and implemented. This allows terminals with increasing traffic demands to use the available capacity of terminals with decreasing traffic.

Although off-site redundancy involves unique problems, it can be achieved using the techniques presented here. With minor changes, these techniques can be used in off-site redundancy designs to handle situations involving catastrophic destruction of the primary site, as well as for situations involving redundant computers in two moving vehicles.

Acknowledgments

The authors wish to acknowledge the significant contributions of B. Irvin in developing the dynamic tracking algorithms presented in this paper. They also wish to acknowledge the contributions of V. Tran to the redundancy designs.

References

[1] W. H. Wolfe, "The DST-1100 TDMA System," 7th International Conference on Digital Satellite Communications, Munich, FRG, May 1986, *Proc.*, pp. 121–128.

[2] S. J. Campanella and D. Schaefer, "Time-Division Multiple-Access Systems (TDMA)," *Digital Satellite Communications*, K. Feher, ed., New York: Academic Press, 1966, pp. 43–57.

[3] O. G. Gabbard and P. Kaul, "Time-Division Multiple-Access," IEEE Electronics and Aerospace Systems Convention (EASCON), October 1974, *Record*, pp. 179–184.

[4] G. D. Dill, "TDMA, The State-of-the-Art," IEEE Electronics and Aerospace Systems Convention (EASCON), September 1977, *Record*, pp. 31-5A–31-5I.

[5] B. A. Pontano, S. J. Campanella, and J. L. Dicks, "The INTELSAT TDMA/DSI System," *COMSAT Technical Review*, Vol. 15, No. 2B, Fall 1985, pp. 369–398.

[6] P. Brossard and F. Rancy, "Telecom 1 DOM Satellite Network," 7th International Conference on Digital Satellite Communications, Munich, FRG, May 1986, *Proc.*, pp. 653–658.
[7] J. L. Diacre, "Architecture and Operation of Telecom 1 Business Data Networks," 7th International Conference on Digital Satellite Communications, Munich, FRG, May 1986, *Proc.*, pp. 263–268.
[8] G. D. Hodge *et al.*, "TDMA Network Control Facility," *COMSAT Technical Review*, Vol. 16, No. 1, Spring 1986, pp. 1–26.
[9] G. D. Hodge *et al.*, "INTELSAT Operations Center TDMA Facility," *International Journal of Satellite Communications*, Vol. 3, Nos. 1 and 2, January–June 1985, pp. 71–76.
[10] G. Zorpette, "Computers That Are 'Never' Down," *IEEE Spectrum*, Vol. 22, No. 4, April 1985, pp. 46–54.
[11] D. A. Rennels, "Fault Tolerant Computing—Concepts and Examples," *IEEE Transactions on Computers*, Vol. C-33, No. 12, December 1984, pp. 1116–1129.
[12] B. W. Johnson, "Fault-Tolerant Microprocessor-Based Systems," *IEEE Micro*, Vol. 4, No. 6, December 1984, pp. 6–21.
[13] B. Irvin, Private communication, February 1985.
[14] S. J. Campanella, Private communication, June 1984.
[15] P. A. Trusty, C. A. King, and P. W. Roach, "Generation of Burst Time Plans for the INTELSAT TDMA System," *COMSAT Technical Review*, Vol. 16, No. 1, Spring 1986, pp. 153–205.

Omkarmurthy Suryadevara received a B.Tech. in mechanical engineering from the Indian Institute of Technology, Bombay, India, in 1983; an M.S. in mechanical engineering from Clarkson University in 1984; and an M.S. in computer science from Virginia Polytechnic Institute and State University in 1986. He is currently a Member of the Technical Staff in the Systems Development Division at COMSAT Laboratories.

Thomas J. deBettencourt received a B.A. in mathematics from the University of Dallas in 1975 and an M.S. in operations research from George Washington University in 1979. He is currently Manager of Network Management Software Development at COMSAT Technology Products, where he is engaged in the development of new StarCom Network Management.

Russell B. Shulman received a B.S. in mathematics from City College, New York, in 1979. He is currently a Software Engineer with COMSAT Technical Services.

Index: direct broadcast satellites, computerized simulation, multipath transmission, frequency shift keying, phase lock demodulators

Application of software simulation to DBS transmission design and evaluation

L. W. WHITE, L. C. PALMER, P. Y. CHANG, AND A. SHENOY

(Manuscript received November 6, 1986)

Abstract

Software simulation was used to evaluate television transmission over the direct broadcast satellite (DBS) channel by investigating certain tradeoffs and predicting impairments prior to hardware design finalization. Major areas of study included predicting impairments to video due to overdeviation and a dual-path phenomenon that can occur in the channel, predicting the performance of alternative techniques for inserting digital data into each scan line, and predicting the performance of a threshold extension demodulator. Software simulation was successfully applied to these diverse topics by adapting existing software elements and developing new modules and techniques. The application of software simulation to specific problem areas associated with the overall DBS transmission link design is emphasized.

Introduction

Transmission planning for the direct broadcast satellite (DBS) channel involves tradeoffs and detailed studies that use analytical techniques and software simulation [1]. These studies support and extend parallel hardware measurement activities and can be especially valuable in areas where hardware components are not yet fully developed. This paper describes software simulation results in three areas related to DBS planning: multipath and overdeviation of the video signal, digital audio transmission, and phase-locked loop demodulation. These three areas are typical examples of the extension of the software simulation techniques described in Reference 1 to specific problems encountered in TV transmission planning.

The results obtained for multipath and overdeviation relied on simulation to examine a dual-path phenomenon that can be encountered in DBS applications. This potential source of impairment occurs when the video signal is amplified in two transponders, producing dual-path interference that can severely impair the desired signal. Studies of the filtering required in order to minimize this effect relied heavily on the simulation program [1]. Results were first obtained using the COMSTAR satellite simulator filter characteristics, which could be compared to hardware measurements to validate the model. Results were then obtained using characteristics for the proposed Satellite Television Corporation (STC) satellite filters for which hardware was not yet available. Some of these results are compared to subsequent results obtained through hardware simulation.

Next, results are given related to the insertion of high-rate digital data directly into the horizontal blanking interval of the video scan line. Filtering these waveforms to minimize intersymbol interference is an important tradeoff area, where extensive Monte Carlo (error counting) simulations were conducted. Comparisons to limited hardware simulation results were extremely good. Software simulation allowed several different filter characteristics to be tested.

The final section of this paper gives results for simulations with a phase-locked demodulator. These results determined the degree of threshold extension achieved for various test patterns, as compared to a conventional limiter/discriminator. Although subjective testing is needed in this area, reasonable results were obtained and the simulation experiments demonstrated some of the problems encountered in limited-duration simulations of TV systems.

Multipath and overdeviation simulations

Software simulation was used to evaluate three different satellite input multiplexer filter characteristics in terms of reducing spectral truncation and multipath. Existing software [1] was modified to model this problem, and initial simulation results were compared to the results from hardware simulations conducted with the COMSTAR satellite simulator [2]. Extensive software simulations were then performed using three candidate input multiplexer filter characteristics. A full frame memory available at COMSAT Laboratories was used to display the simulated outputs, allowing visual comparisons of the effect of interference on color-bar and multiburst test patterns.

Single-channel simulations were performed with each filter characteristic for increasing values of FM peak frequency deviation (ΔF_{pk}) to determine the deviation levels at which filter truncation became noticeable. Cases involving one or two adjacent channels were also simulated to determine the deviation levels at which multipath effects appear. Also, because of the high degree of flexibility afforded by software simulation, wider bandwidth baseband filters could be used to examine the effects of these impairments on video signals that had a wider luminance bandwidth of 6.4 MHz [3].

Subsequent to the software simulations, extensive hardware channel simulations were conducted using one of the three candidate input multiplexer filters. However, only a limited number of the cases examined are identical to those done with software. Where possible, results of hardware simulations are also given.

Statement of the problem

When a wideband signal is amplified by a satellite transponder, portions of the signal at the band edges may spill over into adjacent transponders. These segments of the original signal will generally be frequency-converted by independent oscillators, and may experience different path delays relative to the original signal before being recombined with it at the satellite output multiplexer filters. These "multipath signals" may be partially coherent with the signal from the original channel, depending on the difference in the oscillator frequencies in the two signal paths. If the adjacent channel is provided by a separate, colocated satellite which is also illuminated by the up-link earth station, the multipath delay will be larger than the delay encountered within a single satellite.

A solution to this problem is to use narrow satellite input multiplexer filters or a low peak FM frequency deviation (ΔF_{pk}) to minimize the energy falling into adjacent channels. However, it is also desirable to maximize channel bandwidth to take full advantage of the larger FM processing gain that results from increasing ΔF_{pk}. Increased deviation in the channel results in spectral truncation due to filtering, increased susceptibility to impulse noise, and increased multipath signal power when the dual-path phenomenon exists. Tradeoffs must be made between these impairments by properly selecting the type and bandwidth of the satellite input multiplexer filter and the FM deviation. Dewell and Siddiqi have discussed the related problem of adjacent channel interference [4].

When the simulation studies were conducted, only one of the three candidate input multiplexer filters had actually been built. Therefore, specification values for the three filters were used in the software model for comparison. Figure 1 plots the group delay and amplitude response specifications for the filters. As a result of this simulation, the design and fabrication of one of the three filters was discontinued.

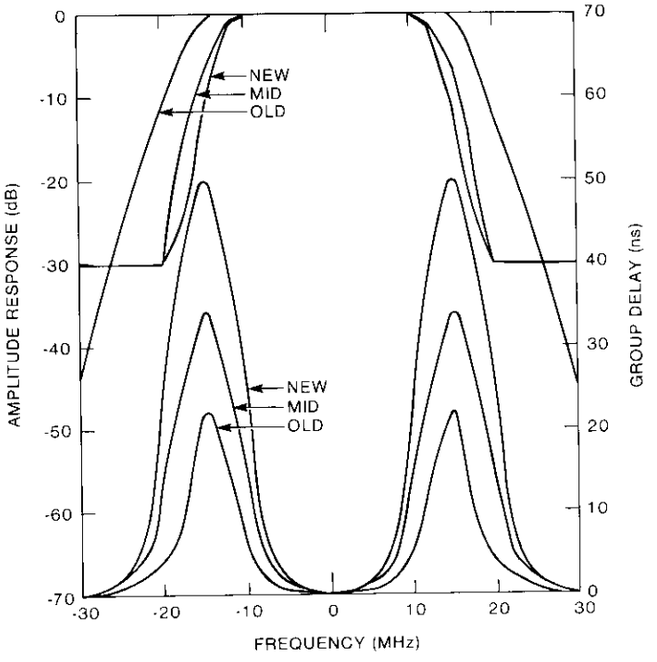

Figure 1. *STC Satellite Input Multiplexer Filters*

The software developed for simulating video signals [1] was modified so that two adjacent satellite channels, in addition to the main channel, were available for the multipath simulations. Other modifications were also necessary, including DC coupling of the baseband signal to the FM modulator, and inclusion of the baseband filters used in COMSAT Laboratories' NMAC* hardware. The characteristics of the input and output multiplexer filters present in the COMSTAR satellite simulator were also added to the program, so that the computer simulation model could be checked against experiments conducted with the hardware simulator. Simulation runs were then made to examine the filter truncation and multipath impairments of the three candidate STC satellite input multiplexer filters when color-bar and multiburst test patterns were transmitted over the channel, using the NMAC format. References 5 through 8 discuss the original work done on the MAC format,

* A multiplexed analog component (MAC) prototype using 4:3/4:1 luminance/chrominance compression that was developed at COMSAT Laboratories for Satellite Television Corporation during 1983–1984.

while Reference 9 compares three independently developed MAC formats and provides extensive references. The work presented in Reference 9 also was based on the software model described in Reference 1.

General description

The software used to simulate multipath impairments can process two scan lines of vertically repeating test patterns. Two scan lines were used because of the alternating line chrominance of the NMAC format. The chrominance portion of alternate lines contains R-Y or B-Y signals. The two scan lines are represented by arrays containing 16,384 complex samples, which gives a sampling rate of approximately 128 MHz and allows representation of the frequency spectrum between -64 and $+64$ MHz (twice the rate used in Reference 1). Figure 2 is a block diagram of the model used, including time waveforms or power spectra at various stages of the simulation.

All of the simulations described here employed the NMAC format. The generating routines create ideal test patterns, as shown by the NMAC color-bar waveform in Figure 2. These test patterns are generated in the compressed time domain, where luminance is compressed 4:3 and chrominance is compressed 4:1. The signals are generated so that a 0-V level represents black and a 1-V level represents white.

The next element in the simulation is a baseband filter that band-limits the test pattern. For most of the simulations, a 5.6-MHz low-pass filter was used, and its output is shown in Figure 2. This filtering operation corresponds to filtering the uncompressed luminance and chrominance signals with similar 4.2- and 1.4-MHz filters, respectively. An 8.53-MHz filter, included for the simulation of wider bandwidth cases, allowed uncompressed luminance and chrominance bandwidths of 6.4 and 2.1 MHz. This gives a luminance compression ratio of 5:3.

The same amplitude response and group delay characteristics were used for the baseband transmit and receive filters. Figure 3 shows the amplitude responses for the normal and wider bandwidth filters. The capability to separately filter the luminance and chrominance signals is included in the program, but was not used for most of the simulations because the hardware NMAC luminance and chrominance filter characteristics were not yet available.

After baseband filtering, the signal is DC-coupled to an FM modulator. The white levels in the baseband put the modulator output at the positive peak deviation ($+\Delta F_{pk}$), and the black levels yield the negative peak deviation ($-\Delta F_{pk}$). The output of the FM modulator is filtered by a 28-MHz earth station transmit filter. The signal is then passed through the input multiplexer of the desired satellite channel, followed by the traveling wave tube amplifier (TWTA) and the satellite output multiplexer filter.

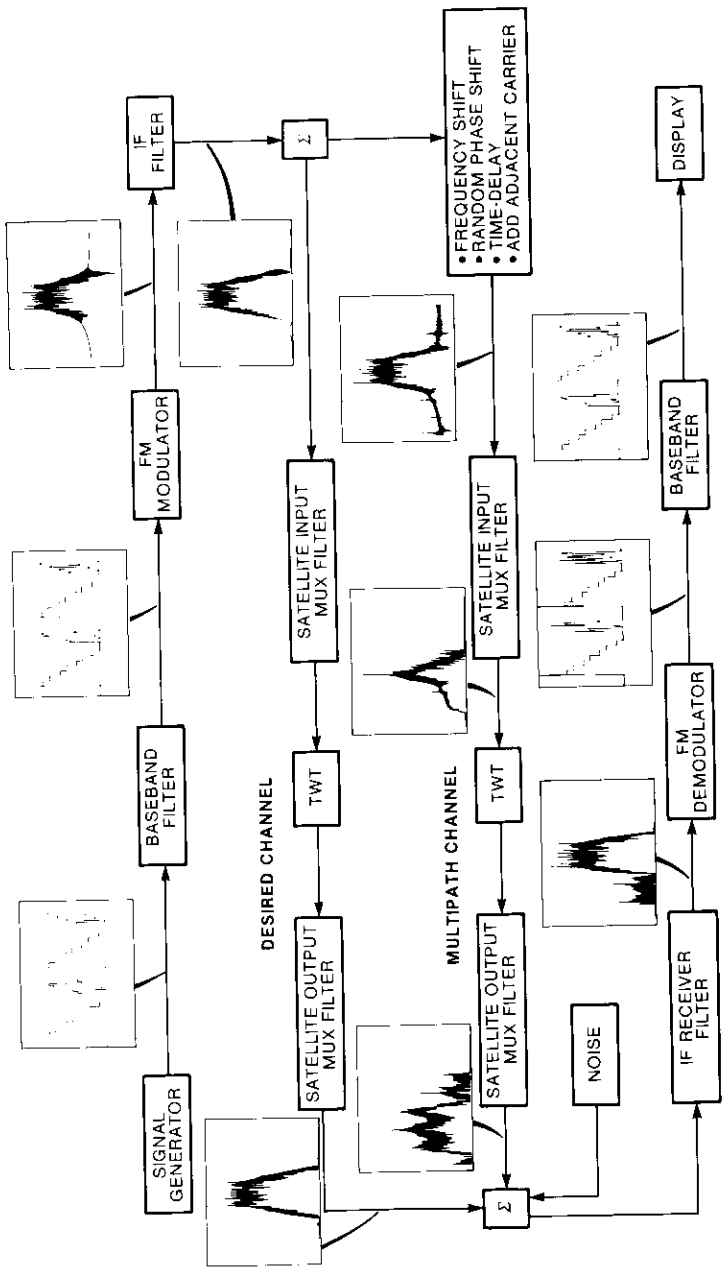

Figure 2. *Multipath Channel Simulation Block Diagram*

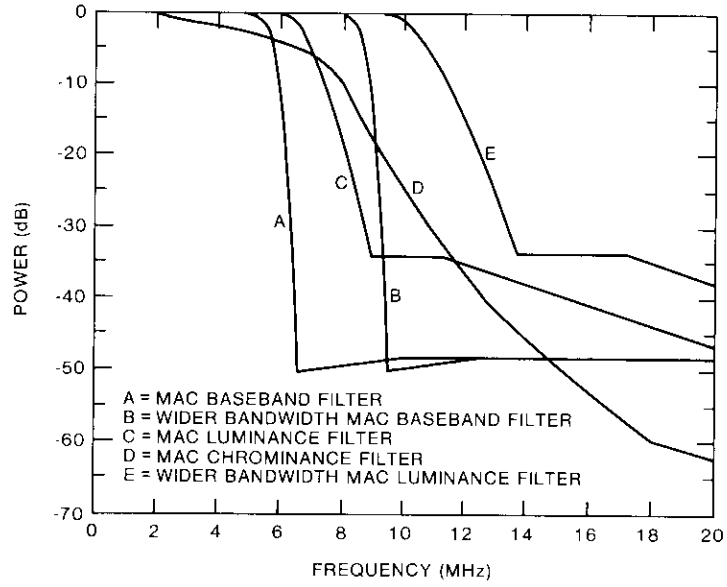

Figure 3. *MAC Baseband Filters*

The output of the earth station filter is also passed through one or two adjacent channels (29.16-MHz spacing) to simulate the multipath situation. To include multipath, several additional steps must be performed to account for the fact that the adjacent channels may be on a different satellite. The signal is given both a small frequency shift and a time delay in order to simulate differences in oscillator frequencies or path length between the two satellites. For most of the cases studied, a frequency shift of 6 kHz and a time delay of 1 μs were used. To represent oscillator short-term phase noise, a random walk process is added to the phase of the signal. A sinusoidal carrier at the center frequency of the adjacent channel is also added to the signal to generate the proper operating point on the nonlinearity in the adjacent channel. The signal is then passed through the input multiplexer filter, the TWTA, and the output multiplexer filter of the adjacent satellite channel.

If only the desired channel is to be used, the output of that channel's output multiplexer filter is passed through the receive filter. If one or two multipath channels are being used, the outputs of those satellite channels are added to the output of the desired channel. Thermal noise can also be added to the signal at this point. The combined signals are then passed through the receive filter, the FM demodulator, and finally a baseband filter.

Once this receive baseband signal was obtained, the effects of the channel on the signal were evaluated using a full frame memory capable of storing one frame of video, coupled to a video display. The software that accessed this memory stored one scan line in the National Television System Committee (NTSC) format as 910 samples of video. For software compatibility, it was necessary to convert the received baseband signal from the MAC format to NTSC and to resample the signal at a slower rate. The MAC-to-NTSC conversion was done at the same sampling rate as the rest of the simulation (16,384 samples/two scan lines). The signal was then resampled to 1,820 samples/two scan lines. Since only vertically repeating test patterns were employed, these two scan lines could be used to fill the entire frame memory two lines at a time. The two lines were used to fill the odd field in the frame memory, and both were again used to fill the even field of the frame memory. This produced a picture composed entirely of the two lines of video, repeated approximately 256 times. Figure 4 shows some of the operations that are performed on the baseband signal in the current version of the software.

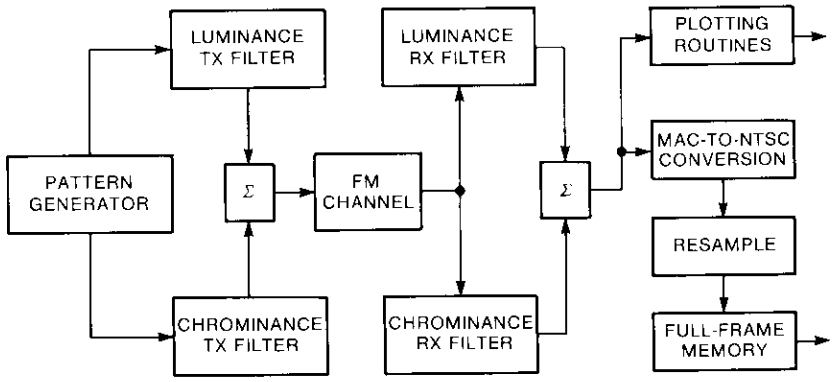

Figure 4. *Baseband Modules*

Results

Before extensive simulations of the STC channel were performed, the characteristics of the COMSTAR simulator channel filters were included in the program and several runs were made with the MAC format for comparison with hardware simulations. The multipath impairments observed in a color-bar test pattern were very similar in the hardware and software MAC simulations. The most noticeable effect was a large drop in the white bar near the leading edge, resulting in a black stripe within the bar. The major difference between the hardware and software simulations was the deviation

at which impairments appeared. In the software, multipath effects could not be seen until 3-dB overdeviation, but were visible at 1- or 2-dB overdeviation in the hardware. Also in the software, truncation distortion did not become noticeable until 6 dB, but could be seen at 3 to 4 dB in the hardware. Because the ultimate goal of the software simulations was to compare the relative performance of the three different satellite input multiplexer filters, this difference in sensitivity to overdeviation between hardware and software did not limit the validity of the comparisons.

After the COMSTAR channel simulations, the software was reconfigured for the proposed STC channel filter characteristics, and many simulation runs were made to compare the truncation and multipath performance of the three candidate input multiplexer filter specifications. The comparisons were made by using the full frame memory to display the output baseband waveform. All of the channel simulations discussed in this section employed the NMAC format. The output waveform was then converted to NTSC for display.

Table 1 summarizes the first sets of simulations, all of which used a color-bar test pattern. Single-channel simulations were performed with each of the three input multiplexer filters for several different levels of deviation. For all three filters, truncation effects became noticeable at 7-dB overdeviation. These effects appeared as shaded vertical bars within the cyan and yellow bars, and white vertical stripes within the black bar. Because only two scan lines are simulated and then repeated for display purposes, all of the degradations are repetitive in the vertical direction and were very similar to the impairments seen in the NMAC hardware. As expected, these truncation effects were most severe for the "new" filter, which is the narrowest of the three (see Figure 1), and least severe for the "old" filter, which is the widest of the three. Subsequent hardware measurements showed degradations first occurring at 8-dB overdeviation.

TABLE 1. COLOR BARS (ONE MULTIPATH CHANNEL)*

FILTER	SINGLE-CHANNEL	TWO-CHANNEL (EQUAL GAIN)	TWO-CHANNEL (10-dB GAIN DIFFERENCE)
Old	7.0 dB 14.3 MHz	5.0 dB 11.4 MHz	4.0 dB 10.1 MHz
Mid	7.0 dB 14.3 MHz	6.0 dB 12.8 MHz	5.0 dB 11.4 MHz
New	7.0 dB 14.3 MHz	7.0 dB 14.3 MHz	5.0 dB 11.4 MHz

* Overdeviation (dB) and peak deviation (MHz) where degradation is first observed.

The second column of Table 1 gives results for cases where multipath was present. The adjacent channel that is lower in frequency than the desired channel was included in these simulations. The results show degradation occurring at lower deviations than in the first column; therefore, these effects are assumed to be due to the multipath. As expected, the wider the filter the lower the deviation at which multipath effects became noticeable. Figures 5a and 5b are photographs of the full frame memory display for two of the simulations.

The third column of Table 1 presents results for cases where the video signal experienced 10 dB more gain in the adjacent channel than in the desired channel. This amplified the multipath signal and caused degradation

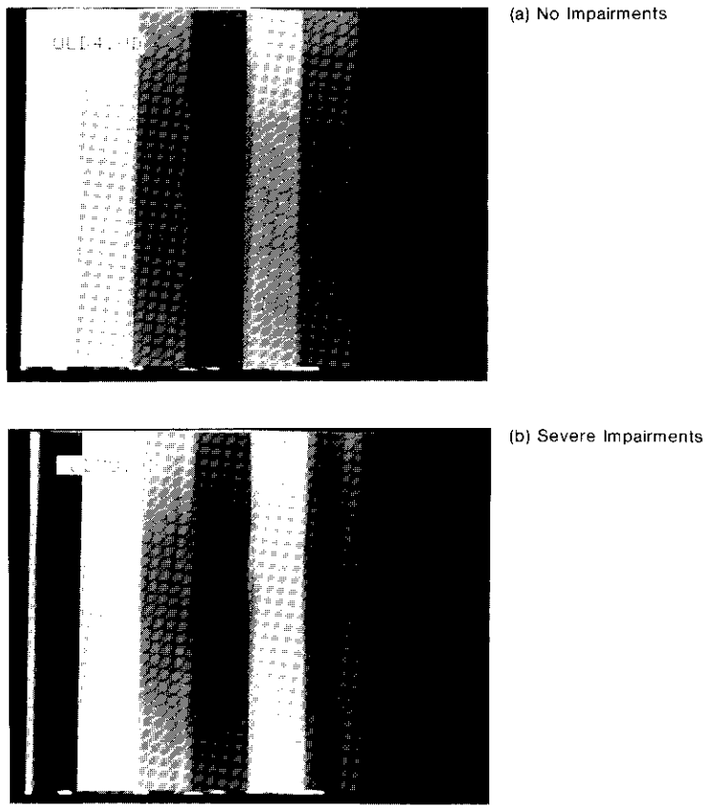

(a) No Impairments

(b) Severe Impairments

Figure 5. *Full-Frame Memory Display*

to occur at lower deviations than in the previous cases where the gain through the two satellite channels was equal. The results show that the new filter did not offer substantial improvements over the mid filter, and that subsequent simulations should use only the old and mid filters. All three filters gave similar truncation performance, but the mid filter allowed about 1 dB greater deviation than the old filter before multipath effects were noticed. The new filter allowed about 0.5-dB additional deviation beyond that of the mid filter. Because this represented little improvement over the mid filter, the new filter was never fabricated.

Table 2 presents the results of runs using both adjacent channels, instead of just the low-side adjacent channel. For the old filter, degradation first appeared at 5-dB overdeviation in the software, but was not noticeable until 8-dB in the hardware results for the equal gain case. For the 10-dB gain difference, the software first showed degradation at 4-dB overdeviation, but the hardware did not show any effects until 6 dB. There are several possible explanations for this. The filter characteristics used in the software were fitted to filter specifications, while the actual filter built for the hardware simulations was narrower than the specification values. The three-channel cases without noise [infinite carrier-to-noise ratio (*C/N*)] were found to be very similar to the corresponding two-channel cases of Table 1. The single-channel cases without noise were identical to the single-channel cases of Table 1.

TABLE 2. COLOR BARS (TWO MULTIPATH CHANNELS)*

FILTER	THREE-CHANNEL (EQUAL GAIN)	THREE-CHANNEL (10-dB GAIN DIFFERENCE)
Old	5.0 dB 11.4 MHz	4.0 dB 10.1 MHz
Mid	6.0 dB 12.8 MHz	6.0 dB 12.8 MHz

* Overdeviation (dB) and peak deviation (MHz) where degradation is first observed.

Several of the simulations shown in Table 2 were repeated with various levels of thermal noise added to the signal just before the IF receive filter. In these cases, the full frame memory was not very useful for evaluating impairments. Thermal noise effects that would appear as small dots or spots in live video appeared as thin vertical lines because of the repetition of the same two scan lines. Impulses showed up as wider and more noticeable vertical lines. When the thermal noise effects show up at exactly the same

place in each scan line (as vertical lines instead of randomly spaced spots) these effects are exaggerated.

Simulating a full video frame was considered as a means of obtaining a more realistic representation of thermal noise effects. However, this would still not give a good representation of noise effects in live video, because in live video the eye integrates noise effects over several frames. To date, no satisfactory way of using the simulation to display noise effects has been found. Routines to calculate signal-to-noise ratios (*S*/*N*s) have been written and used extensively in the original version of the simulation program [1]. However, they were not used in the multipath version of the program.

Simulations were performed to determine the effects of the old and mid satellite input multiplexer filters on the transmission of wider bandwidth baseband material. Table 3 shows results for cases in which an 8.53-MHz baseband filter was used on both the transmit and receive ends of the simulation. This corresponded to uncompressed luminance and chrominance bandwidths of 6.4 MHz and 2.1 MHz, respectively. These results were very similar to those of the previous runs, except that multipath occurred at slightly lower deviations for the cases that employed the old input multiplexer filter. Where the mid filter was used, observable multipath effects occurred at approximately the same deviation levels as in the earlier, regular-definition cases. Because overdeviation (beyond Carson's rule) in dB was used as the input to select the deviation level in the software, the deviations used in the wider bandwidth cases do not exactly match those used in the normal bandwidth cases. The baseband spectra of the NMAC color-bar signal has most of its energy concentrated at the lower frequencies; therefore, it is not surprising that the wider baseband filter made little difference in this case.

TABLE 3. WIDER BANDWIDTH COLOR BARS*

FILTER	SINGLE-CHANNEL	THREE-CHANNEL (EQUAL GAIN)	THREE-CHANNEL (10-dB GAIN DIFFERENCE)
Old	12.1 dB 14.0 MHz	9.1 dB 9.9 MHz	8.1 dB 8.8 MHz
Mid	12.1 dB 14.0 MHz	11.1 dB 12.5 MHz	10.1 dB 11.1 MHz

* Overdeviation (dB) and peak deviation (MHz) where degradation is first observed.

The wider bandwidth signal showed somewhat more sensitivity to multipath than in the previous cases. The mid filter gave the same relative performance; however, the old filter caused degradation at lower deviations in the wider bandwidth cases than in the normal bandwidth runs.

A set of wider bandwidth cases was also run using a multiburst test pattern. The characteristics of the actual luminance and chrominance filters being built for the NMAC hardware were used for baseband filtering. These filters had not been available in the software for previous simulations. Table 4 presents the results.

TABLE 4. WIDER BANDWIDTH MULTIBURST*

FILTER	SINGLE-CHANNEL	THREE-CHANNEL (EQUAL GAIN)	THREE-CHANNEL (10-dB GAIN DIFFERENCE)
Old	12.3 dB 14.3 MHz	12.3 dB 14.3 MHz	12.3 dB 14.3 MHz
Mid	12.3 dB 14.3 MHz	12.3 dB 14.3 MHz	12.3 dB 14.3 MHz

* Overdeviation (dB) and peak deviation (MHz) where degradation is first observed.

In the cases without multipath, truncation effects were first noticed at 14.3-MHz peak deviation. The cases with multipath showed the same effects; however, the effects were more severe in the cases with 10-dB extra gain in the adjacent channels. This indicates that, in the equal-gain case, truncation problems occur before multipath effects as deviation is increased. In the extra-gain cases, truncation and multipath began at about the same deviation levels. Comparison of the multiburst simulations with the wider bandwidth color-bar cases indicates that the color-bar test signal is more sensitive to multipath effects.

Computer simulation of digital audio signals

A separate program was developed to simulate the performance of an *M*-level frequency shift keying (FSK) audio data channel in the DBS transmission system. This channel is included in the 11-ms horizontal blanking interval of the television scan line, whereas the previous section dealt with the 53-ms active video segment of the scan line. The program was used to perform Monte Carlo simulations in order to evaluate bit error rate (BER) performance and determine the optimum transmission parameters for the design of an *M*-level FSK system. Some results were confirmed by comparison to available hardware measurements. While building filters can be costly and time consuming, software simulation can provide a quick and economical means to assess audio channel performance using various filters. This section briefly describes the simulation program and presents simulation results related to digital audio transmission over the DBS channel.

Theoretical background and software structure

Various studies have been conducted on the performance of digital FM (or PM) in the presence of noise, concentrating on the bit error performance of binary FM signals [10] as a function of *S/N*. Klapper [11] has examined the theory linking the threshold mechanism in analog FM signals with error rate in digital FM reception. Digital FM techniques, together with coding schemes, have also been investigated for application in INMARSAT Standard-C ship earth stations [12]. All of these studies have provided promising results. The current effort uses computer simulation to examine the performance of four-level FSK inserted in the DBS channel. The simulation program contains modules corresponding to each hardware element in the channel, including the FM modem and the FSK signal generator.

M-LEVEL FSK SIGNAL GENERATOR

Because of the nonlinear *M*-ary FSK demodulation process, Monte Carlo simulations must be used to evaluate BER performance. A pseudorandom bit sequence is used to simulate the source data at a bit rate of 14.32 Mbit/s, using four amplitude levels sampled at two times the NTSC color sub-carrier frequency for a four-level FSK signal transmission. This sequence is stored for comparison with the bits received over the channel.

The data sequence is mapped into rectangular *M*-level baseband signal pulses using a ($\log_2 M$)-bit Gray encoding, giving a time-domain sequence of pulse amplitude modulated (PAM) pulses. A fixed pattern is inserted ahead of the random data sequence, as shown in Figure 6. This pattern serves as a preamble in the simulation, providing a clamping level, an automatic gain

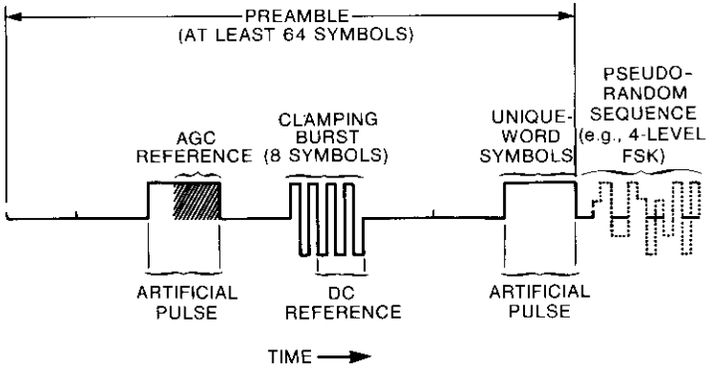

Figure 6. *Fixed-Sequence Pattern (Preamble) in Multilevel FSK Signal Sequence (Timing Diagram)*

control (AGC) reference, and a symbol timing reference. A unique word is also included to establish word timing. The AGC reference sequence and the unique-word signal sequence are included in the simulation only to establish the necessary synchronization.

The AGC burst provides a scaling reference for the analog-to-digital converter in the hardware of the FSK receiver. During the simulation, this segment of the scan line is left noise-free and is also used as an amplitude level reference. The clamping sequence matches realistic signal patterns and has a peak-to-peak level of 1 V. It contains signal bursts that alternate between the two outermost levels at a rate of 14.32 Mbit/s for four-level FSK modulation. The modulating waveform is scaled to produce a normalized peak frequency deviation of $\Delta \doteq \Delta F_{pk}/R_s$, which is the same as that used in the hardware measurements.

FILTERS

Three types of filters are available in the simulation software. These filters appear in the simulation channel in Figure 7. One is a recursive Butterworth filter specified by the number of poles and the bandwidth of the filter. The second is a fast Fourier transform (FFT) filter, which accepts user-specified filter characteristics in terms of amplitude and group delay vs frequency. The third filter type simulates the integrate-and-dump (I&D) operation using a finite impulse response, or tapped delay line, filter. After time synchronization is established, the input signal is integrated in the time domain over one symbol interval to model an analog I&D filter.

FM MODULATOR AND DEMODULATOR

The FM modulator and demodulator modules are identical to those used in CHAMP [13]. The output of the simulated FM modulator is

$$S(t) = R_c[\cos(\beta \int r(t)\ dt) + j \sin(\beta \int r(t)\ dt)]\ e^{j\omega t} \qquad (1)$$

where $r(t)$ is the baseband signal (here, the four-level PAM signal) and ω is the carrier frequency of the modulated FM signal. The modulation index, β, is scaled to the parameter, Δ, which is the frequency interval between discrete baseband frequency levels used in the hardware measurement.

The simulated FM modulator accepts an input modulating signal as a sequence of real numbers and produces a complex output signal sequence, as given by equation (1). The received complex envelope signal is demodulated by calculating the instantaneous phase angle of each pair of complex sample points and computing a phase derivative [1] relative to the previous pair of sample points.

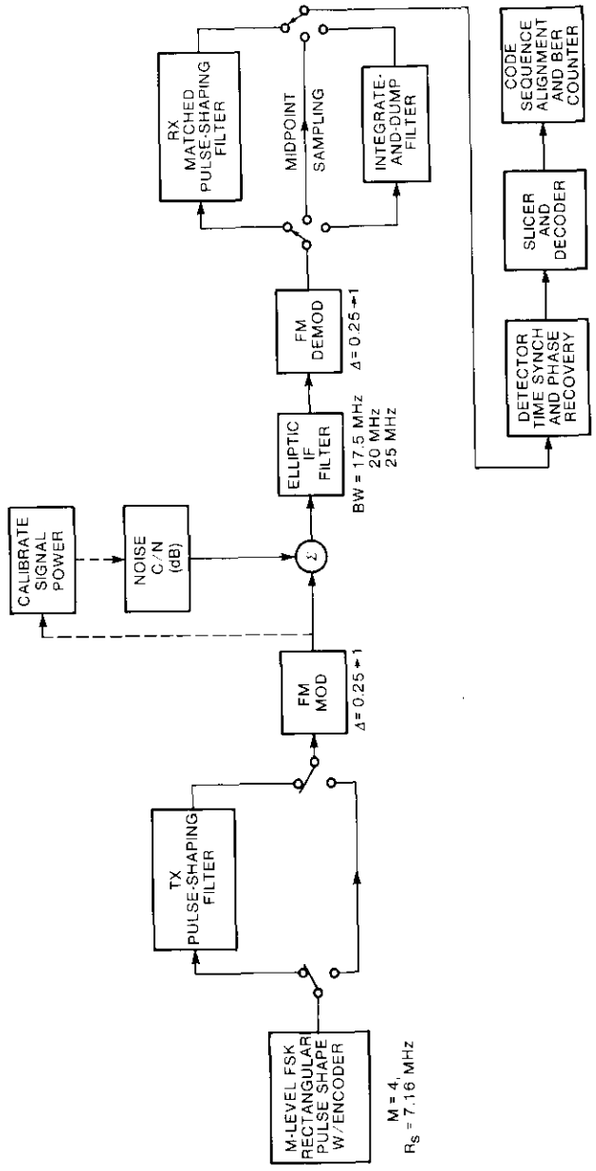

Figure 7. *Simulation Block Diagram*

RECEIVER (DETECTOR)

The detector module establishes symbol synchronization on the received signal. The signal is sampled at each clock sampling instant, which is determined by processing the clamping burst in the acquisition preamble. This processing determines the zero crossing intervals in the transitions (after the DC component is subtracted from the signal), and the average of these intervals is taken as the initial sampling interval for the clock. The AGC level is also calculated using the AGC burst portion in the preamble segment shown in Figure 6. This AGC level is used in the simulated demodulator as a reference to distinguish the FSK baseband signal levels.

OTHER PROGRAM ELEMENTS

The program contains additional elements which are described briefly as follows:

a. *Calibrator*. This module is used to calculate the average power of a signal sequence at any point in the channel which is used to calibrate the relative level of the thermal noise that is to be added to the signal.

b. *Noise Generator*. This module generates a sequence of independent Gaussian random numbers, which are scaled to give the desired *C/N* in the noise bandwidth of the IF filter at the input to the demodulator.

c. *Signal Merger*. This module adds two or more sequences of signal (and/or noise).

d. *Signal Slicer and Decoder*. This module processes the sampled signal sequence provided by the detector module and decodes the 2^n-level FSK signals.

e. *Bit Error Calculator*. This module processes the decoded bit sequence, compares it to the originally generated information bit sequence, and counts bit errors.

f. *Bit Error Summarizer*. This module performs repeated runs to accumulate BER statistics.

Modules (a), (b), and (c) are modified modules from the CHAMP channel simulation software.

Simulation results for the DBS digital audio channel

Extensive software simulations have been conducted for the DBS digital audio channel. These simulations provided the spectra and eye pattern diagrams for the multilevel FSK signal transmitted through the audio channel, and established BER performance using longer continuous simulations. Various

modulation indices (related to Δ ratio) were used, including values that resulted in overdeviation relative to Carson's rule. Several types of matched pulse-shaping filter pairs were tested. Realistic IF filters of three different bandwidths were used to obtain results for comparison with corresponding hardware simulation results.

FOUR-LEVEL FSK SIMULATION

The first group of simulated cases used midpoint sampling, in which the signal at the output of the demodulator is directly detected without a receiving filter. The second group employed either an I&D filter, an RC filter, or a Butterworth filter at the receiver. The third group used matched pulse-shaping filter pairs on the transmitting and receiving ends of the channel. All the received signals were detected using midpoint sampling in the simulated demodulator (see Figure 7). Most of the simulations involve four-level FSK with a symbol rate of 7.16 MHz, which corresponds to a bit rate of 14.32 Mbit/s. This rate was chosen because it is an even multiple of the NTSC color subcarrier frequency.

Figure 8 illustrates the spectrum of the modulated four-level FSK signal before IF filtering. A rectangular pulse shape is used for the baseband four-level FSK signal, and no pulse-shaping filter is used at the transmitter. The parameter Δ is chosen to be 0.4 for the FM modulator and demodulator (which corresponds to a peak frequency of 10.1 MHz for the FM modem module), and an elliptic function IF filter of 20-MHz bandwidth (noise

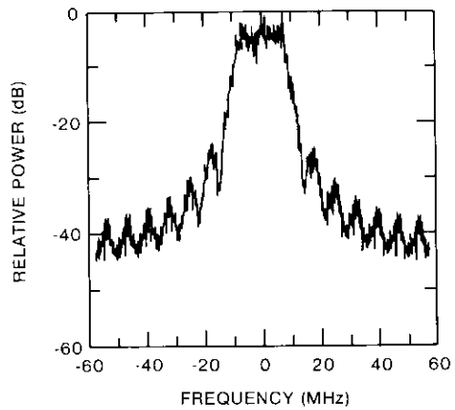

Figure 8. *Spectrum After FM Modulator*

bandwidth ≈ 18.89 MHz) is used. Because the eye patterns of the received FSK signal (shown in Figure 9 for $C/N = \infty$) indicated poor BER performance, the midpoint sampling technique with no receive filtering was discarded as an alternative.

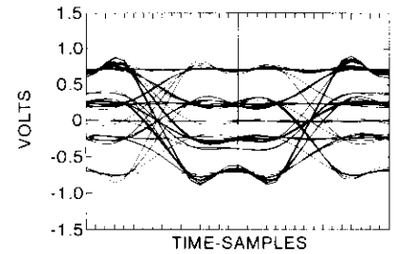

Figure 9. *Eye Pattern After FM Demodulator*

Simulations were then conducted with various receive filters in the channel. When an I&D filter is placed at the receiving end, the eye pattern is significantly improved, as shown in Figure 10a. A simple RC filter with various 3-dB bandwidths (e.g., 5, 6, and 7 MHz) was also tested; however, the eye patterns of these three cases are unacceptable (as shown in Figure 10b for a bandwidth of 6 MHz). A four-pole Butterworth filter was also tested. (A two-pole Butterworth filter is less costly, but has too gradual a cutoff characteristic.) The resulting eye patterns with bandwidths of 5.5, 6, 6.5, and 7 MHz are poor, as shown in Figure 10c for the 7-MHz case.

Comparison of the eye patterns at the output of these receive filters revealed that the I&D filter produces the best pattern. To use any filter other than the I&D filter, it appears necessary to implement a transmit filter to give a proper pulse shape to the four-level FSK signal in order to improve the eye pattern (and the resulting BER performance). The characteristic of the receive filter can then be properly selected to match that of the transmit filter.

Figures 11 and 12 show the eye pattern and power density spectrum, respectively, of a four-level FSK signal pulse-shaped by a four-pole Butterworth transmit filter. The eye pattern of this signal after FM demodulation is shown in Figure 13. Note that, if midpoint sampling detection is applied at this point, BER performance will be relatively poor, as indicated by the eye pattern. Use of a four-pole Butterworth receive filter before the detector results in the eye pattern shown in Figure 14 for an IF C/N of 8 dB. Although four-pole Butterworth filters may not be optimum, this example demonstrates that properly matched transmit and receive filter pairs give good BER performance for a four-level FSK audio channel.

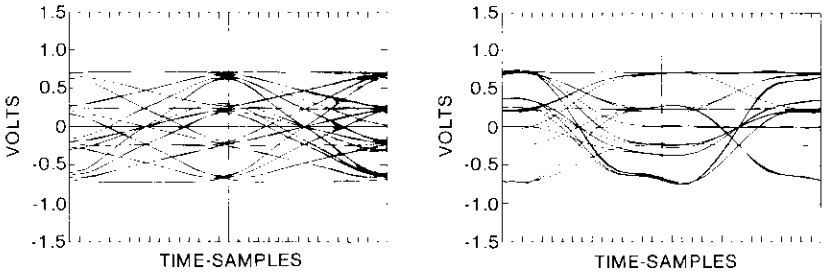

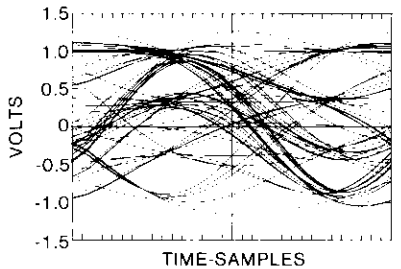

Figure 10. *Eye Patterns Without Noise*

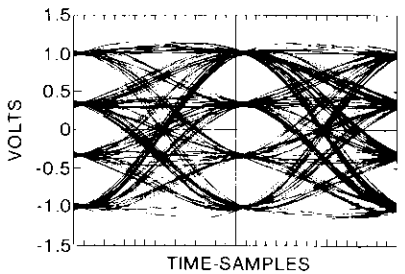

Figure 11. *Eye Pattern With Four-Pole Butterworth Transmit Filter (C/N = ∞)*

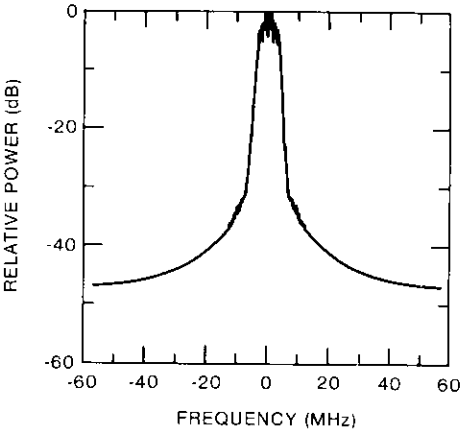

Figure 12. *Relative Power Window After FM Modem and Before IF Filter*

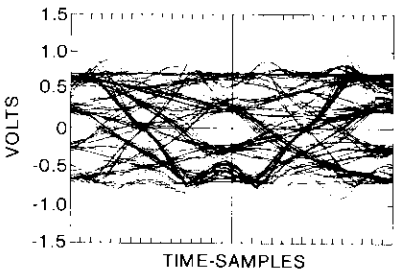

Figure 13. *Eye Pattern for Midpoint Sampling Detection*

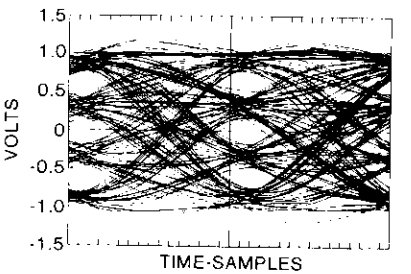

Figure 14. *Eye Pattern With Noise Using Matching Filter on Both Transmit and Receive Ends (C/N = 8 dB)*

A series of simulation runs was conducted to evaluate BER performance numerically as a function of IF filter bandwidth, transmit and receive filter types and bandwidths, and parameters related to the modulation index. Three IF elliptic filters of bandwidths 17.5, 20, and 25 MHz were used in the simulated channel.

Figure 15 shows the software simulation results for two channels of bandwidth 17.5 and 20 MHz with an I&D filter at the receiving end. For the

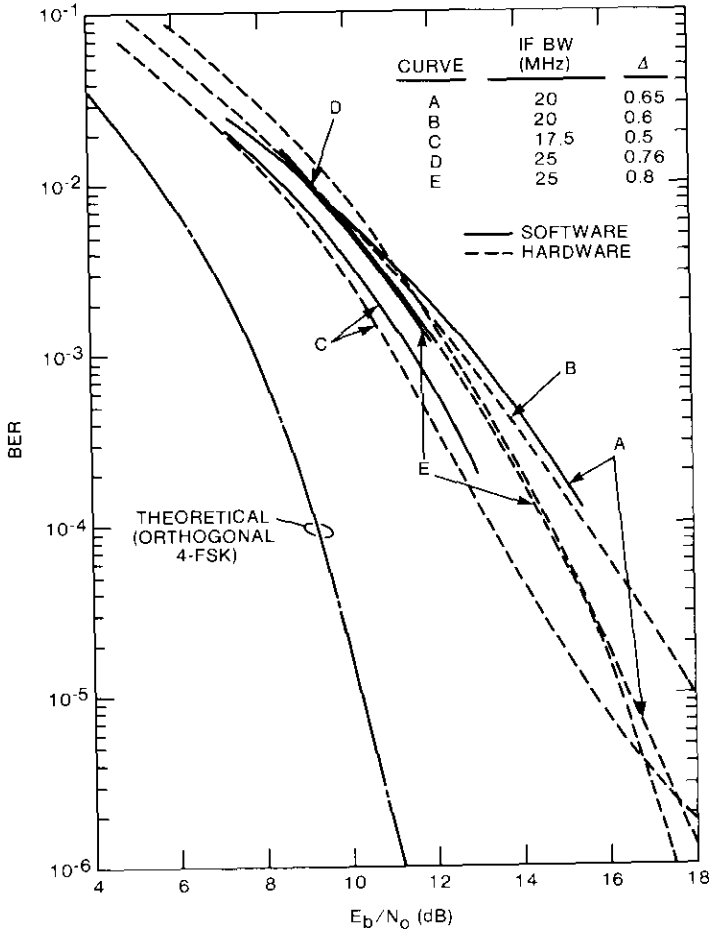

Figure 15. *Computer Simulations of Four-Level FSK in Audio Channel Using I&D Receive Filters*

17.5-MHz IF channel filter, $\Delta = 0.5$ is found to give the best performance, while for the 20-MHz IF channel filter, $\Delta = 0.65$ gives the best result. Compared with corresponding hardware measurements, these simulated results agree to within 1 dB in the low-BER ($\sim 10^{-4}$) region, and agree within a small fraction of a dB in the high-BER region. Two additional simulations using the 25-MHz IF filter and $\Delta = 0.76$ and 0.8 give BER performance curves even closer to the corresponding hardware measurement, as shown in the figure.

To identify a good matched-filter pair, a group of four-pole and two-pole Butterworth filters were used in the channels and tested individually for Δ values ranging from 0.5 to 0.75. The filter bandwidths for transmit and receive filters are either chosen to be identical or are chosen so that the transmit filter bandwidth is slightly wider than that of the receive filter (8/7 MHz in Figure 16). Simulation results indicate that, for the same Δ value, the four-pole Butterworth filter pairs give better BER performance than the two-pole Butterworth filter pairs.

It was also observed that, for the same value of Δ, making the transmit filter slightly wider in bandwidth also results in better BER performance. A test was conducted to investigate the effect of widening the bandwidth of the transmit filter to two or more times that of the receive filter. As shown in Figure 16 for IF filter channels of 17.5- and 25-MHz bandwidth, the BER performances are derived by simulating a channel with a four-pole Butterworth transmit and receive filter bandwidth ratio of 16 to 8 MHz. Such an arrangement does not necessarily give better BER performance than the ratio of 8 to 7 MHz.

To achieve better BER performance for the audio channel, overdeviation was also simulated. The values of Δ were increased to 0.8 and 0.9 in the FM modem. This resulted in poor BER performance, even for the channel with a wide IF filter (bandwidth = 25 MHz).

EIGHT-LEVEL FSK SIMULATION

As an alternative modulation scheme, an eight-level FSK audio channel was investigated using a symbol rate of 5.37 MHz (bit rate of 16.11 Mbit/s). The 25-MHz IF filter was used in the channel, with an I&D filter as the receiving filter. For a noise-free condition, Figure 17a shows the eye pattern of the eight-level FSK signal (with a rectangular pulse shape at the transmit end). The eye pattern immediately at the output of the FM demodulator is shown in Figure 17b, and the signal eye pattern at the output of an I&D filter is shown in Figure 17c. For comparison, the eye patterns at the output of the four-pole Butterworth filters of 5.5-, 6.5-, 7-, and 8-MHz bandwidth

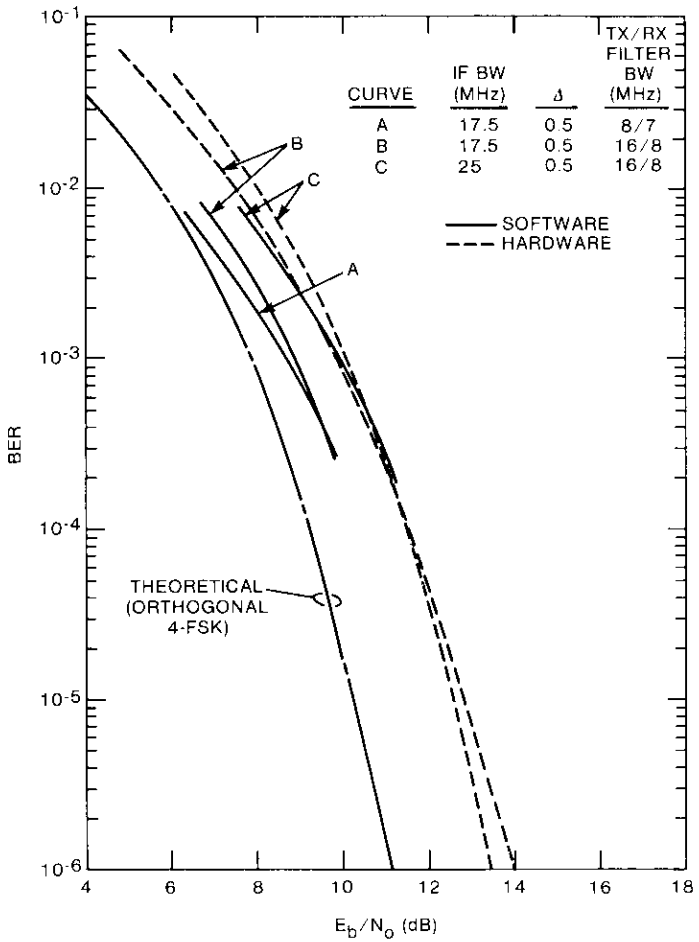

Figure 16. *Computer Simulation of Four-Level FSK in Audio Channel Using Pulse-Shaping Matched Four-Pole Butterworth Filter Pairs*

were also produced, and the best of these is illustrated in Figure 17d. The BER performance of the channel utilizing the four-pole Butterworth filters of 6-MHz bandwidth was evaluated by simulation for two Δ values (0.4 and 0.25), giving the results shown in Figure 18. Based on these two BER performance curves, it was concluded that the eight-level FSK was probably not a promising technique, and the eight-level FSK modulation format was not investigated further.

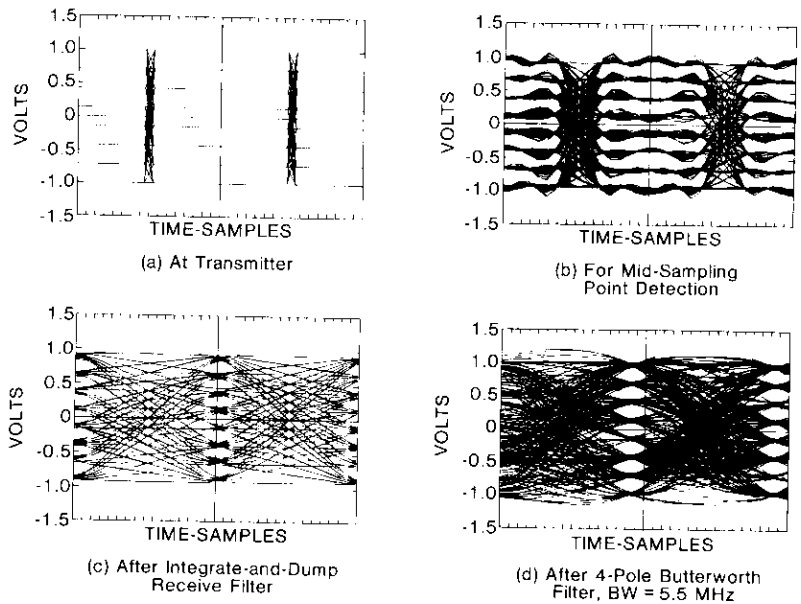

Figure 17. *Eye Patterns for Eight-Level FSK*

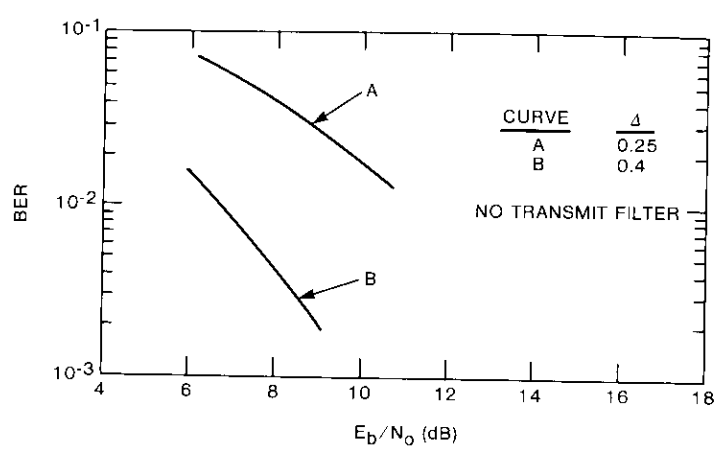

Figure 18. *Eight-Level FM Computer Simulation for 20-MHz IF Channel Using Four-Pole Butterworth Receive Filters (BW = 6 MHz)*

Phase-locked loop simulations

The simulation software [1] contains two FM demodulation subroutines: one for the ideal limiter-discriminator and another for a second-order phase-locked loop (PLL). Most of the simulation results were obtained with the limiter-discriminator because it is easier to realize in hardware than the PLL. In addition, the in-house satellite channel simulator equipment utilized FM modems with limiter-discriminator receivers, thus allowing direct verification of the simulation results. However, some tests were performed with the simulated PLL to study the possibility of threshold extension at low *C/N* values.

The digital version of the PLL uses a difference equation representation of a linearized second-order PLL, as shown in Figure 19. For accurate modeling of the noise performance of the equivalent analog loop, the ratio of the sampling interval to the loop time constant must be small. The analog loop filter is modeled as a simple recursive filter, and the analog voltage-controlled oscillator (VCO) is modeled as an ideal integrator.

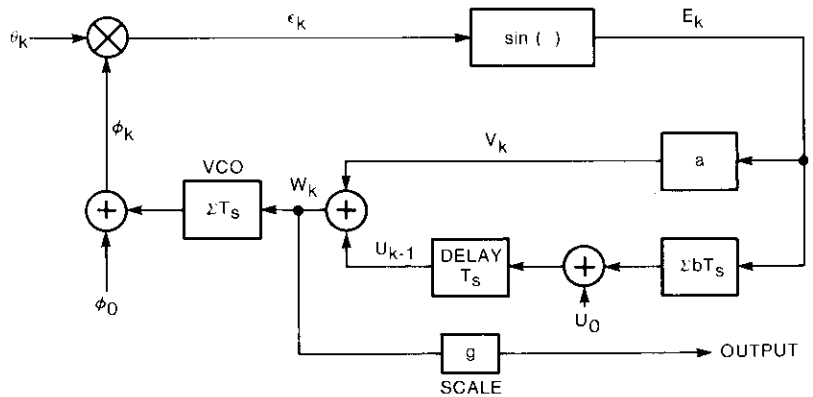

Figure 19. *Difference-Equation Model of Second-Order PLL*

The main variables in the implementation of the second-order PLL are the undamped natural resonant frequency, ω_n, and the damping factor, ζ. The simulation model in Figure 19 utilizes the instantaneous phase of the input signal, θ_k, as an input and forms an error signal, E_k, by comparing this input to the phase of the local VCO, Φ_k. Here k refers to the successive sampling steps kT_s, where T_s is the sampling interval. The loop model is updated at uniform intervals of T_s.

The error signal, E_k, is filtered in the second-order loop filter to produce the input to the VCO, W_k. This input determines the derivative of the VCO phase angle, Φ_k, which provides an estimate of the frequency of the input signal $\dot{\theta}_k$. When suitably scaled, W_k provides an estimate of the frequency modulation of the input signal. The constants a and b are given by

$$a = \omega_n^2$$
$$b = 2\zeta\omega_n \quad .$$

The initial conditions, Φ_0 and U_0, establish the loop integrator outputs at time zero ($k = 0$).

Simulation runs were conducted to verify the PLL demodulator operation and to select reasonably good values for ω_n and ζ. Figure 20 shows the simulated transient response of the PLL demodulator to a portion of the NTSC color bar with the parameters $\omega_n = 24 \times 10^6$ rad/s, $\zeta = 0.707$, and *C/N* of ∞, 14.5 dB, and 4 dB. The demodulator is well below threshold, and impulses dominate the output waveform.

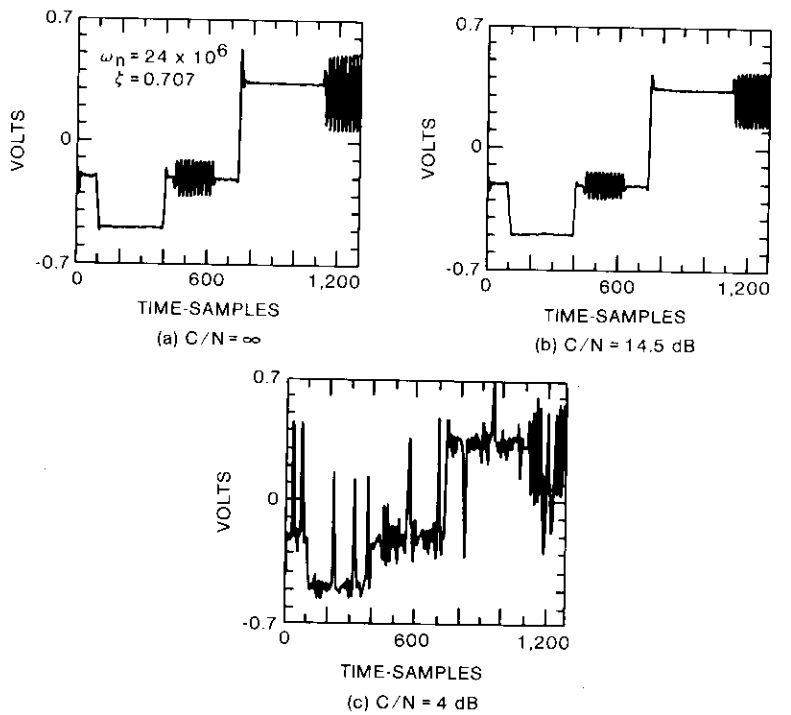

Figure 20. *Response of PLL Demodulator to a Segment of the NTSC Color-Bar Pattern*

The PLL demodulator was exercised with different video test patterns to determine the degree of threshold extension that can be expected compared to a limiter-discriminator. "Threshold" here refers to the 1-dB threshold, that is, the *C/N* value at which the output *S/N* curve departs by 1 dB from linearity. Two sets of loop parameters were used: a wideband PLL with $\omega_n = 24 \times 10^6$ rad/s and $\zeta = 0.707$, and a narrowband PLL with $\omega_n = 5 \times 10^6$ rad/s and $\zeta = 6.0$. In almost all cases, the wideband PLL was found to be superior to the narrowband version. Also, the narrowband PLL did not extend the FM threshold in most cases.

Table 5 summarizes the amount of threshold extension. A blank entry in the table indicates that no threshold extension was experienced for the stated condition. Note that the wideband PLL gives slightly more than 2 dB of threshold extension when the test signal is an NTSC multiburst or a MAC color bar. Less than 1 dB of threshold extension was experienced with the 2T/20T pulse pattern, and no threshold extension was measured for the NTSC color bar. The curves in Figure 21 show that the narrowband PLL consistently gives poorer performance than the wideband loop.

TABLE 5. THRESHOLD EXTENSION WITH THE SIMULATED PLL AS COMPARED TO THE SIMULATED LIMITER-DISCRIMINATOR

SIGNAL	WIDEBAND PLL $\omega_n = 24 \times 10^6$ rad/s $\zeta = 0.707$ (dB)	NARROWBAND PLL $\omega_n = 5 \times 10^6$ rad/s $\zeta = 6.0$ (dB)
MAC Color Bar	2.24	2.56
NTSC Color Bar	—	0
NTSC 2T/20T Pulses	0.82	—
NTSC Multiburst 60 p-p IRE	2.80	—
NTSC Multiburst 90 p-p IRE	2.11	—

A hardware prototype wideband PLL unit was built for FM demodulation at an IF of 70 MHz. Measurements with the standard 751-kHz single-tone test indicated a static threshold extension of about 2.5 dB. However, when active video was used, the data channel BER vs *C/N* performance was about 0.5 dB worse than the limiter-discriminator. In addition, the subjective performance was also perceived to be slightly worse than with the limiter-discriminator [14].

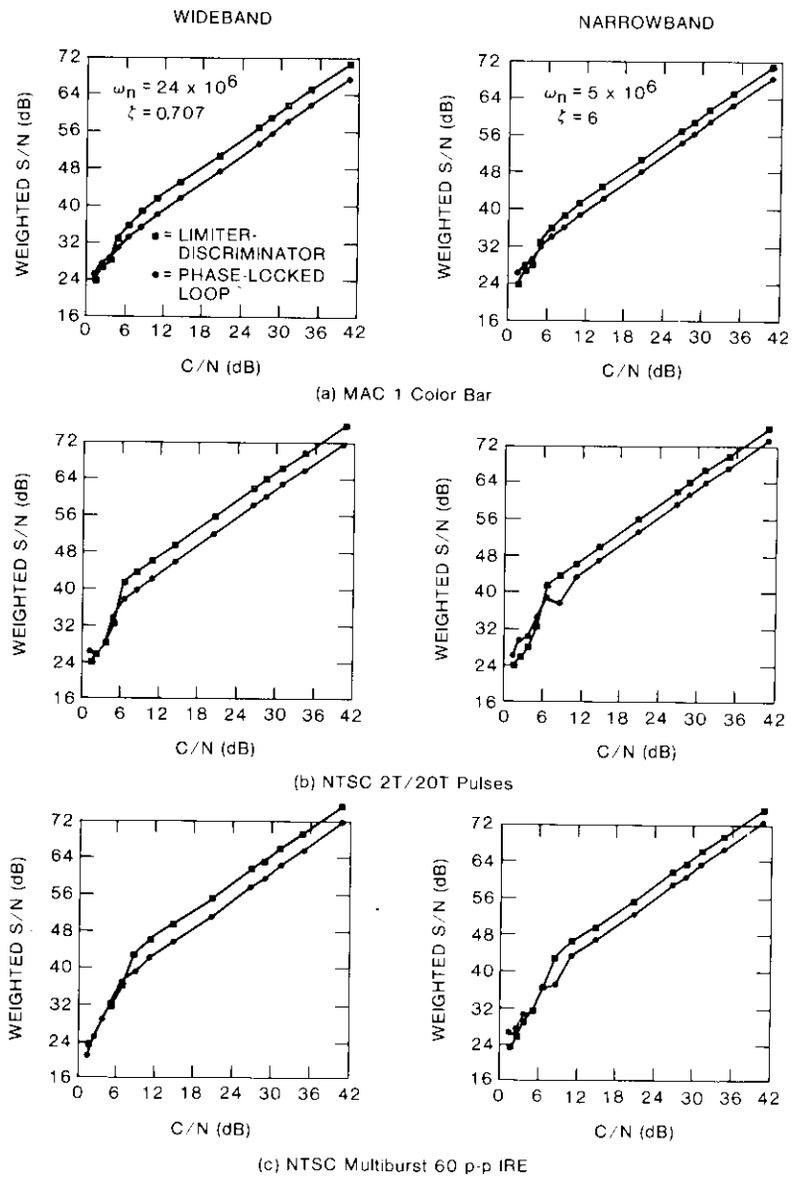

Figure 21. *Output S/N vs C/N for Simulated PLL Demodulator*

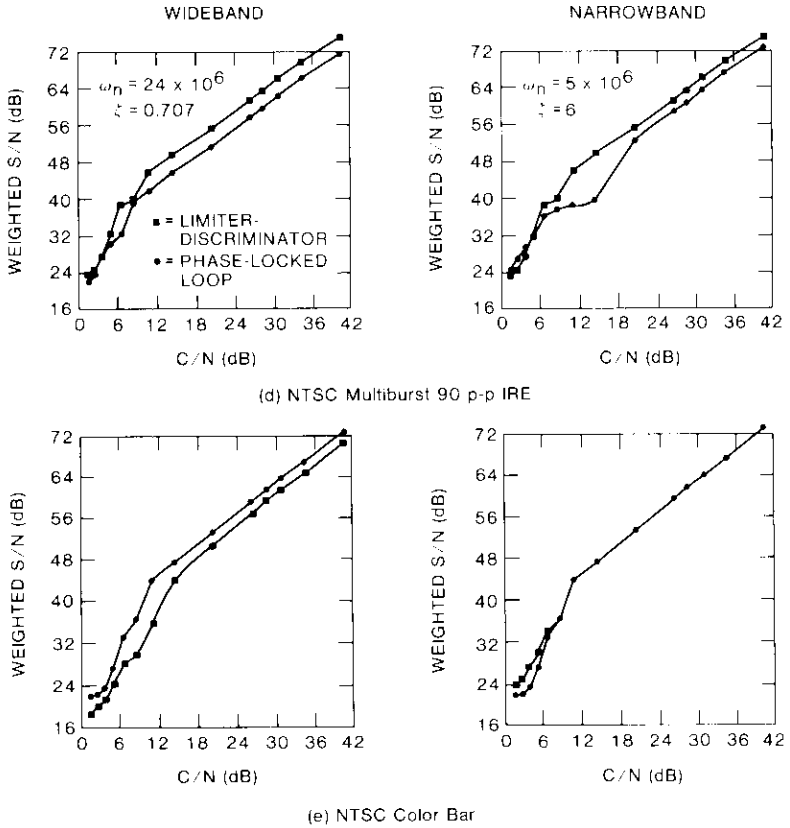

Figure 21 (continued). *Output S/N vs C/N for Simulated PLL Demodulator*

Further hardware tests indicated that, if the loop parameters were adjusted for optimum performance on the data channel (in terms of BER vs *C/N*), then the loop was not optimum for active video, with a performance degradation of 1.5 to 2.0 dB [14]. For MAC transmission, where the data and video are time-multiplexed, this implies the need for dynamic switching of the loop parameters within each scan line.

Due to the poorer subjective performance of the PLL receiver, as well as its numerous hardware implementation complexities, the limiter-discriminator receiver was the demodulator of choice. The limiter-discriminator was less expensive and more robust at low *C/N* than the PLL, and provided a subjectively better picture.

Conclusions

Software simulation has been applied to three different areas related to DBS transmission design: dual-path tradeoff investigations, digital and audio channel filter selection, and threshold-extension demodulator comparisons. Good agreement was noted in selected comparisons to laboratory hardware measurements. The simulations also provided a useful tool for comparing the performance of three satellite input multiplexer filters for a channel that included dual-path effects. As expected, the narrowest filter of the three showed the best multipath performance, and the widest filter showed the best truncation performance.

The color-bar pattern (in particular, the edges between the bars) was found to be a more difficult test than the multiburst in these simulations. Multipath effects appeared at lower deviations than truncation effects for the color-bar signals. The mid filter was found to give approximately 1-dB better multipath performance than the old filter, and the new filter provided an additional 0.5-dB improvement.

Software simulation has shown that digital four-level FSK modulation is a good candidate for DBS audio transmission. Four-level FSK is more bandwidth-efficient than two-level FSK, and simulation has shown that four-level FSK provides better BER performance than eight-level FSK. However, the selection of the transmit and receive filters is a crucial factor in obtaining acceptable BER performance. An I&D receive filter yields acceptable performance with no transmit filter required but, due to cost considerations, inexpensive low-order Butterworth filters are considered to be more practical for the DBS receiver.

Better performance was achieved by using a transmit filter to shape the transmitted waveforms, which are then demodulated using a matched receive filter. Further performance improvement is attained by unbalancing the bandwidths of the transmit and receive filters, with the former having a slightly larger bandwidth. Use of a wider transmit filter reduces the distortion to the waveform, while the narrower receive filter limits noise effects and minimizes intersymbol interference. The BER simulations used the Monte Carlo technique, which permits the simulation of error rates no lower than 10^{-5} within a reasonable time duration.

Simulations that compared a PLL threshold-extension demodulator to a conventional limiter/discriminator have also shown reasonably good agreement with hardware results [14]. In general, the simulation model which employs two video scan lines has proven to be a useful tool for analysis prior to hardware development and subjective testing.

The software simulations could be improved by extending the program to full frames of video and finding a way to represent noise effects with the full frame memory. Mainly because of the long processing time required for full frames, the simulations have been limited to vertically repeating impairments of vertically repeating test patterns. Throughout the software simulation effort, the results were verified by calibration and comparison with corresponding hardware simulations.

Acknowledgments

The authors gratefully acknowledge the contributions of many of their colleagues at both Satellite Television Corporation (STC) and COMSAT Laboratories who contributed to the efforts described in this paper. The work, performed at COMSAT Laboratories in 1984 in support of STC, was coordinated and led by R. Fang. The multipath and overdeviation investigation was initiated and supported by R. Gibbons and T. Kao. S. Struharik and A. Elrefaie performed the subsequent multipath hardware simulations. L-N. Lee, N. Becker, R. Garlow, and Y-S. Kao made major contributions to the design of the NMAC format. L. Mikisits participated in displaying the results of the video simulations using the full frame memory. Contributions to the design of the digital audio transmission technique were made by F. Hemmati. The software simulating the duobinary modulation scheme, as well as the PLL threshold-extension demodulator, were developed with the assistance of W. Hagmann. D. Weinreich contributed to the hardware testing and evaluation of the threshold extension demodulator.

References

[1] L. C. Palmer and A. Shenoy, "Simulation of TV Transmission Over the Communications Satellite Channel," *IEEE Transactions on Communications*, Vol. COM-34, No. 2, February 1986, pp. 188–199.

[2] M. Wachs and R. Mott, "Design and Performance of Satellite Communications Simulator for Domestic Applications," COMSAT Laboratories Technical Memorandum, October 1972, *COMSAT Data Catalog*, Accession No. 87DC123.

[3] Y–S. Kao and L–N. Lee, "An Evolutionary Approach to HDTV Based on Motion-Adaptive Image Processing Techniques," Second International Colloquium on New Television Systems (HDTV '85), Ottawa, Canada, May 1985, *Proc.*, Vol. 1, Paper 3.12.

[4] R. Dewell and S. Siddiqi, "The Calculations of Adjacent Satellite Interference for Direct Broadcast Satellite Systems, *Microwave Journal*, October 1987.

[5] K. Lucas and M. D. Windram, "Direct Television Broadcasts by Satellite, Desirability of a New Transmission Standard," *Independent Broadcasting Authority Experimental and Development Report*, No. 116/81, September 1981.

[6] "MAC—An Enhanced Television Signal Format for Satellite Broadcasting," *Independent Broadcasting Authority Technical Review*, November 1981.

[7] K. Lucas and M. D. Windram, "Standards for Broadcasting Satellite Services," *Independent Broadcasting Authority Technical Review*, No. 18, March 1982.

[8] M. D. Windram, G. Tonge, and R. Morcom, "MAC—A Television System for High Quality Satellite Broadcasting," *Independent Broadcasting Authority Experimental and Development Report*, No. 118/82, August 1982.

[9] L. C. Palmer, "A Comparison of Three MAC TV Transmission Formats," *COMSAT Technical Review*, Vol. 16, No. 2, Fall 1986, pp. 375–423.

[10] W. Bennett and J. Saltz, "Binary Data Transmission by FM Over a Real Channel," *Bell System Technical Journal*, Vol. 42, No. 5, September 1963, pp. 2387–2426.

[11] J. Klapper, "Demodulator Threshold Performance and Error Rates in Angle-Modulated Digital Signal," *RCA Review*, Vol. 27, No. 2, June 1966, pp. 226–244.

[12] S. Rhodes and R. Fang, "Digital Modulation and Coding Techniques Applicable to INMARSAT Standard-C Ship Earth Stations," COMSAT Laboratories Contract Report, Vols. 1 and 2, submitted to INMARSAT under Contract No. INM/83-063, October 1984.

[13] A. Hamid, S. R. Baker, and W. Cook, "A Computer Program for Communications Channel Modeling and Simulation," *COMSAT Technical Review*, Vol. 13, No. 2, Fall 1983, pp. 355–383.

[14] M. E. Jones and P. Chang, Private communication.

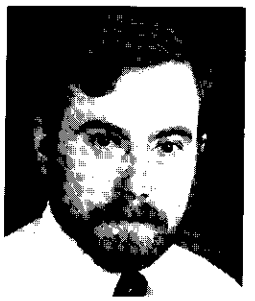

Lawrence W. White received the S.B. and S.M. degrees in electrical engineering from the Massachusetts Institute of Technology in 1983. He joined COMSAT Laboratories in 1982 and is currently a Member of the Technical Staff in the Systems Modeling and Analysis Department of the Communications Techniques Division, where he has developed and applied cost models to evaluate concepts for future communications satellite systems. He has also worked on the computer simulation of video signals transmitted via satellite, and since 1984 has been involved in various aspects of systems engineering for the NASA Advanced Communications Technology Satellite (ACTS) program. Mr. White is a member of IEEE.

Larry C. Palmer received a B.S. from Washington and Lee University and a B.E.E. from Rensselaer Polytechnic Institute, both in 1955, and an M.S. and Ph.D in electrical engineering from the University of Maryland in 1963 and 1970, respectively. From 1955 to 1957, he served in the U.S. Army Signal Corps as an Electronics Officer. Following this, he spent 6 years with the Radcom-Emertron Division of Litton Systems, where he was engaged in the design and development of airborne electronics systems. In 1963, he joined ITT INTELCOM and worked on the military communications satellite system. After the acquisition of INTELCOM by Computer Sciences Corporation in 1965, he was involved in systems analysis, modeling, and simulation related to communications and navigation satellite systems.

Dr. Palmer joined COMSAT Laboratories in 1974 and is presently Principal Scientist in the Communications Techniques Division. During 1979 and 1980 he served as Program Manager for COMSAT's participation in the DARPA SATNET program, and during 1984 and 1985 he was Systems Engineering Project Manager for the NASA Advanced Communications Technology Satellite (ACTS) program under subcontract to RCA. He is a Senior Member of IEEE, and a member of the IEEE Communications Society, the IEEE Information Theory Group, Tau Beta Pi, and Eta Kappa Nu.

Peter Y. Chang received a B.S.E.E. in 1966 from Cheng Kung University, Taiwan, China, and an M.S.E.E., M.Ph., and Ph.D. from Columbia University in 1969, 1972, and 1975, respectively. Prior to joining COMSAT, he was with the Satellite Communications Division of Computer Sciences Corporation. He joined COMSAT Laboratories in 1976 and is currently a Staff Scientist in the Systems Modeling and Analysis Department of the Communications Techniques Division. His work at COMSAT has included TDMA and FDMA modulation, digital signal transmission, intermodulation analysis involving the nonlinear effect of transponders, direct-broadcast (TV video and audio) satellite transmission systems, intersatellite links, simulation of satellite marine

or mobile communications systems with fading channels, and the simulation of digital signal performance in satellite channels involving various modulation and coding schemes. Recently, he was involved in the NASA ACTS project, including low bit rate system study analysis and simulation, and the analysis, modeling, and simulation of rain fade effects. He is also working on the modeling and simulation of a TDMA random-access notification network for the VSAT system. Dr. Chang is a member of IEEE, Eta Kappa Nu, and Sigma Xi.

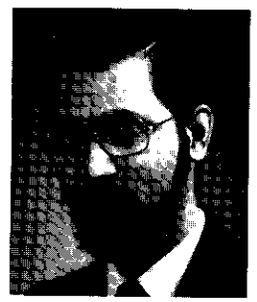

Ajit Shenoy received a B.Tech. in electronics in the First Class, with Distinction, from the Indian Institute of Technology, Madras, India, in 1979, and an M.S.E.E. from the Stevens Institute of Technology in 1981. He completed an additional year of graduate study in telecommunications and digital systems before joining COMSAT Laboratories in June 1982. He is currently Associate Manager of the Image Processing and Digital Techniques Department, where his work involves the design and implementation of microprocessor-based communications hardware using digital signal processing techniques. Prior to joining COMSAT, he worked on electronic motor speed control at Philips India, Ltd., and was a consultant for Synfax Manufacturing, Inc., Belleville, N.J., where he designed instrumentation systems for quality control. Mr. Shenoy is a recipient of several awards and scholarships from the Government of India. He is a member of the IEEE Communications and Computer Societies.

Index: degradation, INTELSAT, solar cells, solar arrays

In-orbit performance of INTELSAT IV-A spacecraft solar arrays

J. W. LYONS III AND A. OZKUL

(Manuscript received January 8, 1987)

Abstract

A computer model developed at COMSAT Laboratories was used to predict the performance of the INTELSAT IV-A solar arrays. These predictions and the array manufacturer's predictions were then compared with the actual in-orbit performance of the INTELSAT IV-A F-6 solar array, which exhibited short-circuit current about 7 percent lower than either prediction. The most likely cause of this discrepancy appears to be greater-than-predicted degradation due to ultraviolet radiation. Corrected predictions have shown good agreement with subsequent telemetry data for all INTELSAT IV-A spacecraft.

Introduction

Accurate modeling of the solar array performance of operational communications satellites is important from the spacecraft operator's viewpoint because it permits assessment of the future in-orbit resources of a communications system and facilitates planning for future launches. This paper describes an investigation of INTELSAT IV-A solar array performance. General characteristics of the INTELSAT IV-A spacecraft electrical power subsystem are summarized, followed by presentation of the results of initial solar array predictions. The in-orbit data are compared with the predictions, and results of the corrected solar array computer predictions are presented. Experience gained through this effort is valuable as a basis for similar predictions for the INTELSAT V and VI spacecraft.

INTELSAT IV-A electrical power subsystem design

The INTELSAT IV-A power subsystem (Figure 1) consists of two cylindrical spinning solar panels (main arrays 1 and 2, and four charge arrays), two 25-cell nickel-cadmium batteries, a battery controller, two commandable relays for bus paralleling, and miscellaneous commandable switches for heater and valve control. Each main array supplies one-half of the required spacecraft load. Power is supplied from each panel directly to the loads on the satellite spinning section, and through slip rings to the loads on the despun section. There are two separate temperature monitors on each panel.

Although the buses are designed to operate independently over the total spacecraft operating life, bus paralleling relays are provided for unanticipated operating modes. Each main solar array panel is conservatively designed to meet load requirements of approximately 200 W, as well as to provide 25 W for battery charging after 7 years in orbit. An additional 14 W of power is provided on each panel's charge array to boost the main bus voltage sufficiently to charge the 25-cell battery.

Table 1 lists the design features of the solar panels, and Figure 2 shows a typical solar panel sector. Cells are mounted on a cylindrical 1.9-cm-thick fiberglass-faced aluminum honeycomb substrate and are presoldered in 1 × 64-cell groups, and in smaller groupings for charge arrays. The presoldered arrays are bonded to the panel, one sector at a time, using an epoxy adhesive. Charge arrays (designated as 1A, 1B, 2A, and 2B in Figure 1) are connected to the batteries through commandable switches. The charge arrays for each battery allow selection of three different battery charge rates [1].

Solar array modeling

Accurate modeling of solar array performance in orbit is influenced by the following:

a. *Solar cell factors,* including adhesive and coverglass darkening due to solar ultraviolet irradiation.

b. *Solar cell characteristics,* including current-voltage measured at 1 sun air-mass zero (AM0) and at standard test temperature (typically 25° or 28°C), and solar cell temperature coefficients.

c. *Mission parameters,* such as solar cell radiation degradation due to trapped electrons and solar flare protons, predicted array temperature (telemetry data from earlier flights are preferred, when available), and seasonal variation in solar illumination due to declination of the sun, and the earth-sun distance.

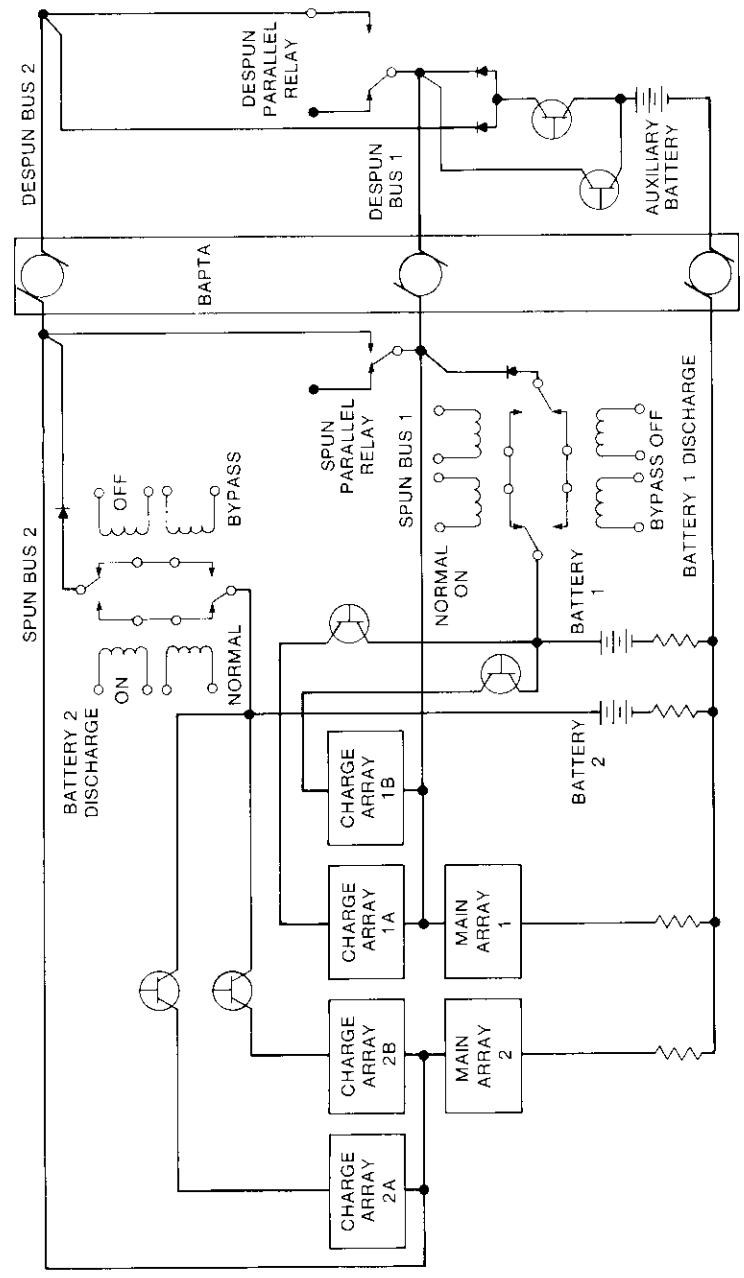

Figure 1. *Electrical Power Subsystem Block Diagram*

TABLE 1. SOLAR PANEL CONFIGURATION DATA

Solar Panels	
Number of Panels	2
Geometric Shape	Cylindrical
Diameter	237.5 cm
Length	137.2 cm/panel
Weight Per Panel	
Substrate	17.05 kg
Cells, Wire, Diodes, Connector, etc.	18.96 kg
Total	36.01 kg
Solar Cells	
Type of Cell	2 × 6.2-cm N/P silicon
Coverglass Thickness	0.030 cm
Nominal Cell Thickness	0.033 cm
Nominal Resistivity	10 Ω-cm
Main Arrays	
Sectors per Panel	11
Cell Groups per Sector	10
Cells in Parallel per Cell Group	1
Total Cells in Parallel per Sector	10
Total Cells in Parallel per Panel	110
Cells in Series per Cell Group	64
Main Array Cells per Panel	7,040
Battery Charge Arrays	
Sectors per Panel	11
Arrays per Sector	3
Cells in Parallel per Array	1
Total Cells in Parallel per Sector	3
Total Cells in Parallel per Panel	33
Cells in Series per Array	42
Charge Array Cells per Panel	1,386
Total Cells per Spacecraft	16,852

d. *Assembly factors*, including losses resulting from soldering and welding, thermal cycling tests, blocking diode voltage losses, and voltage losses attributable to interconnector and wiring resistance [2].

e. *Solar array geometry* (cylindrical, flat, or otherwise), including shadowing.

The environmental factors [(a) and (c)] that degrade solar array power output in geosynchronous orbit include trapped electrons, solar flare protons, and solar ultraviolet radiation. Because coverglasses with ultraviolet cutoff filters (0.4 μm for INTELSAT IV-A) are typically used to minimize the effect of solar flare protons and ultraviolet radiation, trapped electrons are the dominant cause of solar cell degradation.

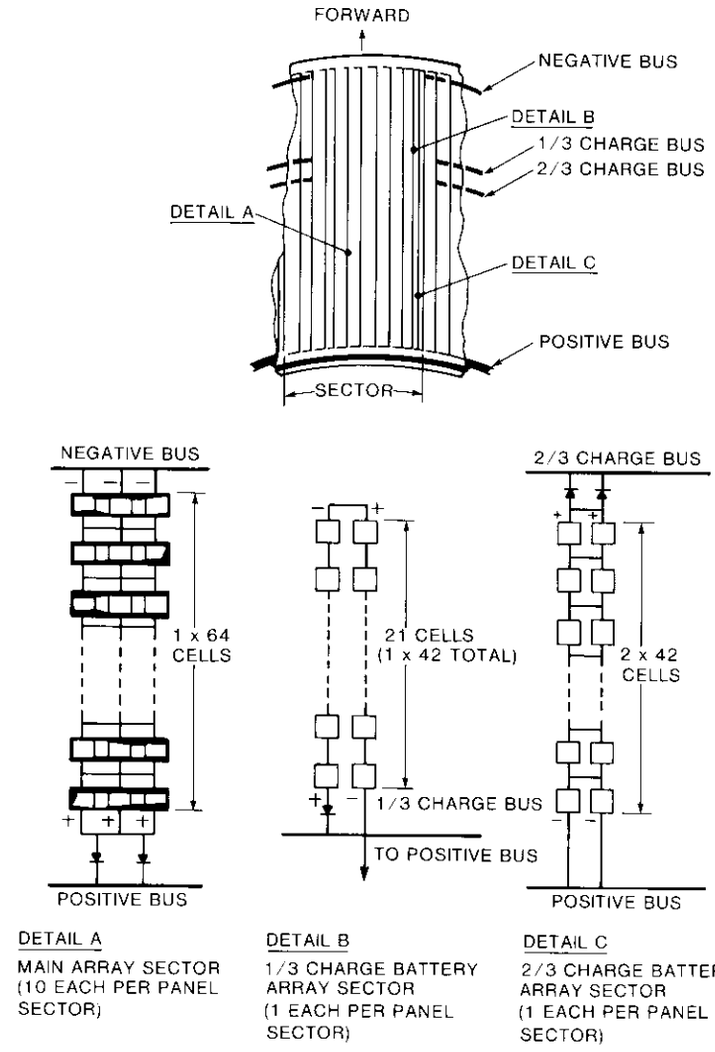

Figure 2. *Typical INTELSAT IV-A Forward Solar Panel Sector*

Since 1973 there has been no evidence of solar array degradation on INTELSAT spacecraft due to solar flare protons [3],[4]. Therefore, such degradation was not included in the predictions, because all of the INTELSAT IV-A spacecraft were launched in 1975 or later.

Seasonal variation in sunlight intensity, and consequently solar array temperature, markedly affects solar array performance. The north-south axis of a geosynchronous communications satellite is nominally fixed with respect to the earth's rotational axis. Consequently, the intensity of sunlight on the solar array changes in accordance with the distance between the near-earth satellite and the sun. For a planar array,

$$I/I_0 = (\cos \theta)/R^2$$

where I/I_0 = solar intensity relative to normal incidence at 1 astronomical unit
θ = declination of the sun
R = distance between the near-earth satellite and the sun (in astronomical units).

The above factors are incorporated into a COMSAT Laboratories array analysis computer program, SOLARRAY. The program begins with the expected performance of the applicable solar cell at AM0, scaled up to array size. For each INTELSAT IV-A spacecraft, plots of array voltage at the operating load current are generated and compared to telemetered flight data. As more flight data become available, the models are corrected for any errors in the initial extrapolation from earth measurements to space performance. Once these corrections have been incorporated, the program is used to assess the accuracy of predicted solar cell degradation. After correlation is achieved between predicted and actual array performance, spacecraft operators are given accurate estimates of future solar array power availability for individual spacecraft.

Prediction results for F-6

The INTELSAT IV-A F-6 solar array (launched March 31, 1978) was analyzed to determine whether or not it could provide sufficient power to support predicted loads through summer solstice 1985. Plots of voltage at operating current *vs* time, as well as entire array I-V curves, were generated for specified times. In addition, plots of current *vs* time at specified bus voltages were generated. After predicted voltage at operating current was fitted to telemetry data, the degradation parameters were used to predict the operating margin for a given load.

Figure 3 depicts INTELSAT IV-A F-6 voltage (at operating current) *vs* time, and Figure 4 shows the percent difference between telemetry and prediction for the data plotted in Figure 3. Figure 5 illustrates the actual telemetered load currents *vs* time for which the voltage at operating current in Figure 3 was calculated. The telemetry data were taken from annual plots.

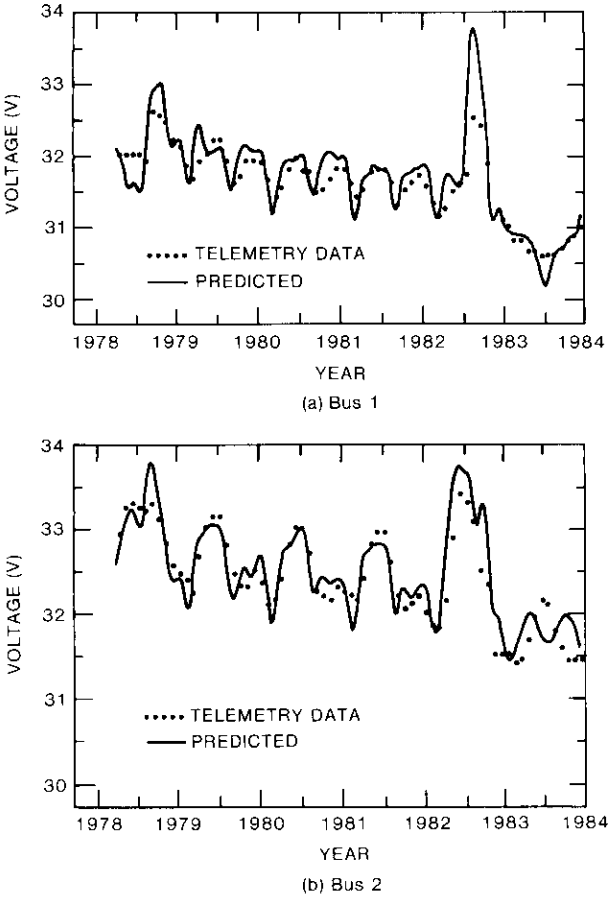

Figure 3. *Voltage at Operating Current*

Note that Figure 4 shows a telemetry data scatter of approximately ±2 percent compared to predictions. This observation indicated that the array predictions were accurate, and array I-V plots such as those presented in Figure 6 appeared to support this conclusion. The plots consist of array I-V curves for 1982 through 1983, with superimposed telemetered I-V points. There is excellent agreement between prediction and telemetry. Because all telemetry data up to that time were near the knee of the I-V curve on the open-circuit voltage side, verification of the predictions against actual performance was not obtained for higher operating currents on the short-circuit current side of the knee.

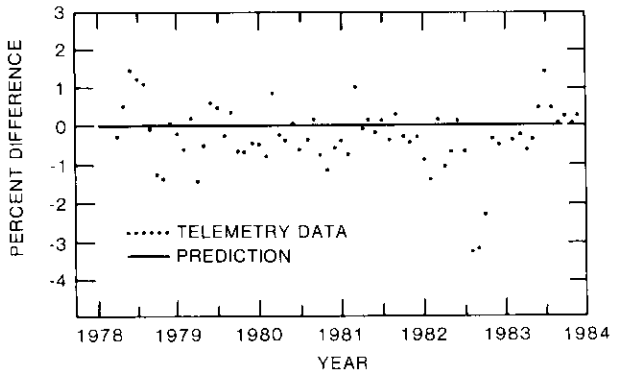

(a) Bus 1

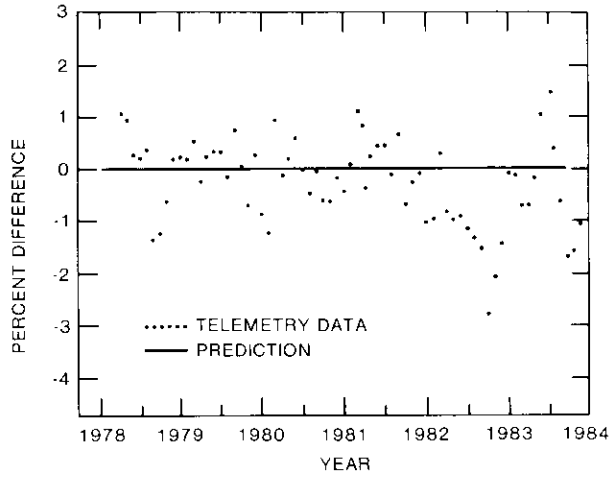

(b) Bus 2

Figure 4. *Comparison Between Telemetry and Prediction*

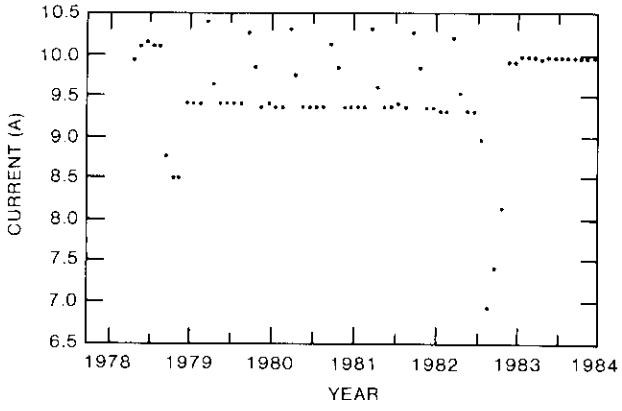

(a) Bus 1

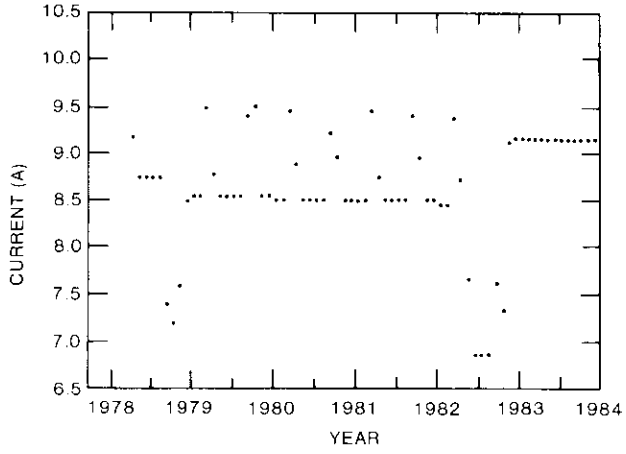

(b) Bus 2

Figure 5. *Telemetered Load Current* vs *Time*

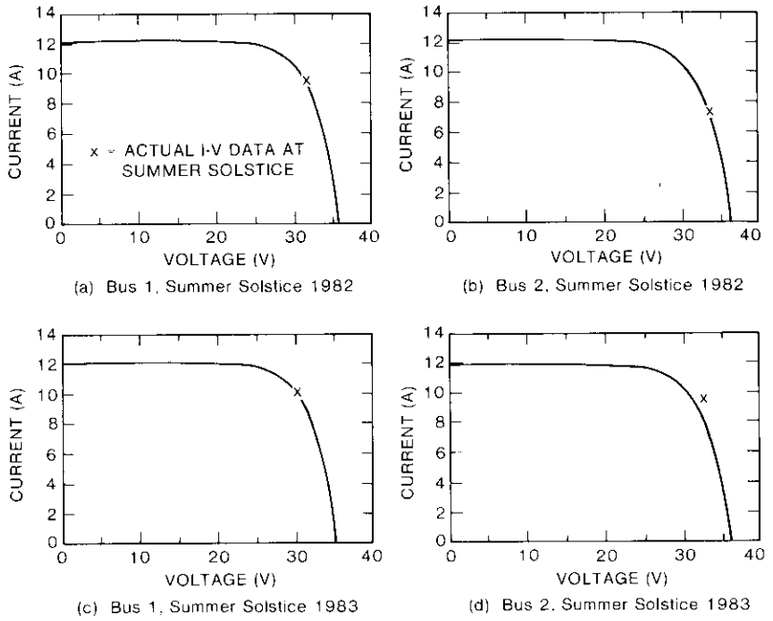

Figure 6. *INTELSAT IV-A F-6 Array I-V Plots*

In-orbit solar array performance tests and results

To check the validity of the predictions, two sets of array tests were performed: one on INTELSAT IV-A F-2 (launched January 29, 1976) and F-6 on May 9, 1985, and another on F-4 (launched May 26, 1977) and F-6 on May 15, 1985. These tests consisted of increasing the loads on each bus until large reductions in voltage were observed, indicating an operating point around the knee of the applicable array I-V curve. Real-time bus current and voltage telemetry data were recorded on a two-channel strip-chart recorder for each test. Power telemetry data were also printed in real time, and the results were plotted using bus current and bus voltage as x-y axes.

Figure 7 shows typical bus current and voltage *vs* time plots for the INTELSAT IV-A F-6 bus 1 test performed on May 9. The first command sequence in this test placed battery 1 on high charge (two-thirds charge), increasing bus 1 loads by 0.7 to 1.6 A. This load change reduced the bus voltage by roughly 5.3 V (peak-to-peak), from 29.5 to 24.2 V. (Figure 7 shows a lower limit of just under 27 V because the strip-chart recorder

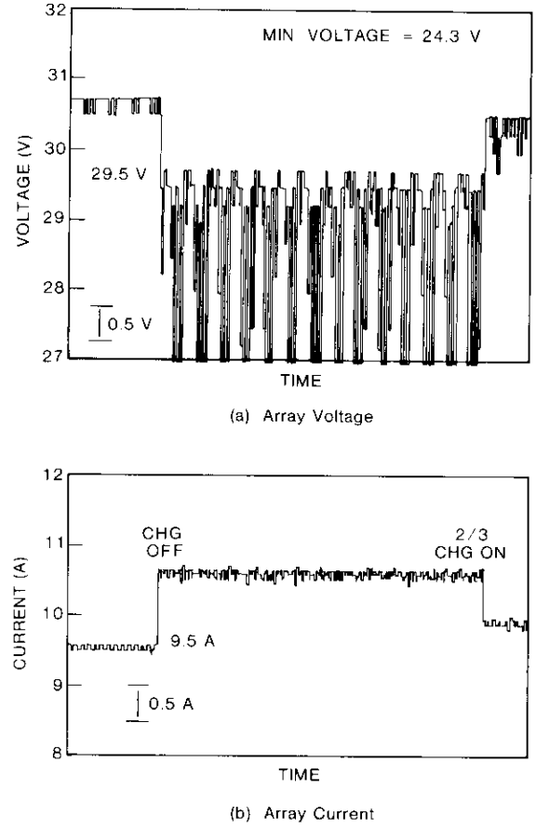

Figure 7. *Solar Array Test Data*

deflection was limited to that value. The 24.2-V value was taken from the video telemetry display at the INTELSAT Control Center.) The large voltage drop for a relatively small load increase indicated that, at the 10.6-A level, this solar array was operating around the knee of the I-V curve; hence, further load increases could have resulted in automatic unit turn-offs. It should also be pointed out that during stationkeeping maneuvers, cyclic or continuous bus current increases due to thruster valve operation are of the same order of magnitude; therefore, similar voltage responses were expected.

The operational I-V curve plot from the May 9 solar array test performed on INTELSAT IV-A F-6 bus 1 is shown in Figure 8, along with the predicted I-V curve for that date.

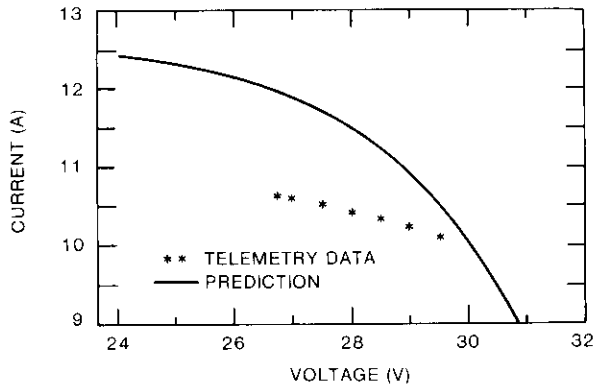

Figure 8. *Bus 1 Solar Array Test Data Summary*

In addition to the solar array tests described above, all of the solar array performance data were examined and the following observations were made:

a. All bus voltages fluctuate when the current exceeds 9.5 A, with peak-to-peak variations increasing with higher bus current.

b. Bus current values fluctuate randomly with time, with a range between ±0.1 A. This range does not appear to depend on the absolute value of the bus load for different spacecraft.

c. For all tests performed, the applicable array temperatures were roughly equal (17° to 20°C), except for the INTELSAT IV-A F-2 aft panel temperature, which was 13°C.

d. The incremental bus currents applied for each test differed because the communications and bus configurations did not allow multiple turn-ons or turn-offs of satellite components, since these spacecraft were still carrying traffic. Also, the uncertainty associated with the I-V curve characteristics requires that caution be exercised to avoid going over the knee and causing array voltage collapse.

Corrected INTELSAT IV-A solar array predictions

In the May 1985 tests, telemetry data were obtained (as described in the previous section) which extended to the short-circuit current side of the knee of the I-V curve. Figure 9 indicates that the array current was about 7 percent lower than predicted. It was also considerably lower than the manufacturer's prediction, based on the radiation environments specified in the contract. The reason is still not fully understood, although solar cell string failure is

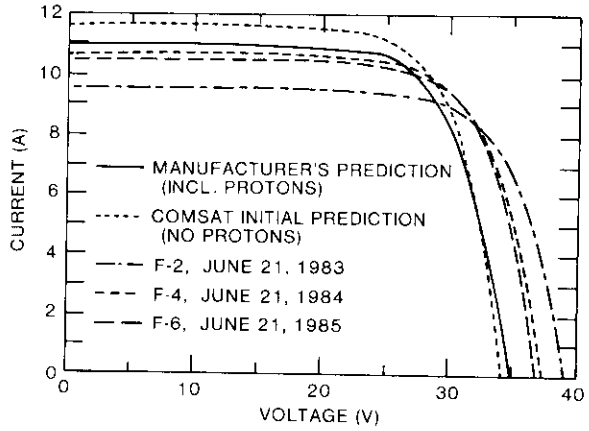

Figure 9. *Solar Panel Array Current* vs *Predictions on June 21 (7 Years)*

one possibility. For each failed solar cell string, the array would lose 1/64 (approximately 1.5 percent) of its short-circuit current performance. However, the low array current appears too consistently in all the spacecraft for this to be likely. Greater-than-predicted particulate radiation degradation is also unlikely because it would have resulted in lower-than-predicted array open-circuit voltage performance, as well as lower-than-predicted current.

The most likely explanation for the low array current appears to be ultraviolet (UV) radiation, which affects cell short-circuit current while having a negligible effect on solar cell open-circuit voltage performance. UV exposure tests performed before launch had a duration of only 1,000 hours. It has since been demonstrated through tests performed at COMSAT Laboratories on the INTELSAT V and VI solar cells that UV exposure tests of at least 2,000 to 3,000 hours are required in order to accurately predict UV degradation at end of life. Still another possibility is that laboratory measurements of solar cells conducted in the early 1970s, upon which the manufacturer's and COMSAT's array predictions were based, may have been inaccurate.

In the absence of a definitive cause for the lower-than-predicted array current, the predictions were fitted to the May 9, 1986, telemetry data for INTELSAT IV-A F-6 by varying the single-cell parameters (short-circuit current, maximum-power current, open-circuit voltage, and maximum-power voltage) used in generating the predictions. Based on this fit, a revised prediction of the INTELSAT IV-A I-V curve was generated for summer solstice 1985 (see Figure 10) which was in good agreement with telemetry data collected near summer solstice.

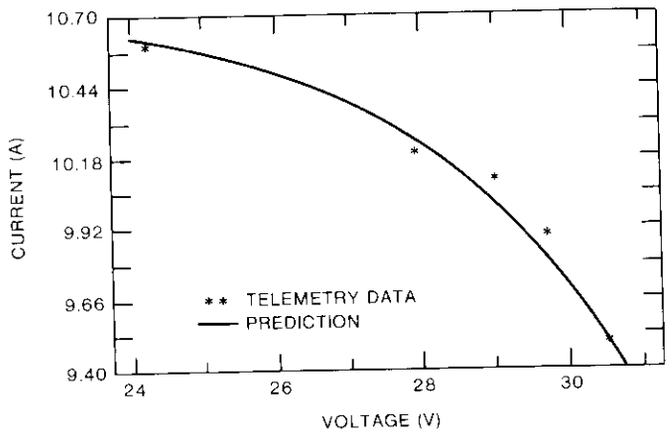

Figure 10. *F-6 Solar Panel I-V Curve Prediction, May 9, 1985*

Based on the agreement of the revised INTELSAT IV-A F-6 predictions with telemetry data, I-V curve predictions were made for INTELSAT IV-A F-1, F-2, F-3, F-4, and F-6 for summer and winter solstices, as well as for vernal and autumnal equinoxes from 1985 through 1988 (see Figure 11 for sample plots). When possible, these predictions will be checked against actual spacecraft performance before the spacecraft are de-orbited.

As shown in Figure 11, batteries are required to supply part of the load current if array voltage drops below 24 V. This is prevented by managing the load so that the operating point stays on the open-circuit voltage side of the knee of the array I-V curve. For example, in Figure 11b the load should not greatly exceed approximately 8.5 to 9 A, to prevent solar array voltage collapse. Similar techniques have been applied to INTELSAT V and are applicable to INTELSAT VI spacecraft, thus giving the operators valuable information concerning spacecraft operating margins.

Conclusions

Comparison of actual in-orbit performance of the INTELSAT IV-A F-6 solar array with predictions made by both COMSAT Laboratories and the array manufacturer revealed a discrepancy in short-circuit current, which is probably attributable to UV radiation degradation. The solar array model was corrected to account for this difference, and subsequent in-orbit data indicate that the correction implemented for F-6 is valid for the other INTELSAT IV-A spacecraft.

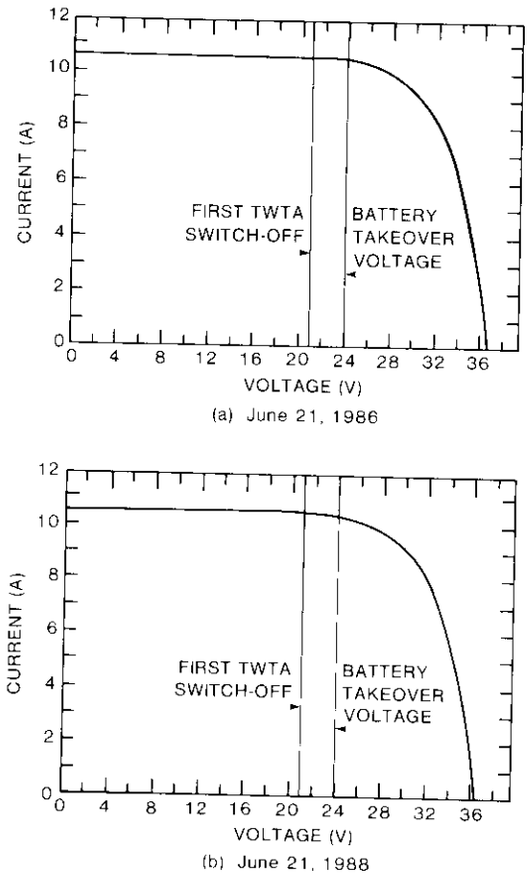

Figure 11. *F-4 Solar Panel I-V Curve Predictions*

Although these spacecraft may soon be retired, the analysis is useful because it demonstrates array degradation performance beyond the end of the design lifetime. It also lays the groundwork for similar work on the INTELSAT V and VI spacecraft.

Acknowledgment

This paper is based on work performed at COMSAT Laboratories under the sponsorship of the International Telecommunications Satellite Organization (INTELSAT). Views expressed are not necessarily those of INTELSAT.

References

[1] E. Levy, Jr., and F. S. Osugi, "Design and Performance of INTELSAT IV Power Subsystem," 7th Intersociety Energy Conversion Engineering Conference, San Diego, California, September 1972, *Proc.*, pp. 483–492.

[2] H. S. Rauschenbach, *The Solar Cell Array Design Handbook*, New York: Van Nostrand, 1980.

[3] L. J. Goldhammer and S. W. Gelb, "Synchronous Orbit Performance of Hughes Aircraft Company Solar Arrays," 11th Intersociety Energy Conversion Engineering Conference, State Line, Nevada, September 1976, *Proc.*, pp. 1379–1386.

[4] J. W. Lyons, "An Improved Technique for Prediction and Analysis of Solar Array Performance for Geosynchronous Spacecraft," 19th Intersociety Energy Conversion Engineering Conference, San Francisco, California, August 1984, *Proc.*, Vol. 1, pp. 464–470.

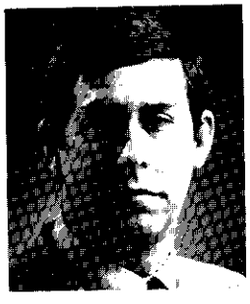

John W. Lyons III received a B.S. in physics from the Virginia Polytechnic Institute and State University in 1979, and an M.S. in applied physics from the Johns Hopkins University in 1985. While an undergraduate he worked at COMSAT Laboratories as a cooperative education student. From 1979 until 1987 he was a Member of the Technical Staff at COMSAT Laboratories, where he developed software for solar array and battery performance prediction and analysis, participated in solar cell and solar panel qualification testing, and performed other tasks in support of COMSAT and INTELSAT spacecraft programs. He is currently a Senior Member of the Technical Staff in the Power Systems Group at the General Electric Astro-Space Division in Hightstown, New Jersey.

Mr. Lyons is a member of AIAA and IEEE. He has authored and coauthored a number of technical papers on solar array and battery performance prediction, as well as on radiation testing of reflector materials.

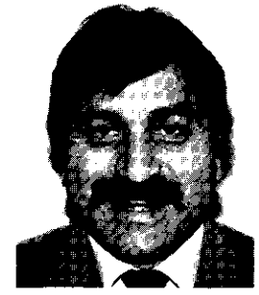

Ahmet Ozkul received a B.S.A.E. from California Institute of Technology in 1971, and an M.S.A.E. and Dr.Ap.Sc. from the George Washington University in 1974 and 1977, respectively, while employed at NASA Langley Research Center in Hampton, Virginia. He joined INTELSAT in 1978 as a Member of the Technical Staff in the Systems Planning Division, where he worked on system configuration and satellite payload/bus analyses of numerous follow-on spacecraft concepts to INTELSAT V. After transferring to the Satellite Operations Department in 1983, Dr. Ozkul worked on electrical power-related aspects of all in-orbit satellites. He developed a solar array performance and prediction model based on historical INTELSAT V telemetry data, and formulated software-backed procedures for operating the batteries and solar arrays of all in-orbit and INTELSAT VI satellites. Currently, as Senior Operations Engineer, he is involved in the development and verification of INTELSAT VI mission operations.

Index: mobile communication, modulation, small terminal design, channel coding, speech coding

Design of an MSAT-X mobile transceiver and related base and gateway stations

R. J. F. FANG, U. BHASKAR, F. HEMMATI, K. M. MACKENTHUN, AND A. SHENOY

(Manuscript received March 13, 1987)

Abstract

This paper summarizes the results of a design study of the mobile transceiver, base station, and gateway station for NASA's proposed Mobile Satellite Experiment (MSAT-X). Major ground segment system design issues such as frequency stability control, modulation method, linear predictive coding vocoder algorithm, and error control technique are addressed. The modular and flexible transceiver design is described in detail, including the core, RF/IF, modem, vocoder, forward error correction codec, amplitude-companded single sideband, and input/output modules, as well as the flexible interface. Designs for a three-carrier base station and a 10-carrier gateway station are also discussed, including the interface with the controllers and with the public-switched telephone networks at the gateway station. Functional specifications are given for the transceiver, the base station, and the gateway station.

Introduction

Various commercial mobile satellite systems have been proposed in the U.S. and abroad to supplement terrestrial cellular mobile radio systems in providing telephony, data, and message services to rural and remote areas, including land, maritime, and aeronautical applications. To accelerate the introduction of commercial mobile satellite services in the U.S., the National

Aeronautics and Space Administration (NASA) has formulated the Mobile Satellite Experiment (MSAT-X) in cooperation with industry, to develop those high-risk technologies that will ensure the future growth of mobile satellite services.

Figure 1 depicts the space and ground segments of the originally proposed MSAT-X system [1]. The space segment would be implemented in several phases, with the phase 1 satellite being provided by commercial operators under lease to NASA, and subsequent phases employing more sophisticated multibeam satellites. The ground segment of the proposed system would consist of mobile terminals, base stations and gateway stations that interface with the public-switched telephone networks (PSTNs), and the network management center (NMC).

In the original system, mobile terminals were to transmit in the 821- to 825-MHz band and receive in the 866- to 870-MHz band, both in the upper UHF spectrum. The 1985 FCC decision on frequency allocation for land-mobile satellite services resulted in this system being modified to employ

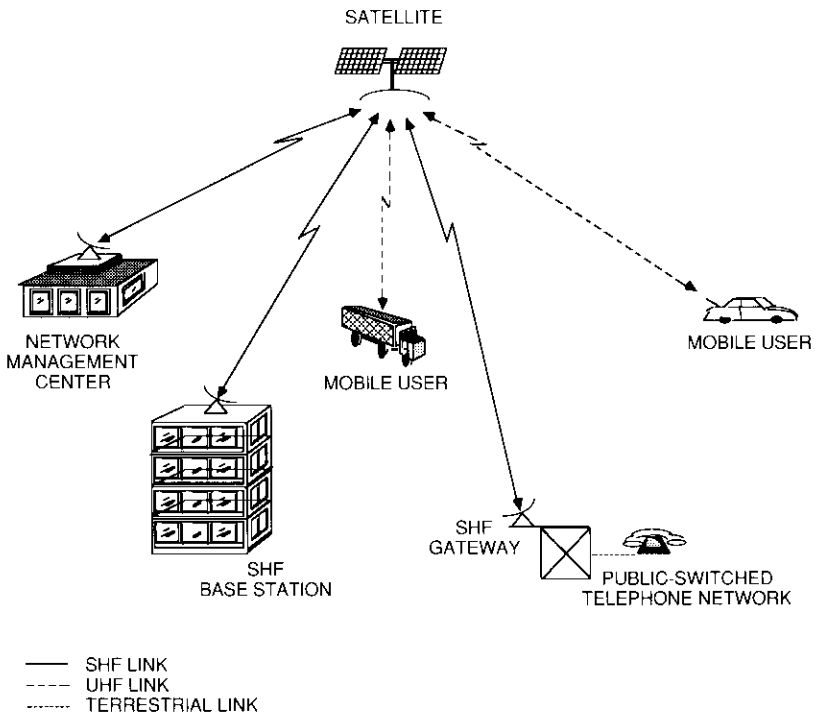

Figure 1. *A Mobile Satellite Network*

mobile terminals operating in the 1,500- to 1,600-MHz bands. Although the frequency change may invalidate some details in the RF portion of the mobile terminal design, the basic concepts remain the same, particularly the vocoder, forward error correction (FEC) codec, modem, and mobile terminal architectures. Since the only differences occur in the mobile RF and vehicle Doppler frequencies and in some details of terminal design, UHF may still be used to illustrate the concept. Fixed terminals, which include base stations, gateway stations, and the NMC, will still operate at K_u-band (i.e., transmit in the 14-GHz and receive in the 12-GHz fixed service bands).

NASA's mobile satellite program, of which MSAT-X is a part, has emphasized the development of spacecraft and earth station technologies that will efficiently utilize the scarce spectral and orbital resources allocated for mobile satellite services. Specifically, the following technologies have been identified for development:

a. multibeam and high-e.i.r.p. satellites to obtain multiple frequency reuse while minimizing mobile terminal size and cost;
b. steerable medium-gain vehicle antennas to enable better orbit usage and power savings;
c. a digital vocoder at 2,400 bit/s to achieve bandwidth efficiency over a multipath fading channel;
d. digital modem/FEC codec for 2,400-bit/s transmission over the 5-kHz channel to achieve bandwidth and power efficiency;
e. network control protocol to maximize the throughput and minimize message delay for a given system capacity; and
f. a modular and flexible mobile terminal architecture design for low-cost implementation to accommodate advances in component subsystem technology.

Items (*a*), (*b*), and (*e*) have been investigated by other contractors for Jet Propulsion Laboratories (JPL) [2]–[6]. The digital vocoder, the digital modem, and the modular and flexible mobile terminal architecture design are discussed in this paper. Specifically, a 2.4-kbit/s vocoder algorithm was developed for multipath landmobile application. Effective modulation and FEC coding techniques were investigated for sending 2.4-kbit/s vocoder speech over 5-kHz channels with multipath fading. Designs for the modular and flexible mobile transceiver, an example base station, and an example gateway station are also presented, including major functional parameters for specifications.

The major systems requirements for the transceiver, base station, and gateway station were established by NASA/JPL [2]. Based on these requirements, the system design issues of frequency stability control, modulation

technique, digital vocoder, amplitude companded single sideband (ACSB) technique [7], error control, transceiver architecture, and flexible interface design are addressed individually. Next, base station and gateway station designs that meet NASA/JPL system requirements are presented, followed by a brief discussion of the interface between the gateway station and the PSTNs. The key parameters for functional specification of the mobile terminals, base stations, and gateway stations are also summarized.

System requirements

NASA/JPL imposed the following systems requirements on this design study. Three types of transponders will be employed on board the phase 1 spacecraft: SHF/UHF* forward transmission to mobile terminals, UHF*/SHF return transmission from mobile terminals, and SHF/SHF backhaul transmission between fixed terminals. There will be no direct UHF/UHF transmission between mobile terminals. Frequency reuse by spatial isolation will be employed only at UHF and for a total of N times, where N is approximately 2 or 4 initially. Each UHF beam has a unique SHF/UHF and UHF/SHF transponder set of about 1-MHz bandwidth; however, the satellite has only one SHF/SHF transponder of about 25 MHz. Since there is no frequency reuse at SHF, an antenna with at least continental U.S. (CONUS) coverage will be required for both up-link and down-link. The channel allocation for carriers within each transponder will be 5 kHz. Circular polarization will be used by all mobile terminals, while linear polarization will be employed by the fixed terminals, including the NMC.

The phase 1 system design must include both analog ACSB voice and 2,400-bit/s vocoder speech, although 4,800-bit/s vocoder speech of higher quality will be employed in the phase 2 design. Digital voice at 2,400 bit/s must be of acceptable quality at a channel bit error rate (BER) of 10^{-3} over the mobile link. After error control, data or message transmission must have an error rate of better than 5×10^{-6} for a raw channel BER of 10^{-3}. The throughput efficiency for data and message transmission should be 0.5 or greater.

In the originally proposed MSAT-X system, mobile telephone service to the PSTNs was full-duplex voice transmitted through the gateway station. Each mobile telephone could be associated with a particular gateway or a group of gateways. Voice dispatch between the mobile and base stations would be half-duplex. With the exception of a mobile-originated call to a dispatch operation, all voice connections, including telephone calls from the PSTN,

*UHF is used to illustrate the design concept, as explained previously.

would be made under a blocked-calls-cleared protocol. Data communications would employ packets. Acknowledgment is required for each hop in point-to-point data communications; however, no acknowledgment is needed for point-to-multipoint data.

In such a system, network users (mobile or fixed) are under the central control of the NMC. Gateway and base stations make connection requests to the NMC over the SHF/SHF backhaul links. A centralized demand-assigned network control protocol termed integrated-adaptive mobile access protocol (I-AMAP) [8],[9] is employed to dynamically partition the available channels into four functional groups: reservation, command, voice, and data (as depicted in Figure 2). Reservation channels occur only on return links and are used for mobile terminal-to-NMC communications regarding terminal initialization and requests to establish connection. The NMC employs command channels to provide network users with control information regarding acknowledgments of reservation channel traffic, connection attempts by other users, and network status information. One command channel is designated as a wake-up channel to provide the information necessary for terminals to log-on to the network. Voice and data channels occur on both forward and return links and are used to transfer user traffic during a connection.

The mobile transceiver must be both flexible and modular. As shown in Figure 3, it is composed of a core module [which includes the RF/IF, microprocessor control unit (MCU), frequency synthesizer, and power supply], as well as peripheral modules for the linear predictive coding (LPC) vocoder, digital modem, ACSB modem, FEC codec, input/output (I/O) devices, and antenna. The interfaces between these modules should be general, so that as

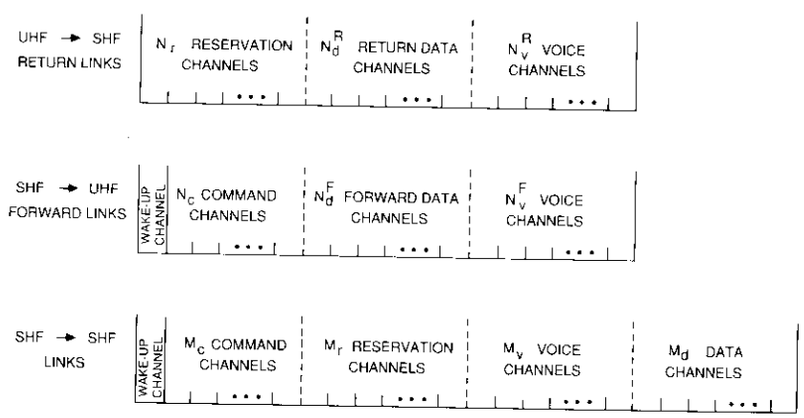

Figure 2. *Channelization*

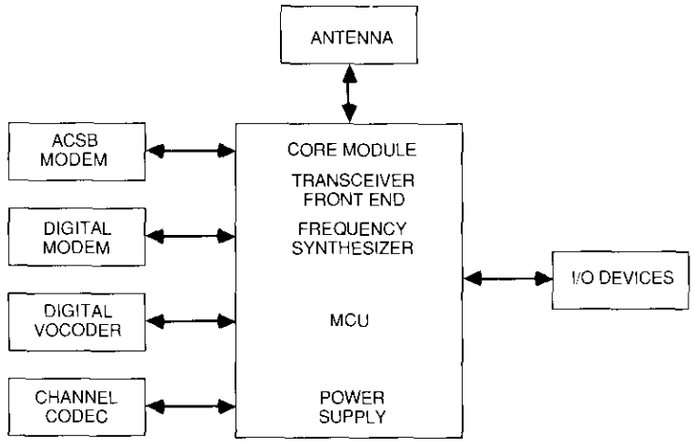

Figure 3. *Mobile Transceiver Block Diagram*

technology advances some modules may be replaced by more sophisticated ones. The modular mobile transceiver is intended to serve as a test bed for the development and testing of technologies for the mobile segment of the mobile satellite system.

NASA/JPL requires [2] that the transceiver high-power amplifier (HPA) be capable of 10-W average and 20-W peak operation. The RF/IF should have a total noise figure not exceeding 2 dB. The frequency synthesizer design may assume paired transmit and receive channels with a fixed 45-MHz separation.

The digital modem is required to have a bit rate of at least 2,400 bit/s over a 5-kHz satellite channel in order to accommodate the 2,400-bit/s LPC vocoder. Modem BER performance at 2,400 bit/s over a 5-kHz additive white Gaussian noise (AWGN) channel must be less than 10^{-3} and 10^{-6} at 44.8- and 49.0-dB-Hz carrier-to-noise-density ratio (C/N_o), respectively. Special provisions must be incorporated into the design to combat impairments caused by frequency errors due to Doppler and other sources, and by adjacent channel interference (ACI) during up-link fades.

JPL also requires that digital voice be sent using a 2,400-bit/s LPC vocoder. Special provisions must be incorporated to provide communications-quality (*vs* toll-quality) speech in the presence of the background noise typical of a moving vehicle environment, and over a multipath fading channel. The 2,400-bit/s LPC vocoder, working with the PSTN at the gateway station, also must produce communications-quality speech. Nominal operation of the vocoder is set for a BER of 10^{-3}, but communications should still be possible with a BER of 2×10^{-2}.

Voice activation will be employed to conserve transponder power. Both digital vocoder and analog ACSB modems must function over the multipath fading channel with a fade margin of about 5 to 10 dB. The multipath fading channel is modeled as a Ricean channel with frequency offsets and a typical Rice factor of 10 dB [10].

Although the mobile antenna is beyond the scope of this study, the transceiver design must be compatible with the closed-loop method for antenna acquisition and tracking, which uses a pilot or beacon from the satellite.

To the extent practical, the base station and gateway stations should use the same modules as the mobile transceivers in order to minimize overall system cost. The base station must be capable of accommodating up to three simultaneous, full-duplexed, analog or digital transmissions with voice activation or data activation, and the gateway station must be capable of accommodating up to 10 simultaneous, full-duplexed, analog or digital transmissions with voice or data activation. All communications between the base station and the NMC or between the gateway station and the NMC are to be accomplished via the SHF/SHF backhaul links. The antenna diameter for the base station and gateway station is about 3 m, and receiver sensitivity is about 23 dB/K. The SHF backhaul links can be assumed to be nearly perfect, due to the ample margin available for fade protection.

Frequency stability control

One of the most important considerations in designing the MSAT-X ground system is frequency stability control, because of the narrowband 5-kHz channel allocation. With a typical satellite on-board frequency source of 10^{-6} long-term stability, the 14/0.868-, 0.823/12-, and 14/12-GHz transponders can produce 13.132-, 11.177-, and 2-kHz translation errors, respectively. Low-cost mobile terminals with a frequency source of 10^{-6} long-term stability can exhibit a frequency error of about 868 Hz at UHF and 1,600 Hz at *L*-band. Moreover, mobile movement and satellite diurnal variation will produce additional Doppler errors. These frequency translation and Doppler errors are very significant given the desired 5-kHz channel allocation, and must be properly controlled.

In developing a method for controlling frequency stability, the following assumptions are made:

- Three independent on-board translation oscillators (OSCS) of 10^{-6} long-term (7- to 10-year) stability for SHF/UHF, UHF/SHF, and SHF/SHF links–one for each transponder type.

- A precise and stable oscillator with a 10^{-9} long-term (5-year) stability at the NMC, and a colocated UHF terminal with sufficient transmit and receive equipment dedicated solely to the control of frequency stability.
- An oscillator of 10^{-7} long-term (5-year) stability and a 10^{-9} daily stability at the base stations and gateway stations.
- An oscillator of 10^{-6} long-term (5-year) stability at the mobile terminals.
- Paired transmit and receive frequencies with a fixed 45-MHz separation at both the fixed terminals and mobile terminals.

The NMC establishes absolute frequency standards in the down-link of the SHF/UHF and SHF/SHF transponders so that mobile and fixed terminals, respectively, may obtain their reference frequencies (Figure 4). The NMC sends a pilot to its own colocated UHF receivers. By preadjusting its up-link SHF transmission frequency, F'_o, the NMC can receive the UHF pilot, f_o, at a predetermined frequency with an accuracy of at least 10^{-9}. This is employed as the UHF frequency standard by all mobile terminals in that beam. By sending $F'_1, F'_2, \ldots, F'_N$ at fixed frequency shifts from F'_o at SHF, the NMC can establish frequency standards ($f_1, f_2, \ldots, f_N$) in other UHF beams, although it cannot view its own transmissions in those beams. Similarly, the NMC can establish a frequency standard, F_K, for the SHF down-link by simply adjusting its own SHF up-link transmission frequency, F'_K.

Using a phase-locked-loop (PLL) receiver, mobile terminals (fixed terminals) can lock their reference oscillator to the UHF (SHF) pilots from the NMC and synthesize the transmit and receive frequencies. However, due to the difference in Doppler between the spacecraft and the NMC, as well as the Doppler between the spacecraft and an arbitrary fixed terminal, the above SHF frequency standard as seen by the fixed terminal may be in error by an amount equal to the differential Doppler.

The NMC can use the data on spacecraft diurnal motion obtained from the telemetry, tracking, and command (TT&C) station to accurately compute the differential Doppler between the NMC and any fixed terminal. It can also measure the UHF/SHF transponder frequency error by sending an accurate UHF pilot, f'_o, via its colocated UHF transmitter and measuring the frequency of the received pilot at SHF. Using these measurements, the NMC can compute the precorrections necessary for each fixed terminal to transmit and receive, and can send the precorrections as data to each fixed terminal via the backhaul wake-up channel.

This approach completely compensates for satellite motion Doppler; reference oscillator drift in the satellite, fixed terminals, and mobile terminals; and mobile terminal Doppler for signals received at mobile terminals.

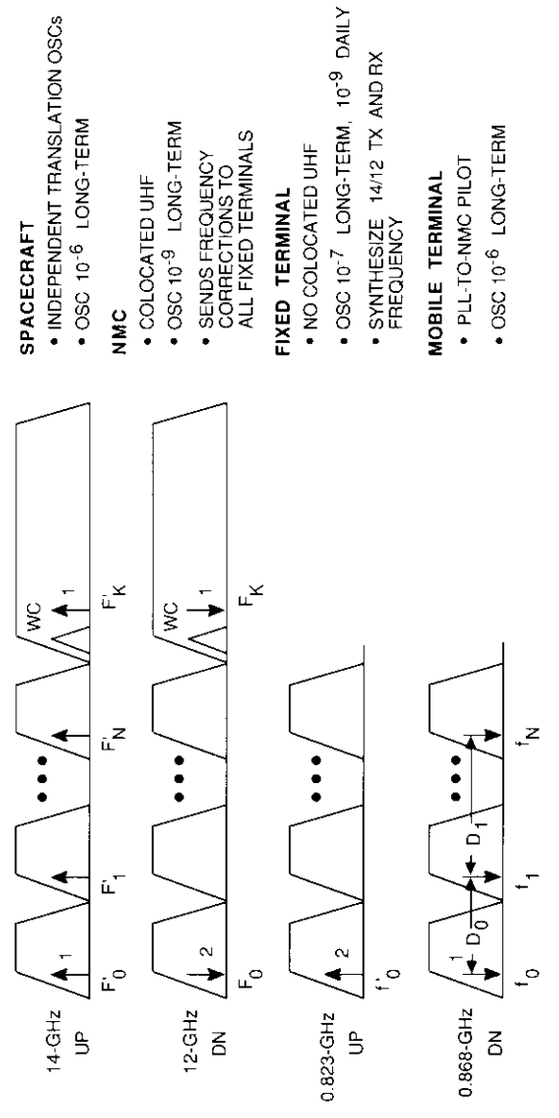

Figure 4. *Out-of-Band Frequency Stability Control*

However, the mobile terminal Doppler is essentially doubled for signals received at fixed terminals. The worst residual frequency error after correction using this method is no more than ±179 Hz in the fixed terminal reception of mobile terminal transmission, assuming a mobile speed of 65 mph. This frequency error will essentially be doubled if the mobile terminals employ *L*-band instead of UHF.

Modulation method

The MSAT-X channel is subject to multipath fade, frequency offset, Doppler spreading, and ACI, particularly when the desired carrier is in the presence of large (*e.g.*, 10-dB) up-link fade. As a result of Doppler spread and frequency shift, the frequency error can be as large as 179 Hz at UHF. The multipath fading channel can be modeled as a Ricean channel [10],[11]. Since the maximum fade rate is 179 Hz for a vehicle traveling at 65 mph, the channel is quasi-static over the longest detection interval at the 2,400-Hz symbol rate. The performance of various modulation system candidates over the Ricean fading channel can be approximated by averaging the energy-per-bit to noise-power-density ratio (E_b/N_o) for an AWGN channel over the first-order statistics of the Ricean density.

Candidate systems

The following eight modulation system candidates were investigated:

- Gaussian minimum shift keying (GMSK) with 2-bit differential detection [12],
- minimum shift keying (MSK) with 1-bit differential detection [13],
- binary FM with limiter/discriminator (LD) detection [14],
- four-level FM with LD detection,
- binary FM with noncoherent detection using observations from three symbol intervals,
- duobinary FM with LD detection and maximum-likelihood sequence estimation (MLSE),
- differential phase-shift keying (DPSK), and
- MSK with 2-bit differential detection and a frequency-locked loop (FLL).

The performance of these candidates was evaluated by Monte Carlo simulation under the following channel conditions:

a. AWGN channel with no frequency offset,
b. AWGN channel with frequency offset,
c. three channels with frequency offset and 10-dB fade on the desired channel and no fade on the two adjacent channels, and
d. Ricean channel with a 10-dB Rice factor (which is typical [10]) and a carrier offset.

Figures 5 and 6 illustrate some aspects of the performance of the candidate systems under channel conditions (*c*) and (*d*). Binary FM with LD and a normalized modulation index, h, of 0.5 significantly outperformed the other candidates, with the exception of the baseline MSK with 2-bit differential detection and an FLL. Here, the difference was slight. However, binary FM with LD detection requires only symbol synchronization, while MSK with FLL requires additional preamble bits for frequency synchronization, which may be difficult to achieve in the short time available for the preamble of short packets. In addition, binary FM with LD detection is relatively insensitive to frequency offset and is robust against ACI, especially in the presence of up-link fade. In the presence of fast Rayleigh fading, it has the lowest error floor of all modulations considered.

Binary FM with LD detection can easily maintain synchronization in the fading channel, since phase noise, Doppler shift, and Doppler rate do not affect symbol synchronization. Also, the constant-envelope feature of binary FM allows transmission by saturated nonlinear amplifiers, without spectral regrowth that could increase the interference to the adjacent channels. Finally, this approach is very simple to implement and low in cost. Based on these advantages, binary FM with LD detection is the recommended

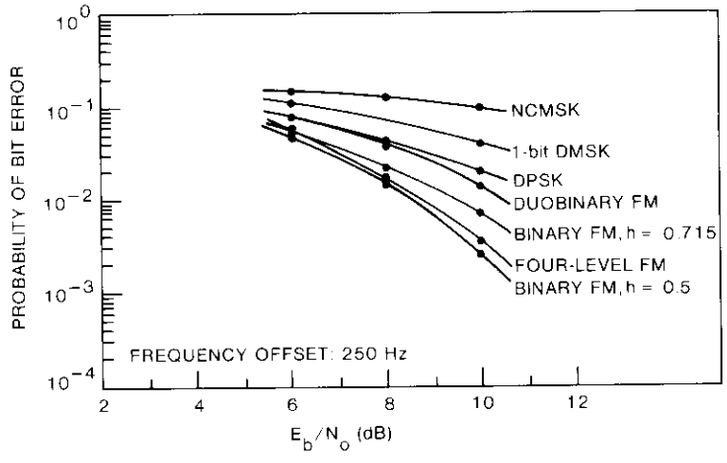

Figure 5. *Performance of Candidate Modulation Systems*

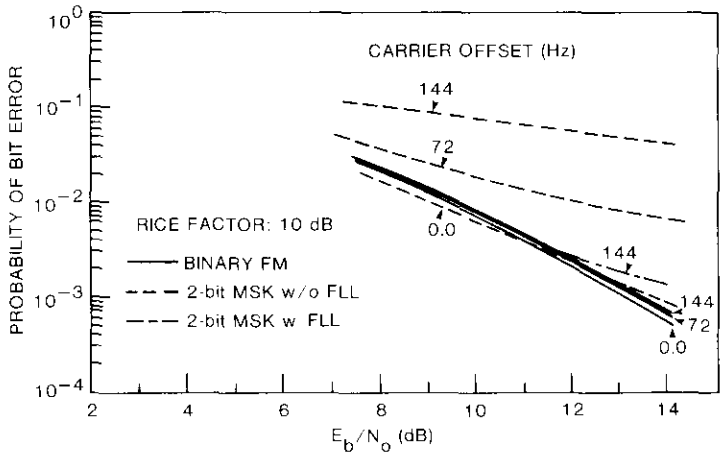

Figure 6. *Comparison of Binary FM With 2-bit Differential MSK Over Multipath Fading Channel*

modulation method for the MSAT-X system. Because of FEC requirements for the 2,400-bit/s vocoder (discussed below), the modem bit rate must be increased from 2,400 to 2,756 bit/s. At this bit rate, channel degradations are practically the same as those at 2,400 bit/s.

Burst preamble

A burst preamble was designed for this modulation system consisting of a 2 N-bit alternating sequence for clock synchronization, followed by a 32-bit unique word. The unique word is composed of a 16-bit Neuman-Hoffman sequence (0000011001101011), followed by the same sequence reversed in time. An optimum symbol synchronizer is proposed which performs an MLSE to the phase of the sinusoid at the low-pass filter (LPF) output of the synchronizer.

The MLSE of the sine wave phase was derived for a synchronizer which samples the LPF output with k samples per symbol. The performance of the symbol synchronizer was simulated by computer for k = 2, 4, and 8; $2N$ = 2, 4, 8, 12, 16, 20, 24, 28, and 32; and E_b/N_o = 13 dB in a Ricean channel with a carrier offset of 144 Hz and a carrier-to-interference ratio (C/I) of 10 dB. An E_b/N_o of 13 dB is required in order to achieve 10^{-3} BER on the Ricean channel. The simulation results, shown in Figure 7, indicate that k = 2 gives negligible degradation compared to k = 8. For k = 2, the even- and odd-numbered samples are added with alternating signs, and are

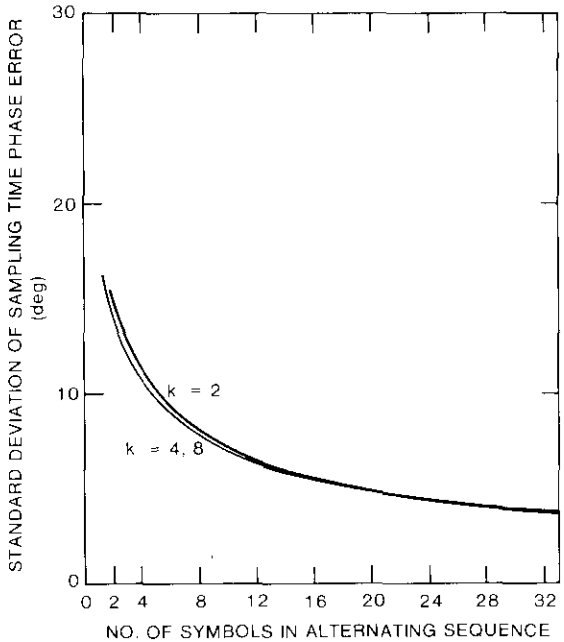

Figure 7. *Standard Deviation of Sampling Time Phase Error as a Function of the Number of Symbols in Alternating Sequence*

input to a read-only memory (ROM) which implements the arctangent function to estimate sine wave phase. The ROM output is used to adjust a digitally controlled oscillator which sets sampling time. The value $2N$ = 40 was selected for the preamble design because it was found to give small timing error. Values of $2N < 40$ could also be used without significant performance degradation. Thus, the k = 2 synchronizer is recommended for the MSAT-X transceiver because of its negligible performance degradation and its extremely simple implementation.

The FM modulator can be implemented digitally at low cost by means of a loop-up table stored in programmable ROM (PROM). The range from 0° to 360° is divided into N points, and the cosine values at each of these points are stored. A waveform is generated at a particular frequency by reading out the stored points in proper order at a clocking rate of N times the desired frequency. If the clocking rate (i.e., the sampling frequency) is fixed, then different frequencies are obtained by changing the step size by which the table pointer is incremented for each point.

Let N, D, and F_s be the table length, step size, and sampling frequency, respectively. Then, the number of samples needed to complete a full cycle in N/D at the frequency of the wave is $F_s\,N/D$. For binary FM at a symbol rate of R_s, with a modulation index of 0.5, the two tones are

$$f_1 = D_1 F_s/N = F_o - R_s/4$$

$$f_2 = D_2 F_s/N = F_o + R_s/4$$

where F_o is the carrier frequency and $f_2 - f_1 = R_s/2$.

Figure 8 is a block diagram of the digital binary FM modulator. The current data bit is used as a multiplexer selector to choose step size D_1 or D_2. An accumulator is constantly incremented at the sampling rate, F_s, by an amount equal to the step size. The accumulator contents form the address pointer for

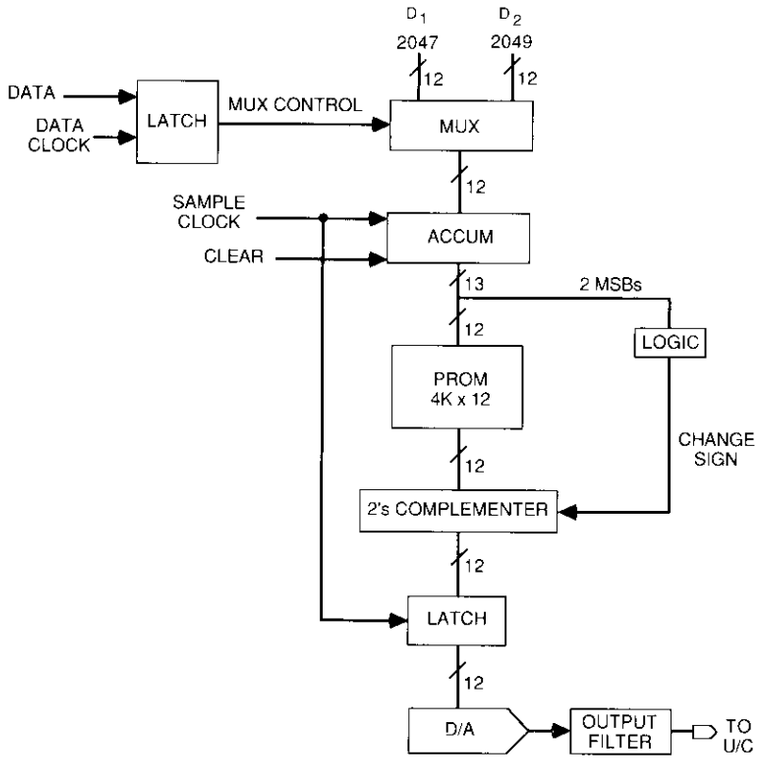

Figure 8. *Digital Binary FM Modulator Block Diagram*

stepping through the look-up table. Only the low 12 bits of the accumulator address are used to access the PROM. The 12th and 13th bits are exclusive-ORed to provide the change sign bit control for the appropriate half of the cosine waveform. The output is latched and passed through a digital-to-analog (D/A) converter, and the analog output is then filtered by an LPF before being sent to the up-converter. The advantages of this implementation are its low cost, high temperature stability, good precision, small size, low harmonic distortion, and good flexibility.

The FM demodulator can be implemented by using an analog integrated circuit (IC) FM demodulator chip, an external crystal discriminator, and an output amplifier (see Figure 9). These chips are readily available commercially. The FM demodulator combines the functions of limiting, three-stage IF amplification, FM demodulation, and power supply regulation on the same chip.

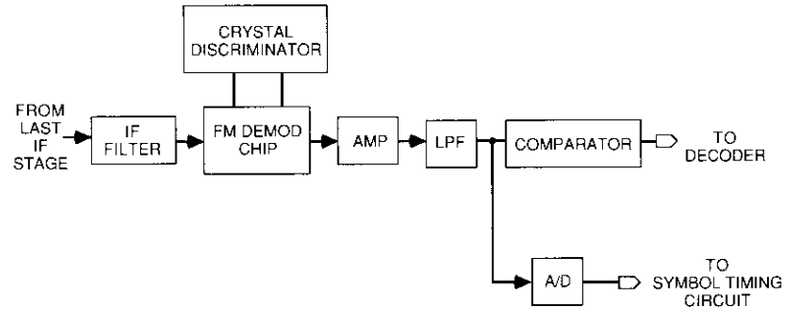

Figure 9. *FM Demodulator Block Diagram*

To perform symbol timing acquisition and tracking, a digital signal processor (DSP) chip can be employed so that the MLSE for symbol timing acquisition described earlier and the conventional zero crossing technique for symbol timing tracking can all be implemented in software at low cost.

Digital ACSB modem

The ACSB modem may be implemented in an all-digital form, as illustrated in Figure 10. The amplitude pumping technique is recommended, in which a pilot tone is inserted above the audio band of the 2:1 compressed voice on the transmit side. The pilot signal level must be accurately determined to ensure good reception. The composite signal is then input into a second 2:1 compander. The reference level of this compander is the pilot level, which must be properly recovered by the automatic gain control (AGC) after

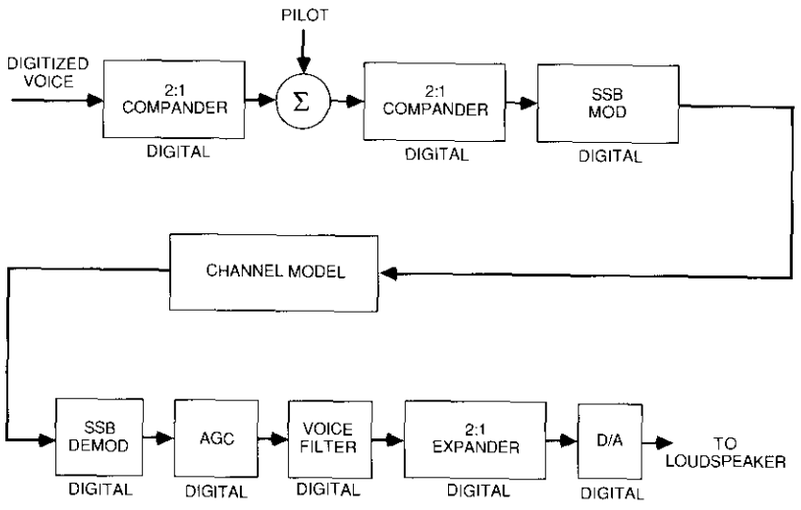

Figure 10. *Block Diagram of ACSB Modem Using Amplitude Pumping*

transmission over the multipath fading channel. If the voice signal power is greater than the pilot power, the composite signal will undergo a 2:1 compression, resulting in an overall 4:1 compression of the voice signal. If the voice signal power is less than or equal to the pilot power, the composite signal will pass through this compander relatively unchanged, resulting in only about 2:1 compression. Therefore, with this technique, signals with large amplitude relative to the reference pilot level go through a 4:1 compression, whereas signals with low amplitude go through a 2:1 compression. At the receiver, the AGC restores the pilot to its proper level, and hence the voice signal is restored to the same level at which it was input to the second compander. The expander then expands the signal to its original level.

Restoration of the pilot is essential for ACSB transmission over a multipath fading channel, because the effect of fades can be measured by the pilot and compensated for by the AGC. The pilot may also be used to measure any Doppler or frequency offsets, which can then be tracked out. An adaptive finite impulse response (FIR) filter can be used to extract the pilot.

Vocoder algorithm

As noted previously, the MSAT-X channel is subject to multipath fades. In designing the 2,400-bit/s LPC vocoder for use in the MSAT-X system, other sources of impairment must be considered, such as background acoustic noise

at the mobile terminal, thermal noise in the channel, and channel distortion, particularly for speech from the PSTN. The vocoder designed for MSAT-X should exhibit the following characteristics:

- insensitivity to acoustically coupled mobile background noise,
- graceful degradation during short-term fades,
- rapid recovery from long fades,
- negligible degradation due to random channel noise at a BER of 10^{-3},
- acceptable pitch estimation performance, producing communications-quality speech with PSTN input at the gateway station, and
- low cost.

Algorithm design

The selected vocoder is based on well-known LPC techniques [15],[16]; however, several modifications must be made to the basic LPC vocoder so that robust operation can be realized in the mobile environment. Figure 11 is a block diagram of the vocoder analyzer, while Figure 12 shows the synthesizer.

The pitch extraction method usually employed in LPC vocoders is based on the average magnitude difference function [15], which is susceptible to error in the presence of background noise. The acoustically coupled noise in a mobile vehicle may contain periodicities (e.g., axle noise) which can mask low-level unvoiced signals, causing erroneous voicing decision. More seriously, these periodicities can cause incorrect pitch period estimation during voiced frames. Errors in voicing are subjectively very objectionable, and accurate pitch extraction is vital to achieving good speech intelligibility and quality.

A more robust pitch extraction method based on the peak location of the autocorrelation function of the prediction residual has been developed for the vocoder (see Figure 13). In this method, the peak value of the autocorrelation function is compared to a set of predetermined thresholds to determine if the frame is voiced. Voiced frames exhibit a strong peak at the lag corresponding to the pitch period. This method was found by computer studies to be accurate in the presence of recorded vehicle noise down to a signal-to-noise ratio (S/N) of 18 dB. For noise above this level, it is desirable to use a noise-cancelling microphone so that the S/N presented to the coder is at least 18 dB.

Pitch estimation is also difficult when the speech signal has passed through the PSTN. In this case, the speech is distorted due to the carbon button transmitter and high-pass filtering above 300 Hz. Removal or distortion of the fundamental pitch frequency component by high-pass filtering can impair the accuracy of pitch extraction. The proposed autocorrelation peak-picking

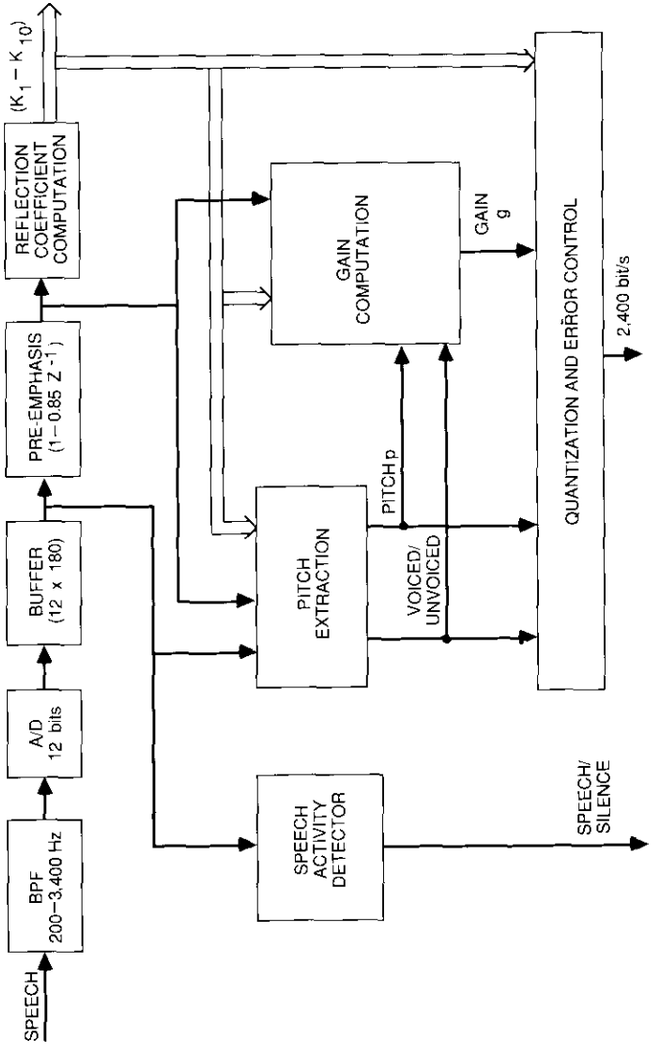

Figure 11. *Vocoder Analyzer Block Diagram*

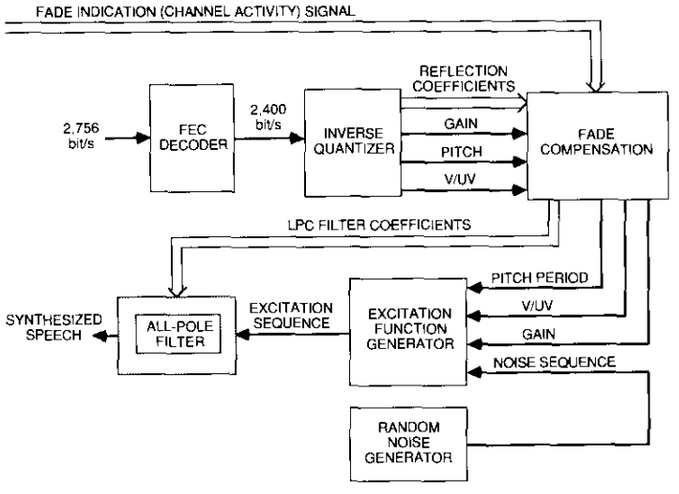

Figure 12. *Vocoder Synthesizer Block Diagram*

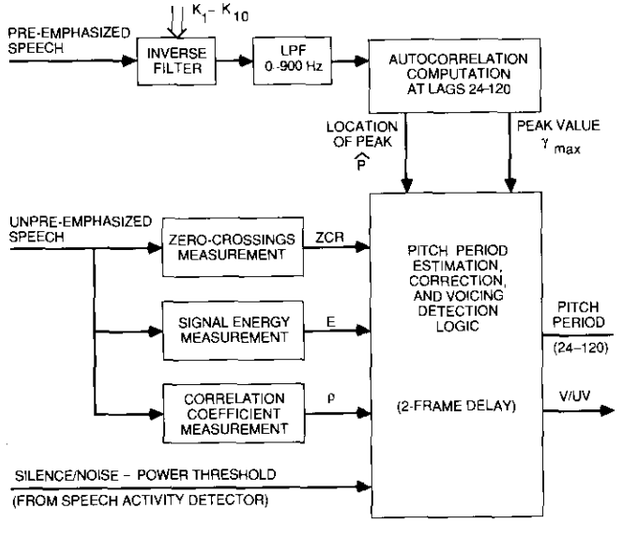

Figure 13. *Pitch Extraction by Autocorrelation Peak-Picking Method*

method is not sensitive to loss of the low-frequency spectrum. It was tested on PSTN speech samples and found to perform well.

Computer simulations revealed that a channel BER of 10^{-3} resulted in significantly lower speech quality. For acceptable performance at this BER, error protection is necessary; however, it must be provided without significantly increasing the channel bit rate or the coding delay. Severe distortion was found to occur if certain critical bits are in error. By protecting only these critical bits, speech quality was practically unaffected by bit errors at 10^{-3} BER.

A rate 1/2 shortened (16, 8) quadratic residue (QR) code was used to protect the eight bits which are most critical to speech quality: the two most significant bits (MSBs) of the first reflection coefficient, the MSB of the second reflection coefficient, two MSBs of gain, and three MSBs of pitch and voiced/unvoiced (V/UV) bits. This code improved the BER for these critical bits from 10^{-3} to 10^{-6}. However, the channel bit rate must be increased to 2.756 bit/s due to redundant bits required by FEC, and the LPC frame length must be increased from 54 to 62 bits. This increase in channel bit rate can be accommodated by the modulation method used for the transceiver, without significantly increasing intersymbol interference or ACI. Figure 14 depicts the voice packet format.

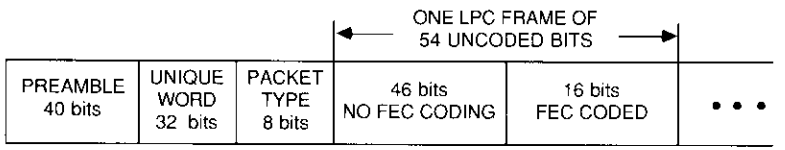

Figure 14. *Format for Transmission of 2,400-bit/s LPC Voice Using a (16, 8) QR Code to Protect the 8 Most Critical Bits in Each 54-bit LPC Frame*

Short fades (of 100 ms or less) can occur frequently in the mobile environment. For example, shadowing due to foliage and highway overpasses can cause such fades. During these fades, several frames of vocoder bits are lost. Unless these frames are replaced by a meaningful approximation, the speech signal will be interrupted by bursts of noise. Interleaving techniques are not useful in mitigating the effects of fades, since they require large delays that are not tolerable for voice communications. Moreover, such interleaving also slows the recovery from longer fades.

For the MSAT-X system, a frame repetition scheme was selected to bridge short fades. In this scheme, the occurrence of a fade is sensed by monitoring the receive channel power. The frames lost due to fade are then replaced by the most recent unfaded frame. Up to four lost frames can be replaced in this manner. This scheme primarily serves to retain intelligibility during frequent short fades. For longer fades, the approximation becomes poorer and it is preferable to mute the vocoder.

Performance of the modified LPC vocoder was evaluated both objectively and subjectively. All tests were conducted on speech from a linear microphone, band-limited to 200–3,400 Hz. Both diagnostic rhyme test (DRT) and diagnostic acceptability measure (DAM) objective tests were conducted under four conditions:

- with no impairments,
- in the presence of truck noise at 18-dB *S/N*,
- in the presence of bit errors at 10^{-3} BER, and
- in the presence of burst errors (simulating the effect of fades).

The test scores [17] indicate that the intelligibility of the modified vocoder is better than that of the standard DOD LPC-10 [18], and the acceptability is very close. Informal subjective listening tests indicate that the modified vocoder has better natural speech quality than vocoders available commercially. It also exhibits better performance in the presence of background noise.

Implementation

The vocoder may be implemented in software by using two DSP chips: one for the analyzer, and the second for the synthesizer. The input speech signal is band-limited to 3,400 Hz, sampled, and quantized by a pulse-code modulation (PCM) coder at a rate of 8 kHz. The samples are stored in memory which is addressed by the analyzer DSP chip. The DSP processes the samples, while the PCM enters new data into another portion of memory. After the LPC parameters are computed, the eight most critical bits are read into a buffer, where they are encoded by a rate 1/2 shortened QR encoder. The 16 bits from the encoder are then interleaved among the remaining LPC bits. The resulting 62-bit LPC frame is written into the output buffer, along with a *Speech Activity* flag.

The LPC synthesizer stores the incoming data bits in an input buffer. The synthesis process is conditioned on receiving *Channel Activity* and *Start Synthesis* signals from the core module. The process begins by verifying the frame synchronization, and then decoding the eight critical bits with the rate 1/2 QR decoder. The assembled 54-bit LPC frame is processed to produce the appropriate digital words, which are sent to the PCM decoder for conversion to analog speech. Fades are recognized by examining the received LPC parameter values and the *Channel Activity* signal. The previous frame is

repeated for short fades. For long fades, the speech output is muted. The rate 1/2 QR codec can be implemented with a look-up table.

Error control method

Error control is employed to mitigate the effects of channel noise, multipath fading, and shadowing. For the data, control, and reservation packets, the objective is to achieve an error rate of less than 5×10^{-6} when the raw channel error rate is 10^{-3}, while maintaining an information throughput of 50 percent or better.

Candidates

As specified by NASA/JPL, the uncoded packet length for control and reservation packets is about 128 bits, and for data packets about 512 bits. Numerous error control techniques were examined, including open-loop FEC coding. However, due to packet collision, coding delay, and complexity considerations, the open-loop FEC approach was rejected. Instead, closed-loop automatic repeat request (ARQ) systems are favored.

Both pure and hybrid ARQ systems were considered. In the pure systems, no channel FEC coding is employed, and the receiver requests retransmission of erroneous packets in accordance with certain specific protocols. In hybrid ARQ systems, FEC coding is employed in the forward channel to improve the channel BER prior to applying ARQ. Error detection is required for both ARQ methods. The Hamming code with 16-bit cyclic redundancy checks (CRCs), as recommended by CCITT, was adequate to perform the error detection.

Four pure ARQ systems were investigated:

- stop-and-wait,
- go-back-N,
- selective repeat, and
- Weldon's nearly optimal strategy (NOS) [19].

Selective-repeat ARQ can be considered as a special case of NOS ARQ, with the number of retransmission parameters, r, in the NOS ARQ set to 1.

Throughput efficiencies for these pure ARQ systems were computed as a function of packet error rate for the packet lengths of interest. For the 512-bit data packets, the throughput efficiency (defined as packet bits divided by binary symbols transmitted) with any of these pure ARQ systems is 0.42 or lower at a packet error rate of 0.4 or a channel error rate of 10^{-3}. This throughput appears to be too low; some form of FEC is needed to reduce the error rate if the packet length is not increased.

For the 128-bit reservation or control packets, the throughput efficiency using Weldon's NOS ARQ system with $r = 2$ appears to achieve a throughput efficiency of 0.78 at a packet error rate of 0.12 or a channel error rate of 10^{-3}. However, at this high channel error rate, message delays may be too long for these crucial packets. Therefore, some form of FEC coding seems necessary for sending the 128-bit packets, so that the resultant error rate is low and the message delay is short. In either case, hybrid ARQ systems are needed.

Recommended hybrid ARQ system design

Various FEC coding techniques were investigated for use in hybrid ARQ systems. The BER performance for these codes was evaluated by Monte Carlo simulation over the Ricean fading channel. Double- and triple-error-correcting Bose-Chaudhuri-Hocquenghem (BCH) codes were found to be too susceptible to channel burst errors during fades and were rejected. Self-orthogonal convolutional codes, although simple to implement, were also found to be sensitive to channel burst errors during fades. Punctured convolutional codes [20] of rate 2/3 and 3/4, derived from the convolutional code of rate 1/2 with Viterbi decoding [21]–[23], were found to be the most immune to channel burst errors during fades when a 12×57-block interleaver was used for transmission of the long 512-bit packets. The rate 1/2 convolutional code with Viterbi decoding was adequate for sending the short 128-bit packets during fades, even when no interleaving was employed. Table 1 summarizes the estimated output BER performance of these codes at an input BER of 10^{-3} over the Ricean channel, with a Rice factor of 10 dB.

TABLE 1. OUTPUT BER OF CANDIDATE PUNCTURED CONVOLUTIONAL CODES WITH VITERBI DECODING

	CODE RATE		
INTERLEAVING	1/2	2/3	3/4
Without	7×10^{-7}	10^{-5}	6.5×10^{-5}
With	N/A	5×10^{-8}	5×10^{-6}

Use of these convolutional codes and Weldon's NOS ARQ schemes results in throughput efficiencies for this hybrid ARQ system as shown in Table 2. Although the rate 3/4 and rate 2/3 codes appear to yield higher throughput efficiencies than the rate 1/2 code for sending packets of 128 bits, the decoded BERs given in Table 1 are about two orders of magnitude worse than the BER of rate 1/2 code, and do not meet the BER objective of 5×10^{-6}. These BERs

TABLE 2. THROUGHPUT EFFICIENCY FOR CANDIDATE PUNCTURED CONVOLUTIONAL CODES

CODE RATE	L = 128 BITS	L = 512 BITS	
		WITHOUT INTERLEAVING	WITH INTERLEAVING
1	0.78	0.40	N/A
3/4	0.73	0.69	0.72
2/3	0.65	0.65	0.66
1/2	0.50	0.50	N/A

could significantly increase message delays for the crucial control and/or reservation packets. Consequently the rate 1/2 code was selected for use with the 128-bit packets.

It can be seen from Table 1 that both rate 2/3 and rate 3/4 codes with interleaving achieved the BER objective of 5×10^{-6}. Assuming that such an objective is achieved and the message delay is acceptable, the choice between these two codes for sending 512-bit packets is based purely on the overall throughput efficiency obtained. The data in Table 2 show that the rate 3/4 code will result in higher throughput than the rate 2/3 code. Therefore the rate 3/4 punctured code with Viterbi decoding and interleaving was selected for sending 512-bit packets.

Finally, burst and packet formats were designed for sending 512-bit data, 128-bit acknowledgment, 128-bit reservation, and 128-bit control packets (Figures 15a through 15d, respectively).

In summary, the recommended error control scheme for the MSAT-X system employs the rate 3/4 convolutional code for sending data packets and the rate 1/2 convolutional code for sending acknowledgment, reservation, and control packets. Both codes use Viterbi decoding at the receiver, and both have 64 states. Because the rate 3/4 code is obtained by puncturing the rate 1/2 code, the same hardware may be used for both codes. The binary FM modem uses a hard-decision Viterbi decoder at the receiver.

Implementation

The encoder can be constructed by using a six-stage shift register and several exclusive-OR gates connected according to the generator polynomials described in octal by (133, 171) for the rate 1/2 encoder, and by (133, 171; 133, 171) for the rate 3/4 encoder. In the rate 3/4 encoding process, the first information bit is rate 1/2 coded to yield two output bits, and the next two information bits are rate 1/1 coded to yield one output bit each. This gives four output bits for three input information bits. Figure 16 is a block diagram of the encoder.

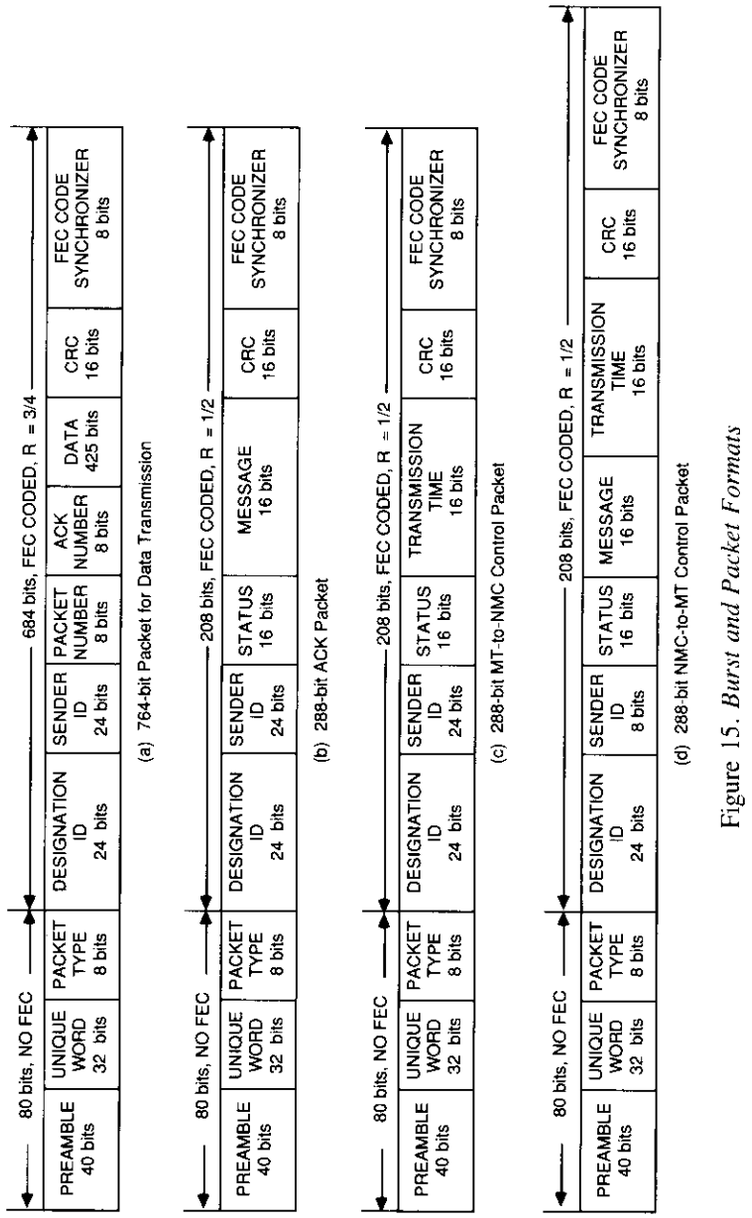

Figure 15. *Burst and Packet Formats*

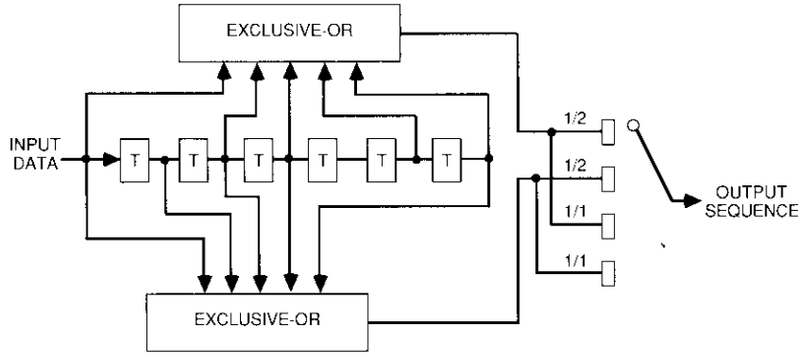

Figure 16. *An Implementation of the Rate 1/2 and Rate 3/4 Punctured Encoder*

The Viterbi decoder [21]–[23] may be implemented in hardware or software. To decode the punctured rate 3/4 code, the puncturing period synchronization must first be established and dummy data must be inserted into the locations from which the original code sequence was deleted. For the inserted dummy data, conventional metric calculation is inhibited and the same metric is given to both code symbols (0 and 1). The conventional Viterbi decoding algorithm can then be employed.

Two possible methods of obtaining code synchronization are discussed in the literature [20]. One method observes the integration value of the difference between the maximum and minimum metrics at consecutive decoding steps. The other method observes the measured channel BER in the received data sequence.

Figure 17 is a block diagram of the punctured Viterbi decoder. Hardware implementation may be accomplished with a custom VLSI chip. Software implementation will use a DSP chip. Assuming 200 ns per instruction, the number of DSP instructions available in a bit period of 1/2,067 or 0.483 ms is 2,415, which is considered adequate for this purpose.

Mobile transceiver design

Mobile transceiver design involves designing the overall flexible and modular transceiver architecture, the baseline peripheral module, and the interface between the modules.

The mobile transceiver (Figure 18) includes all the necessary components of a mobile terminal except the antenna. The transceiver architecture must

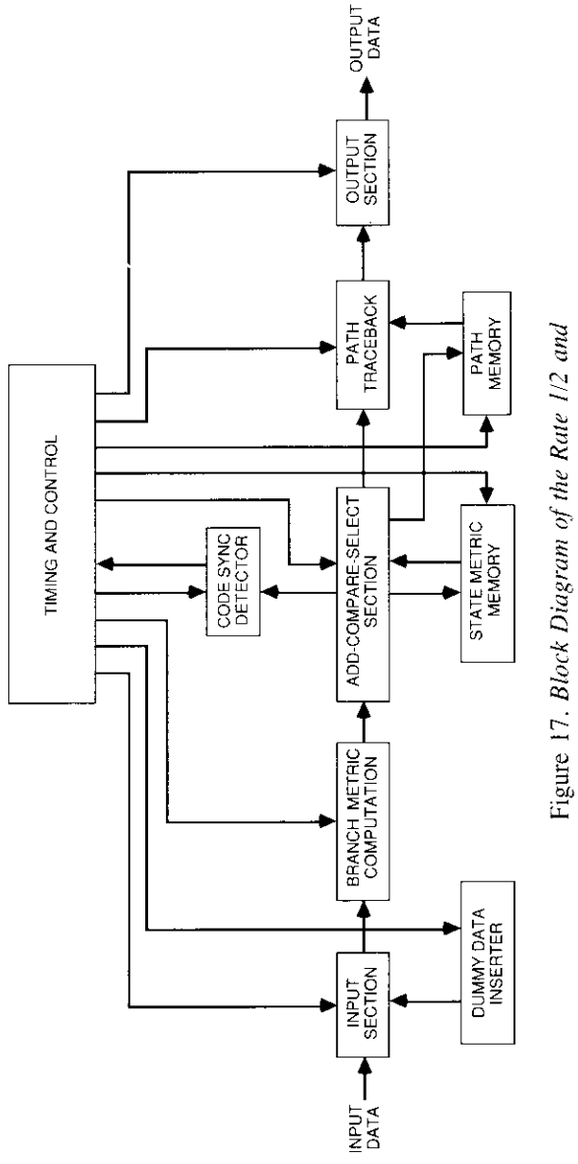

Figure 17. *Block Diagram of the Rate 1/2 and Rate 3/4 Punctured Viterbi Decoder*

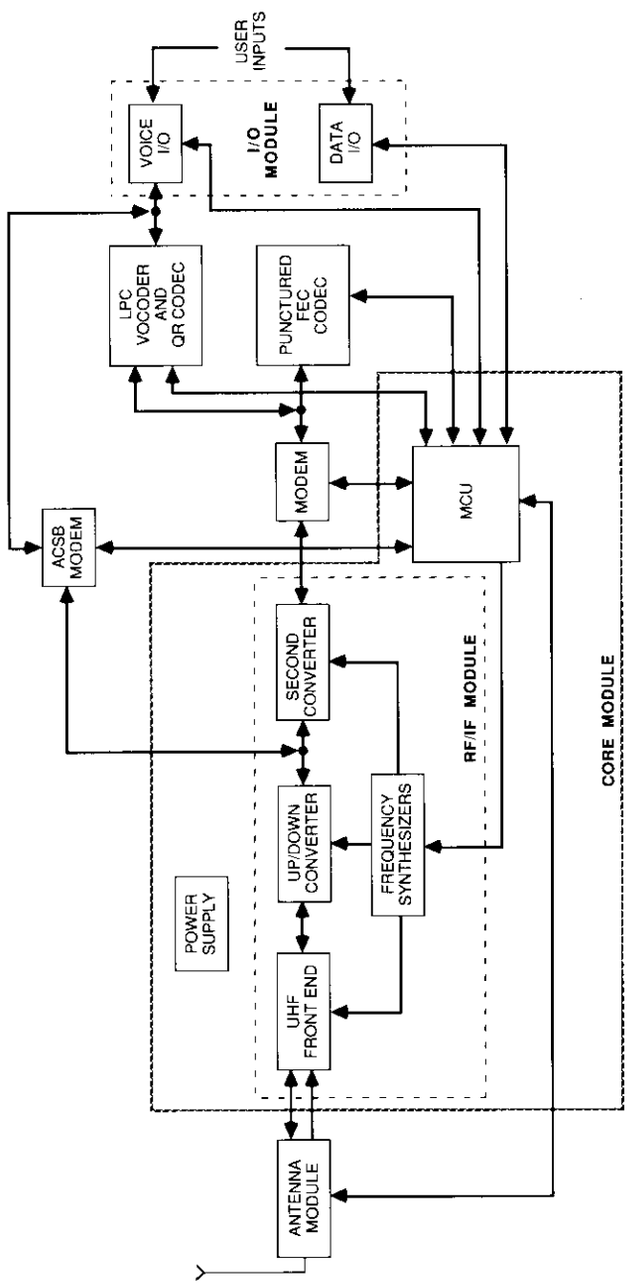

Figure 18. *Schematic of the Mobile Transceiver*

be flexible enough to accommodate future technological changes in such transceiver functions as LPC algorithms, modulation, and error control methods. This flexibility is provided by implementing each subfunction as a physically separate module that plugs into the system backplane. Thus, there are separate modules for the analog and digital modems, the LPC vocoder, the channel codec, the I/O interface, the antenna, and the core module (indicated by the dashed line in the figure). The core module includes the RF/IF front end, the up/down-converters, the frequency synthesizers, the MCU, and the power supply. Digital circuits based on microprocessors or PAL devices are employed for flexibility and ease of upgrading.

Separating the system subfunctions into physical entities requires an architecture that allows control of these individual subfunctions, so that the transceiver can be configured for a given operational mode. Only subsets of the modules are used for the various modes such as voice or data. Figure 19 shows the MCU bus structure for peripheral control. The control unit enables or disables the individual modules as needed by assigning a board control register (BCR) and a board status register (BSR) to each module. The BCRs are designed so that loading them with a specific bit pattern enables or disables the selected board and defines other operating parameters. The BSRs have bit positions allocated that reflect board conditions, such as *Board Fail* and *Sync Loss*.

All board registers are mapped into the MCU address space so that they are treated as memory locations. To configure the transceiver for a given operational mode, the MCU writes the necessary bit patterns into the BCRs.

The boards and the MCU communicate through the system backplane, which has two connectors, P1 and P2. Connector P1 carries the MCU system bus, consisting of the address, data, control, and utility buses. The P1 bus structure is determined by the processor chosen for the MCU board. Connector P2 carries individual lines that are used by the modules to transfer information locally among themselves. The MCU also uses the P2 connector to transfer information or handshaking lines that are inconvenient to send via the system bus. There is no fixed bus structure for P2; lines may be assigned as required.

The MCU contains a 16-bit processor with an addressing range of 16 Mbytes. Such processors have large and powerful instruction sets, and their architecture is well suited for high-level language support. PROMs and erasable PROMs (EPROMs) are used for program memory, and static random-access memories (RAMs) are used for data memory and data buffering.

The MCU is interrupt-driven by the peripherals, requiring an interrupt handler to prepare an interrupt vector that informs the MCU of the source of the interrupt. The MCU controls two synthesizers: the channel select synthesizer and the pilot synthesizer.

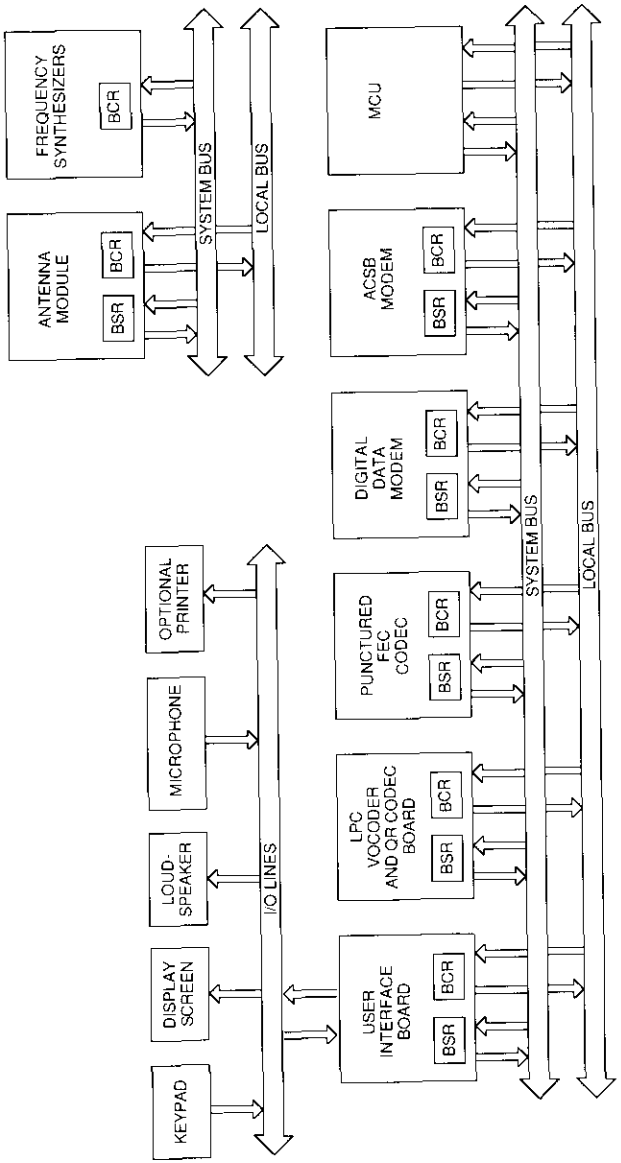

Figure 19. *MCU Bus Structure for Peripheral Control*

The MCU interacts with its peripherals via the P1 and P2 connectors. Because of the large number of interfacing signals, a separate peripheral controller is needed to pre-process these signals. This controller may be composed of discrete digital logic and PALs, or may contain its own limited-purpose processor.

The MCU-RF interface is limited to monitoring-type signals. The UHF RF/IF module design (Figure 20) is given here as an example. Similar concepts can be applied to the *L*-band RF/IF module design. This design approach provides sufficient protection against interference from cellular base stations and from safety and special radio base (SSRB) stations. A diplexer is used to prevent the incidence of transmit power on the low-noise amplifier (LNA) receiver. Interference is rejected by using a 4-MHz UHF filter after the LNA.

The IF subsystems of the transmitter and receiver are designed for use in base and gateway stations as well. The receiver is designed with a channel selector of 2.5-kHz coarse steps and 10-Hz fine steps. Double down-conversions are employed: one from UHF to 10-MHz IF, and the other from 10 to 2.2288 MHz, offset by 1 MHz from the receive IF to achieve decoupling of transmit and receive signals. Up-conversion is accomplished by using a chain of translations to offset the transmitted signal by exactly 45 MHz. An 8-W (saturated) high-power amplifier (HPA) is used for digital transmission, while a 25-W ($P_{1\ dB}$) HPA is used for ACSB, with the 8-W HPA as a driver.

The user I/O module design is limited to the user interface board (UIB). The actual user I/O modules, such as the telephone keypad or the microphone, are not included. The major hardware components of the UIB are as follows:

- Interrupt Handler
- Control/Status Signal Controller
- Telephone Signal Preprocessor and Buffer
- Keyboard Encoder and Buffer
- Display Driver and Buffer
- Tone Generator
- Data Communications Port.

Flexible interface design

The flexible interface is composed of two subsets: the standard control line common to all modules, and module-specific signal lines. The core module uses the first subset to provide the power and master clock to all the boards and to perform the minimum necessary control functions of enabling/disabling, resetting, and initiating self-tests of all boards. Each board must contain at least this control line subset.

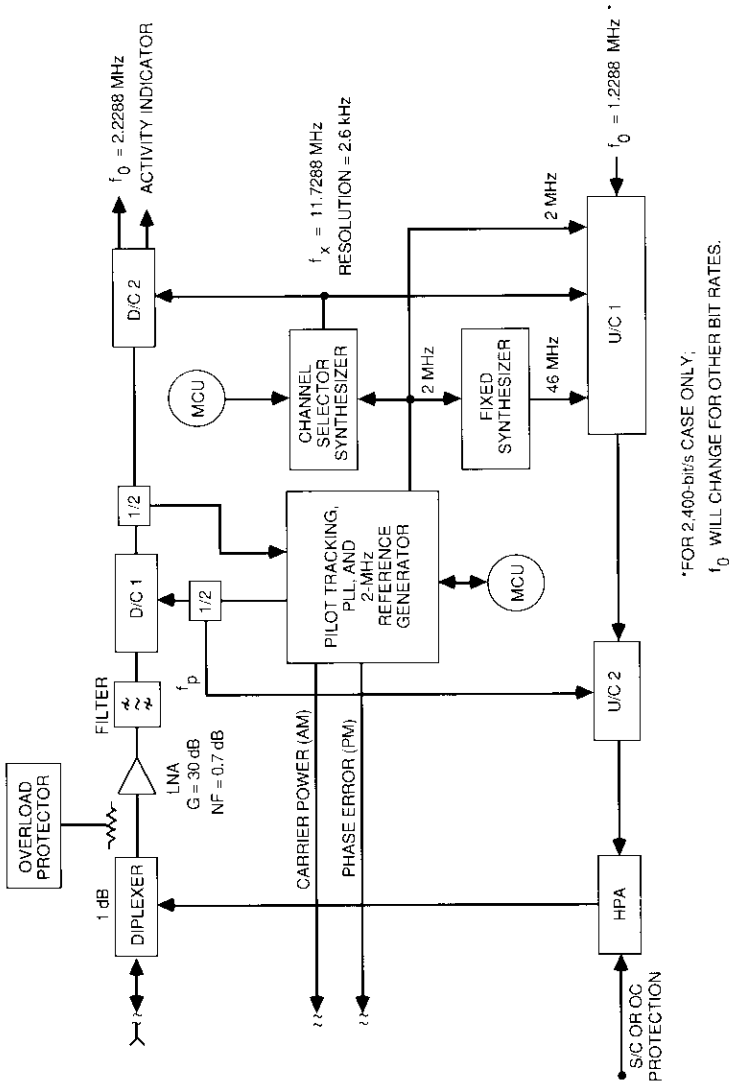

Figure 20. *RF/IF Module Design*

Figure 21 is a hardware block diagram of the user interface signals. The signal lines are allocated logically between the P1 and P2 connectors. Signals directly from or to the MCU are assigned to the MCU system bus on the P1 connector; those that comprise intermodule communications are assigned to the P2 connector. Any MCU signals that are inconvenient to assign to the system bus are also assigned to the P2 connector. Further, some signals are assigned to the BCR and BSR.

Although the number of lines in the interface sets appears to be large, the actual number of physical lines is about one-half to one-third this number because many of the lines are allocated to the MCU system bus. This allows them to be realized as BCR and BSR signals, rather than separate lines on the P2 connector.

Base station and gateway station design

The base stations are employed to communicate with mobile terminals for voice dispatch, data dispatch, or database inquiry/response services, all via half-duplex links. The gateway stations are employed to interconnect mobile terminals with the PSTNs for full-duplex telephony only. All connections are made via the NMC using the I-AMAP demand-assigned network control protocol. The base station is capable of transmitting and receiving three simultaneous carriers, while the gateway station is capable of transmitting and receiving 10 simultaneous carriers. All communications between fixed terminals are accomplished via the backhaul links in the 14/12-GHz band.

To minimize overall system cost, the design of these fixed terminals incorporates the mobile transceiver modules to the greatest extent possible and practical. All baseband modules, including the digital modem, FEC codec, LPC vocoder, ACSB modem, and user interface are essentially identical to those used at the mobile transceiver, with some minor differences. The RF/IF subsystems for the base station and gateway station are very similar, except for the HPA sizes (34 W for the base station *vs* 158 W for the gateway station saturated power, based on 1 W per channel with 11-dB backoff to support ACSB linearity requirements). Figures 22 and 23 are block diagrams of the base station and gateway station, respectively. The major differences between these two stations are in the PSTN interface, the PSTN controller, the base station/gateway station controller, and HPA sizes.

The base station controller is a separate module that is used to receive frequency offset and transponder sub-band information for each of the three base station transceivers. The controller monitors the wake-up channel from the NMC, demodulates the data, disassembles the data into the individual frequency offset and sub-band data, and transfers this information to the

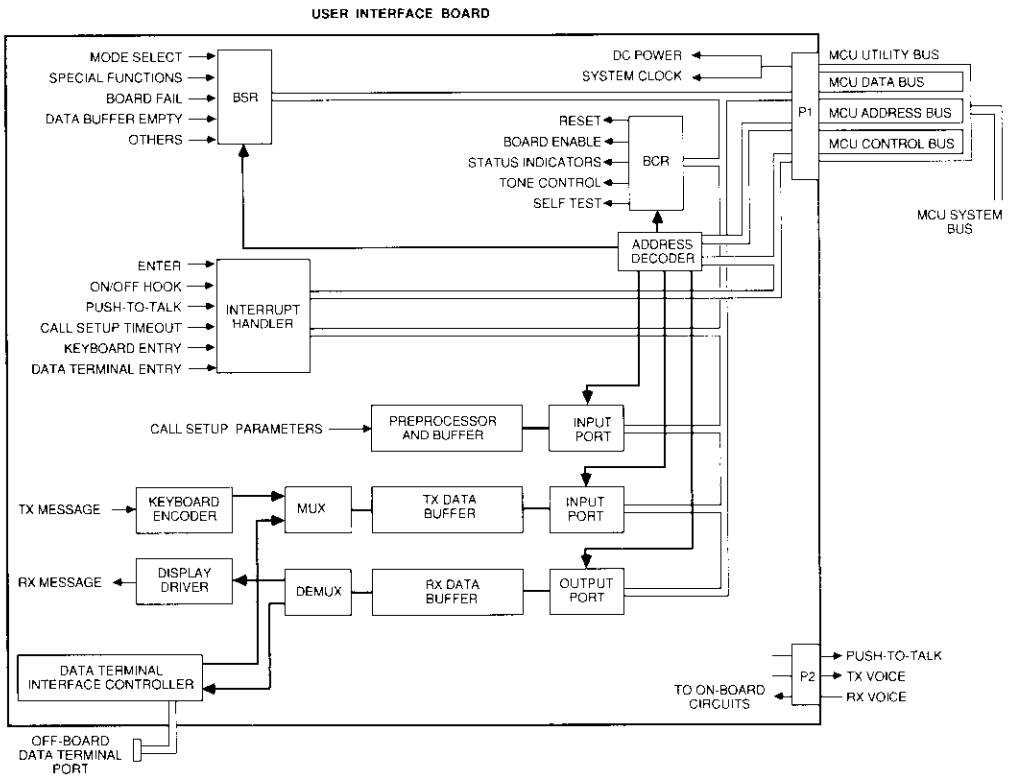

Figure 21. *Hardware Block Diagram of the User Interface Signals*

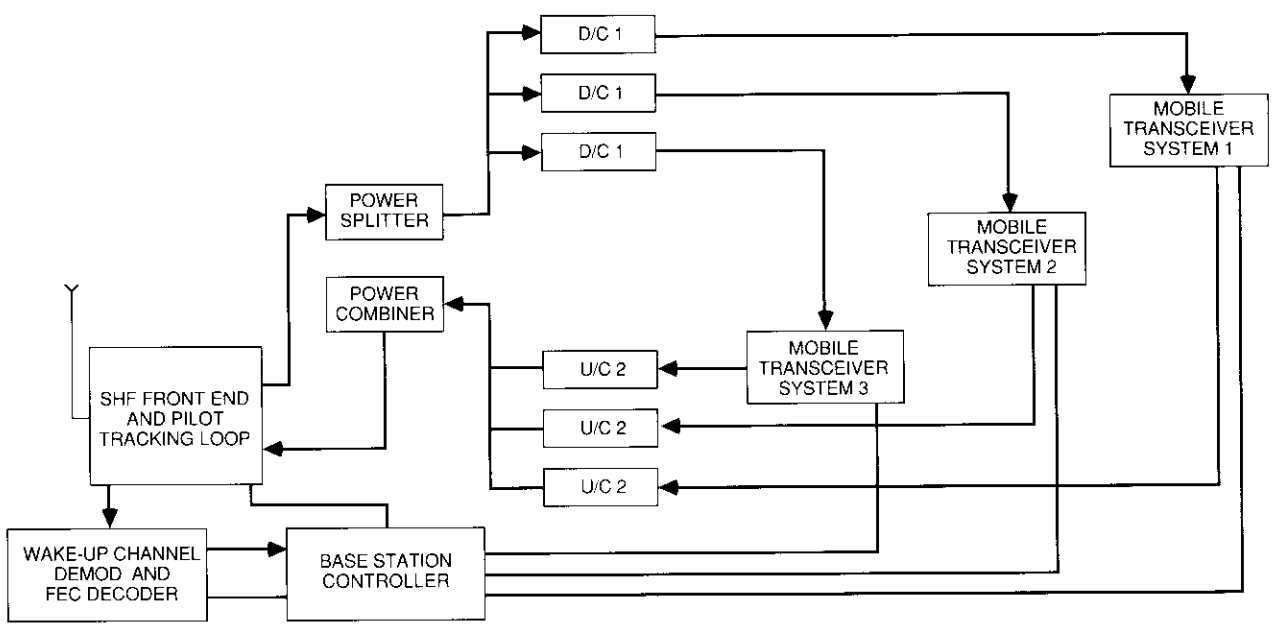

Figure 22. *MSAT-X Base Station Block Diagram*

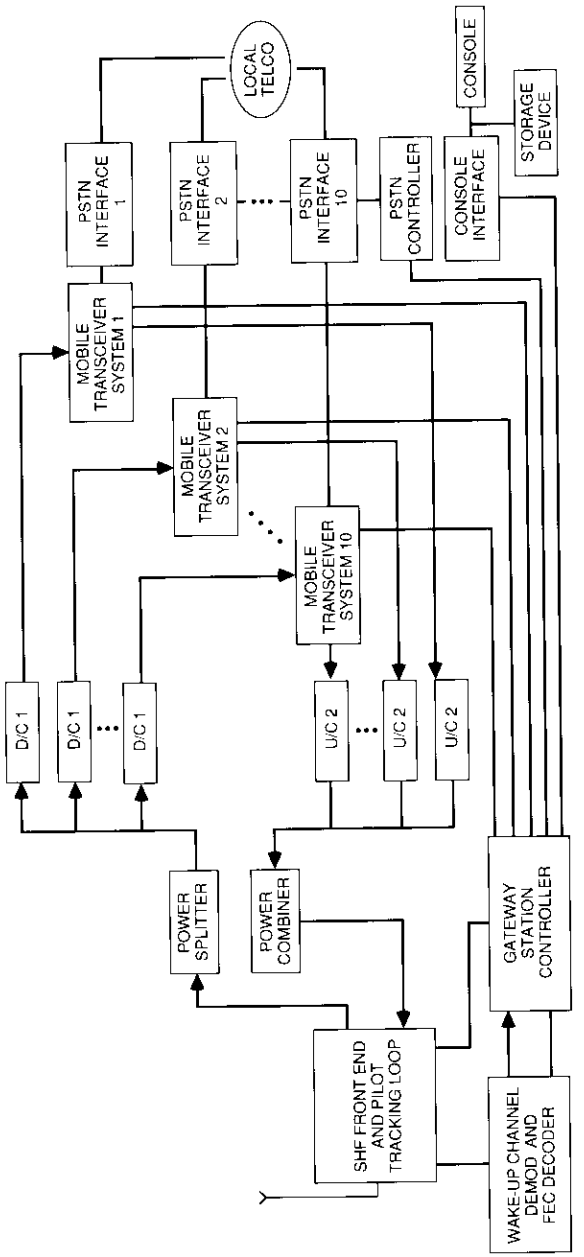

Figure 23. *MSAT-X Gateway Station Block Diagram*

three transceivers. Wake-up channel operation is receive-only. Any base station-to-NMC communications are performed by one of the three transceivers by tuning in to the backhaul channel.

The wake-up channel demodulator is identical to the mobile terminal transceiver demodulator, except that it receives continuous instead of burst-mode data. The wake-up channel FEC decoder is the 64-state, rate 1/2, hard-decision Viterbi decoder. The pilot tracking loop interface enables the controller to provide certain control signals and support functions to the loop. The controller disassembles the received data into information blocks for each transceiver via the base station transceiver interface. The same 16-bit processor used in the transceiver MCU is employed for the controller processor.

The gateway station controller design is similar to that of the base station. Enhanced capabilities are included at the gateway station, such as the control of 10 transceivers instead of three, and interaction with the PSTN controller. The wake-up channel will contain PSTN-related data in addition to the frequency offsets and sub-band assignments. Unlike the base station controller, the gateway station controller is capable of initiating a data message to the NMC by sending command blocks to the selected transceiver. All gateway station-to-NMC communications are PSTN-related. The controller also interfaces with an operator console.

The interface to the PSTN signaling controller includes the transfer of PSTN data (such as the called party number) and status messages (such as ringback, busy codes, or other error messages) between the controller and the PSTN unit. The controller acts as an intermediary for all PSTN-related communications between the NMC and the PSTN signaling interface. PSTN information transfer from the NMC to the PSTN unit is accomplished via the wake-up channel and the controller. Information transfer from the PSTN unit to the NMC is accomplished in two steps. First, information is transferred to the gateway controller. The controller then transfers it to the relevant transceiver using the first-in first-out (FIFO) interface, along with additional command blocks that instruct the addressed transceiver to forward the PSTN message blocks to the NMC on the backhaul channel.

Gateway station-PSTN interface design

The gateway may be interfaced to the PSTN in a variety of ways. The particular method used will be a function of the equipment in the local telephone company office (Telco) which is connected to the gateway. It is assumed that PSTN users attempting to contact a mobile terminal will be using a touch-tone telephone. In addition, it is assumed that four-wire (4-W) trunks connect the gateway to the Telco and that ear/mouth (E/M) supervisory

signaling is used. Since a variety of signaling interfaces are available from a number of Telco equipment manufacturers as standard modules, accommodating a deviation from the assumptions should not present any major problems.

Figure 24 is a block diagram of a gateway-to-PSTN interface. The echo canceller (EC) is a standard off-the-shelf device, and the signaling interface cards are custom designed. The signaling controller passes MSAT-X signaling to the signaling interface card (SIC), where it is converted to PSTN format, and vice versa. The signal lines from the signaling controller to the SIC are as follows:

- Mobile Terminal Offhook
- Mobile Terminal Busy
- Auth # Send
- Auth Denied
- Ringback
- Trunk Busy.

The signal links from the SIC to the signaling controller are as follows:

- Auth Request
- Dialing Information
- Trunk Status
- Trunk ID #.

The SIC serves as the interface between the trunk and the signaling controller. The line side of the card is designed to be a type-selectable, E/M interface. This kind of interface is the most flexible and cost-effective, especially in terms of network interfaces, because it can be switch-selected for type I, II, or III 4-W interfaces. These interfaces can be built out to accommodate 2-W E/M with the purchase of off-the-shelf 2- to 4-W termsets.

After the communications link has been established via the NMC, the voice frequency channel signal is processed through either the LPC or ACSB transmission paths. The echo canceller (EC 4545) at the gateway station protects the mobile terminal user from echo generated either at the gateway (if a 2-W Telco access is used), or in the PSTN where the 4- to 2-W conversion occurs (if a 4-W Telco access is used).

An LPC- or ACSB-to-modulator chain is dedicated to each of the 10 PSTN trunks, where modulator frequency selection under the guidance of the gateway controller effectively switches any MSAT-X originating call to any of the 10 PSTN trunks, or vice versa. Once a channel is connected to the PSTN, it is treated by the PSTN as a normal voice channel.

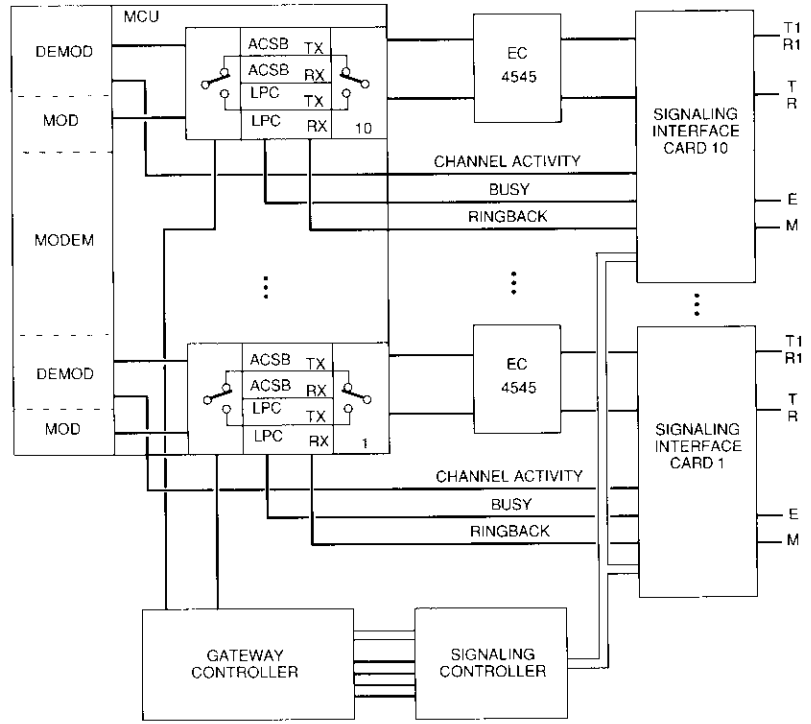

Figure 24. *Gateway-to-PSTN Interface*

To establish a call to a PSTN destination, the mobile terminal must notify the NMC of the request, the NMC must provide a satellite channel assignment to the mobile terminal and to the gateway, and the dialed party number must reach the gateway. The mobile terminal-to-NMC control packet is assumed to be sufficiently large to accommodate a 10-digit CONUS telephone number. A larger called party number field or concatenated packets would be necessary to permit international calls. It is assumed that all of the above will be completed within the MSAT-X system before the gateway is authorized to seize a PSTN trunk and dial the PSTN called party. This avoids terminating call setup attempts due to PSTN signaling timeout constraints, which can occur because of control packet collision within the MSAT-X system. A detailed call setup procedure has also been designed for mobile terminal-to-PSTN signaling [17].

To establish a call to a mobile terminal, the PSTN caller gains access to a gateway by dialing an MSAT-X gateway telephone number. This number is the homing number of a 10-trunk hunt group, and the first idle channel of the sequential hunt group is seized. A new dial tone or a prerecorded message is returned to the PSTN caller, who then enters the mobile terminal number. A voice message instructs the PSTN user to dial an MSAT-X user authorization code, which is necessary for billing purposes. After the code is verified by the gateway controller, the NMC searches its records to ascertain if the called mobile terminal is "logged on" or if it is "logged on and busy." If it is not logged on, the PSTN caller may leave a message in order to avoid repeated call attempts for which the caller will be billed by the Telco. Since the called mobile terminal number has already been forwarded to the NMC, the PSTN caller will be asked to dial a special code (*e.g.*, ##), followed by the number where he or she may be reached. This information is passed to the NMC, where it is time- and date-tagged and stored. When the mobile terminal logs on, the message is forwarded and NMC memory is cleared. The same procedure could be used if the called mobile terminal were busy. If the called mobile terminal is available, the NMC connects the mobile terminal to the calling gateway trunk.

The NMC must keep a log of all calls to the PSTN. The log includes mobile terminal number, called party number, date, time, trunk number, and call duration. The Telco will bill the MSAT-X system for all toll calls placed through the gateway, and this information must be correlated with NMC records to determine the proper charges for each long-distance PSTN call.

For MSAT-X system charges to reach the PSTN caller, an access number is used to identify an account. Based on information stored in the NMC, a separate bill for the MSAT-X system connect time can then be generated and sent to the calling party.

Functional specifications

Detailed functional specifications were generated for mobile terminals, base stations, and gateway stations. The performance specifications for the transceiver were also generated for each module, including RF/IF, MCU, power supply, digital modem, ACSB modem, FEC codec, LPC vocoder, and user interface. Tables 3 and 4 summarize the basic RF/IF and baseband module specifications for the transceiver.

The basic RF parameters for the base station and gateway station specifications are listed in Table 5. The transceiver specifications for the fixed terminals are essentially the same as for the mobile terminals, with minor modifications.

TABLE 3. BASIC RF/IF SPECIFICATIONS FOR THE MOBILE TRANSCEIVER

Received Frequency Band	866–870 MHz
Transmit Frequency Band	821–825 MHz
Receiver G/T	≥ -16.1 dB/K
LNA Noise Figure	≤ 0.8 dB
Receive Circuit Loss	≤ 1.5 dB
Standard-HPA Saturated Power	≥ 7.5 W
ACSB-HPA $P_{1\ dB}$ Compression Power	≥ 25 W
Transmit Circuit Loss	<0.7 dB
Channel Bandwidth	5 kHz

TABLE 4. KEY BASEBAND MODULE SPECIFICATIONS FOR THE TRANSCEIVER

MCU CPU	16-bit processor
Clock Speed	>10 MHz
CRC Generator/Checker	16-bit CRC polynomial (CCITT X.25)
Modulation Format	Binary FM, $h = 0.5$
Modulation Type	Burst mode
Channel Data Rate	2,756 bit/s
Unique-Word Length	32 bits
Design Point E_b/N_o	12.0 dB
Demodulator	Limiter-discriminator
Output Format	Hard-decision TTL data
FEC Code	
• Control Packets	Rate 1/2 convolutional code
• Data Packets	Rate 3/4 punctured convolutional code derived from the rate 1/2 code
Number of States	64
Decoder Type	A single, hard-decision, variable-rate Viterbi for data and control packets. Rate 1/2: 1.2 dB; rate 3/4: 0.4 dB at BER = 10^{-3} over an AWGN channel w. binary FM
Interleaver	12 row × 57 column block interleaver
ARQ Type	NOS Selective repeat (Weldon, $r = 2$)
Voiceband Signal Bandwidth	3.4 kHz
Minimum DRT Scores (%)	
• Benign Condition	91.7
• Truck Noise at 18-dB S/N	86.8
Minimum DAM Scores (%)	
• Benign Condition	46.6
• Truck Noise at 18-dB S/N	42.6
• At BER = 10^{-3}	45.5
• With Fades	40.9
Maximum Processing Delay With LPC Analyzer and Synthesizer Back-to-Back	130 ms
LPC Transmission Bit Rate	2,756 bit/s

TABLE 5. BASIC RF PARAMETERS FOR BASE STATION AND GATEWAY STATION SPECIFICATIONS

Up-Link Frequency	14 GHz
Down-Link Frequency	12 GHz
Polarization	Linear
Antenna Diameter	3 m
Antenna Gain (not including losses)	
• At 14 GHz	50.2 dBi
• At 12 GHz	48.8 dBi
HPA Saturated Output Power	
• Base Station (34 W)	15.3 dBW
• Gateway Station (158 W)	22.0 dBW
Transmit Circuit Loss, HPA-to-Antenna Flange	1.0 dB
Polarization Loss	0.2 dB
e.i.r.p. (total single-carrier saturated power without pointing loss) at 14 GHz	
• Base Station	64.3 dBW
• Gateway Station	71.0 dBW
LNA Noise Temperature (200 K, noise figure = 2.3 dB)	23.0 dBK
Polarization Loss	0.2 dB
Receive Circuit Loss	0.75 dB
Receive Effective System Noise Temperature T_{ANT} = 44 K at 20° elevation angle (T_s = 341 K)	25.3 dBK
Receive G/T (without pointing loss) at 12 GHz	23.3 dBi/K

Conclusions

This study has highlighted several significant factors in the design of the mobile transceiver, base station, and gateway station for the proposed MSAT-X system. It was found that frequency error due to Doppler and frequency translations can be held to an acceptable level by using an out-of-band frequency error control method. The maximum residual error can be kept within 200 Hz for fixed terminal reception of mobile terminal transmissions, assuming a 65-mph vehicle speed. Also, the DOD LPC-10 algorithm can be modified to minimize the degradation to 2,400-bit/s LPC vocoder performance caused by acoustically coupled noise in the vehicle environment, as well as by channel distortions and multipath fades. Eight critical bits in the vocoder speech can be protected by a rate 1/2 shortened (16,8) QR code to reduce vocoder sensitivity to channel errors, particularly during fades. As a result, the channel bit rate is increased from 2,400 to 2,756 bit/s.

Binary FM at 2,756 bit/s with LD detection has been shown to be the most robust modulation technique among all candidate systems considered for the MSAT-X channel. Binary FM not only permits the use of a short preamble (72 bit/s), but also is insensitive to frequency errors due to Doppler and is robust against ACI. Moreover, it can be implemented at low cost.

Error control employing both FEC coding and ARQ is necessary for sending both short (128-bit) and long (512-bit) packets. Punctured convolutional codes of rate 1/2 and 3/4, which can easily be implemented as a single codec with a 64-state Viterbi algorithm processor, are effective for achieving a throughput of 0.5 and 0.7 for short and long packets, respectively.

Cost-effective implementation of ACSB can be achieved with DSP chips, although further work appears to be required. The transceiver can be implemented with a modular architecture, both in hardware and software, and with flexible interfaces between modules. The same transceiver can be employed at both the base and gateway stations with only minor modifications.

Finally, it was determined that off-the-shelf K_u-band RF/IF systems with a 3-m-diameter antenna and a G/T of 23.3 dB/K at 12 GHz can be used at both gateway stations and base stations. In addition, PSTN interfaces can be developed at the gateway stations.

Acknowledgments

This paper is based on work performed at COMSAT Laboratories under NASA/Jet Propulsion Laboratory Contract 957113 entitled, "Design of an MSAT-X Mobile Transceiver and Related Ground Segment Technology," and monitored by R. Winkelstein. Contributions by K. Karimullah, W. Sandrin, M. Onufry, and S. Rhodes are deeply appreciated.

References

[1] F. Naderi, W. J. Weber, and G. H. Knouse, "NASA's Mobile Satellite Communications Program: Ground and Space Segment Technologies," 35th International Astronautical Federation Congress, Lausanne, Switzerland, October 1984, IAF Paper No. 84-84.

[2] D. J. Bell and S. A. Townes, "MSAT-X System Definition and Functional Requirements, Exhibit 1," Revision 2, prepared for NASA by JPL, Pasadena, California, January 10, 1985.

[3] Cubic Corporation, "Mobile Antenna and Beam Pointing Studies for Satellite Mobile Communications," Final Report, Submitted to JPL under Contract No. 956691, February 6, 1985.

[4] Ball Aerospace Systems Division, "Land Vehicle Antennas for Satellite Mobile Communications," Final Report to JPL, F85-02, February 1985.

[5] Signatron, Inc., "MSAT-X Networking System Study," Final Report, Vols. 1 and 2, Submitted to JPL under Contract No. 957173, June 8 and November 15, 1985.

[6] Ford Aerospace and Communications Corporation, "Spacecraft Configuration Study for the Second Generation Mobile Satellite System," MSAT-X Reports Nos. 113 and 114, prepared for JPL, January and June 1985.

[7] C. Stevenson, "An Improved Modulation Format and Signal Processing Scheme for ACSB Systems," 34th IEEE Vehicular Technology Conference, Pittsburgh, Pennsylvania, May 1984.

[8] V. Li and T-Y. Yan, "An Integrated Voice and Data Multiple Access Scheme for a Land Mobile Satellite System," *Proc. IEEE*, Special Issue on Satellite Network Communications, Vol. 72, No. 11, November 1984, pp. 1611–1619.

[9] T-Y. Yan and V. Li, "Adaptive Mobile Access Protocol (AMAP) for the Message Service of a Land Mobile Satellite Experiment (MSAT-X)," *IEEE Journal on Selected Areas in Communications*, Special Issue on Mobile Radio Communications, Vol. SAC-2, No. 4, July 1984, pp. 621–627.

[10] W. J. Vogel, "Land Mobile Satellite Transmission Measurements at 869 MHz," MSAT-X Technical Report No. 106, submitted to JPL by the University of Texas, Austin, April 12, 1985.

[11] F. Davarian and J. Sumida, "Hardware Simulator Assists Mobile Satellite Experiment," 35th Vehicular Technology Conference, Boulder, Colorado, May 1985.

[12] M. K. Simon and C. C. Wang, "Differential Detection of Gaussian MSK in a Mobile Radio Environment," *IEEE Transactions on Vehicular Technology*, Vol. VT-33, No. 4, November 1984, pp. 307–320.

[13] M. K. Simon and C. C. Wang, "Two Bit Differential Detection of MSK," IEEE Global Telecommunications Conference (Globecom '84), Atlanta, Georgia, November 1984, *Conference Record*, pp. 22.3.1–22.3.6.

[14] M. K. Simon and C. C. Wang, "Differential Versus Limiter-Discriminator Detection of Narrowband FM," *IEEE Transactions on Communications*, Vol. COM-31, No. 11, November 1983, pp. 1227–1234.

[15] L. R. Rabiner and R. W. Schafer, *Digital Processing of Speech Signals*, Englewood Cliffs, New Jersey: Prentice-Hall, 1978.

[16] J. D. Markel and A. H. Gray, Jr., *Linear Prediction of Speech*, New York: Springer-Verlag, 1982.

[17] COMSAT Laboratories, "Design of an MSAT-X Mobile Transceiver and Related Ground Segment Technology," Vols. 1–5, Final Report submitted to NASA/JPL under Contract No. 957113, February 1986.

[18] T. E. Tremain, "The Government Standard Linear Predictive Coding Algorithm LPC-10," *Speech Technology*, Vol. 1, No. 2, April 1982, pp. 40–49.

[19] E. J. Weldon, Jr., "An Improved Selective-Repeat ARQ Strategy," *IEEE Transactions on Communications*, Vol. COM-30, 3, March 1982, pp. 480–486.

[20] Y. Yasuda, K. Kashiki, and Y. Hirata, "High Rate Punctured Convolutional Codes for Soft Decision Decoding," *IEEE Transactions on Communications*, Vol. COM-32, No. 3, March 1984, pp. 315–319.

[21] A. J. Viterbi, "Error Bounds for Convolutional Codes and an Asymptotically Optimum Decoding Algorithm," *IEEE Transactions on Information Theory*, Vol. IT-13, April 1967, pp. 260–269.

[22] A. J. Viterbi, "Convolutional Codes and Their Performance in Communication Systems," *IEEE Transactions on Communication Technology*, Vol. COM-19, No. 5, October 1971, pp. 751–772.

[23] J. A. Heller and I. W. Jacobs, "Viterbi Decoding for Satellite and Space Communications," *IEEE Transactions on Communication Technology*, Vol. COM-19, No. 5, October 1971, pp. 835–848.

Russell J. F. Fang received a B.S.E.E. from National Taiwan University, Taipei, China, in 1962, and an M.S.E.E. and Ph.D. from Stanford University in 1964 and 1968, respectively. From 1964 to 1966, he was a Research Engineer at Stanford Research Institute. Since joining COMSAT Laboratories in 1968, Dr. Fang has been a Member of the Technical Staff, Staff Scientist, Department Manager, and Associate Director, and is currently Executive Director of the Communications Techniques Division. He has authored or co-authored more than 30 papers in professional journals, as well as numerous conference papers. He is a Fellow of IEEE.

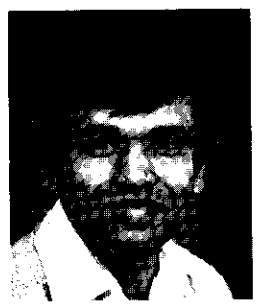

Udaya Bhaskar received a Ph.D. in electrical engineering from Rensselaer Polytechnic Institute in 1985. Since then, he has been a Member of the Technical Staff in the Communications Techniques Division at COMSAT Laboratories. His work has focused on the conceptual development and hardware implementation of speech coders at 16, 2.4, and 4.8 kbit/s. His primary research interests are in digital signal modeling and processing, low- and medium-bit-rate speech coding, and adaptive and recursive parameter estimation algorithms. He is a member of IEEE.

Farhad Hemmati received an M.S.E.E. and Ph.D. from Illinois Institute of Technology in 1973 and 1977, respectively. Since joining COMSAT Laboratories in 1982 he has worked on coding techniques and various signal processing methods for satellite channels. He is currently a Staff Scientist in the Communications Research Department, where his primary research interests are coding, spread spectrum, and multiple access.

Kenneth M. Mackenthun received a B.S.E.E. from George Washington University in 1974 and an M.S.E.E. and Ph.D. from the University of Illinois in 1976 and 1977, respectively. Since 1980, he has held the positions of Member of the Technical Staff and Scientist in the Communications Techniques Division at COMSAT Laboratories. His current interests are in modulation, synchronization, and coding, particularly for mobile terminal applications.

Ajit Shenoy received a B.Tech. in electronics in the First Class, with Distinction, from the Indian Institute of Technology, Madras, India, in 1979, and an M.S.E.E. from the Stevens Institute of Technology in 1981. He completed an additional year of graduate study in telecommunications and digital systems before joining COMSAT Laboratories in June 1982. He is currently Associate Manager of the Image Processing and Digital Techniques Department, where his work involves the design and implementation of microprocessor-based communications hardware using digital signal processing techniques. Prior to joining COMSAT, he worked on electronic motor speed control at Philips India, Ltd., and was a consultant for Synfax Manufacturing, Inc., Belleville, N.J., where he designed instrumentation systems for quality control. Mr. Shenoy is a recipient of several awards and scholarships from the Government of India. He is a member of the IEEE Communications and Computer Societies.

CTR Note

An all-pole approximation for the reciprocal sin (x)/(x) frequency response

J. J. POKLEMBA

(Manuscript received November 16, 1987)

Introduction

An improved all-pole filtering function has been derived that approximates the $x/\sin(x)$ frequency response, which is widely used in data transmission applications. For efficiently modulated bandwidth occupancies of 1.5 times the symbol rate or less, this all-pole approximation exhibits bit error rate (BER) performance which is indistinguishable in practice from the best solutions that have been developed previously and is easier to implement. In particular, the new all-pole magnitude approximation results in a BER degradation of less than 0.05 dB. This degradation can be rendered negligible by including a second-order group delay equalizer section, which also reduces the degradation incurred with wider spectral occupancies to less than 0.1 dB.

Background

Nyquist [1] has shown that digital data can be transmitted in a double-sided half-amplitude bandwidth, $B = R$, without intersymbol interference (ISI), where $R = 1/T$ is the symbol rate in symbols per second. Furthermore, Nyquist defined a set of constraints on the real and imaginary parts of the overall channel transfer function that enables distortionless transmission. These well-known constraints are described in detail in Reference 2. In 1965, Gibby and Smith [3] published a more general exposition on the conditions for distortionless data transmission, and in 1969 a simpler formulation of their results was derived by de Hoe and Van der Wurf [4], based on a sampled system response.

John J. Poklemba is Associate Manager of the Transmission Processing Department at COMSAT Laboratories.

Substantial analysis and simulation results are available that describe the performance of Nyquist filters, particularly the commonly used raised cosine frequency responses. Pole-zero approximations for the raised cosine family have also been obtained, since ideal band-limited Nyquist frequency responses are not physically realizable [5]. The key element of the Nyquist approach involves controlling the impulse response of the channel, so that it exhibits equally spaced zero crossings at time instants that are exactly one symbol apart. Thus, adjacent data symbols do not interfere with one another at their detection sampling points.

Most of the previous work is predicated on driving Nyquist channels with impulses; whereas in practice the source data format is typically a bipolar non-return to zero (NRZ) pulse, which is one symbol long. It is well known that the frequency response which transforms an impulse to a pulse of width $T = 1/R$ is

$$\text{sinc}\,(f/R) \triangleq \frac{\sin(\pi f/R)}{(\pi f/R)} \quad . \tag{1}$$

Hence, making a pulsed source compatible with the conventional Nyquist filter definition requires a whitening filter with a frequency response of sinc ^{2}, as plotted in Figure 1. Because abrupt 180° phase reversals occur at integer multiples of f/R, the group delay is theoretically impulsive. However, when this response is approximated in practice and cascaded with a Nyquist data filter, negligible energy exists at integer multiples of f/R.

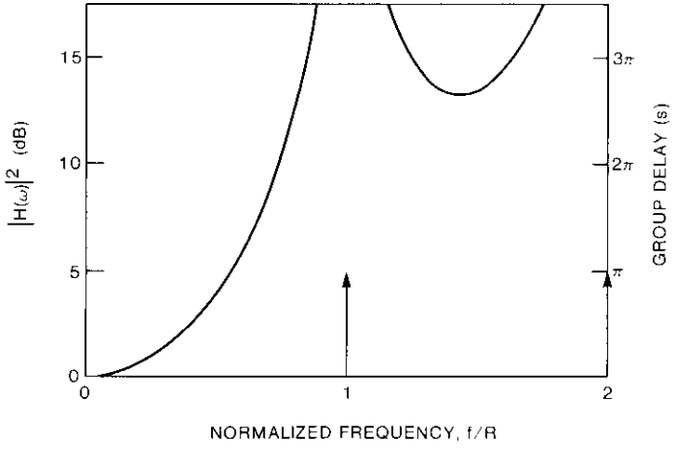

Figure 1. *Sinc ^{2} Magnitude and Group Delay*

Realizable network approximations for the reciprocal sinc frequency response have been obtained [6]. The solutions were quantified according to the number of poles and zeros used in the approximation. There were three candidate cases: a real pole and zero (with dominant zero), a complex pole pair, and a complex pole and zero pair. These were categorized as first-, second-, and fourth-order approximations, respectively. The order of the solution corresponded to the number of terms in a power series expansion for the sinc function, to which the networks could be equated.

The best overall performance was achieved with the highest order solution attempted, which was the complex pole/zero combination. The dominant contributor to the peaking required in the sinc ^{2} magnitude response for this solution was the underdamped pole. However, since complex zeros are generally more difficult to implement, particularly with active structures, this study concentrates on approximating the sinc function by all-pole solutions. It was found that a third-order power series solution does not exist, and thus the primary focus of this study is on the fourth-order all-pole solution. The performance of this solution will only be compared with the previous complex pole and complex pole/zero approximations, as the first-order solution did not yield satisfactory performance.

Problem formulation

The solution is approached as follows. Both the sinc function and the candidate network transfer function are expanded in a power series, as in Reference 6, and like terms are equated. The frequency response for the sinc function can be represented in a power series as

$$\frac{1}{|H(\omega)|^2} \triangleq \frac{\sin^2(\omega/2R)}{(\omega/2R)^2} = \frac{[1 - \cos(\omega/R)]}{2(\omega/2R)^2}$$

$$= \frac{1 - |1 - (\omega R)^2/2! + (\omega R)^4/4! - (\omega R)^6/6! + \ldots|}{1/2(\omega/R)^2}$$

$$= 1 - \frac{2}{4!}(\omega/R)^2 + \frac{2}{6!}(\omega/R)^4 - \frac{2}{8!}(\omega/R)^6 + \frac{2}{10!}(\omega/R)^8 \ldots \tag{2}$$

FOUR-POLE MAGNITUDE APPROXIMATION

A fourth-order all-pole transfer function comprising two complex pole pairs can be written as

$$H(s) = \frac{1}{[1 + s(2\xi_1\tau_1) + s^2(\tau_1^2)][1 + s(2\xi_2\tau_2) + s^2(\tau_2^2)]} \quad . \tag{3}$$

Substituting $s = j\omega$ in equation (3) and taking the magnitude squared of its reciprocal gives

$$|H(\omega)|^{-2} = \{1 + \omega^2[2\tau_1^2(2\xi_1^2 - 1)] + \omega^4(\tau_1^4)\} \cdot \{1 + \omega^2[2\tau_2^2(2\xi_2^2 - 1)] + \omega^4(\tau_2^4)\} \quad . \tag{4}$$

For algebraic convenience, the filter parameters of equation (4) will be redefined as

$$\begin{aligned} |H(\omega)|^{-2} &= [1 + \omega^2(c_1) + \omega^4(d_1^2)][1 + \omega^2(c_2) + \omega^4(d_2^2)] \\ &= 1 + \omega^2(c_1 + c_2) + \omega^4(c_1c_2 + d_1^2 + d_2^2) \\ &\quad + \omega^6(c_1d_2^2 + c_2d_1^2) + \omega^8(d_1^2d_2^2) \quad . \end{aligned} \tag{5}$$

Equating the fourth-order transfer function of equation (5) with the first four terms in the power series expansion for the sinc function in equation (2) yields the following four nonlinear simultaneous equations, the solutions of which characterize the filter approximation parameters:

$$c_1 + c_2 = -2/(4!R^2) \tag{6a}$$

$$c_1c_2 + d_1^2 + d_2^2 = 2/(6!R^4) \tag{6b}$$

$$c_1d_2^2 + c_2d_1^2 = -2/(8!R^6) \tag{6c}$$

$$d_1^2d_2^2 = 2/(10!R^8) \quad . \tag{6d}$$

These equations are not interactive, and the solution cannot be obtained by simple algebraic manipulation as was the case in Reference 6. Consequently, a computer program was written that employs the International Mathematical and Statistical Libraries' (IMSL) subroutine ZSCNT, which uses the secant method for finding the roots of a set of nonlinear simultaneous equations [7]. This resulted in the following values:

$$c_1 = -0.0673161/R^2 \tag{7a}$$

$$c_2 = -0.0160173/R^2 \tag{7b}$$

$$d_1^2 = 0.00126327/R^4 \tag{7c}$$

$$d_2^2 = 0.000436285/R^4 \tag{7d}$$

which lead to

$$\xi_1 = \sqrt{\frac{1}{2}\left(1 + \frac{c_1}{2d_1}\right)} = 0.162819 \tag{8a}$$

$$\xi_2 = \sqrt{\frac{1}{2}\left(1 + \frac{c_2}{2d_2}\right)} = 0.555239 \tag{8b}$$

$$\tau_1 = \sqrt[4]{d_1^2} = 0.188527/R \tag{8c}$$

$$\tau_2 = \sqrt[4]{d_2^2} = 0.144525/R \tag{8d}$$

The corresponding complex pole pair locations from equations (8a) through (8d) are given by

$$\frac{\xi_1}{2\pi\tau_1}\left(1 \pm j\sqrt{1/\xi_1^2 - 1}\right) = (0.137452 \pm j0.832936)R, \text{ Hz} \tag{9a}$$

$$\frac{\xi_2}{2\pi\tau_2}\left(1 \pm j\sqrt{1/\xi_2^2 - 1}\right) = (0.611445 \pm j0.915882)R, \text{ Hz} \quad . \tag{9b}$$

Hence the solution consists of two underdamped complex poles with natural frequencies of $1/2\pi\tau_1$ and $1/2\pi\tau_2$ lying just above and below the symbol rate, R.

THREE-POLE MAGNITUDE APPROXIMATION

As in the four-pole case, the solutions from the ZSCNT program for the three-pole magnitude approximation are

$$c_1 = -0.0367810 \tag{10a}$$

$$d_1 = 0.0326425 \tag{10b}$$

$$d_2 = -0.0465523 \tag{10c}$$

leading to

$$\xi_1 = \sqrt{\frac{1}{2}\left(1 + \frac{c_1}{2d_1}\right)} \tag{11a}$$

$$\tau_1 = \sqrt[4]{d_1^2} \tag{11b}$$

$$\tau_2 = \sqrt{d_2} \quad . \tag{11c}$$

However, a brief inspection of equations (10c) and (11c) reveals that τ_2 must be imaginary. Consequently, the three-pole approximation is not realizable for the power series formulation approach.

Performance comparison

The all-pole, fourth-order, magnitude-squared reciprocal sinc approximation derived here will now be compared with the previous two effective solutions from Reference 6: the second-order complex pole solution and the fourth-order complex pole-zero solution, with and without group delay equalization.

MAGNITUDE RESPONSE

The three magnitude-squared frequency responses are plotted in Figure 2. The best fit is obtained with the complex pole-zero approximation, which follows the sinc curve very closely out to a frequency of about $0.75R$, and exhibits over 14 dB of peaking. However, the four-pole approximation shows almost as good a fit, with a frequency-matching range of $0.70R$ and more than 10 dB of peaking. If the BER results for these two cases are comparable, as would be expected, the four-pole solution would be preferred because of the greater difficulty in implementing complex zeros. The two-pole approximation is considerably poorer than the fourth-order solutions in terms of both peaking and matching range.

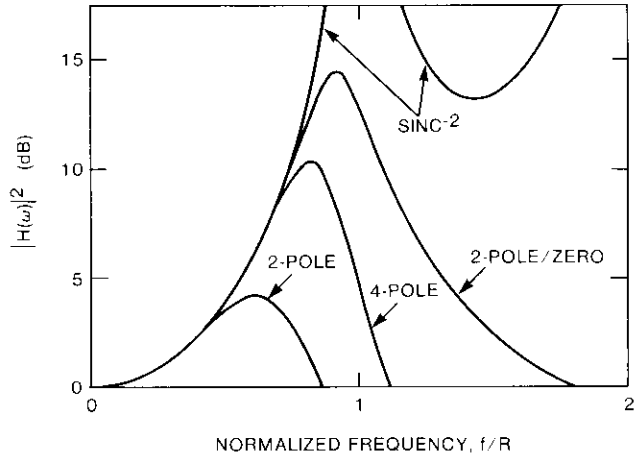

Figure 2. *Sinc^{-2} Magnitude Approximations*

GROUP DELAY EQUALIZATION

Group delay equalization of the sinc magnitude approximation networks was accommodated by using the computer program GRDLOP, which is documented in Reference 5. A second-order group delay network was found to be the most efficient equalizer structure for each of the three candidate sinc approximations. Moreover, the previous sinc solutions have been re-equalized along with the current four-pole solution, because of the recent discovery [5] that the delay need only be compensated out to a bandwidth of $0.6R$ for satisfactory performance. Concentrating the delay equalization over this narrower bandwidth typically results in better overall compensation and improved BER performance.

The raw or unequalized group delay responses for the three approximations are plotted in Figure 3, and their equalized counterparts are illustrated in Figure 4. The raw group delay for the two-pole/zero and four-pole approximations in Figure 3 has about the same overall peak-to-peak variation (about 1.3 s when $R = 1$ symbol/s). The equalization bandwidth from DC out to $0.6R$ is evident in the delay-compensated responses of Figure 4. Although large delay variations occur in the vicinity of $0.85R$ for the delay-equalized two-pole/zero and four-pole solutions, there is insufficient signal energy present at these frequencies to affect the BER. This latter point is validated below.

Table 1 compiles the results for the three candidate approximation networks. It presents the magnitude response poles and zeros, the mirror-image roots

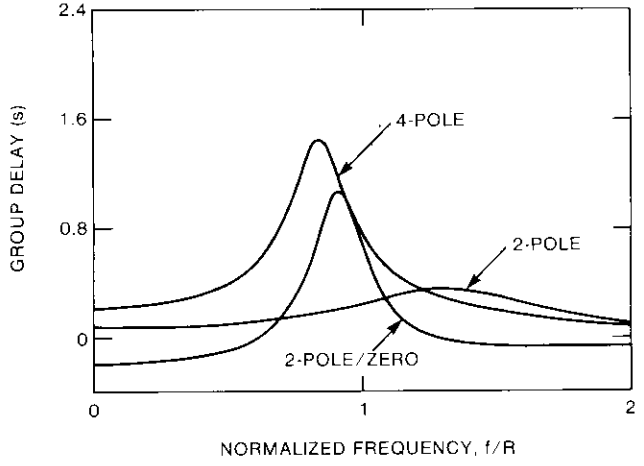

Figure 3. *Unequalized Group Delay*

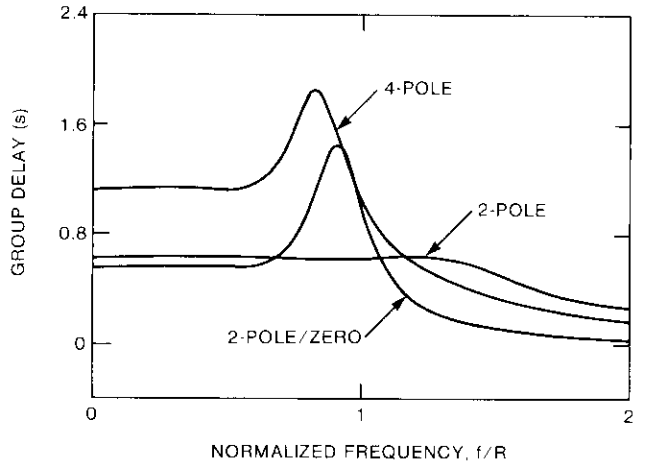

Figure 4. *Equalized Group Delay*

for the second-order group delay networks, and their corresponding degradations in BER at 10^{-3} and 10^{-7} for quadrature phase-shift keying (QPSK) data transmission, with and without delay equalization. The BERs were obtained through computer simulation by cascading each approximation with an ideal raised cosine data filter. The communications channel simulation program has been described by Palmer and Lebowitz [8]. Three rolloff rates were tested: r = 10, 50, and 100 percent.

In viewing the table, it should be recalled that most data transmission systems operate with spectral rolloff rates in the neighborhood of 40 to 50 percent. The two-pole/zero and four-pole solutions exhibit negligible degradation for 10- through 50-percent rolloffs, with an implementation requirement of only two complex root pairs (one complex pole and zero, or two complex poles). Also, adding group delay equalization to the two-pole/zero and four-pole approximations provides excellent performance for softer spectral shaping applications (60 through 100 percent), at the expense of a three-complex-root-pair implementation. If 0.1- to 0.2-dB degradation is acceptable, the unequalized two-pole approximation yields a low-implementation-complexity solution of only one complex pole pair; while with delay equalization, the two-pole approximation shows negligible degradation for rolloff rates from 10 to 50 percent at an implementation cost of three complex root pairs (one complex zero and two complex poles).

For comparison, Figures 5 through 7 show the eye diagrams for the three candidate approximation networks for rolloff rates of 10, 50, and 100 percent, respectively. In each figure, the two-pole, two-pole/zero, and four-pole

TABLE 1. COMPARISON OF SINC^{-1} APPROXIMATION NETWORKS (R = 1 symbol/s)

SOLUTIONS	MAGNITUDE APPROXIMATION (Hz)		GROUP DELAY*	$\Delta E_b/N_o$			$\Delta E_b/N_o$		
	ZEROS	POLES	ROOTS (Hz)	r	10^{-3}	10^{-7}	r	10^{-3}	10^{-7}
Two-Pole		−0.22435 ± *j*0.65596	±0.41154 ± *j*0.26016	10	0.08	0.19	10	0.01	0.02
				50	0.13	0.21	50	0.03	0.06
				100	0.56	0.85	100	0.15	0.21
Complex Pole/Zero	−1.18831 ± *j*0.40058	−0.12784 ± *j*0.90983	±0.63906 ± *j*0.36541	10	0.01	0.01	10	0.00	0.00
				50	0.01	0.01	50	0.00	0.00
				100	0.15	0.22	100	0.02	0.03
Four-Pole		−0.13745 ± *j*0.83294	±0.50707 ± *j*0.30984	10	0.02	0.04	10	0.00	0.00
		−0.61145 ± *j*0.91588		50	0.03	0.04	50	0.00	0.00
				100	0.38	0.64	100	0.05	0.07

* Group delay equalization bandwidth was 0.6R.

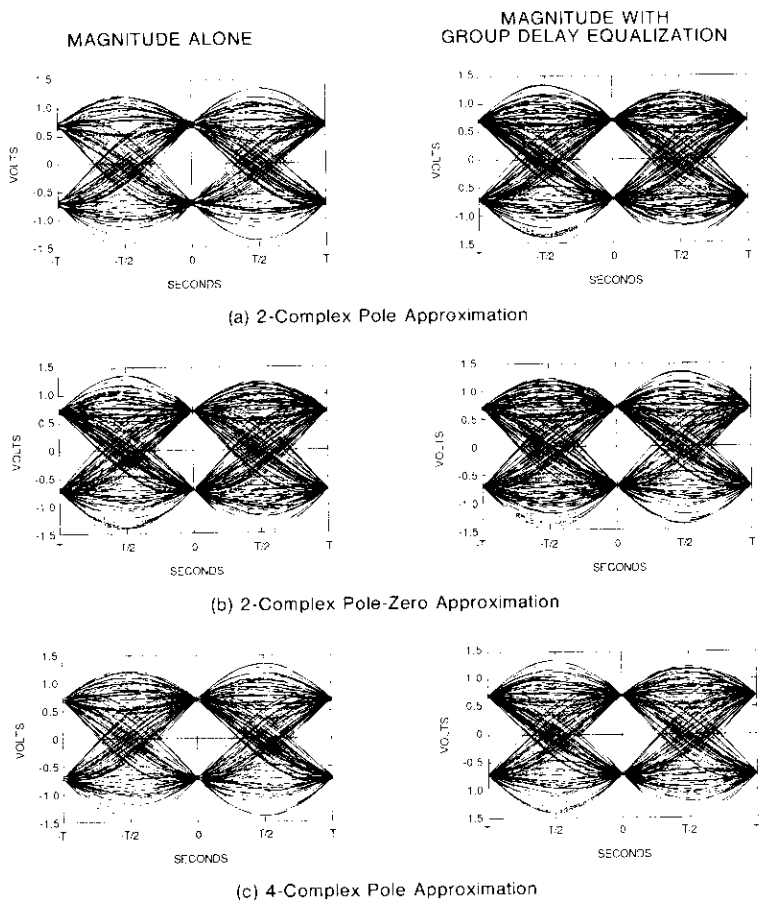

Figure 5. *Eye Patterns With 10-Percent Raised Cosine Filtering*

solutions are depicted from top to bottom. The eyes on the left side do not have group delay equalization, while those on the right side have been equalized.

Conclusions

A four-pole approximation for the reciprocal sinc frequency response has been derived which yields a BER performance in a Nyquist-filtered data channel that is equivalent to the best approximation previously found–a complex pole and complex zero pair. Since complex zeros are typically more

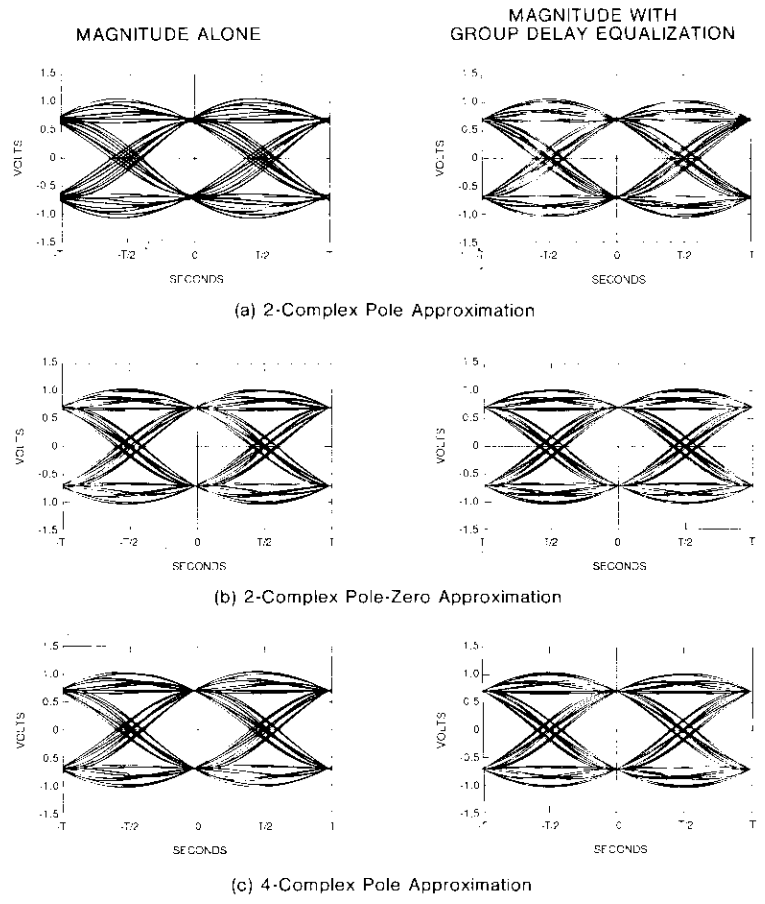

Figure 6. *Eye Patterns With 50-Percent Raised Cosine Filtering*

difficult to implement than complex poles, the four-pole approximation is the preferred solution. The QPSK BER performance for the four-pole sinc^2 power series approximation was compared with two previous solutions: a fourth-order power series complex pole-zero solution and a second-order complex pole solution. The BER performance was computer-simulated by cascading the sinc^{-2} approximations with ideal raised cosine data filters with rolloff rates of 10, 50, and 100 percent.

An additional benefit of sinc compensation is that it facilitates transmission at the Nyquist rate (double-sided $BT = 1.0$). The BER results show that for

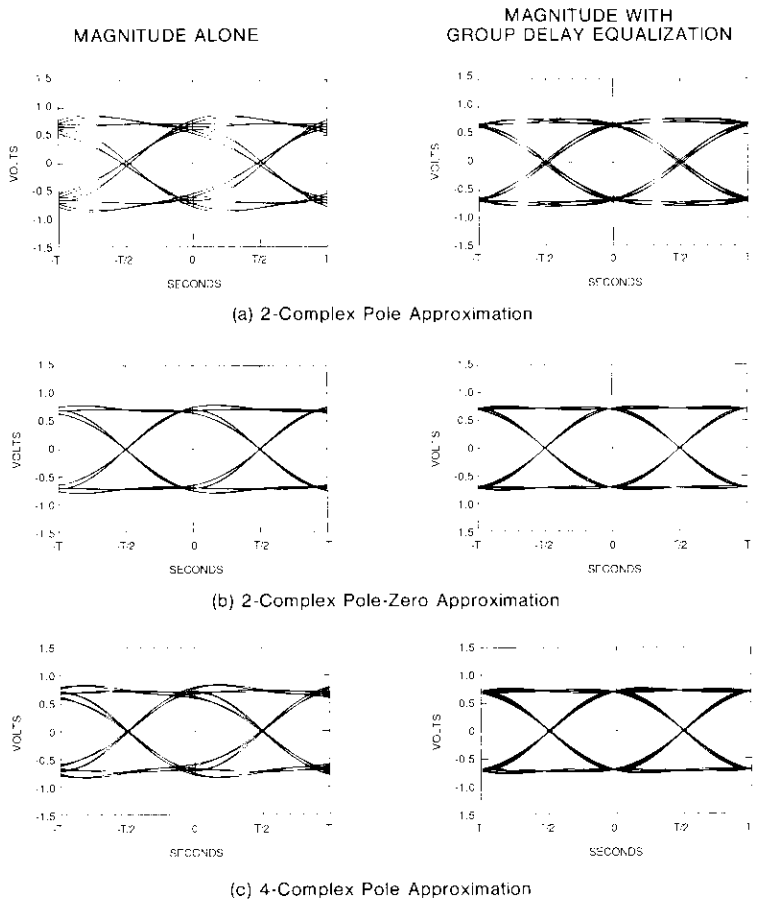

Figure 7. *Eye Patterns With 100-Percent Raised Cosine Filtering*

a practical range of spectral rolloff rates (10 through 50 percent), the unequalized two-pole/zero and four-pole approximations are virtually equivalent in performance, and both achieve BER degradations of less than 0.05 dB. The easy-to-implement unequalized two-pole solution could be used if 0.1- to 0.2-dB degradation were tolerable. With softer 60- through 100-percent spectral shaping, the two-pole/zero and four-pole group delay equalized solutions again perform equivalently and yield BER degradations of less than 0.1 dB.

Acknowledgment

The author would like to thank H. Suyderhoud for his helpful suggestions on organizing this material.

References

[1] H. Nyquist, "Certain Topics in Telegraph Transmission Theory," *AIEE Transactions*, Vol. 47, April 1928, pp. 617–644.

[2] W. A. Bennett and J. R. Davey, *Data Transmission*, New York: McGraw-Hill, 1965.

[3] R. A. Gibby and J. W. Smith, "Some Extensions of Nyquist's Telegraph Transmission Theory," *Bell System Technical Journal*, Vol. 44, September 1965, pp. 1487–1510.

[4] R. de Hoe and P. Van der Wurf, "On Some Extensions of Nyquist's Telegraph Transmission Theory," *Proc. IEEE*, Vol. 57, No. 4, April 1969, pp. 701–702.

[5] J. J. Poklemba, "Pole-Zero Approximations for the Raised Cosine Filter Family," *COMSAT Technical Review*, Vol. 17, No. 1, Spring 1987, pp. 127–157.

[6] J. J. Poklemba, "An Approximation Technique for Realizing the Reciprocal sin $(x)/(x)$ Frequency Response," *COMSAT Technical Review*, Vol. 12, No. 1, Spring 1982, pp. 121–156.

[7] *IMSL Reference Manual*, Vol. 4, 9th ed., International Mathematical and Statistical Libraries, Houston, Texas, 1982.

[8] L. C. Palmer and S. Lebowitz, "Including Synchronization in Time-Domain Channel Simulations," *COMSAT Technical Review*, Vol. 7, No. 2, Fall 1977, pp. 475–526.

Translations of Abstracts

Codage en bloc différentiel cohérent de la correction d'erreurs sans voie de retour (FEC)

S. A. RHODES

Sommaire

Les principes sous-tendant les télécommunications différentielles cohérentes sur une base de symbole par symbole sont appliqués aux codes en bloc (ou "codes complets"). Les mises en phase relatives des diagrammes de code à l'intérieur de chaque bloc et les phases de porteuses relatives des blocs successifs sont utilisées pour produire la modulation par déplacement de phase binaire (MDPB) combinée avec le codage en bloc en vue de la correction d'erreur sans voie de retour (codage FEC). Ce codage en bloc différentiel cohérent (CBDC) peut engendrer un gain de codage important en comparaison de la MDPB non codée avec détection différentielle cohérente (DC-MDPB).

Le CBDC revêt une importance particulière dans le cas des télécommunications numériques où la dynamique de voie engendrée par le bruit de phase de l'oscillateur et de l'effet Doppler risquent d'empêcher une détection cohérente fiable. S'agissant d'une voie statique dégradée par du bruit gaussien additionnel, on a démontré que le CBDC donne de meilleurs résultats que la DC-MDPB avec d'autres codages FEC de complexité similaire. Un code en bloc de longueur $N = 16$ symboles MDPB pour le CBCD permet d'obtenir un gain de codage de 3,9 dB par rapport à la DC-MDPB non codée avec une possibilité d'erreur sur les bits de 10^{-6}.

Décodage du code de mémoire d'unité partielle à huit états

F. HEMMATI

Sommaire

On décrit dans cet exposé des méthodes efficaces de mise en oeuvre, totalement en série ou totalement en parallèle, d'un décodeur pour code de mémoire d'unité partielle à huit états, de rendement 4/8. Le décodeur à grande vitesse et maximum de vraisemblance proposé utilise une architecture de transformation Hadamard rapide pour calculer la métrique des branchements (nœuds), et l'on utilise le concept de co-ensembles pour réduire au minimum la complexité du matériel. Cette grande vitesse de décodage est réalisable du fait que quatre bits d'information sont produits dans chaque étape du codage, au lieu d'un seul bit d'information dans les codes à rendement 1/2.